Università
degli Studi
di Padova

Tesi di Dottorato di Ricerca in Fisica

Università degli Studi di Padova

Dipartimento di Fisica ed Astronomia “G. Galilei”

Scuola di Dottorato di Ricerca in Fisica
Indirizzo Comune
Ciclo XXVI

INNOVATIVE PLASMONIC NANOSTRUCTURES BASED ON TRANSLATION OR SCALE INVARIANCE FOR NANO-PHOTONICS

Direttore della Scuola: Ch.mo Prof. Andrea Vitturi
Supervisore: Ch.mo Prof. Giovanni Mattei

Dottorando: Niccolò Tomaso Michieli

To Anna.

I have a friend who's an artist, and he sometimes takes a view which I don't agree with. He'll hold up a flower and say, "Look how beautiful it is," and I'll agree. But then he'll say, "I, as an artist, can see how beautiful a flower is. But you, as a scientist, take it all apart and it becomes dull."
I think he's kind of nutty. There are all kinds of interesting questions that come from a knowledge of science, which only adds to the excitement and mystery and awe of a flower. It only adds. I don't understand how it subtracts.

R. Feynman (1988)

Abstract

In this thesis innovative plasmonic nanostructures have been studied under many aspects, from the synthesis to the characterization and finite elements modeling. We focused on two kinds of ordered nanostructures: (i) those exhibiting bidimensional (2D) translational invariance and (ii) those possessing autosimilarity and fractal character.

Three kinds of nanostructures characterized by 2D periodicity have been analyzed: nanoprism arrays (NPA), nanohole arrays (NHA) and quasishell arrays (QSA), whose building blocks are, respectively, metallic prisms with triangular-like base, holes passing through a metal thin film and metallic non-closed shells around a dielectric core. The first kind is the base for biosensors, and in this case an optimization study has been performed to maximize sensivity. The second one is the key for a fine control of the emission from excited Erbium ions, which overcomes the previous results obtained without nano-patterning. The third one is based on a novel approach to bi-metallic nanostructures fabrication, enabling the realization of plasmonic and magneto-plasmonic materials. The patterning at nano scales has been made cost-effective, as all these periodic systems are based on a cheap synthesis technique.

Finally, nanostructures showing scale invariance, *fractals*, have been synthesized and thoroughly studied, both experimentally and with simulations. As a result, a universal role of correlation has been recognized in these plasmonic systems.

Overall, this thesis gives insights on the physics underlying the plasmonic response of nanostructures which base their outstanding properties on symmetry, either on scaling or on translation.

Estratto

In questa tesi nanostrutture plasmoniche innovative sono state studiate sotto molteplici aspetti, a partire dalla sintesi fino alla caratterizzazione e alla modellizzazione ad elementi finiti. L'attenzione è stata focalizzata su due tipi di nanostrutture ordinate: (i) quelle che mostrano invarianza traslazionale bidimensionale (2D) e (ii) quelle che hanno autosimilarità e carattere frattale.

Tre tipi di nanostrutture caratterizzate dalla periodicità 2D sono state analizzate: matrici di nanoprismi, matrici di nanobuchi e matrici di gusci quasi chiusi, i cui elementi di base sono, rispettivamente, prismi metallici a base triangolare, buchi che attraversano strati sottili di metallo e gusci metallici non chiusi attorno a un nucleo dielettrico. Il primo tipo è la base per dei biosensori, e in questo caso uno studio di ottimizzazione è stato compiuto per massimizzare la sensibilità. Il secondo tipo è la chiave per il controllo fine dell'emissione da ioni di Erbio eccitati, e il risultato supera i precedenti, ottenuti senza nanostrutturazione. Il terzo tipo è basato su di un nuovo approccio per la fabbricazione di nanostrutture bi-metalliche, consentendo la produzione di materiali plasmonici e magnetoplasmonici. La strutturazione alla nanoscala è stata portata avanti in modo economicamente vantaggioso, essento tutti e tre i sistemi periodici basati su di una tecnica poco costosa di sintesi.

Infine, nanostrutture che mostrano invarianza di scala, *frattali*, sono state sintetizzate e studiate meticolosamente, sia sperimentalmente che con simulazioni. Come risultato, il ruolo universale della correlazione è stato identificato in questo tipo di sistemi plasmonici. Complessivamente, la presente tesi fornisce una comprensione della fisica alla base della risposta plasmonica delle nanstrutture che basano le loro notevoli proprietà sulle simmetrie, siano esse di scala o per translazione.

Contents

List of Acronyms

AFM	Atomic Force Microscope. The AFM is made by a cantilever with a tip at its end, used to scan the surface to examine. The cantilever is usually silicon or silicon nitride, and the tip radius of curvature is on the order of nanometres. When the tip is brought into proximity of the surface, forces between the tip and the sample lead to a deflection of the cantilever. Depending on the situation, forces that are measured in AFM include mechanical contact force, electrostatic forces, magnetic forces, Van der Waals forces, capillary forces, chemical bonding, Casimir forces, etc. The resolution is a fraction of nanometre.
APTES	(3-Aminopropyl)- triethoxysilane
AuNP	Gold Nanoparticles
CAD	Computer Assisted Design
CGM	Conjugate Gradient Method. An efficient algorithm to solve linear systems.
CB	Cantor Box
CD	Cantor Dust
CS	Cross Section
DDA	Discrete Dipole Approximation. A simulation technique for computing the Mie cross sections of arbitrary systems. Cf. section 2.1
DLA	Diffusion Limited Aggregation. A random process taking to the formation of fractals starting from a solution of colloidal nanoparticles. The universality of this regime makes it a very interesting system for fractal analysis.
DOF	Degree of Freedom
EBL	Electron Beam Lithography. Lithographic technique in which a polymeric substrate is patterned using an electron beam controlled by a computer. Current best resolution: 10-20nm.
EOT	Extraordinary Optical Transmission. It is the ability to transmit light beyond the limits of geometrical optics. Here, in particular, is the transmission of light through holes smaller than the diffraction limit.
FDTD	Finite Difference Time Domain. A FEM simulation technique for solving the Maxwell equations in time domain. Cf. section 2.1
FDFD	Finite Difference Frequency Domain. A FEM simulation technique for solving the Maxwell equations in frequency domain. Cf. section 2.1

FEM	Finite Element Method. A simulation technique for solving partial differential equations in spatially finite domains.
FIB	Focused Ion Beam. Lithographic technique in which a cristalline substrate is ablated using a focused beam of heavy ions (typically Gallium), and controlled by a computer.
FON	Film on Nanospheres
L4	Fourth-Order Lorentzian Model. A functionally simple model for the correction of the Drude model of dielectric function for metals. It adds four lorentzian resonances, enabling to describe also band transitions effects.
GMM	Generalised Multiparticle Mie
GMRES	Generalised Minimum Residual
LDOS	Local Density of Optical States
LFE	Local Field Enhancement
LSP	Localised Surface Plasmon. Cf. section 1.2.2
LSPR	Localised Surface Plasmon Resonance
MUA	Mercapto Undecanoic Acid
NHA	Nano Hole Array
NIL	Nano Imprint Lithography . A pattern replica method. It can reproduce high quality patterns up to a resolution of 20 nm.
NP	Nano Prisms
NPA	Nano Prisms Array
NSL	Nanosphere Lithography. A bottom-up technique to build up high-quality, large areas, array patterned nanostructures.
PBC	Periodic Boundary Condition
PDE	Partial (derivative) Differential Equation
PL	Photoluminescence
PML	Perfectly Matched Layer. An additional subdomain added to FEM models to ensure proper scattering boundary conditions also for tangent component of radiation.
QS	Quasi Shell
RIE	Reactive Ion Etching. A controlled Etching technique. A confined plasma of suitable composition is used to etch the samples. The technique mantains the patterns of the sample during the etching.

RIU	Refractive Index Unit
RLA	Reaction Limited Aggregation. A random process taking to the formation of fractals starting from a solution of colloidal nanoparticles. The universality of this regime makes it a very interesting system for fractal analysis.
RBS	Rutherford Back Scattering. A compositional analysis technique. ^{4}He nuclei are shot on the sample and the section-wise composition is obtained by a fitting procedure.
SAM	Self-Assembled Monolayer
SC	Sierpinski Carpet
SEM	Scanning Electron Microscope. In this scanning microscope, a focused beam of electrons (energy from 100 eV to 30 keV) is used as probe. The detectors use secondary electrons produced in the sample, backscattered electrons and characteristic x-rays.
SERS	Surface-Enhanced Raman Scattering
SIMS	Secondary Ions Mass Spectroscopy
SPP	Surface Plasmon Polariton. Cf. section 1.2.2
SPR	Surface Plasmon Resonance
STM	Scanning Tunnelling Microscope. A powerful microscope exploiting the quantum tunnel effect. A small tip is placed very near to the surface to be examined, and a difference of potential is applied, giving rise to a *tunnelling current* when electrons pass through the vacuum from the tip to the surface. The current is a function of the local density of states, making it possible to image the surface by scanning it with the tip and monitoring the tunnelling current. The best STMs can have a resolution of 0.01 nm in depth and $0.1nm$ on the surface.
TEM	Transmission Electron Microscope. In this microscope the sample is in the objective lens. The electron beam (energy from tens of keV to 1 MeV) passes through a suitably thinned sample (10 nm) and forms contrast in different modes, particularly in imaging (direct space) and diffraction (spatial fourier transform)

List of Figures

List of Tables

Introduction

Nanotechnology is a relatively new discipline, which focuses on the control of structures on atomic and molecular scales. Nanotechnology typically deals with lengths of about 100 nm or less at least in one dimension, and the scope is to produce devices within such dimensions. It comes out of the contributions by many sciences, such as physics, chemistry, biology, material sciences and engineering.

Historically, the first suggestion came from Richard Feynman, in the famous talk "There's Plenty of Room at the Bottom" at Caltech in 1959 [1]. Feynman proposed to build machines, say 10 times smaller than normal, using regular-sized ones. Then, he said, it would have been possible to use these new machines to build even smaller machines. Applying these steps recursively, one would finally get nanometric machines. Many cares were to be kept in count, because the ratios between different forces weren't constant along this process, as gravitational force is negligible on small dimensions whereas phenomena like Van der Waals forces and surface tension become predominant, and Feynman analysed these aspects, too.

The term “Nanotechnology” was first used by N. Taniguchi in a 1974 paper [2]: “'Nanotechnology' mainly consists of the processing of, separation, consolidation, and deformation of materials by one atom or by one molecule.” These ideas were explored in more depth by E. Drexler in the 1980s.

Experimentally nanosciences had their crucial boost due to the birth of *cluster science* and to the invention of the *Scanning Tunnelling Microscope (STM)* in early 1980s. Soon after *fullerenes* were discovered (1985), and a few years later *carbon nanotubes* were obtained. Nanotechnologies had then after a great expansion, and many achievements came out, e.g. *nanocrystals* synthesis, *quantum dots* technology, *Atomic Force Microscopes (AFMs).*

To assemble a microscopical system there are basically two approaches, called *Top-Down* and *Bottom-Up.* Both have advantages and drawbacks, and one should choose the most suitable for his purposes.

In the Top-Down approach one constructs a device capable of operating directly on nanoscales, and controls the process macroscopically, for example by a computer. This technique enables to manufacture virtually every object one may want, but is generally expensive and often requires a new planning if the design of the wanted result changes. Thus, it is perfect to mass-produce devices, once the final design is achieved and remains unchanged. Actually, in this way initial costs to get the producing machine are amortised. A classical example of Top-Down is *Photolithograpy*: firstly a mask is created, mechanically or electro-mechanically, and then, using a beam of photons (UV, X-rays) or particles (electrons, ions), the negative of the mask is “printed” on a surface, that becomes nanostructured. Producing the mask may be quite expensive (thousands Euros). However one mask enables to fabricate even millions of products, and this process is inexpensive, making it possible to amortise mask costs. This is the way microprocessors (whose transistors arrive to be only 32 nm wide) usually fabricated.

On the other hand in the Bottom-Up method, one exploits particular properties of atoms and molecules, and, to a larger extent, of nanoparticles, so that they reach by themselves the wanted form or geometry. Advantages of this way of proceeding are that one doesn't need complex machinery to manufacture products, and that the results may have incredible precisions (down to a few Å, such as for *Self-Assembled Monolayers (SAMs)* or *Nanosphere Lithographys (NSLs)*). It is clear however that only relatively few configurations may be achieved in this way, as the system will evolve only towards energetically and thermodynamically advantageous ones. When this is possible, anyway, one gets very good results in an inexpensive way. In micro and nano-systems it is often exploited the SAM technique, which enables to get a single layer of molecules on a substrate tuning the affinity of molecules with substrate.

Nanostructures and Interaction with Electromagnetic Radiation

The part of the electromagnetic spectrum which we refer to as “light” spans over the wavelenghts that are visible to human’s eye, roughly from 400 to 700 nm. With a slight abuse, even the near infrared and the near ultra-violetcan be included in the “light” definition, given that the sources of photons, the detectors and the optics work in a comparable way for wavelengths from about 200 nm to about 2000 nm. The discipline that studies the production, propagation and detection of radiation in the NIR-Vis-NUV range, called photonics, made great improvements in all the machinery necessary to exploit light as a probe and, more generally, as a carrier of information. In this particular range research and technology can benefit from the presence of a wide range of sources of light (from vapour lamps to Lasers), of relatively cheap and easy to use and implement optics (such as mirrors and lenses), and of efficient detectors of many kinds (from photomultipliers to Single Photon Avalanche Detectors or SPADs). This mature field makes light an extremely interesting tool for a wide range of applications, from sensors to communication, from renewable energies to opto-electronics. However, photons both have a size (the wavelength) and carry energy, and not always the correct energy for a given phenomenon corresponds to the most suitable wavelength, and thus the coupling of devices to light can be not optimal. As an example, biological molecules often have a rich and detailed spectrum in the near infrared region. Photons in the near infrared however have a wavelength of some thousands of nanometres, whereas the molecules are no more than some nanometre in size. Thus, in absence of a device which mediates these two scales, the couplig of molecules to light (i.e. its cross section) is poor, making it necessary to use more powerful sources and/or more efficient detectors, both of which are undesirably more expensive. Nanophotonics is the branch of photonics which is focused on the enhancement of the coupling of the light to systems at the nanometric scale. Plasmonics has then become one of the most important fields in the framework of photonics [3], and is focused on the interaction of electromagnetic fields with nanostructures, mainly made of noble metals, with the objective to control light on scales below the $\lambda/2$ diffraction limits. When this happens, usually an enhancement of the field intensity is associated to its confinement below its wavelength. Moreover, the confinement in very narrow zones (demonstrated in slits under 1 nm) makes it possible to efficiently couple molecules and, more generally, emitters (atoms, quantum dots...) to light, making it possible to achieve impressive results such as single molecule recognition, photon cutting, optical amplification. These aspects will be reviewed more deeply in chapter 1.

Innovative Nanostructures

The availability of more and more efficient and precise top-down techniques such as *Electron Beam Lithography (EBL)* and *Focused Ion Beam (FIB) lithography* enable researchers to investigate more and more complex nano-patterns for plasmonics. However, those methods still have strong disadvantages: the costs, the relatively limited resolution and the poor control over the vertical direction in patterning. The design of innovative nanostructures, as performed in this thesis, has the objective to build nanostructures with interesting plasmonic properties in a cost-effective way. In particular, two strategies have been followed: on one hand, to find efficient and cheap methods of nano-patterning based on the bottom-up approach; on the other hand, to investigate the properties and behaviour of systems that don't show translational symmetry. In particular, this second way focused on topologies that, in place of periodicity, have the scale invariance as a fundamental feature. These topologies are currently called *fractals*, and have been studied both in the deterministic and random parts. Deterministic fractals are mathematically simpler and they are much easier to treat for the investigation on their fundamental properties. However, the experimental realization of these structures currently involve the use of expensive lithographic methods, thus the basic features of deterministic fractals have been searched for in random fractals, that are less easy to treat, but have been realized in cost-effective ways.
The process of design of innovative structures involves many steps: from the idea, to the *Computer Assisted Designs (CADs)* production of model and computer simulation of the electromagnetic properties, from the sample realization to its structural and optical characterization. All of these steps have been taken into account in this work, and particular interest has been given to the computer simulation of the designed geometries. This crucial step, using continous feedback and control on the experimentally realized samples, enabled to optimize performances and foresee new behaviours of analyzed nanostructures.

Why Translational Invariance?

The concept of translational invariance and periodicity is fundamental in physics. The physical optics is based on the interference of waves, and the periodicity of the system is a key to diffraction patterns, mode selection, photonic crystals, etc. The role of periodicity is thus fundamental for many aspects. In this work, the periodicity has multiple roles, exploited by the different presented applications. Periodicity is exploited at two levels: when the “monomers” do not interact, and when they interact, giving rise to new “collective” properties. For nanoprisms, the periodicity is the key to obtain a large set of *copies* of the same monomer, all of which behave in the same way, thus enabling the detection of a signal which would be too weak if generated by only one prism. Nano Hole Arrays (NHAs) are based on the presence of periodicity as the key to extraordinary transmission of light, the same periodicity enables the use of nanohole arrays as (2D) diffraction gratings, and the Bloch formalism foresees the presence of crystal modes due to the periodicity. All these aspects are exploited in the NHA-emitter interaction, and all are based on the translational invariance. Finally, the importance of ordered systems in Quasishells is in the fabrication process: the ordered, close-packing lattice which forms the array is the key for the maximization of density of nanostructures, and thus the base of a high-perfomance device which exploits this kind of nanosystems. Obviously, as in the case of nanoprisms and nanohole arrays, the collective effects due to the periodicity, just as diffraction, are still present, and the exploiting of these modes opens up still other opportunities. Thus, the translational invariance has a deep signifiance, and is an invaluable resource in the nanosystems design and modeling, since it allows also to deal just with the unit cell to describe the entire array physics.

Fractals and Self-Similarity

A fractal is a geometric object whose structure is repeated at different length scales. Although fractals were discovered in XIX century, the term "fractal" was coined only in 1975 by B. Mandelbrot. He describes a fractal as "a rough or fragmented geometric shape that can be split into parts, each of which is (at least approximately) a reduced-size copy of the whole." [4] The stress is then laid on the property called *self-similarity.* A self-similar object is characterised by the presence of a particular symmetry, the symmetry of scale. This means that a fractal may be magnified remaining equal to the original object. Perhaps the most important consequence of this symmetry is that in a fractal structure any *typical length* disappears.
Fractals are present everywhere in nature, from biological systems to mountains and coast profiles. Fractals are also a typical result of non-linear (chaotic) dynamical systems, and in this perspective there are deep connections between fractals and chaos theory. Understanding the behaviour of a structure involving fractal geometries often allow to broaden knowledge about chaotic and complex systems connected with that structure. Three examples of fractals are given in figure 0.1: Appendix B will provide some results and techniques on fractals.

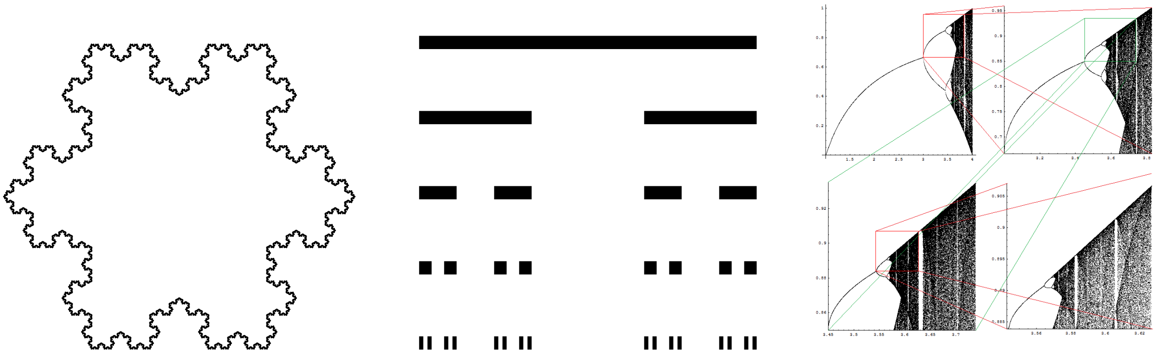

(a) A Koch snowflake

(b) Construction of Cantor dust set

(c) Self-similarity in a logistic map

Figure 0.1.: Three examples of fractals.

Why Self-Similarity?

In last years a few works came out tackling the use of fractal nanostructures in plasmonics, dealing with some particular cases, in which both dimensions of single particles and geometry have some self similar nature. Systems consisting of few particles whose dimension and distances scale with a fixed ratio are exploited for *nanolensing* [5,6]. Simple aperiodic [7,8] and fractal [9–11] geometries have been investigated, suggesting that interesting phenomena take place even in self-similar systems. On the other hand in macroscopic communication technologies, fractal geometries for antennae have been known and exploited since decades [12], and works still are made in lately interesting ranges such as THz [13]. Thus, interesting properties should arise when dealing with self-similar nanostructures, and it is desirable to systematically detect the effects of geometric characteristics on the interaction with radiation.

A promising application of plasmonic systems is in the bio-medical sector, as properties like field enhancement and confinement may be very useful for diagnostics and imaging [14]. In this perspective exploitation of self-similar configurations is very interesting, as the result of many dynamical, complex phenomena, such as those occurring in biological system, have a rather self-similar looking. It's also clear that using the evolution of a chaotic system for the production of a configuration is very similar to the self-assembling techniques [15], with all related advantages on costs [9]. As a system looses its regularities, its order, on the other hand it acquires self-similarity. And that is a not negligible resource.

Investigating this field is thus interesting, both for basic physics involving self-similar geometries and for possible applications.

The present thesis is organizad as follows:

Chapter 1 will describe the fundamental properties of the light-matter interaction at nanoscales, and in particular the formation and features of localized and propagating plasmons.

Chapter 2 will describe the simulation techniques here used, and in particular the processes of discretization of both geometry and equations.

Chapter 3 will deal with the considered nanostructures which show translational invariance, and in particular nanotriangles arrays (NTA), nanohole arrays (NHA) and quasishell arrays (QSA).

Chapter 4 will deal with nanostructures showing the scale invariance, fractals, both in random and in deterministic configurations.

1. Interaction between Nanostructures and Electromagnetic Radiation

1.1. Electronic Properties of Metals

The interaction between radiation and metals is complex, depending both on the frequency of the field and on the electronic structure of the metal. For low frequency radiation metals are highly reflective, so that the fields don't enter in the material more than a fraction of a wavelength called skin depth. When the frequency approaches the visible range, the energy dissipation in the metals becomes considerable, and makes it difficult to scale the behaviour of the metal from the low frequency regime. Starting from near ultraviolet, metals behave as dielectrics when interacting with the radiation, and so they support propagation of EM waves with refractive index and absorption depending on the electronic structure.
For the description of the interaction in a classical fashion, a relevant quantity turns out to be the complex dielectric function $\varepsilon(\omega)$. The determination of $\varepsilon(\omega)$ may be experimental or theoretical, and a simple model is given by the *Drude model*, which works particularly well for alkali metals in the visible range. The model can be derived from the Maxwell's Equations

$$\nabla \cdot \mathbf{D} = \rho_{ext} \tag{1.1}$$

$$\nabla \cdot \mathbf{B} = 0 \tag{1.2}$$

$$\nabla \times \mathbf{E} = -\frac{\partial \mathbf{B}}{\partial t} \tag{1.3}$$

$$\nabla \times \mathbf{H} = \frac{\partial \mathbf{D}}{\partial t} + \mathbf{J_{ext}} \tag{1.4}$$

in terms of the electric field (**E**), magnetic field (**H**), electric displacement (**D**) and magnetic induction (**B**). These four fields are linked by the following relations to the polarisation **P** and the magnetisation **M**:

$$\mathbf{D} = \varepsilon_0 \mathbf{E} + \mathbf{P} \tag{1.5}$$

$$\mathbf{H} = \frac{1}{\mu_0}\mathbf{B} - \mathbf{M}. \tag{1.6}$$

As only nonmagnetic media will be considered, the term **M** will be neglected. The polarisation **P** is linked to the internal charge density ρ_{int} by $\nabla \cdot \mathbf{P} = -\rho_{int}$, thus the equation of continuity ($\nabla \cdot \mathbf{J} = -\frac{\partial \rho}{\partial t}$) imposes that

$$\mathbf{J} = \frac{\partial \mathbf{P}}{\partial t}. \tag{1.7}$$

Moreover, as definition of the conductivity σ can be defined by the following equation:

$$\mathbf{J} = \sigma \mathbf{E}. \tag{1.8}$$

If the medium is linear, isotropic and nonmagnetic, relations 1.5 and 1.6 can be expressed in terms of relative electrical permittivity ε and magnetic permeability μ:

$$\mathbf{D} = \varepsilon\varepsilon_0\mathbf{E} \tag{1.9}$$

$$\mathbf{B} = \mu\mu_0\mathbf{H}. \tag{1.10}$$

Equations 1.8 and 1.9 are however correct only if the medium does not exhibit spatial or temporal dispersion. This condition is clearly non satisfied by metals, as their response is strongly dependent on frequency. The generalisation is then:

$$\mathbf{D}\left(\mathbf{r},t\right) = \varepsilon_0 \int \mathrm{d}\mathbf{r}'\mathrm{d}t'\varepsilon\left(\mathbf{r}-\mathbf{r}',t-t'\right)\mathbf{E}\left(\mathbf{r}',t'\right) \tag{1.11}$$

$$\mathbf{J}\left(\mathbf{r},t\right) = \int \mathrm{d}\mathbf{r}'\mathrm{d}t'\sigma\left(\mathbf{r}-\mathbf{r}',t-t'\right)\mathbf{E}\left(\mathbf{r}',t'\right). \tag{1.12}$$

These equations become significantly simpler when taking the Fourier Transform, which turns convolutions into multiplications. In the Fourier domain $(\mathbf{k},\omega)$ equations 1.11 and 1.12 then become

$$\mathbf{D}\left(\mathbf{k},\omega\right) = \varepsilon_0\varepsilon\left(\mathbf{k},\omega\right)\mathbf{E}\left(\mathbf{k},\omega\right) \tag{1.13}$$

$$\mathbf{J}\left(\mathbf{k},\omega\right) = \sigma\left(\mathbf{k},\omega\right)\mathbf{E}\left(\mathbf{k},\omega\right). \tag{1.14}$$

A further simplification can be made in the approximation of spatially local interaction. This approximation is good whenever the wavelength λ is larger than other relevant lengths, in particular the size of the unit cell and the mean free path of the electrons. In general this condition is satisfied if $\lambda \gtrsim 10^{-7}m$, that is up to the ultraviolet. In this case the relative permeability ε (from now on called dielectric function) becomes $\varepsilon\left(\mathbf{k}=0,\omega\right) = \varepsilon\left(\omega\right)$.

1.1.1. Drude Model

Most of the interesting information about metal-radiation interaction is embedded in the dielectric function $\varepsilon\left(\omega\right)$ of the metal. A very simple way of calculating this function is given by the Drude model or the free electron gas model. In this model the electrons of a metal move in a lattice formed by positive ions. The number of electrons ensure the charge neutrality, and no electron-electron interaction is considered. Electrons move according to the external fields, until they collide with a ion of the lattice. Collisions randomise the velocity of electrons, and take place with a frequency $\gamma = \frac{1}{\tau}$, where τ is the relaxation time of electrons.

Despite these drastic assumptions, the model works well in a wide range of frequencies, usually up to the energies of interband transitions of the metal. These transitions occour in the visible range for noble metals and in the near ultraviolet for alkali metals. When they become important a more refined treatment is necessary.

For an electron satisfying the assumptions of the model, the equation of motion in presence of an external electric field $\mathbf{E}$ results

$$m\ddot{\mathbf{x}} + m\gamma\dot{\mathbf{x}} = -e\mathbf{E}. \tag{1.15}$$

Assuming a harmonic dependance of the driving field, $\mathbf{E} = \mathbf{E_0}e^{-i\omega t}$, then the steady state solution too will have the harmonic dependance, $\mathbf{x} = \mathbf{x_0}e^{-i\omega t}$, and substituting in eq.1.15 the result is:

$$\mathbf{x}\left(t\right) = \frac{e}{m\left(\omega^2 + i\gamma\omega\right)}\mathbf{E}\left(t\right). \tag{1.16}$$

The macroscopic polarisation $\mathbf{P}$ will get a contribute from the displaced electrons $\mathbf{P} = -ne\mathbf{x}$, or, explicitly:

$$\mathbf{P} = -\frac{ne^2}{m\left(\omega^2 + i\gamma\omega\right)}\mathbf{E}, \tag{1.17}$$

which, once inserted into 1.5 yields:

$$\mathbf{D} = \varepsilon_0 \left(1 - \frac{\omega_p^2}{\omega^2 + i\gamma\omega}\right)\mathbf{E}, \tag{1.18}$$

where $\omega_p^2 = \frac{ne^2}{\varepsilon_0 m}$ defines the *plasma frequency* of the free electron gas. From equation 1.18 the dielectric function results:

$$\varepsilon\left(\omega\right) = 1 - \frac{\omega_p^2}{\omega^2 + i\gamma\omega} = 1 - \frac{\omega_p^2}{\omega^2 + \gamma^2} + i\frac{\omega_p^2\gamma}{\omega\left(\omega^2 + \gamma^2\right)} = \varepsilon_1\left(\omega\right) + i\varepsilon_2\left(\omega\right). \tag{1.19}$$

In the limit of $\omega \gg \omega_p$ the dielectric function would asymptotically reach the constant value $\varepsilon\left(\omega\right) = 1$. In real metals, and particularly in noble metals this is not true, as there are d electrons near the Fermi surface, taking to a greater polarisation. This effect can be embedded in equations by adding the term $\mathbf{P}_\infty = \varepsilon_0\left(\varepsilon_\infty - 1\right)\mathbf{E}$ to eq. 1.5, where now $\mathbf{P}$ describes only the polarisation due to free electrons. The dielectric function now becomes:

$$\varepsilon\left(\omega\right) = \varepsilon_\infty - \frac{\omega_p^2}{\omega^2 + i\gamma\omega}. \tag{1.20}$$

Figure 1.1 compares the Drude model with experimental data from Johnson and Christy [17] for three noble metals. The model agrees well with experimental points until interband transitions become important ($\approx 2eV$ for copper and gold, $\approx 4eV$ for silver).

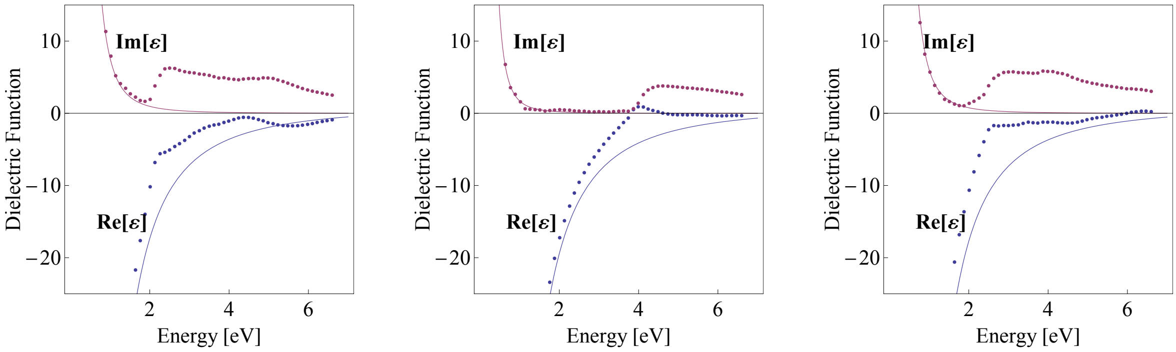

(a) Copper **(b)** Silver **(c)** Gold

Figure 1.1.: Drude model for real metals. Dots represent experimental data from Johnson and Christy [17], lines are best fits with Drude model.

1.1.2. Lorentzian Model

An improvement of the Drude model takes into account also bounded electrons, i.e. those involved in transitions, by adding a term to the equation of motion 1.15:

$$m\ddot{\mathbf{x}} + m\gamma\dot{\mathbf{x}} + m\omega_0^2\mathbf{x} = -e\mathbf{E}. \tag{1.21}$$

The term $m\omega_0^2\mathbf{x}$ describes the absorption and emission processes due to a interband transition with energy $\hbar\omega_0$. The result in the dielectric function is an additional term of Lorentzian form. When considering more then one transition, multiple terms come out, and the final result for N transitions is:

$$\varepsilon(\omega) = \varepsilon_\infty + \frac{i\sigma}{\varepsilon_0\omega} + \sum_{j=1}^{N} \frac{C_j}{\omega^2 + iA_j\omega + B_j}. \tag{1.22}$$

Depending on how many terms are considered, the model has different names. For example, the model with four transitions is called L4. Using the coefficients A_j, B_j and C_j in tab.1.1 from Nordlander and Hao [18], figure 1.2 compares the L4 model with experimental data from Johnson and Christy. The L4 model agrees very well with experimental data, and is particularly helpful for Finite Difference Time Domain (FDTD) calculations, being the form of $\varepsilon(\omega)$ however simple.

Table 1.1.: Parameters for the L4 fit of Au and Ag dielectric data

	Au ($\varepsilon_\infty = 1.0$, $\sigma/\varepsilon_0 = 1355.01 s^{-1}$)			Ag ($\varepsilon_\infty = 1.0$, $\sigma/\varepsilon_0 = 3157.56 s^{-1}$)		
	A_j $[eV]$	B_j $[eV^2]$	C_j $[eV^2]$	A_j $[eV]$	B_j $[eV^2]$	C_j $[eV^2]$
j=1	$8.577 \cdot 10^4$	$-1.156 \cdot 10^4$	$5.557 \cdot 10^7$	$1.160 \cdot 10^5$	-3050	$3.634 \cdot 10^8$
j=2	2.875	0	$2.079 \cdot 10^3$	4.252	-0.8385	112.2
j=3	997.6	-3090	$6.921 \cdot 10^5$	0.496	-13.85	1.815
j=4	1.63	-4.409	26.15	2.118	-10.23	14.31

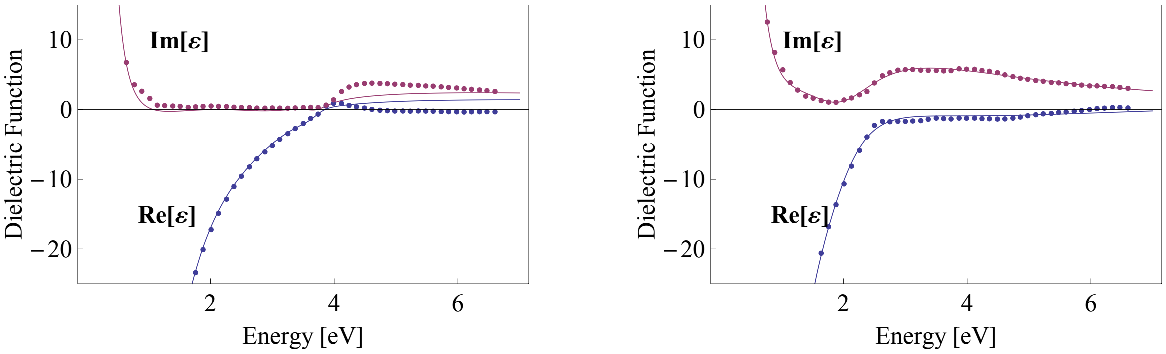

(a) Silver **(b)** Gold

Figure 1.2.: Comparison of the L4 model with experimental data from Johnson and Christy.

1.1.3. Size Dependent Corrections

These models describe bulk metals, thus when working with nanoparticles, with sizes of the order of 20nm or less, they may not work well [19] due to quantum confinement effects. In particular, the assumption of collisions only with ions is no longer correct, as surface scattering become important. It's possible to consider the effect of this scattering in a semi-classical fashion and valid for spherical particles, inserting a term describing the dependance of $\varepsilon = \varepsilon(\omega, R)$ on the dimension of the particle R. The frequency of surface scattering will be a function of the shape and size of the particles. In particular, a coefficient A will describe the shape (for a spherical particle, $A \approx 1$). The average time for an electron to cross the particle is of order of $\frac{R}{v_F}$, v_F being the Fermi velocity of the electron. So, the frequency of surface scattering results $\gamma_S = A\frac{v_F}{R}$. Because the relaxation processes are described in the Drude model by the electron-electron scattering frequency γ_∞, when dealing with small particles, the surface scattering must be added to it, $\gamma(R) = \gamma_\infty + \gamma_S(R)$. The dielectric function then becomes:

$$\varepsilon(\omega, R) = \varepsilon_\infty - \frac{\omega_p^2}{\omega^2 + i\gamma(R)\,\omega}. \tag{1.23}$$

In general, if $\varepsilon_{bulk}(\omega)$ is the dielectric function of a metal, it can be corrected for size dependance in the following way (cf. [19]):

$$\begin{aligned} \varepsilon(\omega, R) = \varepsilon_{bulk}(\omega) + \omega_p^2 &\left(\frac{1}{\omega^2 + (2\pi\gamma_\infty)^2} - \frac{1}{\omega^2 + (2\pi\gamma(R))^2}\right) + && (1.24) \\ + i\frac{\omega_p^2}{\omega} &\left(\frac{2\pi\gamma(R)}{\omega^2 + (2\pi\gamma(R))^2} - \frac{2\pi\gamma_\infty}{\omega^2 + (2\pi\gamma_\infty)^2}\right). && (1.25) \end{aligned}$$

Table 1.2 gives the values of the inverse of relaxation time $\gamma_\infty = \tau^{-1}$ and of the Fermi velocity at $273K$ for Gold, Silver and Copper from [20]. This correction is particularly important for the imaginary part of the dielectric function, as fig.1.3 shows.

Table 1.2.: Relaxation time, Fermi velocity and Plasma frequency of Au,Ag and Cu

	Relaxation Time τ $(10^{-14}s)$	Scattering Frequency γ_∞ $(10^{13}s^{-1})$	Fermi Velocity v_F $(10^6 m/s)$	Plasma Frequency ω_p $(10^{16} rad \cdot s^{-1})$
Au	3.0	3.3	1.40	1.370
Ag	4.0	2.5	1.39	1.366
Cu	2.7	3.7	1.57	1.642

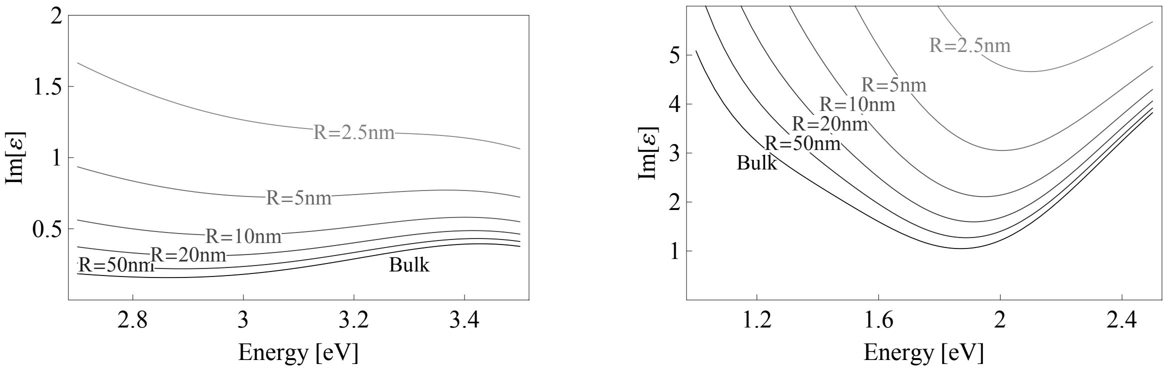

(a) Silver **(b)** Gold

Figure 1.3.: Effects of the size-dependent corrections to the dielectric function for nano spheres of radius R.

1.2. Plasmon Polaritons

1.2.1. Volume Plasmons

Neglecting corrections due to size and interband transitions, and assuming $\omega\tau \gg 1$ (high frequency approximation), the dielectric function of the Drude model simplifies to

$$\varepsilon(\omega) \approx \varepsilon_1(\omega) = 1 - \frac{\omega_p^2}{\omega^2} \tag{1.26}$$

in the regime $\omega > \omega_p$, where the metal is transparent to radiation. It thus supports travelling waves, whose dispersion relation results:

$$\omega^2 = \omega_p^2 + k^2 c^2. \tag{1.27}$$

These travelling waves can be thought as collective oscillations of the electrons against the fixed ions, with frequency ω_p. The quanta of these oscillations are called (*volume*) *plasmons*. Because volume plasmons result uncoupled to EM radiation, the only way of getting excited is by the impact of charged particles.

1.2.2. Surface Plasmon Polaritons

Other kinds of plasmons are more interesting because of their interaction with light, namely *Surface Plasmon Polaritons (SPPs)* and *Localised Surface Plasmons (LSPs).*

When electromagnetic radiation couples with the oscillations of the electron plasma, electromagnetic surface waves may arise. This is possible at the interface of two materials with opposite signs of the real part of their dielectric function, i.e. a metal and an insulator. In this case the wave is trapped at the interface, evanescently confined in the perpendicular direction. The resulting excitations are called SPPs. Because of the confinement, in this situation field enhancement is possible, due to concentration of radiation in sub-wavelength volumes.

The starting point to study this phenomenon is the wave equation:

$$\nabla^2 \mathbf{E} - \frac{\varepsilon}{c^2} \frac{\partial^2 \mathbf{E}}{\partial t^2} = 0. \tag{1.28}$$

Assuming, in all generality, a harmonic dependance of $\mathbf{E}$, i.e. $\mathbf{E}(\mathbf{r}, t) = \mathbf{E}(\mathbf{r})\, e^{-i\omega t}$, this yelds the *Helmholtz equation*:

$$\nabla^2 \mathbf{E} + k_0^2 \varepsilon \mathbf{E} = 0, \tag{1.29}$$

where $k_0 = \frac{\omega}{c}$ is the wave vector of the propagating wave in vacuum. To keep the problem simple, let's assume the wave travelling along the x direction, and the dielectric function ε to vary only in the z direction, $\varepsilon = \varepsilon(z)$, i.e. planar interfaces are assumed. At $z = 0$ there is the interface between metal and insulator. The propagating waves are described in this geometry by the equation $\mathbf{E}(x, y, z) = \mathbf{E}(z)\, e^{i\beta x}$, $\beta = k_x$ being a complex parameter called *propagation constant.* It corresponds to the component of the wave vector of the SPP in the direction of propagation. Resolving eq.1.29 (together with the similar one for $\mathbf{H}$) and imposing proper boundary conditions on fields yields the dispersion relations of a SPP:

$$\beta = k_0 \sqrt{\frac{\varepsilon_m \varepsilon_d}{\varepsilon_m + \varepsilon_d}}, \tag{1.30}$$

where ε_m and ε_d are the dielectric functions of metal and insulator, respectively. This relation is valid both for ε_m complex and real, i.e., for metals with or without attenuation. Figure 1.4 shows the dispersion relations of SPP at interface between a Drude metal and air and silica. The SPP excitations correspond to the part of the dispersion curve at the right of the light line, thus special techniques are needed for phase matching, as light is not sufficient. The simplest techniques are the *prism coupling* and the *grating coupling*.

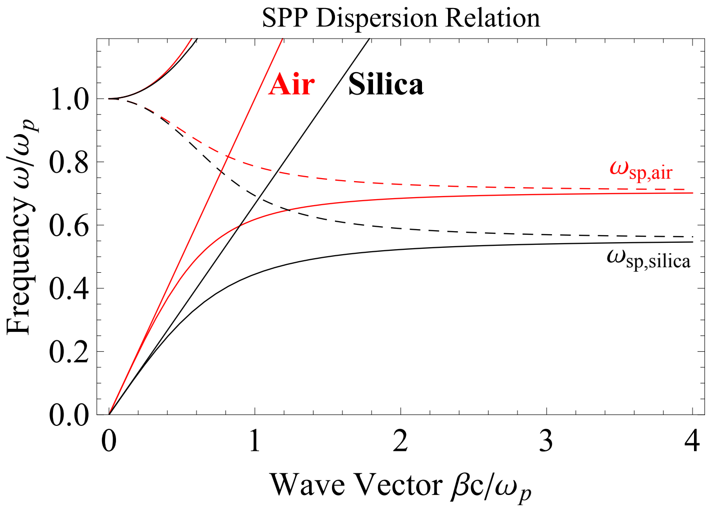

Figure 1.4.: Dispersion relations at Drude metal/air and Drude metal/silica interface. Solid lines represent real wave vector β, dashed lines represent imaginary wave vector. Also light lines ($\omega = kc$) are shown.

1.2.3. Localised Surface Plasmons

SPPs are propagating, dispersive EM waves coupled to the electron plasma of a conductor at a dielectric interface. Another fundamental excitation can exist, in presence of confined nanostructures. In fact, the electrons of a nanostructure can couple to the electromagnetic field, and the excitations of this coupling are the LSPs. The curved surface of a particle with sub-wavelength size exerts a restoring force on electrons, so that resonances may arise when the particle is placed in an oscillating EM field. These resonances take to a field enhancement both inside the particle and in the near-field zone around it. Contrary to SPPs, these modes can be directly excited by light, without any special technique. The frequency of the resonance depends on the shape and the size of the particles. Except for spherical or spheroidal particles, a general analytic solution does not exist. For instance, the Mie theory allows a full treatment of the scattering by a single non-interacting spherical particle cite kreibig95,bohren98. However, when the shape of a particle has no particular symmetry or when dealing with ensembles of interacting and/or arbitrarily shaped particles, the problem becomes very complex, and computational methods become necessary. At a first approximation, if the particle size R is small with respect to the wavelength of the radiation λ and to the distance between particles d, the system may be approximated by a set of interacting dipoles. Two different regimes are found, depending on the distance between particles being much smaller or greater than the wavelength. If $d \ll \lambda$, then the near field interaction dominates, giving rise to terms of the order of $1/d^3$ for the field. On the other hand, if $d \gg \lambda$, the far field interactions dominates,

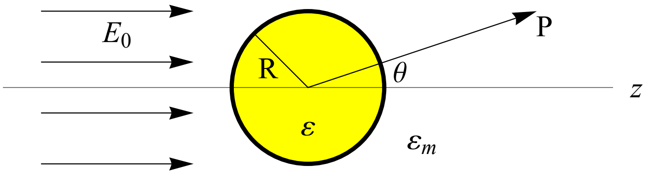

Figure 1.5.: A simple geometry for the quasi-static approxiamtion

with terms proportional to $1/d$.

1.3. Single Particle

The full problem of the scattering of light by a single non-interacting sphere has been tackled and solved by Mie [21]. He proposed, given the spherical symmetry of the system, to expand the the internal and scattered fields into a set of normal modes (multipolar expansion) described by vectorial spherical harmonics. A further extension of the theory, proposed by Gans [22], provides exact results for ellipsoidal non-interacting particles.

1.3.1. Quasi-static Regime

The Mie and Gans solutions are exact, but many terms may be needed for the multipolar expansion to properly converge e.g. when $R \gg \lambda$, so the computational efforts for calculations can become considerable. It's then useful to use approximations, to keep calculations simple. For particles much smaller than the wavelength in the surrounding medium, $R \ll \lambda$, the *quasi-static approximation* is suitable. In this case the spatial variations of the fields over the particle can be neglected, and the problem can be regarded as a particle in an uniform and slowly varying field. Therefore, once the distribution of the field is known over the space, the harmonic time dependance can then be added.

For an analytical treatment consider this convenient geometry: a homogeneous, isotropic sphere of radius R located at the origin in a uniform, static electric field $\mathbf{E} = E_0\hat{\mathbf{z}}$, as in fig.1.5. The sphere is surrounded by an isotropic, non-absorbing medium of dielectric constant ε_m. Sufficiently far from the sphere the field lines are parallel to $\hat{\mathbf{z}}$. The metal has the dielectric function $\varepsilon(\omega)$, which is, for the moment, a constant ε. The equation to solve is the Laplace equation, $\nabla^2\Phi = 0$, from which the electric field results $\mathbf{E} = -\nabla\Phi$. Due to the spherical symmetry of the problem, the solutions will be of the form [23]:

$$\Phi(r,\theta) = \sum_{l=0}^{\infty} \left[A_l r^l + B_l r^{-(l+1)}\right] P_l(\cos\theta). \tag{1.31}$$

By imposing the solution to be finite at the origin and the continuity relations on the surface of the sphere, the final solutions for the fields inside and outside the sphere read:

$$\Phi_{in} = \frac{-3\varepsilon_m}{\varepsilon + 2\varepsilon_m} E_0 r\cos\theta \tag{1.32a}$$

$$\Phi_{out} = -E_0 r\cos\theta + \frac{\varepsilon - \varepsilon_m}{\varepsilon + 2\varepsilon_m} E_0 R^3 \frac{\cos\theta}{r^2}. \tag{1.32b}$$

Physically, the solution 1.32b is the superposition of the applied electric field and of a dipole placed at the centre of the particle:

$$\Phi_{out} = -E_0 r \cos\theta + \frac{\mathbf{p}\cdot\mathbf{r}}{4\pi\varepsilon_0\varepsilon_m r^3} \tag{1.33a}$$

$$\mathbf{p} = 4\pi\varepsilon_0\varepsilon_m R^3 \frac{\varepsilon - \varepsilon_m}{\varepsilon + 2\varepsilon_m}\mathbf{E_0}. \tag{1.33b}$$

The magnitude of the dipole moment is proportional to $|\mathbf{E_0}|$, thus, the polarizability α, defined by $\mathbf{p} = \varepsilon_0\varepsilon_m\alpha\mathbf{E_0}$, results:

$$\alpha = 4\pi R^3 \frac{\varepsilon - \varepsilon_m}{\varepsilon + 2\varepsilon_m}. \tag{1.34}$$

The polarizability experiences a resonant enhancement when the denominator in 1.34 is small. For a Drude metal with slow varying imaginary part of $\varepsilon(\omega)$ the resonance condition leads to the *Fröhlich condition*:

$$\varepsilon_1(\omega) = -2\varepsilon_m. \tag{1.35}$$

The normal mode associated with the *dipole surface plasmon* of the metal nanoparticle gives rise to a resonance. If a sphere is placed in air or vacuum, the resonance frequency results, in the Drude approximation, $\omega_0 = \frac{\omega_p}{\sqrt{3}}$. Equation 1.35 further shows that, for a Drude metal, the resonance frequency redshifts as the dielectric constant of the medium is increased.
From equation 1.32 the fields are obtained via $\mathbf{E} = -\nabla\Phi$:

$$\mathbf{E}_{in} = \frac{3\varepsilon_m}{\varepsilon + 2\varepsilon_m}\mathbf{E_0} \tag{1.36a}$$

$$\mathbf{E}_{out} = \mathbf{E_0} + \frac{3\mathbf{n}(\mathbf{n}\cdot\mathbf{p}) - \mathbf{p}}{4\pi r^3\varepsilon_0\varepsilon_m}, \tag{1.36b}$$

where $\mathbf{n}$ is the unit vector. When the polarizability α is enhanced, the internal and dipolar fields are enhanced, too. It's this enhancement to be the basis of many applications of interest of metal nanoparticles in optical devices and sensors.
For particles much smaller than the wavelength, the harmonic dependance of the fields can be restored in a very simple way, indeed the dipole representation is valid in the quasi-static regime, and the retardation effects can be neglected over the volume of the particle. So, if an external field of the form $\mathbf{E}_0(\mathbf{r}, t) = \mathbf{E}_0 e^{-i\omega t}$ is applied, then the dipole moment results

$$\mathbf{p} = \varepsilon_0\varepsilon_m\alpha\mathbf{E_0}e^{-i\omega t}, \tag{1.37}$$

and α is the same as equation 1.34, where now $\varepsilon = \varepsilon(\omega)$. The dipole radiation constitutes the waves scattered by the particle. It is known from electromagnetism (cf. [23]) that the total fields of a dipole can be written as:

$$\mathbf{E} = \frac{1}{4\pi\varepsilon_0\varepsilon_m}\left[k^2(\mathbf{n}\times\mathbf{p})\times\mathbf{n}\frac{e^{ikr}}{r} + (3\mathbf{n}(\mathbf{n}\cdot\mathbf{p}) - \mathbf{p})\left(\frac{1}{r^3} - \frac{ik}{r^2}\right)e^{ikr}\right] \tag{1.38a}$$

$$\mathbf{H} = \frac{ck^2}{4\pi}(\mathbf{n}\times\mathbf{p})\frac{e^{ikr}}{r}\left(1 - \frac{1}{ikr}\right), \tag{1.38b}$$

where $k = \dfrac{2\pi}{\lambda}$ and $\mathbf{n}$ is the unit vector in the direction of the point P of interest.
For optical applications and for imaging, the scattering and absorption cross sections are interesting, and can be computed using the Poynting vector from equations 1.38 (cf. [24]):

$$\sigma_{sca} = \frac{k^4}{6\pi}|\alpha|^2 = \frac{8\pi}{3}k^4R^6\left|\frac{\varepsilon - \varepsilon_m}{\varepsilon + 2\varepsilon_m}\right|^2 \tag{1.39a}$$

$$\sigma_{abs} = kIm\left[\alpha\right] = 4\pi kR^3Im\left[\frac{\varepsilon - \varepsilon_m}{\varepsilon + 2\varepsilon_m}\right]. \tag{1.39b}$$

It is interesting to note that in the derivation of (1.39), it was not supposed that the particle should be metallic. Indeed, these results keep their validity even for dielectric particles. Equations and fig. 1.6 show that both scattering and absorption cross sections (and thus extinction cross section) are resonantly enhanced when the Fröhlich condition 1.35 is satisfied. For a sphere of volume V the extinction cross section $\sigma_{ext} = \sigma_{sca} + \sigma_{abs}$ has the explicit expression

$$\sigma_{ext} = 9\frac{\omega}{c}\varepsilon_m^{3/2}V\frac{\varepsilon_2}{(\varepsilon_1 + 2\varepsilon_m)^2 + \varepsilon_2^2}, \tag{1.40}$$

where ε_1 and ε_2 are the real and imaginary parts of the dielectric function of the sphere.

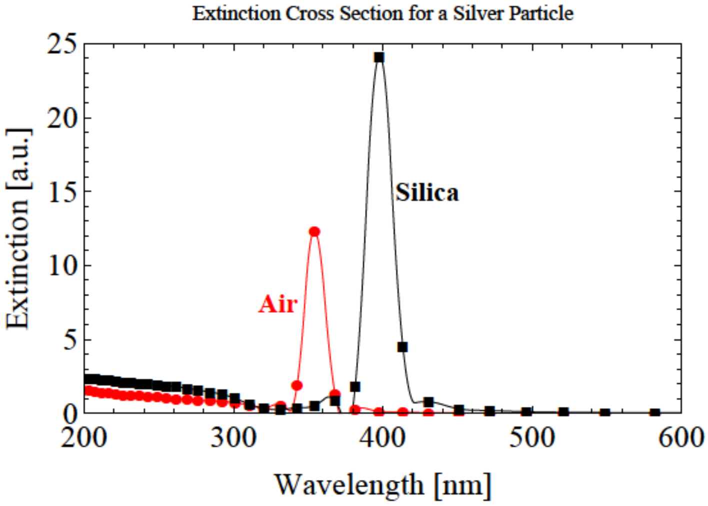

Figure 1.6.: Extinction Cross Section for a Silver Particle in air (red) and in silica (black), obtained using (1.40) on Johnson and Christy data.

1.3.2. First-order Corrections and Plasmon Lifetime

The picture given by the quasi-static approximation agrees well with experiments for particles much smaller than the wavelength of the radiation and larger than about $10 - 20$nm. First order corrections extend the model to large particles and to very small particles, down to ~ 1nm, where quantum corrections are no more negligible.
For larger radius particles, the polarizability can be easily obtained from Mie theory [25, 26]. The expression of α for a sphere of volume V results:

$$\alpha = \frac{1 - \frac{1}{10}\left(\varepsilon + \varepsilon_m\right)x^2 + O\left(x^4\right)}{\frac{1}{3} + \frac{\varepsilon_m}{\varepsilon - \varepsilon_m} - \frac{1}{30}\left(\varepsilon + 10\varepsilon_m\right)x^2 - i\frac{4\pi^2\varepsilon_m^{3/2}}{3}\frac{V}{\lambda_0^3} + O\left(x^4\right)}, \tag{1.41}$$

and the expansion parameter $x = \frac{\pi R}{\lambda_0}$ is called the *size parameter*, relating the radius to the free space wavelength. Each new term appearing in the expression has a physical significance. The term quadratic in x in the numerator leads to a shift of the resonance, and accounts for the retardation effects over the volume of the particle. Another shift is caused by the quadratic term in the denominator, describing the retardation of the *depolarisation field* [25] inside the particle. For Drude and noble metals, these effects lead to a red-shift when the size of the particle increases. The effects of interband transitions described by the imaginary part of ε, and not captured by the simple Drude model, become less important as a consequence of increasing size, as the resonance moves away from the interband region.

The quadratic term in the denominator also has the effect to enhance polarisation, thus reducing the importance of the imaginary part of the dielectric function ε, describing the absorption processes. However, the purely imaginary new term counteract this increase, and describe the *radiation damping*. This phenomenon is caused by the presence of a direct radiative decay route of the SPP into photons [27]. The radiative damping becomes the main decay channel as the size of the particle increases [28].

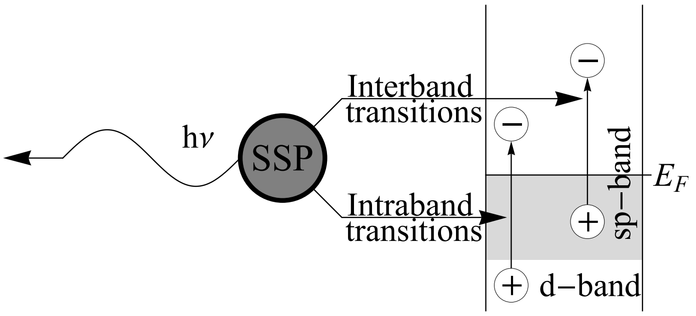

Figure 1.7.: Possible decay modes for a SPP: radiative (left) and non-radiative (right).

Summarising, there are three main channels of decay for a plasmon, as shown in fig 1.7: the radiative damping, increasingly important for larger particles, and the two non-radiative decays, Intraband and Interband transitions, dominant for smaller particles. These describe the formation of an electron-hole pair by exciting an electron either from *sp* conduction band or from the low lying *d* valence band. To give a quantitative explanation of decays, a simple two-level model from Heilweil and Hochstrasser [29] is used. The homogeneous width Γ of the plasmon resonance can be obtained by extinction microscopy, and can be related to the internal damping processes by introducing a dephasing time T_2, defined by:

$$\Gamma = \frac{2\hbar}{T_2}. \tag{1.42}$$

The coherent excitation can go through dephasing due to two kinds of processes, namely decays or scatterings, in which electrons conserve their energy, and only the momenta are changed. To take into account both effects, the dephasing time T_2 can be related to a population relaxation or decay time T_1, describing radiative and non radiative processes involving energy loss, and a *pure dephasing time* T_2^*, due to elastic processes:

$$\frac{1}{T_2} = \frac{1}{2T_1} + \frac{1}{T_2^*}. \tag{1.43}$$

Experiments by Link and El-Sayed [30] showed that, for gold and silver nanoparticles $T_2^* \gg T_1$, and so $T_2 \approx 2T_1$. The dephasing time resulted, for noble metals and depending on size and surrounding medium, in the range $5fs < T_2 < 10fs$.

The relative importance of the decay channels may be relevant for specific applications. For example, if sample heating or quenching of fluorescence must be avoided, the radiative decay should dominate. Sönnichsen and co-workers [31] performed investigations to maximise the radiative contribution, $T_{1,r}$ to the dephasing time. This is the same as maximising the quantum efficiency η for resonant light scattering:

$$\eta = \frac{T_{1,r}^{-1}}{T_1^{-1}} = \frac{T_{1,r}^{-1}}{T_{1,r}^{-1} + T_{1,nr}^{-1}}. \tag{1.44}$$

That study shows that turning to a spheroidal geometry, the non radiative damping is decreased. Dephasing times of $T_2 \approx 18fs$ have been approached, and a 3-fold quantum efficiency improvement has been achieved.

When dealing with small particles, the physics is the same reviewed in sec.1.1.3. Thus, it is sufficient to use a dielectric function including size-dependent corrections, such as (1.23), or to correct the dielectric function in use with equation 1.24. The result is the broadening of the plasmon linewidth, of the form:

$$\gamma\left(R\right) = \gamma_\infty + \frac{Av_F}{R}. \tag{1.45}$$

For very small particles, shifts of the resonance have been observed, however both redshift and blueshift appear, depending on fine details, such as the chemical termination of molecules of the particle.

The quantum limit is approached as the energy of the quanta $E \approx \hbar\omega$ becomes comparable with $k_B T$. However, given the high electronic density of metals, a classical description remains valid down to 1nm size.

1.4. Full Mie Theory

The Mie Theory, as seen, is a fundamental tool in the study of the collective electron resonances in nanostructured metals. It is strictly valid only for spheres (of any size), and in homegeneous non-absorbing media, given the correct expression for the permittivity fuction $\varepsilon\left(\omega\right)$ of the metal. However, the prediction on these simple systems can be greatly helpful to understand the behaviour of more complex structures. Here, a rapid survey of the theory is given, and a few fundamental results will be presented, which will hold more or less strictly even in very different geometric/dielectric configurations.

In the original form by Mie, the problem is formulated in the following way: the input quantities are the sphere radius (R) and the dielectric functions of both the sphere ($\varepsilon\left(\omega\right) = \varepsilon_1\left(\omega\right) + i\varepsilon_2\left(\omega\right)$) and of surrounding medium (ε_m). The solution is based upon the determination of two sets of scalar potentials (one for electric field, one for magnetic field), from which the fields are derived. The potentials must satisfy the wave equation in spherical coordinates:

$$\nabla^2 \Pi + |\mathbf{k}|^2 \Pi = 0 \tag{1.46}$$

The sets of potentials which satisfy the equation are:

$$\begin{aligned} &\Pi^{inc}_{e,m} && \text{for the incident fields,}\\ &\Pi^{in}_{e,m} && \text{for the fields inside the sphere, and}\\ &\Pi^{sc}_{e,m} && \text{for scattered field.} \end{aligned}$$

Given the spherical symmetry of the sistem, spherical polar coordiantes result the most suitable for solving the problem. The solution potentials can thus be separated in spherical coordinates:

$$\Pi\left(r,\theta,\phi\right)=R\left(r\right)\Theta\left(\theta\right)\Phi\left(\phi\right), \tag{1.47}$$

and have the functional form:

$$\Pi=\{\text{cylindrical factor}\}\cdot\{\text{Legendre spherical factor}\}\cdot\{\text{trigonomrtric factor}\}. \tag{1.48}$$

In all the formulas, the relevant parameter is the size parameter defined as $x=|\mathbf{k}|R$. Stratton [32] carried over a different development, formally introducing the vector functions **L**, **M** and **N**, which solve the wave equation and the divergency condition:

$$\mathbf{L}=\nabla\psi \tag{1.49}$$

$$\mathbf{M}=\nabla\times\left(\mathbf{R}\psi\right) \tag{1.50}$$

$$\mathbf{N}=\frac{1}{|\mathbf{k}|}\nabla\times\mathbf{M}, \tag{1.51}$$

where **k** is the wavevector and ψ is a scalar function. The fields **E** and **H** can then be derived from the vector potentials **M** and **N** in the same way as from the Mie potentials Π. Setting $\mathbf{L}=0$ means neglecting the longitudinal plasmons, which have not recognizable experimental effects.

1.4.1. Response of Isolated Metal Spheres

The complete electrodynamic solution of the single sphere problem is obtained by finding a solution of Maxwell's equations with proper boudary conditions at the sphere surface (continuity of the tangential component of electric field). Following the approach by Stratton, three macroscopic parameters can be defined and related to experiment in a straightforward way. The cross sections, which will be described in details in a subsequent sections, account for the absorption (σ_{abs}) and scattering (σ_{sca}) of light as an effect of the interaction with the metal sphere. The cross sections are related to the intensity loss $I\left(z\right)$ of a parallel beam of incident light. Using the Lambert-Beer equation, the intensity loss can be expressed as:

$$\Delta I_{abs}\left(z\right)=\left(1-e^{-\rho\sigma_{abs}z}\right)\quad\text{and} \tag{1.52}$$

$$\Delta I_{sca}\left(z\right)=\left(1-e^{-\rho\sigma_{sca}z}\right) \tag{1.53}$$

if the loss is purely from absorption or scattering, respectively, and where ρ denotes the numerical density of spheres. For real particles, both absorption and scattering contribute, and the extinction cross section is the sum of the two cross sections, describing the whole intensity loss:

$$I\left(z\right)=I_0e^{-\rho\sigma_{ext}z}. \tag{1.54}$$

The quantity $\rho\sigma_{ext}z$ is often called *absorbance*, or, more properly, *optical density.* The cross sections can be calculated from the theory as series expansions in terms of *multipoles*:

$$\sigma_{ext} = \frac{2\pi}{|\mathbf{k}^2|}\sum_{L=1}^{\infty}(2L+1)\,Re\left(a_L+b_L\right), \tag{1.55}$$

$$\sigma_{sca} = \frac{2\pi}{|\mathbf{k}^2|}\sum_{L=1}^{\infty}(2L+1)\left(|a_L|^2+|b_L|^2\right), \tag{1.56}$$

$$\sigma_{abs} = \sigma_{ext}-\sigma_{sca}. \tag{1.57}$$

The coefficients a_L and b_L are defined as:

$$a_L = \frac{m\psi_L\left(mx\right)\psi_L'\left(x\right)-\psi_L'\left(mx\right)\psi_L\left(x\right)}{m\psi_L\left(mx\right)\eta_L'\left(x\right)-\psi_L'\left(mx\right)\eta_L\left(x\right)} \tag{1.58}$$

$$b_L = \frac{\psi_L\left(mx\right)\psi_L'\left(x\right)-m\psi_L'\left(mx\right)\psi_L\left(x\right)}{\psi_L\left(mx\right)\eta_L'\left(x\right)-m\psi_L'\left(mx\right)\eta_L\left(x\right)}. \tag{1.59}$$

In these expressions, $m = n/n_m$, where n is the complex refractive index of the metal and n_m is the real refractive index of the surrounding medium. $\psi_L\left(z\right)$ and $\eta_L\left(z\right)$ are the Riccati-Bessel cylindrical functions. The prime indicates differentiation with respect to the argument in parentheses. Each term of the series is indicated by its summation index L, which denotes the corresponding multipole in the expansion. The $L = 1$ term indicates the dipole fields, $L = 2$ the quadrupolar fields, $L = 3$ the octupolar and so on. Far from the sphere surface, the fields are the same as the ones produced by a point multipole. The multipolar description of scattering is general, also in systems where spherical symmetry is not present, thus making this framework useful for the interpretation of results even in much complex systems.

Response dependance on Material, Size, Medium

Using equations 1.55 it is possible to see the effects of particle size and of dielectric function in the extinction of isolated spheres. Also the role of different multipoles can be recognized. Though the strictness of hypothesis used, it is surprising to see how these results will be helpful in the interpretation of response of much elaborated structures.

Figure 1.8a shows the extinction of a sphere, with radius $R = 10$nm, in vacuum, made of different noble metals (Gold, Silver and Copper). In this $R \ll \lambda$, quasi-static regime, the shape and intensity of the resonance is similar to that of a point dipole having the same polarizability of the metal. Thus, the dielectric function is responsible of the great difference among the responses of these three metals. On one hand, silver has a near-vanishing ε_2 in the region where the Fröhlich condition (eq. 1.35) is satisfied. As a consequence, the resonance is strong and narrow, much more than in the case of gold and copper. On the other hand, in copper the Fröhlich condition causes the resonance to be in a region where inter-band transitions can be excited, thus, a large damping is present (in the form of a non-negligible value of ε_2), giving rise to a weak and broad resonance. The case of gold is an intemediate: though the inter-band transitions are neglectable at the resonance, they are much closer to it. This causes a higher-valued ε_2 than in the case of silver, and a resonance which is in the middle between silver and copper in terms of both strenght and width of the resonance. This is the reason why silver often gives the best plasmonic performances, and why copper is not suitable for standard

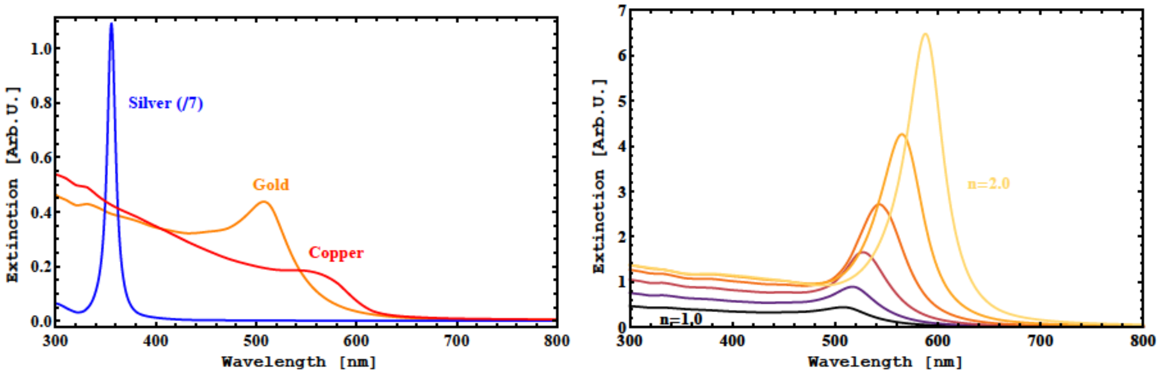

(a) Materials dependance of response for a $R = 10\text{nm}$ sphere in vacuum.
(b) Embedding medium dependance of response for a $R = 10\text{nm}$ gold sphere.

Figure 1.8.: Effect of sphere and medium materials on Mie extinction cross section resonance

localized-plasmon applications. Though the response is significantly worse than for silver (however, this behaviour is partially recovered when using larger structures, as the resonance is in this case more decoupled from interband transitions), gold is still interesting because of better chemical stability against, as an example, the oxidation. Also the dielectric properties of the surrounding medium have a significant role controlling the position of resonance, as shown by figure 1.8b. The increase of refractive index in this case causes both a redshift and an enhancement of the resonance. This particular behaviour will be exploited in the netx chapters to control the position of the resonance and, more interestigly, to design devices which are sensitive to small variations in the surrounding refractive index.

Figure 1.9a shows how the extinction varies when changing the radius of a sphere. Two effects are clearly recognisable: a redshift and a broadening of the resonance as the particle size grows. The redshift is caused by the presence of retardation effects (a first order correction, as discussed in sect.1.3.2) inside the sphere. Also the broadening of resonance is ultimately due to retardation effects: on one hand, a first-order correction term has been already discussed; on the other hand, the presence of different field values over the sphere makes it possible to excite higher order multipoles (which in the case of spheres are more energetic with respect to the dipole), giving rise to a broder resonance, result of the convolution of the multipole peaks.

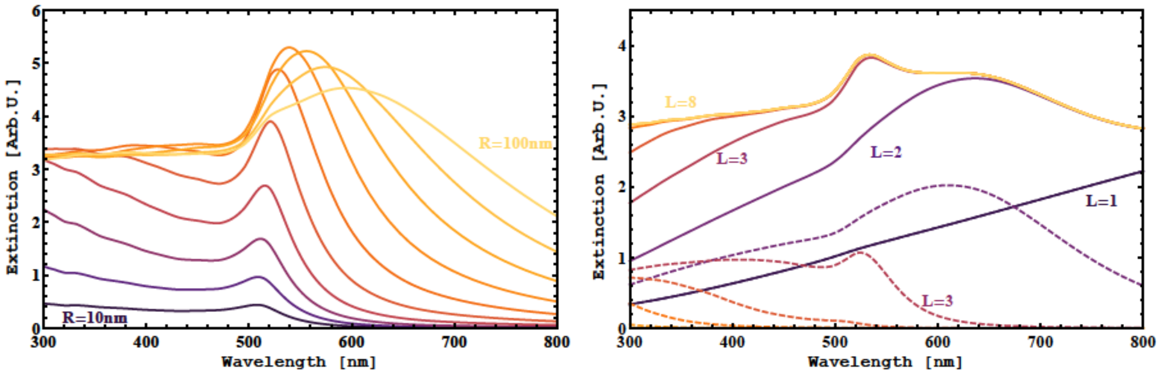

(a) Radius dependance of response for a gold sphere in vacuum.
(b) Contributions of successive multipoles to the extinction spectrum of a $R = 200\text{nm}$ gold sphere.

Figure 1.9.: Effect of radius and multipoles on Mie Resonance. Dashed lines plot the single multipoles.

Thus, when the size of the sphere increases, it is necessary to consider higher order multipoles, as shown by fig.1.9b. In this case, $R = 200$nm, the spectrum converges when multipoles up to $L = 8$ are considered. In particular it is evident that the dipole alone doesn't exhibit a peak at all, and that quadrupole and octupole are not sufficient to give the correct response.
As a last result from Mie Theory, it is interesting to compare the contribution of absorption and scattering to the whole extinction. Fig.1.10a show the separation of absorption and scattering for a $R = 10$nm, gold sphere. The scattering is in this case completely negligible (due to its R^6 scaling) with respect to absorption (scaling as R^3 in the dipolar regime). Fig.1.10b, on the other hand shows the two cross sections for a $R = 100$nm sphere: in this case absorption and scattering are of the same order of magnitude, with scattering dominating all over the visible spectrum. It worth noting also the important shift between absorption and scattering. This is due to the way multipoles interact to form the far-field pattern of extinction; the same reason makes it subtle to strightly deduce near-field spectrum from far field ones.

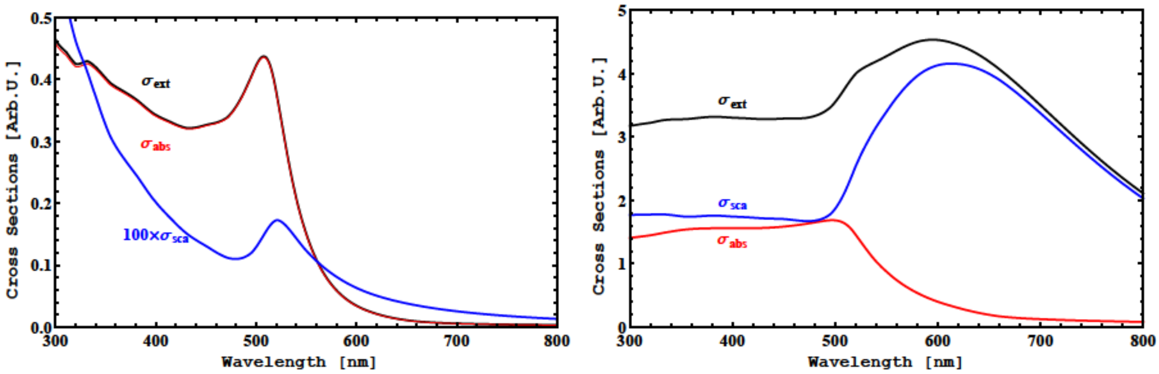

(a) Absorption and scattering cross sections in a $R =$ 10nm gold sphere.

(b) Absorption and scattering cross sections in a $R =$ 100nm gold sphere

Figure 1.10.: Comparison of absorption and scattering.

1.4.2. Generalizations

Beyond the spherical model by Mie, only a few systems can be treated rigorously. Nevertheless, the qualitative behaviour of such configurations is still present in many complex structures, so it is interesting to review some of these extensions.

Core-shell particles

A full electrodynamic treatment can be carried out to compute the response of core-shell spherical particles. In the frame of Mie Theory, the multipole coefficient a_L and b_L are in this case modified to take into acconut the presence of shells around a core sphere. The situation is that of many kinds of systems, where the presence of different materials make it possible to gather the desired properties from each of them. As an example, a plasmonic core and a magnetic shell give rise to magneto-plasmonic nanoshell showing the coupling of the magnetic and optical properties of the two metals. The presence of an active medium, or gain medium is in some case useful, as the presence of quantum dots or emitters as a core. All these cases (still in a spherical symmetry framework) can be treated with this formalism. Finally, the presence of a thin layer of dielectric around a plasmonic particle is the typical situation in a (bio- or chemical) sensor, thus the results from these calculations can be used for interpretation and comparison to those kinds of devices. The solution, suggested by Sinzig and coworkers [33,34] and is based on recursive calculation over the layers of the core-shell(s). The recursive terms are defined as (ψ_L and χ_L are Riccati-Neumann and Riccati-Hankel functions):

$$T_L^s = -\frac{m_s\psi_L(m_s x_s)\left[\psi_L'(x) + T_L^{s-1}\chi_L'(x_s)\right] - \psi_L'(m_s x_s)\left[\psi_L(x_s) + T_L^{s-1}\chi_L(x_s)\right]}{m_s\chi_L(m_s x_s)\left[\psi_L'(x) + T_L^{s-1}\chi_L'(x_s)\right] - \chi_L'(m_s x_s)\left[\psi_L(x_s) + T_L^{s-1}\chi_L(x_s)\right]} \tag{1.60}$$

$$S_L^s = -\frac{\psi_L(m_s x_s)\left[\psi_L'(x) + S_L^{s-1}\chi_L'(x_s)\right] - m_s\psi_L'(m_s x_s)\left[\psi_L(x_s) + S_L^{s-1}\chi_L(x_s)\right]}{\chi_L(m_s x_s)\left[\psi_L'(x) + S_L^{s-1}\chi_L'(x_s)\right] - m_s\chi_L'(m_s x_s)\left[\psi_L(x_s) + S_L^{s-1}\chi_L(x_s)\right]}, \tag{1.61}$$

while the first two terms are set to zero, $T_L^0 = S_L^0 = 0$. These coefficients are computed recursively, starting from the core ($s = 1$) and going outer through the $r - 1$ shells ($s = r$). Finally, the coefficients T_L^r and S_L^r are written in the terms of the multipolar expansion, in analogy with original Mie form:

$$a_L = -\frac{m_s\psi_L(m_s x_s)\left[\psi_L'(x) + T_L^r\eta_L'(x_s)\right] - \psi_L'(m_s x_s)\left[\psi_L(x_s) + T_L^r\eta_L(x_s)\right]}{m_s\eta_L(m_s x_s)\left[\psi_L'(x) + T_L^r\eta_L'(x_s)\right] - \eta_L'(m_s x_s)\left[\psi_L(x_s) + T_L^r\eta_L(x_s)\right]} \tag{1.62}$$

$$b_L = -\frac{\psi_L(m_s x_s)\left[\psi_L'(x) + S_L^r\eta_L'(x_s)\right] - m_s\psi_L'(m_s x_s)\left[\psi_L(x_s) + S_L^r\eta_L(x_s)\right]}{\eta_L(m_s x_s)\left[\psi_L'(x) + S_L^r\eta_L'(x_s)\right] - m_s\eta_L'(m_s x_s)\left[\psi_L(x_s) + S_L^r\eta_L(x_s)\right]} \tag{1.63}$$

In anology with the homogeneous sphere case, in the formulas, $m_s = n_{s+1}/n_s$ is the ratio between the refractive index of two adjacent layers, and $m_r = n_m$ is the refractive index of the host medium. The size parameters are defined as $x_s = k_s \cdot R_s = 2\pi n_s R_s/\lambda_0$. Figs. 1.11a and 1.11b show the dependance of the extinction on, respectively, the thickness of a dielectric shell of a fixed refractive index, and on the dielectric refractive index for a fixed thickness. The two insets show the feasibility of sensing using plasmonics, by relating the analyte properties (refractive index, thickness) to the spectral position and intensity variations in the Surface Plasmon Resonance (SPR).

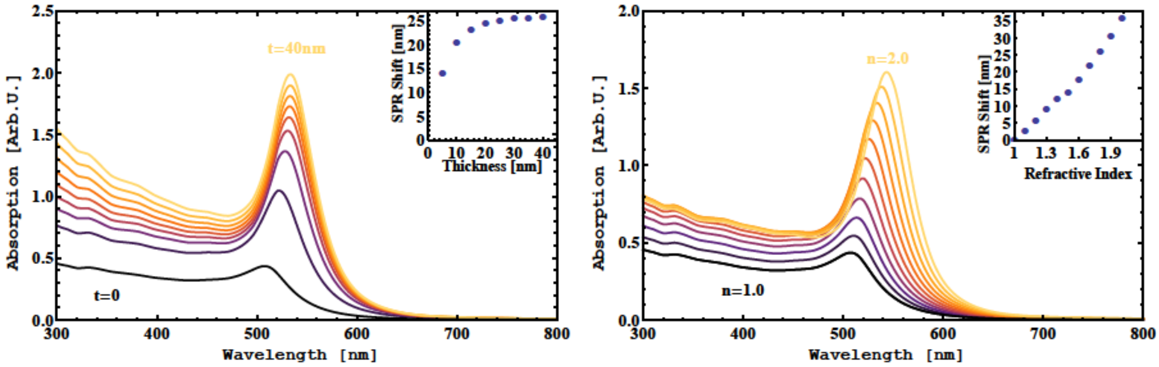

(a) Extinction for a coated ($n = 1.5$) $R = 10$nm gold sphere as a function of coating thickness.

(b) Extinction for a coated ($t = 5$nm) $R = 10$nm gold sphere as a function of coating refractive index.

Figure 1.11.: Response of coated spheres using core-shell Mie generalization.

Nonspherical particles

In a quasi-static regime (i.e. considering only the dipolar fields), a generalization of the Mie Theory has been derived by Gans [22,35] for ellipsoidal particles. In the case of a generic ellipsoid, whose axes are a, b and c,

$$\frac{x^2}{a^2}+\frac{y^2}{b^2}+\frac{z^2}{c^2}=1, \tag{1.64}$$

the polarizability along the principal axes can be found by defining the three geometrical factors L_1, L_2 and L_3:

$$L_1=\frac{abc}{2}\int_0^\infty\frac{\mathrm{d}q}{(a^2+q)\,f(q)},\quad L_2=\frac{abc}{2}\int_0^\infty\frac{\mathrm{d}q}{(b^2+q)\,f(q)},\quad L_3=\frac{abc}{2}\int_0^\infty\frac{\mathrm{d}q}{(c^2+q)\,f(q)}, \tag{1.65}$$

where $f(q)=\left[\left(q+a^2\right)\left(q+b^2\right)\left(q+c^2\right)\right]^{1/2}$. The polarizations along the three axes then result to be:

$$\alpha_i=4\pi abc\frac{\varepsilon-\varepsilon_m}{3\varepsilon_m+3L_i\left(\varepsilon-\varepsilon_m\right)},\quad i=1,2,3. \tag{1.66}$$

If the axes sizes satisfy the inequalities $a\geq b\geq c$, then the geometrical factors will satisfy the inequalities:

$$L_1\leq L_2\leq L_3,$$

and $L1+L2+L3=1$.

Interacting particles

A fast and accurate solution of the Maxwell's equations for a finite distribution of particles have been derive by Garcia de Abajo [36, 37]. In this approach, a self-consistent calculation of multiscattering is performed, in the framework of multipole expansion.
The effect of interaction is shown in fig. 1.12, where the extinction from a dimer formed by two identical gold spheres is presented, varying the distance between the two particles. The electric field polarization is along the dimer axis. The effect of the interaction is visible as both an increase in extinction and in a redshift of the peak. The increase of extinction is due to the formation of a hot spot located between the two spheres. In this gap, the field is strongly confined, thus its norm grows signifincantly, up to three orders of magnitude. The absoption, which is proportional to E^2, results enhanced in the region of the gap. Though this region is rather small (of the order of the gap in all three directions), the enhancement is sufficiently high to give visible results in the spectrum. The redshift is due to the coupling of the modes of the two particles. In the dipolar approximation, this phenomenon can be described as due to the weak coupling of harmonic oscillators. The effect of coupling in this model is the lowering of resonance energy, exactly what a redshift means in the case of photons and plasmons.

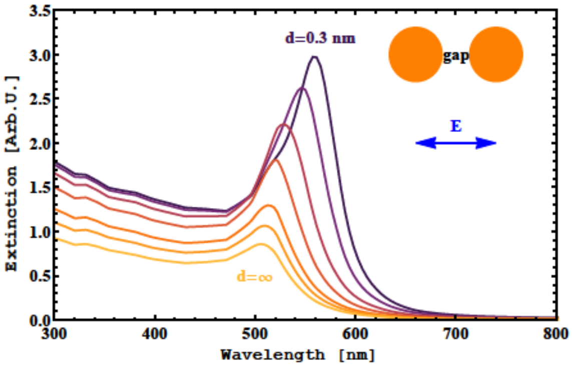

Figure 1.12.: Response of two interacting gold spheres ($r=10$nm) as a function of the gap between the two. The electric field is polarized along the centre-centre axis.

1.5. Many Particle Systems

When dealing with many particle systems, one must take into account the interactions between all particles. As the number of elements increase, clearly the number of their mutual interactions increases. An analytical approach is not in this case affordable, and other techniques are used.

The first attempt to describe interacting particles systems is the Maxwell-Garnett [38] technique, useful for small particles ($R \lesssim 10\text{nm}$), which can be described as dipoles and not too large filling factor p (i.e. the fraction of volume occupied by nano particles). This is an effective medium theory that describes the entire system (nano particles with dielectric function $\varepsilon(\omega)$ and medium with dielectric constant ε_m) as an homogeneous system with an effective dielectric function ε_{eff}, defined by the relation

$$\frac{\varepsilon_{eff} - \varepsilon_m}{\varepsilon_{eff} + 2\varepsilon_m} = p\frac{\varepsilon - \varepsilon_m}{\varepsilon + 2\varepsilon_m}, \tag{1.67}$$

where p is the nanoparticle filling factor. Two interesting properties of the theory are the redshift of the SPR absorption with increasing filling factor and the agreement with exact Mie Theory in the limit of small p.

If particles are perfect spheres, a multipolar expansion can be considered, the result is the so-called *Generalised Multiparticle Mie Theory*, GMM [39]. In absence of a such spherical symmetry, the only reliable resource is computer simulation with approximations. The next chapter will briefly review these methods along with GMM approach.

1.6. Imaging Experiments: Cross Sections and Efficiencies

The simplest experimental method to optically characterise nanostructures or ensembles of nanoparticles consists in the measurement of Cross Sections (CSs). The two most important cross sections are the scattering σ_{sca} and the absorption σ_{abs} cross sections. Their sum gives the extinction CS, σ_{ext}. The absorption CS describes the absorption of incident radiation by nanostructures and successive non radiative decays. It can be computed as the ratio between the power absorbed and the total incident power. Experimentally, a spectrophotometer is used to measure the extinction cross section[1]: two identical beams are produced, and one of them passes through the sample. When the light passes through the nanostructures, its intensity decays exponentially, following the Lambert-Beer equation:

$$I(z) = I_0 \exp(-\beta z), \tag{1.68}$$

and β is equal to the density of nano-particles multiplied by their extinction cross section. The extinction cross section given by the spectrometer is defined by the reciprocal of the logarithm of the transmittance:

$$A = -\log_{10}\left(\frac{I}{I_0}\right), \tag{1.69}$$

so that the extinction cross section is proportional to the extinction A:

$$A = C\sigma_{ext}. \tag{1.70}$$

---

[1] In imaging experiments the quantity measured is called absorption. In fact the difference between the reference and the sample beam gives the sum of the absorption and the scattering. For nanometric samples, however, the absorption dominates over the scattering and the extinciton is very close to it.

The constant C is proportional to the density of clusters ρ and to the sample thickness z: $C = \rho z \log_{10}(e)$. To get the scattering cross section the spectrophotometer is used with an integrating sphere. This tool is a chamber covered with detectors, that integrate the flux scattered by the sample[2]. The absorption CS is then computed as $\sigma_{abs} = \sigma_{ext} - \sigma_{sca}$.

Following Messinger et al. [40], two different scattering CSs can be defined for a sphere of radius R, to take into account different effects and phenomena. The (far field) scattering cross section is the ratio between the scattered and the incident time averaged flux, and can be written as a function of the scattered field $\mathbf{E}^{(\mathbf{s})}$ as:

$$\sigma_{sca} = \lim_{r \gg R} \frac{r^2}{E_0^2} \int_0^{2\pi} \int_0^{\pi} \left| \mathbf{E}^{(\mathbf{s})} (r, \theta, \phi) \right|^2 \sin\theta \mathrm{d}\theta \mathrm{d}\phi. \tag{1.71}$$

Taking the limit for $r \gg R$ means to integrate over a sphere far from the particles, where only scattered radiation field survives. As the radiation field decays ar $1/r$, the CS becomes independent of the integration sphere. If the integration is made directly on the surface of the nanoparticle, one obtains the Near Field CS:

$$\sigma_{NF} = \frac{R^2}{E_0^2} \int_0^{2\pi} \int_0^{\pi} \left| \mathbf{E}^{(\mathbf{s})} (R, \theta, \phi) \right|^2 \sin\theta \mathrm{d}\theta \mathrm{d}\phi. \tag{1.72}$$

This CS is in general larger than the far field one, as it comprises the fields that decay faster than $1/r$. This CS is very useful as it is a very good measure of the Local Field Enhancement (LFE), exploited by Surface-Enhanced Raman Scattering (SERS).

These definitions can be generalised to particles of any shape and to ensembles of particles. In particular, the far field CS can be integrated over a sphere, whose radius is much larger than the scatterer system, irrespectively if it refers to a single particle or an ensamble. The near-field CS can still be integrated over the surface(s) of the particle(s), and still remains a good measure of LFE. For systems with reduced symmetry this cross sections is less meaningful, as the LFE can be limited only to few points, also called *hot spots*, so the integration over all the particle surfaces may hide a local hot-spot. Once the hot-spots of a configurations are found, however, is still possible to compute the near field CS over the surfaces of the particles close to the hot spot.

For each Cross Section it is customary to define the (adimensional) efficiency Q:

$$Q = \frac{\sigma_i}{\sigma_{geom}} \qquad i = sca, abs, ext, NF, ... \tag{1.73}$$

where σ_{geom} is the geometric cross section defined as the surface of the projection of the system on a plane orthogonal to the incident light wavevector. The efficiency can be used to compare systems that may be different in size, shape or number of particles.

---

[2] It is possible to measure both the forward scattering (light scattered past the sample) and backward scattering, by placing the integrating sphere respectively after or before the sample. Usually, the backscattering dominates over the forward scattering and constitutes most of the total scattering.

2. Computer Simulation

Theoretically, the topic of a body immersed in a radiation field is simple, and the Maxwell equations, together with the information about the body and the surrounding media (geometries, dielectric functions...) are sufficient to completely solve the problem. Unfortunately, except for very simple and symmetrical geometries, this solution can't be analytical, and simulation techniques and/or approximations must be adopted. As pointed out in the previous chapter, these resources become capital when many particle systems are considered.
In this thesis three different computational methods will be used, and the next section will briefly review them. These techniques are the Generalised Multiparticle Mie (GMM), the Finite Element Method and the Discrete Dipole Approximation (DDA). In different situations one can exploit the advantages of each of them.

2.1. Simulation Techniques

Mie and Generalised Multiparticle Mie Theory(GMM)

GMM is the only exact method among the three considered, as directly derives from an exact theory, the Mie Theory. G. Mie, in a famous paper [21] proposed to tackle the problem of the interaction between radiation and metal clusters by expanding the fields in a multipolar fashion. As result, the scattered fields are described as a superposition of multipoles and are expressed by vectorial spherical harmonics. The application of this theory to many (spherical) particles systems is the GMM. In this theory each particle is expected to feel both the external field and the fields scattered by all the other particles, in a self-consistent way. The precision of this method is limited by the number of multipolar terms considered in the expansions. A number of the order of one thousand terms may be required to guarantee proper convergence of the series. The software used for the exact Mie Theory calculations is MiePlot, version 4.2.03 [43].

Finite Elements Methods (FEM)

These methods take into account a finite space domain, discretise it in small cells (the finite elements) and the solve the equations on every node of the discretisation.
The Finite Element Method [44,45] can work in the frequency domain (Finite Difference Frequency Domain (FDFD)) or in the time domain (FDTD). The FDFD the Helmoltz equation 1.29 is solved, with standard boundary conditions. The condition of finite domain is necessary to keep the equation system sufficiently small to be manageable, but creates problems due to back-scattering of waves by the surface. The proper scattering boundary condition must then be imposed at the outer boundary, to permit the numerical analogous of the outgoing waves [46]. The method transforms the problem in a linear system or matrix, with a Helmholtz equation for each node, and solves this system with a linear solver. The computational efforts are limited by the fact that a node is influenced only by nearby nodes, and so the matrix results sparse. Solving the

system with a Gaussian Elimination (GE) method the complexity[1] is $O\left(x^7\right)$, whereas with the Conjugate Gradient Method (CGM) it is $O\left(x^4\right)$.

The Finite Difference Time Domain method ([47]) is analogous to the FDFD, but in the time domain. Thus, it solves directly the Maxwell's curl equations 1.1, for finite successive time steps. The complexity is $O\left(x^4\right)$, but this time the memory usage is much lower than FDFD because the previous and current values of the fields at a point are used to compute the next value, making the equation fully explicit. As in the FDFD approach, a proper boundary condition must be given ([48–50]). The software used for Finite Element computations is COMSOL Multiphysics 4.3b (build 4.3.2.189). The FDTD method is faster than the FDFD method for arbitrary spectrum of incident light, however, when dealing with a single wavelength, the FDFD method has to solve only one matrix, where the FDTD method has to compute solutions for time steps until a wave period, and thus it is slower.

Discrete Dipole Approximation (DDA)

The Discrete Dipole Approximation is a simple method to tackle the problem of scattering from arbitrarily shaped particles. It is based on subdivision of the scatterer in a set of discrete points, each one described as a polarisable dipole. This way, all the points have a dipolar behaviour, described by equations such as eqs.1.38, from which the cross sections are computed. As the dipolar approximations holds only for small particles, the dipole size must be small, an adequate criterion being

$$|m|kl < 1, \tag{2.1}$$

where $|m|$ is the modulus of the refractive index and l the size of the nanostructure (in the following also called "target"), and k is the modulus of the wavevector in vacuum. If the refractive index is large compared to unity ($|m-1| \gtrsim 2$), the criterion should be refined, with smaller-sized dipoles, as the Absorption cross section may be overestimated in these cases. The method was firstly introduced by Purcell and Pennypacker in 1973 ([51]), and then after was reviewed and developed further by Draine ([52]), Draine and Goodman ([53]). It has been recently extended to periodic structures by Draine and Flatau ([54]). The software used is in this case is DDSCAT, version 7.1.0 [55].

2.2. The Finite Element Method

The finite element method is a technique used to solve Partial Differential Equations (PDEs) by computational approximate procedures. The key to the method, as the name suggests, is the sub-division of the domain in which the equations live in finite elements. This process is called *meshing* and the resulting elements are called *mesh elements.* In a general 3D problem, meshing elements may refer to solid elements (typically tetrahedra), surfaces (forming the boundaries of solid elements, typically triangles), curves (forming the edges of boundaries), or points. Where not specified, in a d-dimensional problem, mesh element is meant to be the d-dimensional mesh element, i.e. in a 3D problem, mesh elements are polyhedra.

---

[1] The computational complexity of an algorithm is defined as the number of steps required as a function of the size of the result x.

2.2.1. Meshing Process

The meshing process has a paramount importance in FEM. If the mesh is too coarse, the solution may be incorrect, or neglect important phemomena taking place at small scales with respect to the meshing scale. On the other hand, if the mesh is too fine, the computational efforts necessary for a solution may overcome the available resources. In particular, the solution of nano-photonic problem using finite elements is yet more challenging for the meshing process, as two very different scales come into play together. Far-field radiation is mainly composed by plane waves, which can be described correctly only in domains larger than half the wavelength (Shannon's theorem). Using visible to near infrared light, the minimum (far-field) domain consists of several hundreds of nanometres. On the other hand, the nanostructures have details and features on the scale of a few nanometres, and, most important, close to the surfaces of metals the decay of fields takes place in not more than some tens of nanometres, thus the correct description of fields needs a very fine meshing in these regions. As a rule of thumb, using a uniform meshing (i.e., all elements have the same size) taking into account a mesh size of 5 nm (which however in some situation may be too rough in some regions), to mesh a 3D domain with a linear size of 500 nm (necessary to describe a field with $\lambda \sim 1000$nm), the total number of mesh elements is about $(500\text{nm}/5\text{nm})^3 = 10^6$. A model consisting of one million mesh elements is not solvable with *direct solvers* even in a 128 GB, 64 core server, and on the same machine it saturates all the resources using the *iterative solvers* (cfr. sect.2.3).
A precise strategy for meshing is necessary, and it should take into account the physical nature of the phenomena one wants to explore. A good starting point is to have at least an approximate idea of the near-field distribution, using analogies with Mie calculations, experimental data, or simple explorative simplified models. Where the near-fields become neglectable (usually no more than some tens of nanometres for localized plasmons), the far field patterns can be described in terms of plane waves, and the mesh can be considered accurate if it is finer than $\lambda/6$. So, a model with elements not larger than 50 nm can describe consistently light with wavelengths not shorter than 300nm. Near the surface of metals, and in general where near-fields are important, on the other hand, the mesh should be much finer, in particular where the geometry have sharp edges or vertices. As a general rule, the mesh can be considered sufficient when, changing settings to finer and finer, the results of the computations remain the same with different meshings. Figure 2.1 show these concepts. In fig.2.1a, the section of the model is shown. The red sphere in the center is a gold nanoshpere, surrounded by vacuum. The mesh is much finer in the interior of the sphere subdomain, as the fields have large variations here. The region close to the surface, outside the nanoparticle, is also finely meshed, to correctly describe the evanescent field. The mesh in the rest of the domain becomes less fine, but always fulfilling the $\lambda/6$ condition. Finally, the volume embedding the gold nanosphere has a radius which is defined to be $\lambda/2$, to satisfy Shannon's condition. Note an additional sub-domain, outside the other two, which has a different kind of meshing (rectangular boundaries take the place of triangular boundaries). This region is dedicated to the Perfectly Matched Layer (PML), which prevents backscattering of outgoing waves from the external boundaries, and it will be better described later. Fig.2.1b show the meshing strategy for a nano-prism with triangular-like base. In this case, given the *extruded* geometry, the vertical meshing is a pure replica of the base meshing over a certain number of levels. This procedure on one hand assures that the precautions taken to correctly mesh the base will extend to the whole volume; on the other hand, it optimizes the number of mesh elements by preventing a too fine meshing in region where it is not necessary. For the meshing

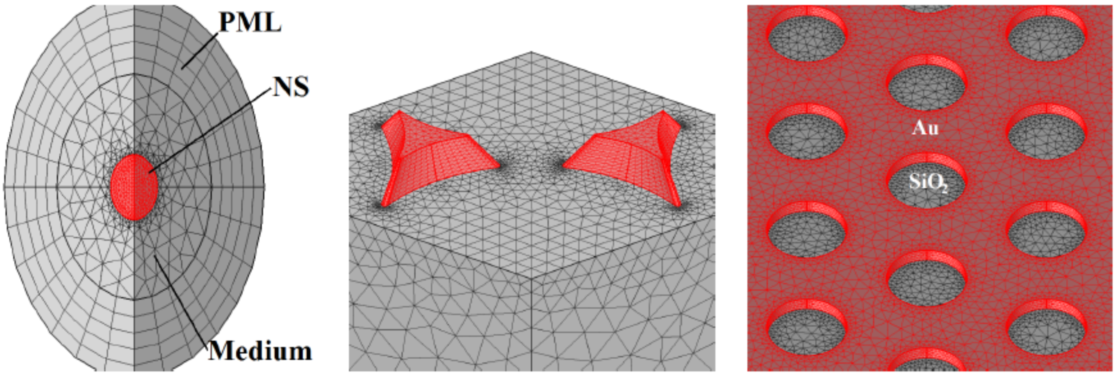

(a) Gold Nanosphere in Vacuum. **(b)** Silver Nanoprisms on SLG. **(c)** Gold Nanohole Array on Silica.

Figure 2.1.: Samples of meshing, adapted to geometry and field distributions (in red the plasmonic nanostructures).

of the base, some physical hints should be taken into account. First, the higher field values are concentrated at sharp edges, or at regions with high curvature. This is the case of the angles of the base. Thus, the region close to the angles will be finely meshed. A less fine mesh is possible along the edges of the triangle, where the curvature is weak or null. Another aspect to consider is the interaction between nanostructures. If such interaction is present, it is capital to have a sufficiently fine mesh also in the region where this interaction takes place. Given the geometry of the lattice, where the triangles face each other with the sharp tips, it is necessary to use a fine meshing in the gap between the triangles. Fig.2.1c show a different kind of nanostructure. In this case the gold forms a continous film with holes. The plasmons that are supported by this kind of structure are no more the localized ones, but the propagating plasmons. Because the field confinement is much weaker in this case, the mesh can be coarser in general. Because the interesting plasmonic behaviour of this nanostructure arises from holes, it will be sufficient to use a finer mesh only inside and close to the holes.

Also the shape of mesh elements is important: high aspect ratios in one or two directions can take to a degradation of the whole mesh, taking to poor quality results. If the shape of the mesh elements is particularly bad, the element may become a *inverted mesh element*, for which the inside-outside relations are nomore correct. In presence of such elements, the solution is not possible and the mesh must be modified.

Once the mesh is set, it is possible to proceed in the solution of Partial (derivative) Differential Equation (PDE)s using finite elements. Appendix A reviews the formalism used to obtain from the PDEs the equations solved by the solvers. As a result of this derivation, the system of equations which is elaborated by a solver has the form:

$$\begin{cases} 0 = \mathbf{L}\left(\mathbf{U}\right) - N_F\left(\mathbf{U}\right)\boldsymbol{\Lambda} \\ 0 = \mathbf{M}\left(\mathbf{U}\right). \end{cases} \tag{2.2}$$

The objective is to solve this system for the solution vector $\mathbf{U}$ and the Lagrange multiplier vector $\boldsymbol{\Lambda}$.

2.3. Solvers

The result of the discretization process is a linear system of equations in the degrees of freedom. In turn, the system can be written as a $n \times n$ matrix, where n is the number of degrees of freedom of the problem. The *numerical inversion* of the matrix is the job for the linear solvers. Two main approaches to the inversion exist, giving rise to two kinds of solvers. *Direct* solvers try to invert the matrix in a single step, considering the whole matrix at a time. *Iterative* solvers start from a *guess* initial solution and try to converge to the actual solution by a many-step procedure. Both approaches have advantages and disadvantages. Additional numerical algorithms, called *presmoothers* and *preconditioners* execute linear transforms on the matrix in order to reduce the dynamical range of values and to maximize the efficiency of the solvers.

2.3.1. Iterative Solvers

Iterative solvers have the advantage that memory usage is much lower than direct solvers, and also are computationally faster. As a drawback, the solution is not the result of the inversion of the matrix, but it is the result of a step by step refinement, controlled by some kind of error estimation. Thus, the solution may have a poorer quality with respect to the direct solvers' one, and the risk of trapping in a local minimum is always present, as for all iterative methods. Further, if the problem is complex and/or the initial solution is bad, the convergence may be slow or, in the worst case, the solver may not converge at all. The only iterative solver used in this work is the Generalised Minimum Residual (GMRES).
GMRES [57, 58] is an iterative method for solving systems of the form $Ax = b$. The choice of the correct preconditioner is important for a fast convergence.

2.3.2. Direct Solvers

Direct solvers have the advantage that the matrix is actually inverted, so that the solution is always possible (there are no convergence issues), and the numerical quality of the solution is better than for iterative solver. The main drawback of direct solvers is the huge amount of needed resources, in terms of computation power and memory. Direct solvers are in general also slower than the iterative ones. Two different direct solvers have been used in the present work, namely PARDISO and MUMPS, the choice between the two being determined by the usage of parallelism during computations.

MUMPS

The parallel sparse direct linear solver MUMPS (MUltifrontal Massively Parallel sparse direct Solver) [59–61] works on general systems of the form $Ax = b$. MUMPS uses several preordering algorithms to permute the columns and thereby minimize the fill-in. MUMPS is multithreaded on platforms that support multithreading and also supports solving on distributed memory architectures through the use of MPI (libraries for shared-memory, multi-nodes computations). This solver is the most indicated for cluster computing.

PARDISO

The parallel sparse direct linear solver PARDISO [62–64] works on general systems of the form $Ax = b$. In order to improve sequential and parallel sparse numerical factorization performance, the solver algorithms are based on a Level-3 BLAS update, and they exploit pipelining parallelism with a combination of left-looking and right-looking supernode techniques. This solver is the most indicated for single machine computations.

2.4. Electromagnetic Equations and Boundary Conditions

The weak form of the electromagnetic equations must be discretized and solved as described in previous sections. The fundamental equation which is considered here is the *wave equation* in the frequency domain, namely, the Helmholtz's equation.

Helmholtz Equation

The derivation of the wave equation from Maxwell's equations is presented in chapter 1. The same equation, in the following form, is solved as the fundamental equations in all considered models, the dependent variable being the (complex) electric field **E**:

$$\nabla \times \left(\mu_r^{-1} \nabla \times \mathbf{E}\right) - k_0^2 \varepsilon_r \mathbf{E} = \mathbf{0}. \tag{2.3}$$

The wavenumber of the freespace is defined as

$$k_0 = \omega \sqrt{\varepsilon_0 \mu_0} = \frac{\omega}{c}. \tag{2.4}$$

A slightly different approach can be used for solving the electromagnetic problem. If it is possible to make a difference between an *incident field*, which is a sort of external excitation, and a *scattered field*, which is the result of the interaction between the incident field and the modeled system, the so-called *scattered field formulation* can be used. In this formulation, the electric field is separated into two components, the incident field ($\mathbf{E}_i$) and the scattered field ($\mathbf{E}_{sca}$) as follows:

$$\mathbf{E}_{tot} = \mathbf{E}_i + \mathbf{E}_{sca}. \tag{2.5}$$

The field that must solve the wave equation is still the total field, but in this case the dependent variable is $\mathbf{E}_{sca}$.

From the electric field, and using the constitutive relations for materials derived from Maxwell's equation, it is straightforward to derive all other fields. In particular,

$$\mathbf{P} = \varepsilon_0 \chi_r \mathbf{E}, \tag{2.6}$$

$$\mathbf{D} = \varepsilon_0 \mathbf{E} + \mathbf{P} = \varepsilon_0 \mathbf{E} \left(1 + \chi_r\right). \tag{2.7}$$

In the frequency domain, where time derivatives d/dt are converted in the multiplication by $-i\omega$, the Faraday's law gives the magnetic field:

$$\mathbf{B} = \frac{\nabla \times \mathbf{E}}{i\omega}, \tag{2.8}$$

$$\mathbf{H} = \frac{\mathbf{B}}{\mu_0 \mu_r}. \tag{2.9}$$

Material Properties

The electromagnetic properties of the materials are described in this approach by defining two parameters, the relative electric permettivity (ε_r) and the relative magnetic permeability (μ_r). When no magnetic metals (Fe, Co, Ni, etc...) are present, the magnetic permeability can be set to unity, thus the complete description of the materials is achieved by inserting the (complex) dielectric functions:

$$\tilde{\varepsilon_r}\left(\omega\right)=\varepsilon_1\left(\omega\right)+i\varepsilon_2\left(\omega\right). \tag{2.10}$$

In principle, $\tilde{\varepsilon_r}\left(\omega\right)$ is a tensor, but materials studied in this work are always isotropic, thus the dielectric function is supposed scalar (i.e. a diagonal tensor with equal diagonal elements).

Far Field Calculations

In some situations it may be useful to know the *far-field* pattern generated by a given near field distribution. In particular, the latter is always computed in the solution of models. The fields far from the interaction region, on the other hand, are not directly accessible in the finite element formulation, given the huge number of Degree of Freedoms (DOFs) which would be needed for modeling the radiation zone.
A solution to this inconvenient is given by a well-known equation, relating a distribution of fields inside a close surface Σ and the far field generated by them. This equation is known as the Stratton-Chu formula:

$$\mathbf{E_p}=\frac{ik_0}{4\pi}\mathbf{r_p}\times\int_\Sigma\left[\mathbf{n}\times\mathbf{E}-\eta_0\mathbf{r_p}\times\left(\mathbf{n}\times\mathbf{H}\right)\right]\exp\left(ik_0\mathbf{r}\cdot\mathbf{r_p}\right)dS. \tag{2.11}$$

In this formula, $\eta_0=\sqrt{\mu_0/\varepsilon_0}$ is the free space impedance, $\mathbf{r_p}$ is the unit vector pointing from the origin to the field point p and $\mathbf{r}$ is the radius vector of the surface Σ. The Stratton-Chu formula can be obtained in a two-step derivation. First, the computation of the eddy currents generated on the particle surface Σ by the considered fields; and second, the computation of the radiation pattern generated by those currents.

Electromagnetic Losses and Absorption

The absorption of energy by nanostructures can be straightforwardly modeled using the constitutive relations of the materials. The general form of losses is

$$Q=\frac{dW}{dt}=-\omega\varepsilon_0\varepsilon_2\left(\omega\right)\left\langle\mathbf{E}\left(\mathbf{x},t\right)\cdot\mathbf{E}\left(\mathbf{x},t\right)\right\rangle-\omega\mu_0\mu_2\left(\omega\right)\left\langle\mathbf{H}\left(\mathbf{x},t\right)\cdot\mathbf{H}\left(\mathbf{x},t\right)\right\rangle, \tag{2.12}$$

where brackets indicate the harmonic time averaging. Because non-magnetic media have been considered, non magnetic losses are present, and the second term of losses vanishes. Electric losses density reduce to

$$Q=\frac{1}{2}\omega\varepsilon_0\varepsilon_2E^2, \tag{2.13}$$

which, integrated in the volume, gives the total losses, i.e. the absorption:

$$P_{abs}=\frac{1}{2}\omega\int_V\varepsilon_0\varepsilon_2E^2dV. \tag{2.14}$$

The absorption cross section can be derived form this value by normalizing to the total incident flux of a plane wave $P_0 = \frac{1}{2} c \varepsilon_0 E_0^2$:

$$\sigma_{abs} = \frac{P_{abs}}{P_0} = c \int_V \omega \varepsilon_2 \frac{E^2}{E_0^2} dV. \tag{2.15}$$

Poynting Vector and Surface Fluxes Computations

Electromagnetic energy fluxes are described by the Poynting's vector:

$$\mathbf{S} = \mathbf{E} \times \mathbf{H} = \frac{1}{\mu_0} \mathbf{E} \times \mathbf{B}. \tag{2.16}$$

In models where the periodic boundary conditions are used in the plane orthogonal to the wavevector $\mathbf{k}$, transmittance T and reflectance R can be computed by integrating the Poynting vector over the boundaries parallel to the periodic plane in the opposite (Σ_{out}) or in the same (Σ_{in}) hemispace of the incoming wave, respectively. In particular,

$$T \equiv \frac{I_T}{I_0} = \frac{\int_{\Sigma_{out}} \mathbf{S} \cdot d\sigma}{\int_{\Sigma_{in}} \mathbf{S_{in}} \cdot d\sigma}, \tag{2.17}$$

and

$$R \equiv \frac{I_R}{I_0} = \frac{\int_{\Sigma_{in}} \mathbf{S} \cdot d\sigma}{\int_{\Sigma_{in}} \mathbf{S_{in}} \cdot d\sigma}. \tag{2.18}$$

For models in which the scattered field formulation is used, from Poynting's vector also the scattering cross section can be computed:

$$\sigma_{sca} = \frac{1}{P_0} \int_\Sigma \mathbf{S} \cdot d\sigma, \tag{2.19}$$

where now Σ is a closed surface enclosing all the interaction volume.

Periodic and Floquet Boundary Conditions

Periodic conditions are necessary to model periodic ordered systems using finite elements. This condition equals the electric and magnetic fields of two boundaries, the source boundary (**src**) and the destination boundary (**dst**). A key requisite is that the two boundaries have the same shape and size, and that also the mesh is equal.

The simplest periodic condition has the following equations, which hold pointwise on all the elements of involved boundaries:

$$\mathbf{E_{dst}} = \mathbf{E_{src}} \tag{2.20}$$

$$\mathbf{H_{dst}} = \mathbf{H_{src}}. \tag{2.21}$$

This periodic condition is efficient when the wavevector of the incident light is orthogonal to the plane in which the periodicity exists. In the case of a non-orthogonal propagation (i.e. in the modeling of oblique incidence), the correct periodic condition is the *Floquet boundary condition*. In this case, a phase factor is inserted in the equations, making it possible to describe systems in which the periodicity of incident field is different from that of the geometry. The equations become:

$$\mathbf{E_{dst}} = \mathbf{E_{src}} e^{-i\mathbf{k}_F \cdot (\mathbf{r}_{dst} - \mathbf{r}_{src})} \tag{2.22}$$

$$\mathbf{H_{dst}} = \mathbf{H_{src}} e^{-i\mathbf{k}_F\cdot(\mathbf{r}_{dst}-\mathbf{r}_{src})}, \tag{2.23}$$

where $\mathbf{k}_F$ is the so-called *Floquet vector*, and is the projection of the wavevector on the periodicity plane. For normal incidence, the Floquet periodic condition turns into the standard periodic condition.

Perfect Electric Conductor and Perfect Magnetic Conductor

Two other useful boundary conditions are the Perfect Electric Conductior (PEC) and Perfect Magnetic Conductor (PMC) ones. The PEC describes a perfect metal, i.e. a metal with no resistance. It sets the tangential component of the electric field to zero, and can be used to describe a symmetry plane for the electric field. The equation is:

$$\mathbf{n} \times \mathbf{E} = \mathbf{0}. \tag{2.24}$$

Perfect Magnetic Conductor condition sets the tangential component of the magnetic field to zero, and can be used to describe a symmetry plane for the magnetic field. The equation is:

$$\mathbf{n} \times \mathbf{H} = \mathbf{0}. \tag{2.25}$$

External Boundaries and Backreflected waves. Perfectly Matched Layers

Finite element methods by definition can't handle *infinite* spaces. However, in electromagnetic problems, the presence of external boundaries may cause big problems related to the back-reflection of outgoing waves. According to the form of the field in a few simple situations, some methods can be used to computationally suppress backscattered waves. In general, a method for handling external boundaries is however necessary to assure the suppression of unphysical backscattered waves. For spherical, cylindrical or plane outgoing waves, it is possible to suppress almost all the backscattering by suitably design the external boundaries (i.e., respectively, using spherical, cylindrical or cartesian boundaries). When the geometry and the nature of radiation permit this, the scattering boundary condition can be imposed to suppress reflection of waves. This condition, for spherical geometry of the boundary (the most useful) can be written as:

$$\mathbf{E} = \mathbf{E_{sc}} \frac{e^{-ik(\mathbf{n}\cdot\mathbf{r})}}{r_s} + \mathbf{E_0} e^{-i(\mathbf{k}\cdot\mathbf{r})}. \tag{2.26}$$

This condition makes the boundary transparent for a (spherical) scattered wave. The boundary condition is written to be also transparent for an incoming plane wave (i.e., the plane wave).

To handle waves with non-zero tangential component, a PML is needed before the outer boundary to suppress reflected waves. A PML is strictly speaking not a boundary condition but an additional (artificial) domain that absorbs the incident radiation without producing reflections. The PML formulation can be deduced from Maxwell's equations by introducing a complex-valued coordinate transformation under the additional requirement that the wave impedance should remain unaffected, as pointed out in [65]. These operations can be achieved by using the following coordinate transform for the general coordinate variable t:

$$t' = t\frac{\lambda}{\delta t}(1-i). \tag{2.27}$$

The coordinate, t, and the width of the infinite element region, δt, are input parameters for each region. The software embeds an algorithm to automatically initialise these parameters for spherical, cylindrical and cartesian PML geometries.

2.5. Computing Performances

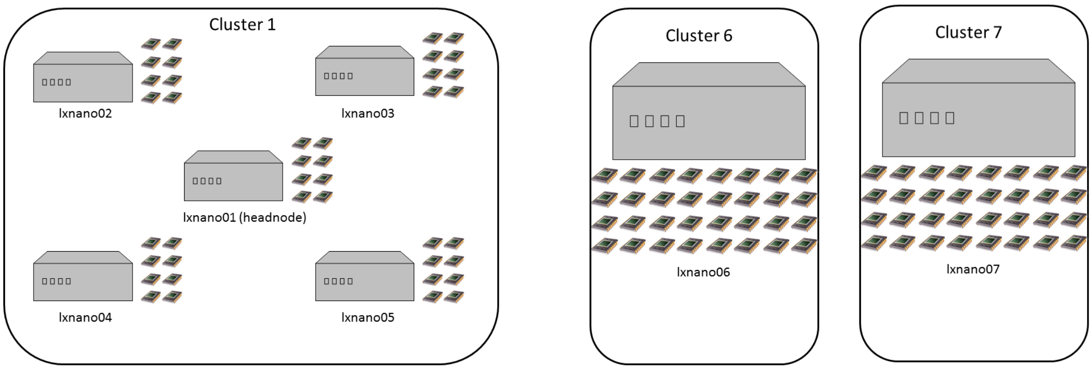

(a) Cluster 1. **(b)** Clusters 6 and 7.

Figure 2.2.: Scheme of the clusters used for computations.

The computations in the present work have been performed on 7 computation servers grouped in 3 clusters. Fig. 2.2 show the composition of the three clusters:

`Cluster 1` is formed by 5 (identical) Intel Xeon servers, `lxnano01` to `lxnano05`.

`Cluster 6` is formed by a AMD Opteron server, `lxnano06`.

`Cluster 7` is formed by a AMD Opteron server, `lxnano07`.

Tab.2.1 lists the main features of the servers used. All the servers run `Scientific Linux 6.3 (Carbon)`, kernel version `2.6.32-279.19.1.el6.x86_64`.

Table 2.1.: Server features.

Machine	**Processor**	**No. Processors**	**Total No. Cores**	**RAM (GB)**
lxnano01	Intel Xeon E5520	2	8 (16 HT)	64
lxnano02	Intel Xeon E5520	2	8 (16 HT)	64
lxnano03	Intel Xeon E5520	2	8 (16 HT)	64
lxnano04	Intel Xeon E5520	2	8 (16 HT)	64
lxnano05	Intel Xeon E5520	2	8 (16 HT)	64
lxnano06	AMD Opteron 6274	4	32 (64 HT)	128
lxnano07	AMD Opteron 6274	4	32 (64 HT)	128

Two benchmark models have been used for the tests on the performances of various configurations. In particular, the use of `Cluster 1` against singles machines have been tested; two direct solvers, `MUMPS` and `Pardiso`. Further, all the configurations have been tested both assigning 1 or 2 nodes per machine (i.e. 1 or 2 wavelength at time, each using N_c or $N_c/2$ cores of each machine). Test Model 1 simulates a NHA with Periodic Boundary Conditions (PBCs), it has 90000 mesh elements and 600000 DOFs. Test Model 2 simulate a 2D domain, is much smaller than Test Model 1, and it consists of 13000 mesh elements and 100000 DOFs. A fast comparison between the results of the two models show that the scaling of the computation time is not linear on the number of DOFs. Fig. 2.3 shows the results for the considered configurations. The cluster `Cluster 7`, formed by the single machine `lxnano07` is the faster configuration (using 2 nodes per machine and MUMPS as solver) for models with a limited number of mesh elements ($N \lesssim 40000$). On the other hand `Cluster 1` is the fastest when the model is constitued by a large number of mesh elements, due to the higher memory-per-core availability. The differences between MUMPS and PARDISO are neglectable overall; as no shared memory calculations (i.e. calculations involving multiple machines for the solution of a single matrix) are not performed, MUMPS is not strictly needed, and PARDISO is choosen as the standard solver because of a slightly higher speed. Iterative solvers (namely, GMRES) have been used only in the case of large simulation domains without periodic boundary conditions and only spherical PML.

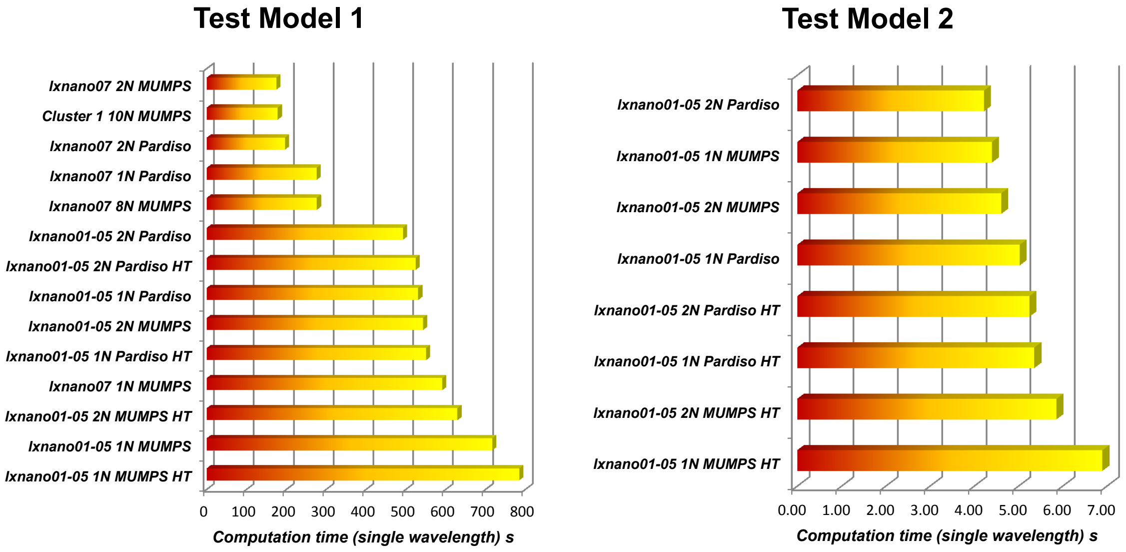

Figure 2.3.: Performances in models solving. Lower number means faster solution. In the legend, 1N means 1 node (a set of processors and memory solving the same matrix together) per machine, 2N means 2 nodes per machine. HT means that HyperThreading (i.e. virtual cores) is active. Model 1: $N_{el} = 90000$ mesh elements and $N_{DOF} = 600000$; model 2: $N_{el} = 13000$ mesh elements and $N_{DOF} = 100000$.

3. Periodic Nanostructures

In this chapter the results obtained on periodic nanostructures will be presented. The first kind of nanostructure, Nano Prisms Arrays (NPAs), support localized plasmons. The field confinement and enhancement obtained by this system are used for sensing applications, and an optimization study is carried out. The second kind of nanostructure is Nano Hole Array (NHA), which supports extended plasmons and couples them to the light, thanks to a grating-like design. The effects of the presence of close NHAs or metal films on the emission of rare earths will be studied in this section. A third type of nanostructure is the Quasi Shell (QS), an open shell configuration which shows interesting properties. A focus on experimental methods for the synthesis and charachterization of these structures is given. The Finite Element Method (FEM) simulations will be used to get a deeper insight on the observed phenomena and to give the correct interpretation of them.
From an experimental point of view, the 2D (hexagonal) lattices charachterizing all the three analyzed systems are fabricated using a cheap, colloidal, self-assembled technique, Nanosphere Lithography (NSL). This way, the advantages of a periodic lattice are combined with the cost-effectiveness of the self-assembling and with an optimal surface coverage. When dealing with LSP-supporting nanostructures, the control over several parameters of the fabrication makes it possible to finely control, in addition to the response of the single monomers, also the level of their mutual interaction. In the case of NHAs, the poriodicity is responsible for the enhanced coupling of the SPP to the far-field, optimizing the extaction of plasmons and giving rise to the Extraordinary Optical Transmission (EOT). From a simulative point of view, the presence of periodicity makes it possible to exploit Periodic Boundary Condition (PBC), thus modeling just the unit cell. PBCs give two major advantages: on one hand, no boundary effects are introduced in the simulation; on the other hand, all the information can be obtained by solving the equations only on a small part of the structure (the unit cell), thus optimizing computational efforts.

3.1. Nanosphere Lithography

Nanosphere lithography is an inexpensive and versatile hybrid bottom-up procedure, for fabricating periodic arrays of nanoparticles with controlled shape, size, and interparticle spacing [66]. NSL was developed by Van Duyne and co-workers and provides a method to fabricate nanoparticle arrays with a tunable Localised Surface Plasmon Resonance (LSPR). This technique is a variant of "natural lithography", from the work of Fischer and Zingsheim, where "naturally"-assembled polystyrene (PS) nanospheres were used as a mask for contact imaging with visible light. This methodology always employed a single layer (SL) of nanospheres as mask, while in NSL there can be double layer (DL) nanosphere mask. The latter permits the fabrication of SL and DL periodic metallic particle arrays with defect-free areas of $10 - 100\mu\text{m}^2$, large enough to permit microprobe studies of nanoparticle optical properties [67]. After the assembly of the SL or DL mask, a metal or other material is deposited through the nanosphere mask, from a source normal to the substrate, to produce a metallic

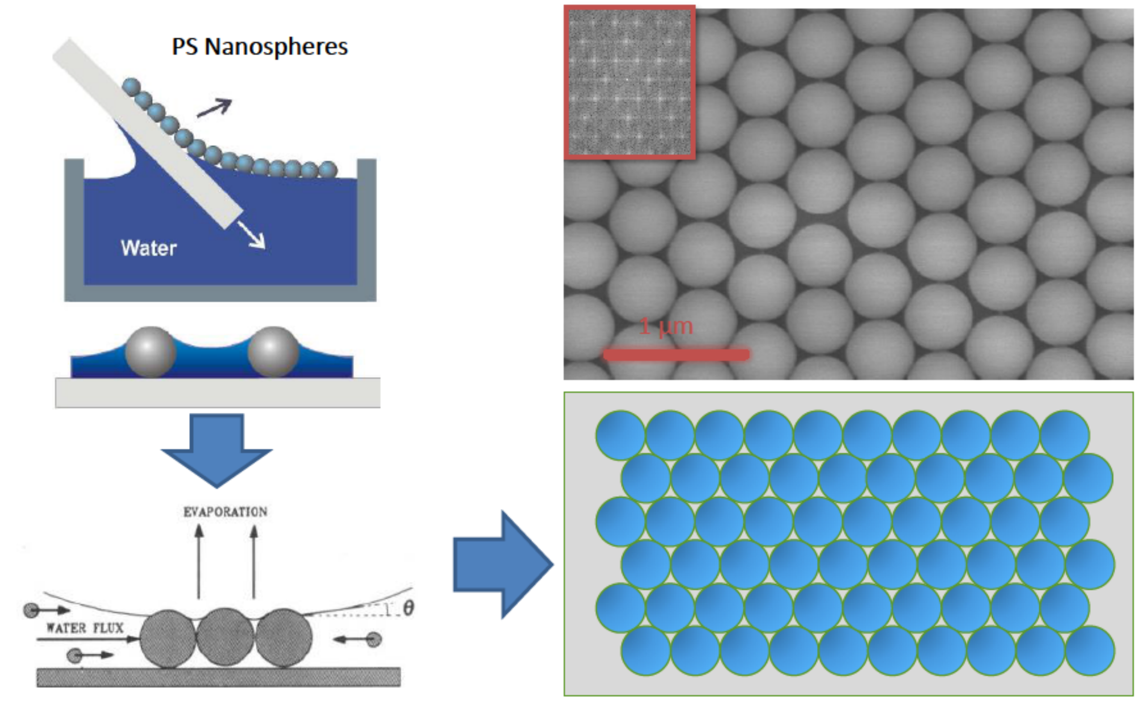

Figure 3.1.: NSL process: monolayer acquisition on selected substrate; close-packing lattice formation due to capillary forces; obtained mask.

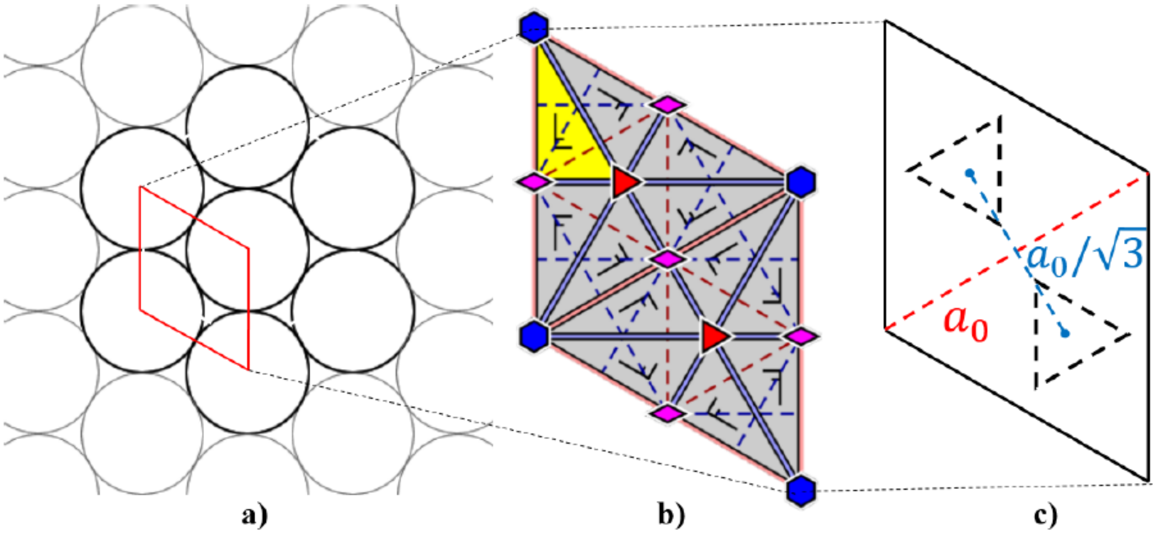

Figure 3.2.: The lattice resulting from NSL: a) a nanosphere together its 6 first nearbies, and the unit cell definition; b) simmetries in the unit cell; c) relevant parameters in the unit cell: the lattice parameter $a_0 = D$ and the centre-centre distance $d_{cc} = a_0/\sqrt{3}$

Film on Nanospheres (FON) structure. The mask is then removed, leaving a periodic array of metal nanostructure on the substrate. The PS nanospheres are available in a variety of sizes ($D = 100 \div 2000$nm), and by changing their diameter and the deposited metal thickness, it is possible to control the position, shape and intensity of the LSPR band. The nanostructures obtained by NSL are usually triangular nanoprisms, but it is possible to create a wide range of other nanostructures, e.g. rhombic or cubic nanoparticles. It has been demonstrated both experimentally and theoretically that sharp tips of the nanostructures give rise to electromagnetic enhancement factor of about 10^3. For this reason they are intensively used for SERS.

3.1.1. Self assembly of polystyrene nanospheres

The process starts with the deposition of a single-layer colloidal crystal mask of monodisperse polystyrene nanospheres. They can be deposited on the desired substrate in various way, e.g. spin coating, drop coating, dip coating and thermoelectrically cooled angle coating. The chosen method is based on the works of Schatz [68], using a colloidal suspension of polystyrene nanospheres in ultrapure water and isopropyl alcohol, as depicted in fig.3.1. This solution is deposited on a Soda-Lime glass slab and distributed over it. Using a custom-made set-up, the slab is then carefully and slowly dipped into a crystallizing glass vessel, containing ultrapure water. A monolayer of NS is formed on the water surface, thanks to the meniscus between the alcoholic dispersion and the water, and the slab is moved is such a way to increase the size of the formed monolayer by the flux of nanospheres from the SLG slab. When the monolayer is formed, another substrate (which can be Si, SiO_2, soda-lime glass, etc.) is immersed and under the monolayer is slowly pulled out to collect the formed mask. A successive drying in air for about half an hour gives the final mask on the substrate.

During the drying, as the solvent evaporates, the nanospheres are subject to capillary forces that draw them together and make them organize in an hexagonal, close-packed pattern. The nanospheres masks include a variety of defects that arise as a results of nanospheres polydispersity, site randomness, point defects (vacancies), line defects (slip dislocations), and polycrystalline domains [67]. The size of the defect-free domains can reach about 100 to 1000 μm^2. Fig.3.2 shows the lattice obtained together with the roperties of the unit cell.

3.2. Nanoprisms: Plasmonic Biosensors

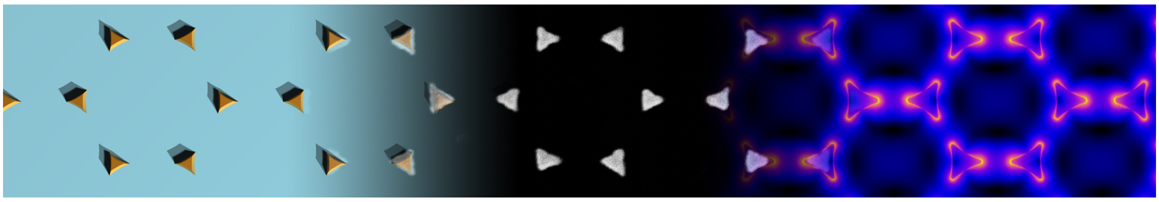

Design, synthesis and modeling of 2D arrays of nanoprisms.

Since the discovery of field localization, one of the most studied application of plasmonics has been in biosensing. The Localized Surface Plasmon Resonance (LSPR) is strongly dependent in shape and position on the dielectric properties of the local surrounding medium [69–71], as moreover already observed in the case of spherical particles (cfr. section 1.4.2). This gives a powerful tool to detect small changes in the refractive index, due to the presence of an analyte, exploited in a number of nanostructures configurations, from single colloidal particles to ordered arrays [72–78]. Geometric details of the nanostructures have been demonstrated to play an important role in the formation of plasmons. In particular, monomer size [79–83], shape [79, 84–90] and mutual interaction [91–94] can be tuned to control field enhancement and confinement. Our group investigated both bio-sensors and gas sensors [95–97]. Among other fabrication approaches, the presence of ordered arrays of nanostructures is appealing for the reproducibility and for the possibility of fine tuning the resonance. On the other hand, traditional top-down techniques (EBL, FIB, etc.) are still expensive, and also if coupled to pattern reproduction, can yield only few mm^2 of active substrate. Since the work by Van Duyne's group on Nano Sphere Lithography (NSL) [67,98,99], cheap, wide area, ordered array LSPR biosensors can be fabricated. This technique easily provides 2D honeycomb lattice patterned structures up to an area of several cm^2.

3.2.1. Analysis of the Nanoprism

As a preliminary step, simple configurations involving both interacting and non-interacting nanoprisms have been analyzed. The effects of the polarization of light has been considered, together with the consequences of interactions between monomers. The results helped in the design of the full, periodic models, pointing out the important parameters for a correct solution.

Polarization

Due to the description of the physics in FEM models, the light is always polarized in simulations. Thus, it is necessary to check the role of polarization in the resulted spectra, as usual experiments make use of unpolarized light. Fig.3.3a shows the absorbance spectra of an isolated nanoprism (silver, base side $L = 90$nm and height $h = 30$nm) for the two polarizations of light. For isolated triangles the effect is almost negligible, the only slight differences appearing only in the quadrupolar peak ($\lambda \sim 545$nm). The effect of polarization is more important in the case of strong interacting nanostructures, as the presence of the gap between two tips oriented in the direction of the electric field (X-POL) enables a stronger field confinement, and gives rise to a shift and to larger absorption. This difference is however visible only for prisms separated by very narrow gaps ($g \lesssim 30$nm): as it will be shown in the next paragraph, the interaction effects almost vanish for more distant monomers. Even for very low values of the tip-tip distance, $d_{tt} = 4$nm, the difference in the peak position between the two polarizations is less than 10nm for the dipolar resonance and less than 20nm for the quadrupolar resonance.

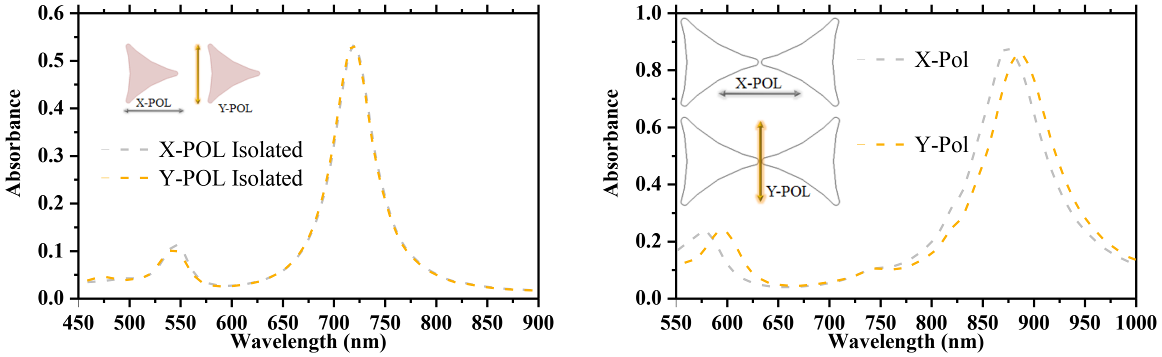

(a) Isolated nanoprism

(b) Honeycomb-arranged interacting nanoprisms (tip-tip distance $d_{tt} = 4nm$

Figure 3.3.: Effects of polarization on absorbance of nanoprisms (silver, base side $L = 90$nm and height $h = 30$nm).

As in the following the distances between monomers are always larger than this value, the polarization effects will be neglected, and only the X polarization models will be solved.

Prism-Prism Gap

As seen in the previous paragraph, the interaction plays a significant role whenever two nanoprisms are close each other. This is enhanced by the fact that in the honeycomb lattice, the prisms face each other towards the diraction of their tips, the region where the field is most enhanced. Thus, it is necessary to check the role of interaction in the NPAs. Fig.3.4 shows the absorbace spectra of an array of interacting nanoprisms (silver, base side $L = 90$nm and height $h = 30$nm) as a function of the gap between the tips, d_{tt}, together with the isolated prism configuration. It is possible to conclude that the effects of the polarization are appreciably suppressed for $d_{tt} \gtrsim 32$nm, and are not present for the case of $d_{tt} = 62$nm. By the way, the gaps considered in the following will be always $d_{tt} > 60$nm, thus assuring that the considered prisms will behave as non-interacting. A consequence of this is that the periodicity will be exploited essentially to obtain the best surface coverage, with no additional electro-magnetic effects.

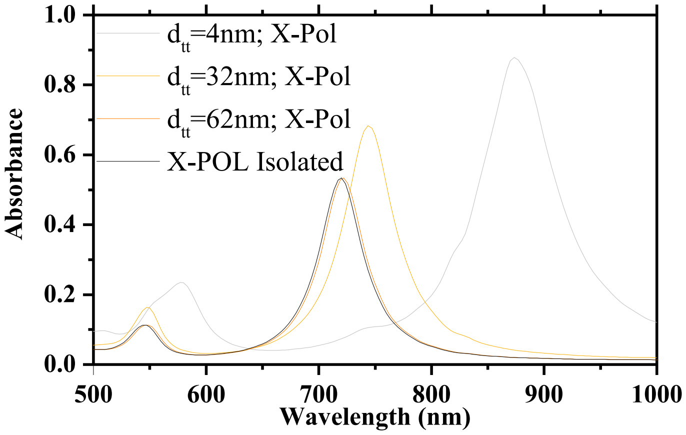

Figure 3.4.: Effects of interaction in nanoprisms array. The size of the prisms is constant (silver, base side $L = 90$nm and height $h = 30$nm), and the lattice parameter is varied to vary the gap between prisms (tip-tip distance d_{tt}).

3.2.2. The Physics of the Problem

Sensors for biological and chemical applications exploit the field confinement given by plasmons: on one hand, the molecules one wants to detect are no larger than a few nanometres; on the other hand, the best electromagnetic region for this kind of analyses extend from the near UV to the IR, where waves are some to several hundreds nanometres long. The mismatch between these two scales can be bridged by using suitably designed nanostructures, in order to confine and localize fields beyond the diffraction limit (i.e., confinement of the EM fields in regions with size much smaller than $\lambda/2$).

Nanoprisms achieve this result pretty well, providing *hot spots* at the tips, where the electric field is focused and therefore the interaction with *analytes* is enhanced. Moreover, the used fabrication approach yields large arrays of nanotriagles, oriented in such a way that the tips of

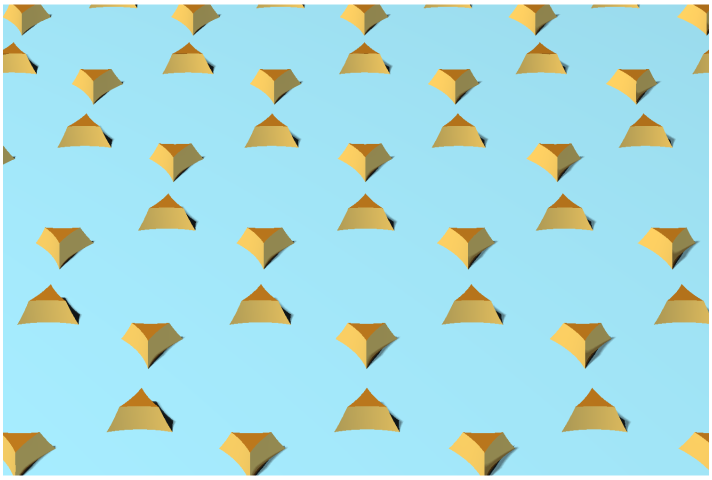

Figure 3.5.: Nanoprisms 3D models

two nearby prisms face each other, and so that the field confinement results even larger than for isolated prisms. Fig. 3.5 show a computer graphics rendering of a nanoprisms array as an example. The use of nanoprisms as sensors is based on the extreme sensitivity of the plasmonic resonance to the local environment around nanostructures. As pointed out in section 1.4, the presence of thin layers of a dielectric (with $n > 1$) produces a redshift in the resonance with respect to the air. This effect is exploited in sensors, where a redshift corresponds to the presence of a precise quantity (or concentration) of analyte (typical, biological molecules arranged in layers can be modeled as a uniform dielectric layer with the same refractive index, close to 1.5). The performances of nanoprisms as sensors can be summarized in two figures of merit (FOMs), the *bulk sensitivity* S_∞ and the *differential sensitivity* S_0. Both these parameters are usually normalized to a unitary refractive index variation, thus introducing the Refractive Index Unit (RIU) scale. Bulk sensitivity describes the redshift experienced by the resonance if the refractive index of the medium of the environment around the sensor (except for the substrate) is increased (with respect to the "empty" sensor) by one unit. Because the field confinement of nanoprisms is strong, the modification of the refractive index in the first nanometres from the surface has a much larger effect than the modification at further distances. A *sensitivity curve* $\Delta\lambda\,(r)$ can be drawn by relating the redshift of the SPR and the thickness of a thin layer of analyte around the nanostructures. This curve can be fitted with a saturated exponential (the factor 2 in the exponent is due to the fact that the decay is referred to intensities and not to fields),

$$\Delta\lambda\,(r) = S_\infty \left(1 - e^{-\frac{2r}{r_0}}\right), \tag{3.1}$$

and the differential, or *local*, sensitivity S_0 is the derivative of this curve at zero thickness:

$$S_0 = \frac{\partial}{\partial r}\Delta\lambda\,(r)\bigg|_{r=0} = \frac{2S_\infty}{r_0}. \tag{3.2}$$

The sensitivities of sensors exploiting nanoprisms is dependent on the geometrical features of the nanostructures, an in particular on the height of the nanoprisms h, on the side of the base l and on the lattice parameter a_0 of the array.

3.2.3. Sensors Nanofabrication and Characterization

The first step for the fabrication of the sensors is an ordered array of polystirene spheres. The NSL method used to obtain the array is described in the previous section. Fig.3.6 shows the successive steps for the fabrication: once the nanoshpere array is posed on glass, nanoprisms are formed by thermally evaporating metal orthogonally to the glass. The shadow of the nanospheres prevent the metal from reaching the glass except for the triangular-like zones between spheres. Once the metalization is achieved, the nanospheres are removed together with the metal deposited on them. To this aim, a stripping process using 3M tape is used. As a result, a nanoprisms array is formed. The height h of the prisms can be easily controlled

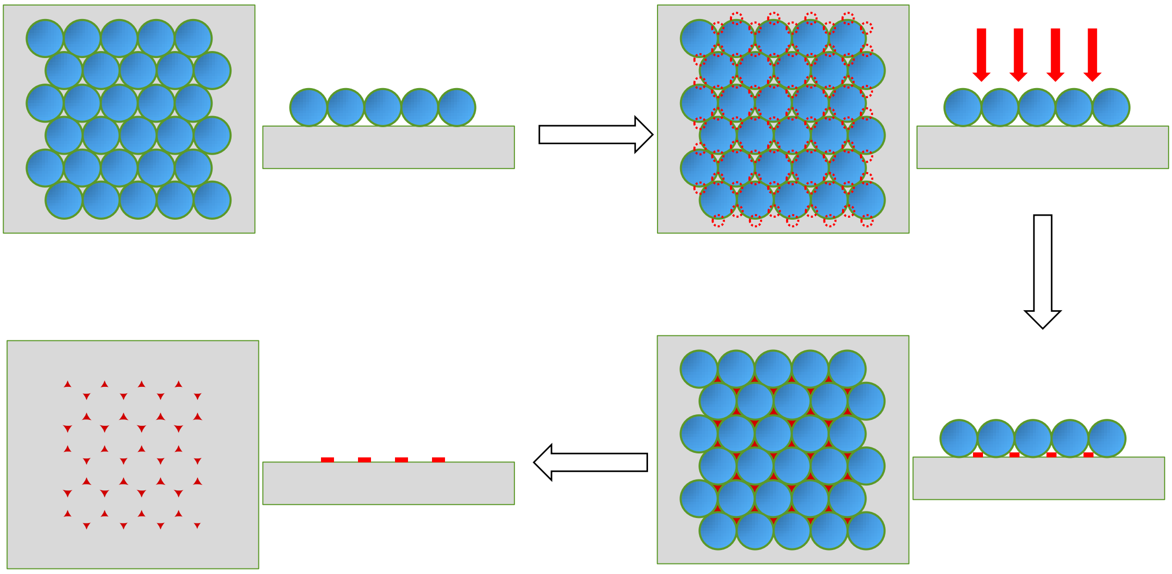

Figure 3.6.: Nanoprisms fabrication by NSL: mask deposition; metal deposition; mask removal.

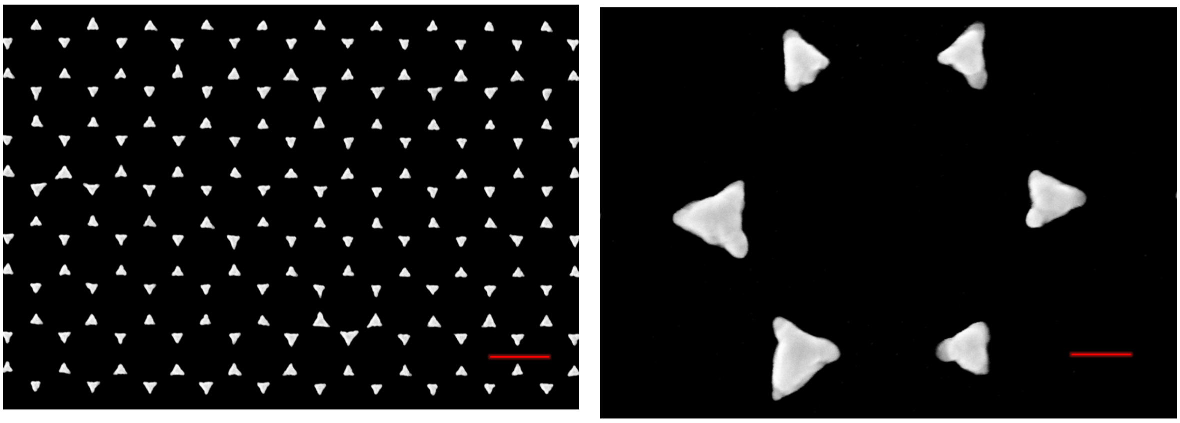

(a) Magnification: 50k, bar:500nm

(b) Magnification: 250k, bar:100nm

Figure 3.7.: SEM images of nanoprisms at different magnifications. In the sample, $a_0 = 522$nm, the metal is evaporated silver.

by adjusting the power and time of evaporation (typically, $50-100$W and 10 to 100 s); the lattice parameter a_0 is equal to the diameter D of the used polystirene nanospheres (for Nano Prismss (NPs), D typically ranges from 200nm to 750nm); the side of the base triangles is controllable through the collimation of the evaporator. The evaporator used in the fabrication produces structures with a constant relation between the side of prisms and the lattice parameter, so in the next the side of the prisms will be always considered to be $l = a_0 f$, where f is material dependent factor, due to different degree of collimation, and measured as $f_{Ag} = 0.26$ and $f_{Au} = 0.30$.
For the validation of the simulations, the used arrays had a lattice constant $a_0 = 496$nm, and both gold and silver nanoprisms have been fabricated starting from those arrays. The Gold NPs resulted, using AFM, $h_{Au} = 50$nm tall, and their base side was measured $l_{Au} = 149$nm. The silver NPs were $h_{Ag} = 55$nm tall and the base side was $l_{Ag} = 129$nm. Fig. 3.7 shows the Scanning Electron Microscope (SEM) images taken from one of the silver samples. The quality of the array is satisfactory, having many prisms in an ordered domain, and the shape of the prisms is reproducible over the sample. The tips of the prisms result not sharp. The effect can be due to the high temperature ($T \sim 100°$C) in the evaporation process, which takes the metal to soften sharp edges. The effect reduces the hot spot intensity, but increases the stability against small-scale defects. The optical characterization of the sensors have been performed using a Jasco V-670 spectrophotometer in the *Transmittance* acquisition mode. The transmittance spectra of all the samples have been taken, in three different $1mm^2$ areas for each sample, and averaged, to get a intra- and inter-sample variation-robust measure. Absorbance has been derived from transmittance using the equation:

$$A = -\log_{10}(T)\,. \tag{3.3}$$

For the measurement of the bulk sensitivity, the samples have been immersed into three solutions (ultrapure water, ethanol 99% and glicerol) with different refractive index, reported in tab. 3.1, and the transmittance spectra have been acquired to measure the SPR shift.

For the measurement of the local sensitivity, incremental thin layers of silica have been sputtered onto the samples. At each step, the thickness of the obtained layers was measured both by AFM and by ellipsometry (on a flat portion of a Si substrate) as a check. The sputtered silica refractive index was determined by ellipsometry measurements as well. Fig.3.8 show the transmittance spectra of the gold and silver nanoprisms as deposited. Gold NPs show an absorption peak at 811 ± 2 nm, corresponding to the dipolar resonance of the prisms. The same feature, more sharp, is present also in silver NPs, at 706 ± 2nm. In silver it si evident also the presence of a quadrupolar resonance in the blue region, the same can be recognised,

Table 3.1.: Refractive index of the materials used as analytes. Silica is used for thin layers, the other three liquids for bulk.

Solution/Material	Refractive Index
Water	1.33
Ethanol 99%	1.36
Glicerol	1.467
Silica	1.45

though much less sharp, also in the spectrum of gold NPs. The differences in the peak shape and amplitude are due to the different material properties, and in particular to the higher imaginary part of the dielectric function of gold against the one of silver. The same effect is visible in the simple case of spherical nanoparticles in the Mie framework (cfr. section 1.4). The presence of defects and variance in prisms shape and size, together with the unpolarized light, has the effect of broadening the experimentally observed peaks. Thus, the simulated spectra will show narrower resonances. However, for the aims of this work, the average behaviour, represented by the peak position, is sufficient to derive sensitivities. Fig.3.12 shows the shifts measured when the NPs are immersed in the considered solutions, as a function of the dielectric refractive index for gold NPs, in comparison with the simulated results. For the measurement of the bulk sensitivity, gold NPs have been immersed in solutions having different refractive indexes, and the absorbance spectrum has been measured. The shift of the peak as an effect of the change in refractive index have been calculated. The bulk sensitivity, computed as the slope from the linear fit of the experimental shifts, resulted:

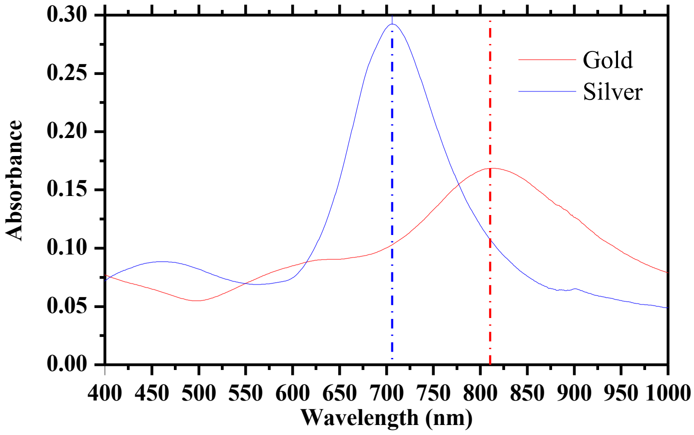

Figure 3.8.: Experimental optical spectra of silver and gold NPs as deposited. For both samples evaporation is used, $a_0 = 496$nm, $h_{Ag} = 55$nm and $h_{Au} = 50$nm.

$$S_\infty^{(Au)} = (263 \pm 5)\,\mathrm{nm}/RIU. \tag{3.4}$$

For silver nanoprisms, also the local sensitivity have been tested, and figure 3.9 show the absorbances after each incremental layer deposition.

$$S_0^{(Ag)} = (10 \pm 2)\,RIU^{-1}. \tag{3.5}$$

The resonance wavelengths, local sensitivities and bulk sensitivities have been used to check and tune simulations, as shown in the next section. The simulation framework has then been used for the optimization of the sensitivities varying the geometric parameters of the nanostructures.

3.2.4. Simulations and Optimization

Simulations are performed on the Honeycomb lattice unit cell, as depicted in fig.3.10. The cell contains 2 prisms with a snipped-trianglular base. The boundaries orthogonal to the substrate plane are modeled by putting periodic boundary conditions. In the $\hat{z}$ direction, orthogonal

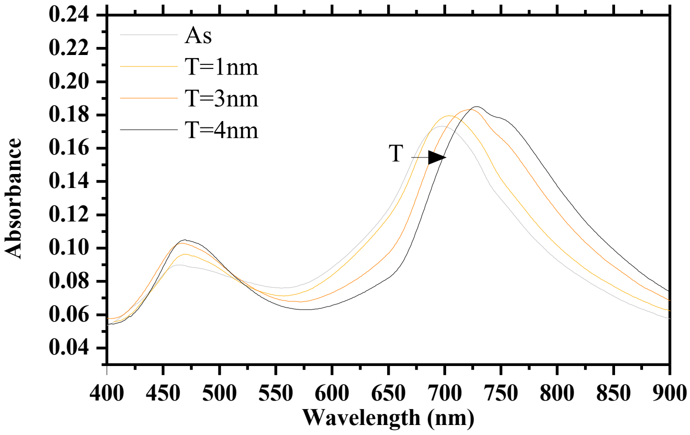

Figure 3.9.: Measured absorbance spectra for silver NPs covered with incremental layers of silica. $a_0 =$ 496nm, $h = 55$nm

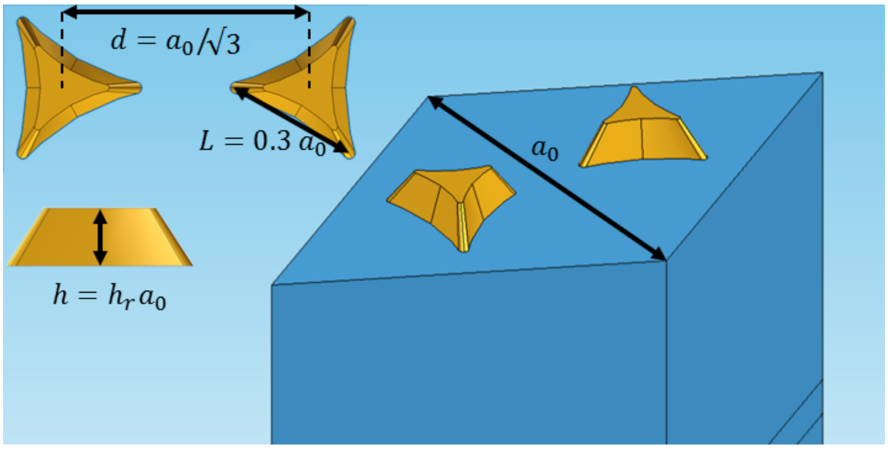

Figure 3.10.: Simulation geometry definition for unit cell and nanoprisms.

to the prisms plane, the substrate is modeled as semi-infinite using PML (cfr. sec.2.4). The functionalization layer is conformal to the prisms, and has variable thickness. The relevant geometrical parameters in the simulations are the lattice parameter a_0, the base prism side L and the height h. The side of the prisms have been kept fixed at a constant ratio f to the lattice parameter:

$$L = f a_0, \tag{3.6}$$

with $f = 0.3$. To validate the models and the simulations, the same experimental conditions have been simulated and compared to the result from samples. The experimental results have been used in the FEM simulation, and the transmittance spectra, as shown in fig.3.11, plotting the comparison between the spectra from simulations and experiments for gold and silver NPs, well reproduce the experimentally taken one. The width of the resonances in experiment are sensibly broader, due to defects in the periodic pattern and in the NP shape. However, the mean behaviour, represented by the peak, is well reproduced; the simulated peak integral, which describes the amount of extinction over the peak's spectral range is also consistent with experiment. For the comparison between simulations and experiment for the bulk sensitivity, the simulations have been carried out using the same refractive index values as the experiment.

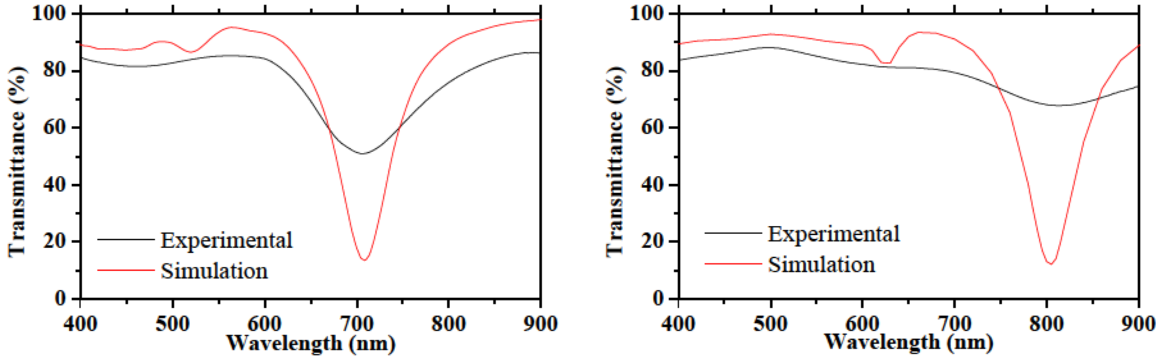

(a) Silver.

(b) Gold.

Figure 3.11.: Comparison between simulated (FEM) and experimental transmittance for gold and silver NPs. For both samples evaporation is used, $a_0 = 496\text{nm}$, $h_{Ag} = 55\text{nm}$ and $h_{Au} = 50\text{nm}$.

The resulting simulated bulk sensitivities result, for gold and silver:

$$S_\infty^{(Au)} = (279 \pm 5)\,\text{nm}/RIU; \qquad S_\infty^{(Ag)} = (280 \pm 5)\,\text{nm}/RIU. \tag{3.7}$$

For gold, the results have been compared with The simulated sensitivities result slightly higher

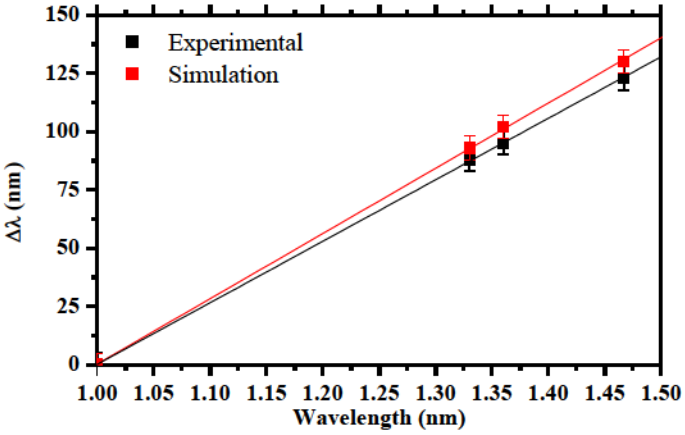

Figure 3.12.: Measured and simulated bulk sensitivity S_∞ for gold NPs. The lines are the linear fits of the two series.

with respect to the measured ones. This effect is probably due to disuniformities in the experimental samples and to defects in the nanostructure which lower the overall quality and, in turn, the sensitivity performances. However, the difference is not large, and the agreement is satisfactory taking into account the role of defects.

The local sensitivity have been experimentally measured only for silver, and the comparison between the simulated sensitivity curve and the measured shifts is plotted in fig.3.13. Also in this case, the agreement is good, and all the points result compatible with the simulated curve. Again, the experimental shifts result lower than the simulated one. In this case the difference is however smaller than in the case of bulk.

The first parameter one can be interested in when dealing with plasmonic biosensors is the SPR wavelength. In fact, for a proper operation of a sensor, the nanostructures must be

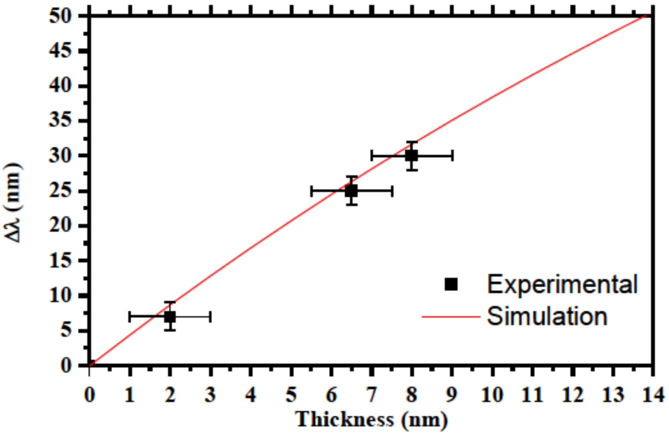

Figure 3.13.: Measured shift and comparison with simulated sensitivity curve for silver NPs.

resonant in a region where light sources, optics and detectors work in an optimal way. To match the plasmonic properties of the NPs with the optical equipment, the knownledge of the dependance of the resonance wavelength on the geometrical parameters is thus of paramount importance. From this point of view, simulations have been carried out for different combinations of height and lattice parameter. In particular, the lattice parameter have been varied from $a_0 = 300$nm to $a_0 = 600$nm. In place of the height, aspect ratio is more suitable for the description of the resonance position dependance. Thus, the *normalized aspect ratio* or *relative height*, defined as $h_r = h/a_0$, has been used. The actual aspect ratio is defined as $AR = h/L$, and is related to h_r by $h_r = f \cdot AR$ (with $f = 0.3$ in this work). By considering this parameter instead of the actual height, the shape of the prisms is conserved when varying only a_0, and keeping h_r constant, the variation producing a uniform scale effect in all three dimensions. The normalized aspect ratio h_r was varied from $h_r = 0.05$ to $h_r = 0.20$ (corresponding to aspect ratios from $AR = 0.16$ to $AR = 0.66$). For both gold and silver the maps of the resonance position have been obtained, as plotted in fig.3.14. The resonance shifts towards the red (lower energies) when the lattice parameter (and thus all the linear dimensions of the monomers) increases, and when the aspect ratio decreases. On the other hand, the resonance can be obtained at higher energies by reducing the lattice parameter or increasing the aspect ratio towards 1. All the considered combinations of a_0 and h_r are easily experimentally accessible, thus simulations show that the resonance can be tuned from about 600nm to about 1000nm. These ranges can however be further extended by successive thermal annealing (due to an induced change in the morphology of the NPs, which, upon annealing, tend to transform into ellipsoids), but the topic won't be covered here.

Bulk Sensors

The response of the sensors when fully embedded in an homogeneous medium is shown in fig. 3.15, where the shifts due to a medium with a 1.47 refractive index is plotted as a function of height and lattice parameter. It is clear that the highest sensitivities are sistematically associated to taller and larger nanoprisms. This effect is due to the fact that the distribution of the homogeneous analyte is neglectably dependent on the shape and volume of nanostructures. The sensitivity is dependent only on the coupling of the medium to the metal, and this, in

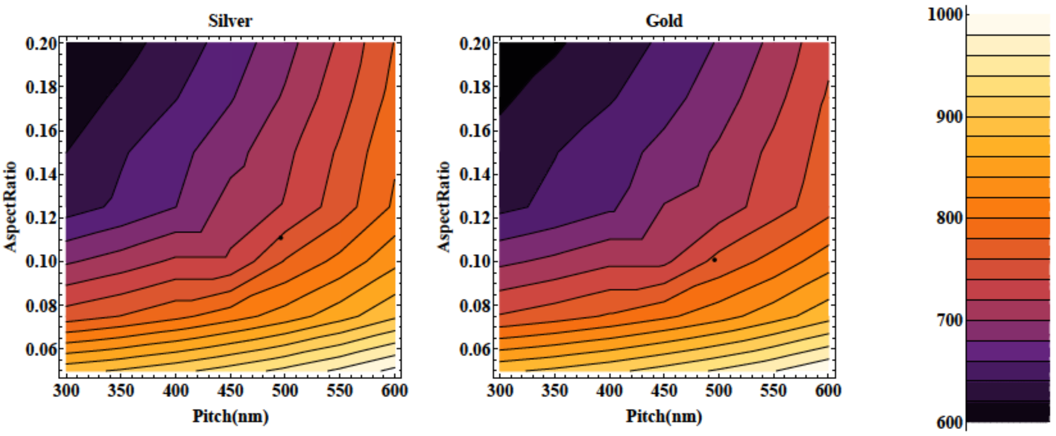

Figure 3.14.: SPR wavelength (nm) as a function of geometrical parameters a_0 (pitch) and h_r (normalized aspect ratio) for gold and silver NP.

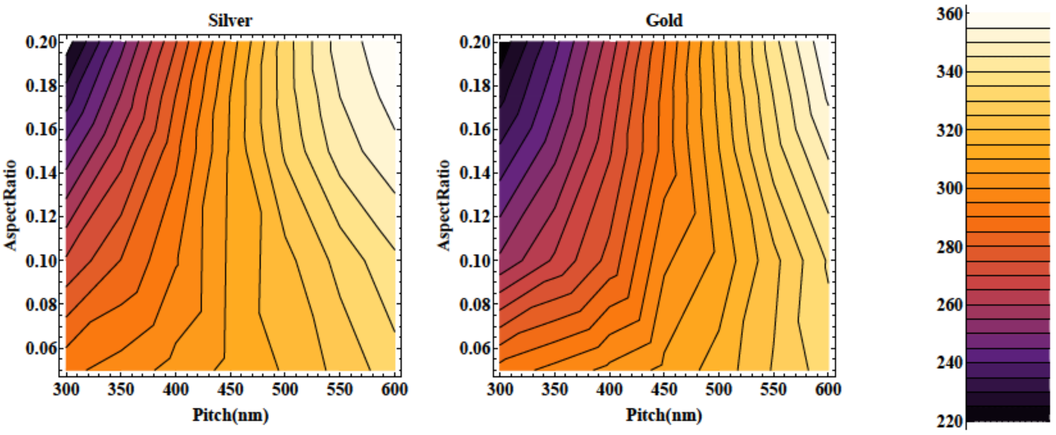

Figure 3.15.: Simulated bulk sensitivity S_∞ (nm/RIU) as a function of geometrical parameters a_0 (pitch) and h_r (normalized aspect ratio) for silver and gold NP.

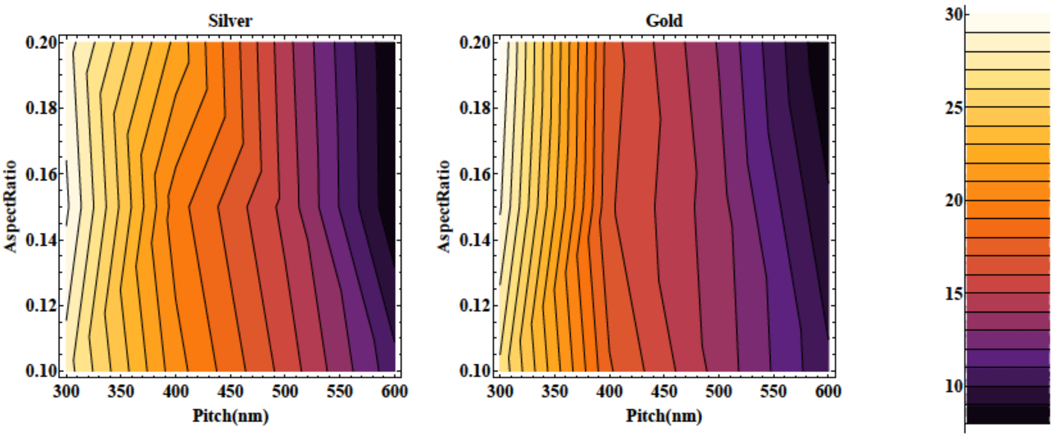

Figure 3.16.: Simulated differential sensitivity $S_0\left(RIU^{-1}\right)$ as a function of geometrical parameters a_0 (pitch) and h_r (normalized aspect ratio) for silver and gold NP.

turn, is related to the contact surface. Thus, the larger the prisms, the wider the surface of the nanostructures, the higher is the sensitivity.
In the considered region no maxima appear for the bulk sensitivity. However, the maps in fig. 3.15 give hints on the features of the optimal bulk sensors. Thus, the intervals of parameters have been extended to search for the best performances: further simulations have been carried out for large lattice parameter up to $a_0 = 800\text{nm}$. As the lattice parameter grows, however, a maximum is found, and for even larger values the sensitivity starts to drop, as shown in fig. 3.17. This is due to the fact that the first nearby prisms start to be sufficiently far away from each other to let the enhanced field vanish in a large portion of the unit cell volume. So, the plasmon interaction volume due to the single prism does not grow anymore; on the other hand, the numerical density of prisms decreases, taking to a drop in the volume where the plasmon leakage is strong enough. Around the maximum, no clear dependance on aspect ratio is detected. For bulk sensors, the best parameters set, giving the highest sensitivity, has been determined, and it works best in silver sensors:

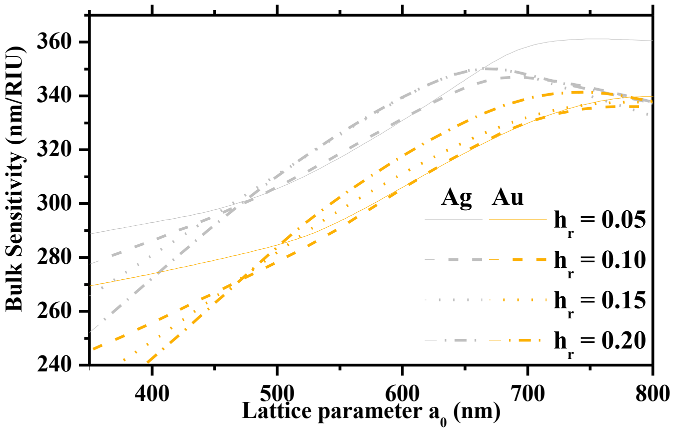

Figure 3.17.: Simulated bulk sensitivities as a function of the geometric parameters for Ag (gray lines) and Au (yellow lines).

$$a_0^{(max)} = 700\text{nm}; \quad h_r^{(max)} = 0.05; \quad S_\infty^{(max)} = 362\text{nm/RIU}, \tag{3.8}$$

Fig. 3.18 shows the EM field configurations for the best performing sensor ($a_0 = 700\text{nm}$ and $h_r = 0.05$) and for a sensor with $a_0 = 900\text{nm}$ and $h_r = 0.05$, which has a lower sensitivity for the same h_r. This drop is due to the fact that in this case the regions where the field enhancement is $E_F > 1$ are less extended in the analyte volume. In the first 500nm over the sensor surface, the region with field enhancement over 1 results the 42.5%, to be compared with a value of 48.6% for the best performing configuration, thus confirming the drop in enhanced interaction volume.

Thin Layer Sensors

Simulations have been performed in this case for prisms surrounded by a conformal thin layer of $n = 1.5$ dielectric of increasing thickness. Using equations 3.1 and 3.2, the differential sensitivity S_0 has been computed as the derivative at zero thickness of the sensitivity curve

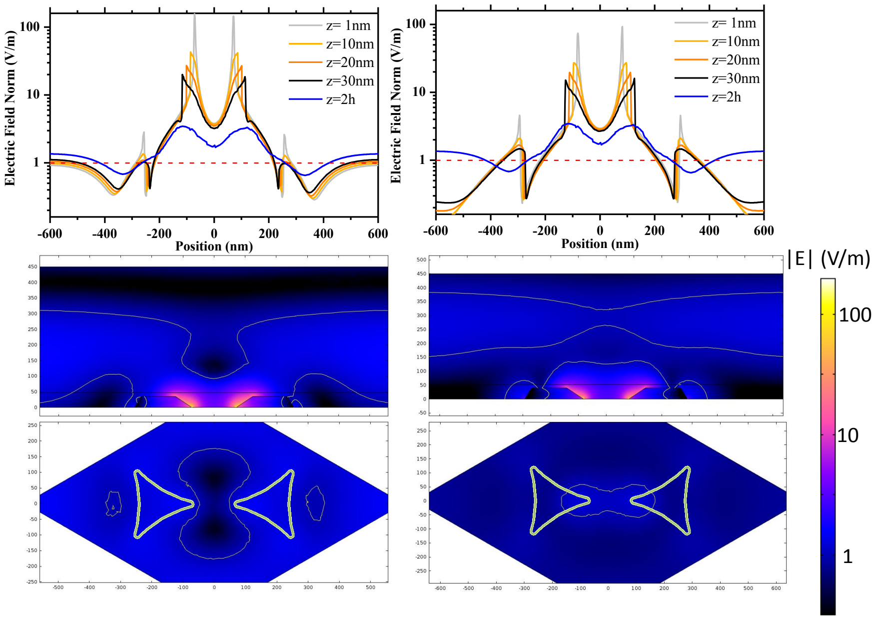

Figure 3.18.: Electric field enhancement maps: a) best performing bulk configuration b) less performing configuration. Profiles in the first neighbors at different z quotes; field map in the XZ plane; field map in the XY plane. The yellow line encircle the zones where $E_F > 1$.

obtained from the redshifts at different thickness values of the dielectric layer. Fig. 3.16 shows the simulated differential sensitivity for silver and gold. In this case a less pronounced dependence of the sensitivity on the aspect ratio is obtained. The explanantion of this behaviour is quite simple. Given that the polarization of light is parallel to the substrate, the enhanced plasmonic oscillations are perpendicular to the height of the prisms. Thus, this parameter does not affect much the intensity of the local fields. Because the thickness is in this case lower than the plasmons decay length, the relative amount of analyte which falls in the interaction volume is independent on the volume of the nanostructures, and thus on their height. The dependance on the lattice parameter is, on the other hand, still present. The larger the lattice parameter (and thus the cross section of the nanostructures), the lower is the sensitivity. This behaviour is due to the field confinement: in the case of smaller cross section, the field confinement is better, taking to higher field values and, most important, shorter decay lengths. Because the analyte is close to the nanostructure surface, it can experience an enhanced interaction resulting in a better sensitivity. The effect of the aspect ratio is negligible for large prisms, but is crucial for the best performing ones, as for optimal values of the lattice parameter, the sensitivity varies by over 10% passing from $h_s = 0.1$ to $h_s = 0.05$. The height is in this case important because it contributions to the field confinement and thus to higher field enhancements in the vicinity of the prisms surface.

Also in this case, in the considered region no maxima appear for local sensitivity. However, the maps in figs. 3.16 and 3.15 give hints on the features of the optimal sensors. Thus, the intervals of parameters have been extended to seek the best performances: further simulations for local sensitivity have been made for small lattice parameters, down to $a_0 = 150$nm. The expansion of the limits made it possible to find out maxima in both cases, as figs.3.19 show. For thin layer sensors, a maximum is found for $a_0 = 200$nm and $h_r = 0.05$. The presence of

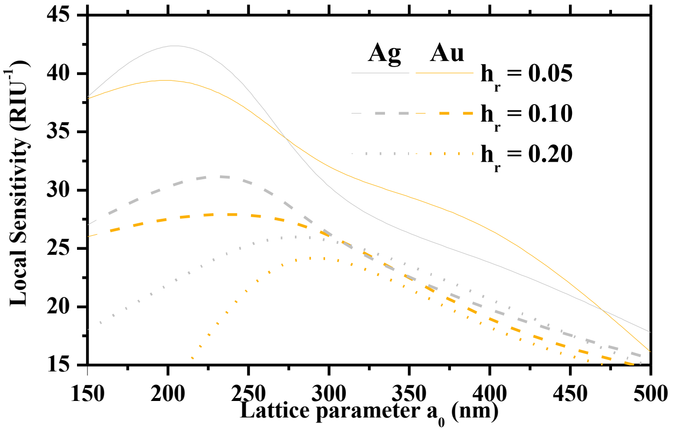

Figure 3.19.: Simulated local sensitivities as a function of the geometric parameters.

the maximum is explained by the fact that decreasing the size fo the nanoprisms, the field localization and enhancement does not grow indefinitely, but starts to saturate. On the other hand, the geometric cross section of the prisms decrases as the square of the linear dimensions, so that at a certain point, the efficiency of light-plasmon coupling drops and the better enhancement of field inside the analyte does not compensate anymore the decrease of cross section, taking to a drop in sensitivity. For thin layer sensors, the best parameters for highest sensitivity have been determined, also in this case for silver:

$$a_0^{Ag,M} = 200\,\mathrm{nm}; \quad h_r^{Ag,M} = 0.05; \quad S_0^{Ag,M} = 44\,\mathrm{RIU}^{-1}. \tag{3.9}$$

3.2.5. Biosensors based on SERS

The simulation framework can give many useful information on the physics of the interaction of nanostructures with light. In particular, in this section the application of the near-field patterns of the NPs will be briefly reviewed. The local field map for a NPs array is shown in fig.3.20 as an example of the field distribution. In the case of biosensors based on SERS, the near-field is exploited for the resonant anelastic spectroscopy, in contrast with the previously considered biosensors, which relay on a far-field approach.

SERS

SERS is a spectroscopic technique which exploits the LFE effect to compensate for the low Raman cross-section ($\sigma \sim 10^{-30}\mathrm{cm}^2$) to enhance the intensity of the *Raman Scattering*, thus making it possible to have access to the roto-vibrational spectrum of molecoles. Since those spectra are distinctive of each molecole, the SERS can be used to identify the analytes. The Raman scattering is an inelastic scattering process, thus the excitation wavelength λ_{in} is different (usually shorter) from the emission wavelength λ_{out}. As the Raman scattering is dominated by elastic scattering and fluorescence emission, the enhancement from the substrate is capital for a proper acquisition of the signal, given the $|\mathbf{E}|^4$ dependance of this enhancement, at variance with the $|\mathbf{E}|^2$ of the other two. The most relevant figure of merit in this case is thus the *enhancement factor* G_{SERS}. This factor can be computed once the local field distribution is known inside the volume of the analyte both for the excitation and emission frequencies.

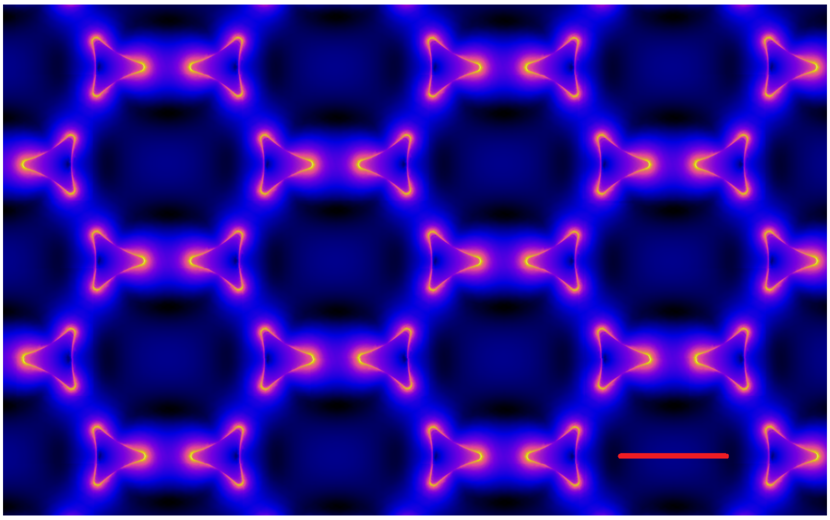

Figure 3.20.: Field distribution in an array of silver NPs, resonating at $\lambda = 706$nm. The color map is logarithmic, black and blue stand for low electric field norm, magenta and yellow for high field norm. Bar: 500nm

The pointwise enhancement factor is given as a function of the electric field $\mathbf{E}(\mathbf{r}, \omega)$:

$$G_{SERS}(\mathbf{r}, \omega_{in}, \Delta\omega) = \frac{1}{3} \frac{|\mathbf{E}(\mathbf{r}, \omega_{in})|^2 \cdot |\mathbf{E}(\mathbf{r}, \omega_{in} - \Delta\omega)|^2}{|\mathbf{E_0}|^4}, \tag{3.10}$$

where $\mathbf{E_0}$ denotes the amplitude of the incident wave, $\mathbf{E}$ is the computed local field, and the factor $1/3$ is due to the integration of the cosine given by the mutual orientation of the local electric field and the excited molecule dipole moment. The overall enhancement factor can then be computed by integrating the local factor over the volume of the analyte molecule V:

$$G_{SERS}(\omega_{in}, \Delta\omega) = \int_V G_{SERS}(\mathbf{r}, \omega_{in}, \Delta\omega)\, \mathrm{d}V. \tag{3.11}$$

The SERS enhancement factor is thus dependent on two parameters, the incident electric field frequency and the difference between excitation and emission frequencies. The second is characteristic of each molecule: in general, a molecule has many transitions, for instance, Benzenethiol has strong Raman peaks at $\delta\omega = 422\text{cm}^{-1}$, 1075cm^{-1} and 1575cm^{-1}. Those transitions will be used for testing the performances of the considered NPAs. The excitation wavelength can be choosen (compatibly with the availability of light sources and detectors) to get the best performances on the desired transitions, and the optimization of the substrate can improve the intensity of the signal by orders of magnitude. The importance of the simulations of the near-field in contrast to the far-field absorbance spectrum, often used as a benchmark of the SERS enhancement, can be easily pointed out. In fact, the SERS enhancement factor is not simply maximized when the SPR is located at the excitation wavelength: eq.3.10 shows that the factor is a convolution of the field enhancement both in excitation and in emission. Thus, the correct G_{SERS} computation must take into account the field distribution at both frequencies, an operation which can be easily achieved by FDFD simulations. Simulated NPA has a lattice parameter $a_0 = 500$nm, prisms height 70nm, side factor $f = 0.25$, and the metal is silver. The SERS enhancement has been integrated inside a 4nm-thick layer on the surface of prisms, to taylor the actual distribution of the Benzenethiol molecoles. Fig.3.21a shows the computed G_{SERS} factors (left scale) in comparison with the absorbance spectrum (right scale, dashed curve) of the same NPs array.

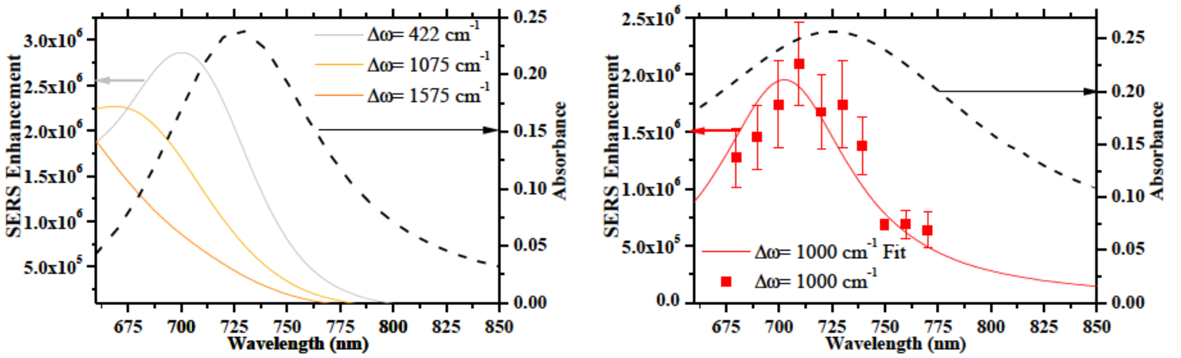

(a) Comparison between absorbance (black dashed curve, right scale) and G_{SERS} enhancement factors (coloured curves, left scale) for the same nanostructure.

(b) Comparison between experimental absorbance (black dashed curve, right scale) and experimental G_{SERS} enhancement factor at 1000cm^{-1} for the same nanostructure, measured with a Ti-Sapphire tunable laser.

Figure 3.21.: Simulated and experimental pectral-resolved SERS enhancement factors and far-field absorbance. NPA has a lattice parameter $a_0 = 500$nm, prisms height 70nm, side factor $f = 0.25$, and the metal is silver.

It is evident that the maximum of the G_{SERS} is at shorter wavelengths with respect to the absorbance maximum. Further, for different transitions (in this example, the three main transitions of benzenthyol have been considered), the maximum is at different wavelengths. This mismatch is due to two different effects: on one hand, it has been already discussed the role of the convolution of excitation and emission field distributions; on the other hand, the E^4 dependance of the G_{SERS} greatly enhances the importance of the hotspots, the (relatively small) regions with the highest field values. Because the peak of the resonance in these regions can in general be at slightly different wavelengths with respect to the rest of the nanostructure; thus, even in the approximation of $\Delta\omega = 0$, the G_{SERS} may show its maximum at a different wavelength with respect to the absorbance, which is less sensitive to the hotspots in the volume integration.
The same behaviour have been observed experimentally: the simulated prisms have been tested as a SERS substrate using the 1000cm^{-1} Raman band of benzenethyol (BT) as probe, and fig.3.21b show the results of the measurements. The enhancement factor is in good agreement with the simulated value, and also the blue-shift of the Raman peak is recovered, even if the shift is sensitive to the precise spectral dependance of the local field in the experimental structure.

3.2.6. Plasmon-Induced Thermal Heating of Nanostructures

As noted in chapter 1, plasmons can decay in two ways: radiatively and non-radiatively. In the second case, the final effect is to convert the plasmon energy into heat, thus causing an increase in the temperature of the nanostructure. For many aspects, an uncontrolled increase in temperature can cause a device to malfunction. As an example, if the local temperature grows up over 100 °C, any solution in water may start boiling. At even low temperatures, biological molecules can experience unwanted modifications or denaturation. As an example, DNA double strand denaturates at $T \sim 70°\text{C}$. In general, the control of local temperature is not trivial with macroscopic methods, due to the extremely low heat quantities, fast dynamics and possible strong gradients.

Simulation can give an hint on how much light flux can be safely shined on a plasmonic device, in the form of temperature maps on the surface of the sample and determination of heating dynamics. The starting point is once again the local field distribution map. Starting from this information, the heat generation in stationary conditions can be expressed as:

$$Q\left(\mathbf{r}\right)=\frac{1}{2}\omega\varepsilon_2\left(\mathbf{r}\right)E^2\left(\mathbf{r}\right). \tag{3.12}$$

This way, any point where the imaginary part of the dielectric function is non zero becomes a source of heat; the thermal dynamics of the system can be derived on the base of the thermal properties of materials, using the heat transfer equation:

$$\rho C_p\frac{\partial T}{\partial t}+\rho C_p u\cdot\nabla T=\nabla\cdot\left(k\nabla T\right)+Q, \tag{3.13}$$

where ρ is the density, C_p is the heat capacity and k is the thermal conductivity; and the stationary one once the thermal equilibrium is reached. As boundary conditions, the heat transfer to the environment must be modeled. Due to the modest temperature increase experienced by the samples (as will be shown in the following) it is possible to neglect thermal black body irradiation. The considered model has vacuum over the sample and silica as substrate. Thus, the convective heat transfer is not present and the only non trivial boundary condition is the heat conduction by the silica substrate to the sample holder. Given the very small amount of electromagnetic energy absorbed and converted to heat, the sample holder is modeled to be at constant (room) temperature, and the thermal flux equation reduces to the linear form.

On these assumptions, the heating of an ordered array of nanostructures have been derived, and the results have been compared to experimental data. To carry out the experiment, a NPs array sample obtained by NSL and silver sputtering have been thermally annealed to get ellipsoidal-like silver nanoparticles, resonating in the region of the Ar laser (main lines at 488nm and 515nm), as shown in fig.3.22. In the experiment, as reported in [100], the local heating induced by Ar laser illumination at different power rates is measured exploiting the dependance on temperature of the photoemission of an Eu-based molecule, EuTTA (Eu-theonyltrifluoracetate), embedded in a 10nm-thick layer of PMMA deposited on the NPA. The optical and thermal features of the experiment have been modeled and the simulation has been checked using far-field spectra. The effect of the illumination by the 488nm and 515nm lines of the Ar laser at different powers has been computed. As previously explained, the electromagnetic absorption worked as the source of heat, and the dynamics of the heating process has been simulated for the three power values investigated. Also the stationary, equilibrium temperatures have been calculated in the three cases. Fig.3.23a shows the variation in temperature for the three power values. The plotted temperature is the average of the temperatures sampled in a 10nm thick conformal layer over the substrate, and outside the metal nanostructures, to reproduce the domain in which in the experiment the Eu is present. The dynamics is in this case very fast, and this is due to the nanometric scale of the system. On such small scales, the thermal conduction is very efficient, and thermal equilibrium is

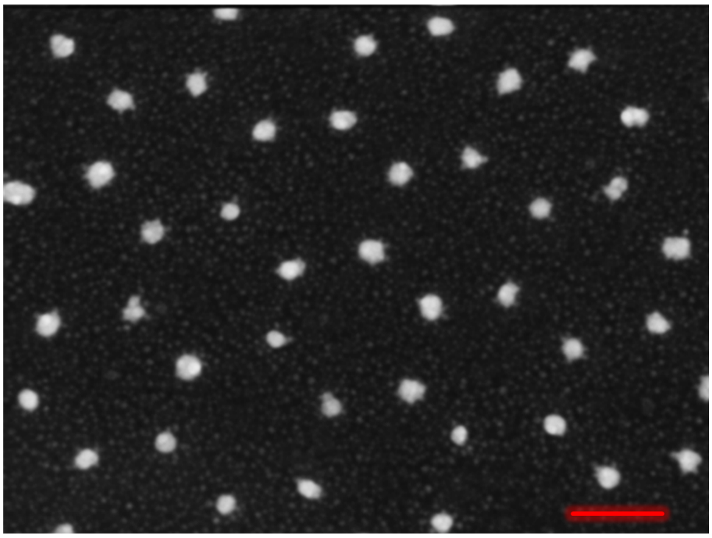

Figure 3.22.: SEM image of thermally annealed silver NPs. The starting lattice parameter is $a_0 = 330$nm, and the metal is silver. The annealing has been performed at 300°C for 30 minutes. Bar:200nm.

reached with an exponential curve. For all the three powers, the time constant of the exponential resulted $\tau = 0.45 \pm 0.01\mu$s. Figure 3.23b shows a comparison between the simulated and the measured temperatures as a function of the laser power. The two series are in very good agreement. From a linear fit of the data, it has been possible to find out the differential temperature increase per mW of laser power:

$$T(P) = T_0 + \gamma P, \tag{3.14}$$

and the resulting value is $\gamma = 0.11$°C/mW. In conslusion, experiment and simulation proved the possibility to locally measure the heating due to interaction with light in plasmonic nanostructures. The results also show that the chosen class of nanostructures heat up by no more than about 20°C, even under the strongest illumination here considered (153 mW). This on one hand assures that the structures don't modify during the operation, as power flux is far

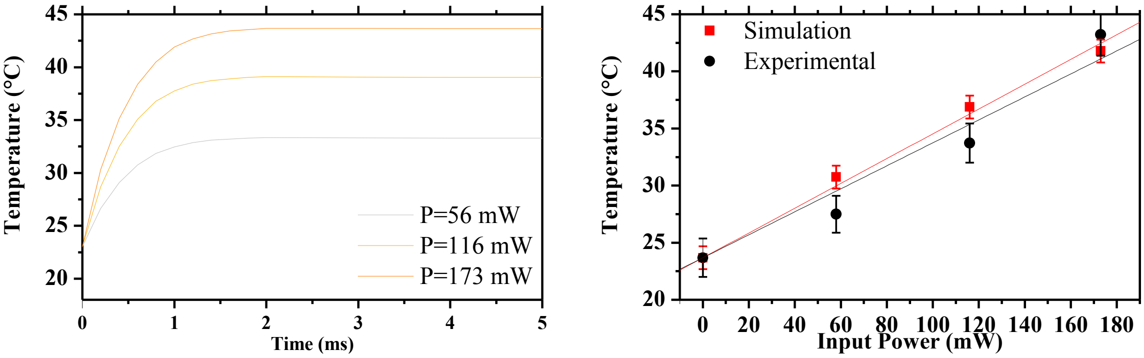

(a) Heating dynamics at different powers.

(b) Comparison between simulation and experiment at equilibrium.

Figure 3.23.: Results of the heating of nanostructures simulations.

lower for usual applications. On the other hand, this kind of nanostructures can be safely used in interaction with biological material, which may denature or decompose as an effect of high temperature.

3.2.7. Conclusions

The optimal geometric parameters for NPA-based biosensors have been derived. In particular, the best sensitivity have been found for both bulk sensors and thin layer sensors. These two class have been demonstrated to behave in an opposite way: the bulk sensors yield best performances with large NPs, as the thin layer sensors give best results for small-sized nanostructures. The explanation of this opposite behaviour has been found in the different requirements of localization for the two approaches, and this explanation has been confirmed by field maps. The best performing bulk sensors are constitued by silver NPs, having $a_0 =$ 700nm and $h_r = 0.05$, and the best sensitivity is:

$$S_\infty^{(max)} = 362\,\mathrm{nm/RIU}. \tag{3.15}$$

The best performing bulk sensors are constitued by silver NPs, having $a_0 = 200$nm and $h_r = 0.05$, and the best sensitivity is:

$$S_0^{Ag,M} = 44\,\mathrm{RIU}^{-1}. \tag{3.16}$$

Nanoprisms are a promising system to be used also as a SERS substrate: the enhancement factor is not as large as the best achieved using other kinds of substrates, but the ordered structure give a solid base for reproducibility. Indeed, the fact that the fabricated samples, which carry defects and imperfections, behave in a very similar way with respect to the ideal simulated system is a proof of the stability of this kind of system against defects.

Finally, thermal analysis of the NPA architecture showed that the heating of the nanostructures due to the illumination at a plasmonic resonance is well below the limits for a safe use with biological materials. With an average heating rate of 0.11°C/mW, it is possible to use high power lasers without the risk of denaturation.

3.3. Nanohole Arrays: Emitter-Nanostructure Interaction

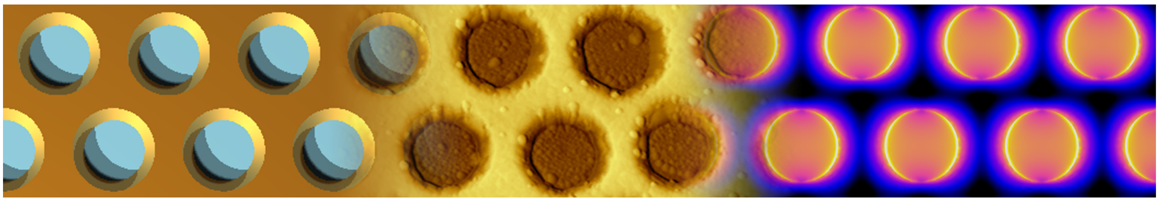

Design, synthesis and modeling of Nano Hole Arrays.

Erbium doped materials are of strategic interest in the field of optical communication, due to the fact that trivalent Er ions exhibit a radiative emission at 1.54μm, a wavelength that matches the range of minimum transmission loss for silica-based optical fibers [101,102]. In the recent years, a large amount of research has been carried out on Er-doped thin films and nanostructures, since they can find application in the realization of planar optical amplifiers [103], solid state lasers [104] and light sources [105]. In the Er^{3+} excitation process originating the characteristic $^4I_{13/2} \rightarrow {}^4I_{15/2}$ transition at 1.54μm, the photon absorption occurs in one of the higher-lying levels and it is followed by fast relaxation to the metastable first excited state ($^4I_{13/2}$) via non-radiative multiphonon emission. The transition from the $^4I_{13/2}$ state to the ground state ($^4I_{15/2}$) has large relaxation energy of about 0.8eV, and a spontaneous lifetime for Er^{3+} can be of several milliseconds. The long lifetime of the $^4I_{13/2}$ metastable level makes the Er^{3+} emission sensitive to nonradiative decay processes, such as upconversion and concentration quenching [106]. Since the early work of Purcell [107], it is well known that the variation of the local photonic density of states can modify the spontaneous emission rate. The presence of a reflecting surface in the vicinity of the emitter will modify the free space boundary conditions and thus change the photonic density of states. For example, the pioneering work of Drexhage [108] has experimentally studied the modification of the radiative lifetime of Eu^{3+} ions near a silver mirror. The model proposed by Chance et al. [109] describes and predicts the variation of the spontaneous lifetime of an emitter in close proximity of a surface using a well-tested classical approach. The emitter is indeed considered as a forced damped dipole oscillator and the influence of the surface is taken into account by determining the total electromagnetic field acting on the dipole, including the dipole back-reflected field from the surface. The distance between the emitter and the surface is a crucial parameter for controlling the emitter lifetime, since the amplitude and the phase of the reflected field will determine whether the emission rate will be enhanced or suppressed. Moreover, when the separation between the emitter and the metal surface is less than approximately 1/4 of the emission wavelength, resonant coupling between the emitter and the surface plasmon polariton mode may occur, leading to shorter lifetime and smaller Photoluminescence (PL) intensity [110, 111]. In recent years, a considerable amount of work has been carried out on the modification of spontaneous emission in the presence of an reflecting surface [112–114], however these systems are characterized by the presence of an emitting sources with an intrinsic high quantum efficiency (e.g., quantum dots).

Nanohole arrays can interact with emitters both as a reflecting surface (usual values of reflectance are over 50%) and as plasmon-supporting structure. Moreover, in holes circular surface modes can be excited, as EOT shows. The interaction and coupling of emitters with such modes will be studied as an extension of the semi-infinite film framework.

3.3.1. The Physics of the Problem

The modification of the quantum efficiency of an emitter in presence of a nanostructure (NHA) is here analyzed only in its Electromagnetic part, inserting the lifetime in absence of nanostructures and interfaces as an experimental parameter, and computing only the relative variations of emission rates. A full quantum tratment of the emitter is beyond the scope of this work, but the used approach can nevertheless give wanted results once the correct unperturbed emission rate is considered. Since the framework is purely electrodynamical, all non-radiative decays won't be covered by the analysis. Thus, only the modifications of the radiative emission rate are computed. The total emission rate can then be recovered by adding the non-radiative decay rate as

$$\gamma = \frac{1}{\tau} = \frac{1}{\tau_{nr}} + \frac{1}{\tau_r} = \gamma_{nr} + \gamma_r. \tag{3.17}$$

A full electrodynamical derivation of the lifetime modification exists (in a dipole approximation) for the interaction of emitters in a dielectric matrix with a semi-infinite space filled by another material (in general, both a metal or a dielectric can be used). The model (fig.3.24a), proposed by Chance and collaborators [109], expresses the radiative decay rate γ as a function of the uniform matrix decay rate Γ_0^{Rad}. The forms for emitters with dipoles oriented in a parallel or transverse direction with respect to the interface have been derived and are:

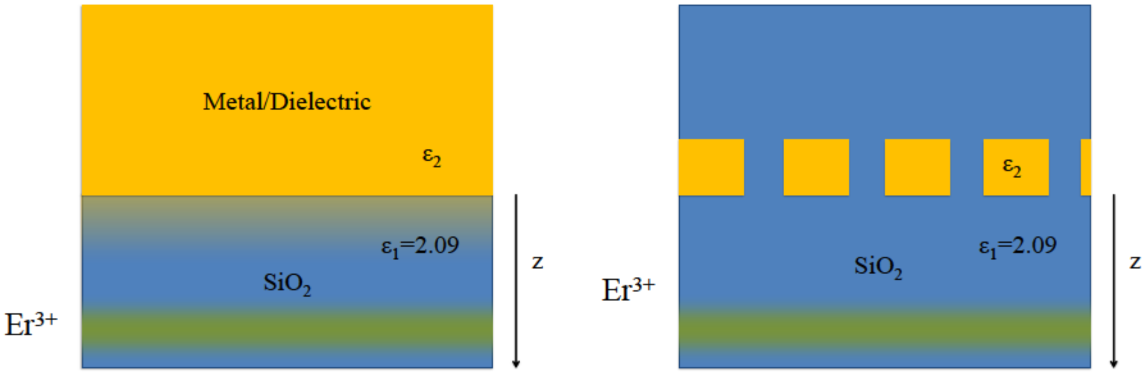

(a) Interaction with a semi-infinite film. **(b)** Interaction with a NHA

Figure 3.24.: Schemes for the problem. The erbium emitters are embedded in a SiO$_2$ matrix in proximity of a film/NHA.

$$\Gamma_t^r = \Gamma_0^r \left\{ 1 - \frac{3}{2} Im \left[\int_0^{+\infty} R_p \frac{u^3}{a_1} \exp\left(-4\pi n_1 a_1 z_0/\lambda\right) \mathrm{d}u \right] \right\} \tag{3.18}$$

$$\Gamma_p^r = \Gamma_0^r \left\{ 1 + \frac{3}{4} Im \left[\int_0^{+\infty} \left[\left(1 - u^2\right) R_p + R_t \right] \frac{u}{a_1} \exp\left(-4\pi n_1 a_1 z_0/\lambda\right) \mathrm{d}u \right] \right\}, \tag{3.19}$$

where $u = k/k_1$ is the normalized wavevector and k_1 is the wavevector in the medium 1, $\lambda = 2\pi c/\omega$ is the freespace wavelength of the emission. The parametric functions are defined as follows:

$$R_t = \frac{a_1 - a_2}{a_1 + a_2}; \qquad R_p = \frac{\varepsilon_1 a_2 - \varepsilon_2 a_1}{\varepsilon_1 a_2 + \varepsilon_2 a_1}; \qquad a_1 = -i\sqrt{1 - u^2}; \qquad a_2 = -i\sqrt{\varepsilon 2/\varepsilon 1 - u^2}. \tag{3.20}$$

The total decay rate can then be computed straightforwardly by averaging over the polarizations:

$$\frac{1}{\tau_r} \equiv \gamma_r = \frac{1}{3}\left(\gamma_t + 2\gamma_p\right). \tag{3.21}$$

Figure 3.25 shows the computed γ_r modifications due to interaction with semi-infinite films of different materials as a function of the depth of the emitter from the interface z, using the 1.54μm line deacy rate in silica as $\Gamma_0^r = 70s^{-1}$. The effect of the presence of the film is the modification in the decay rate, which is now dependent on depth, with an oscillatory behaviour. In this experiment Er is introduced in the silica matrix by co-sputtering with a constant in-depth profile.

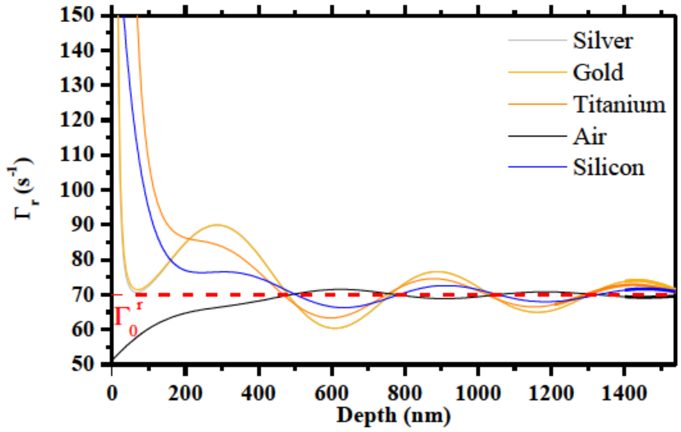

Figure 3.25.: Erbium radiative dacay rates modifications due to the presence of semi-infinite films of different materials.

To model a distribution $f(z)$ of emitters starting from eqq.3.19, which gives the pointwise decay rate, the total emission signal is computed. In this step, suppose that at the time $t = 0$, all the emitters in the distribution are excited. Then, the signal from the distribution, due to incoherent emission form the emitters, is given by the integral:

$$I_{PL}(t) = I_0 \int_0^{+\infty} f(z) \exp\left[-t\gamma_r(z)\right] \mathrm{d}z, \tag{3.22}$$

where I_0 is a constant dependent on the total number of emitters. To find the modification of the emission decay rate, the last step is to process the obtained I_{PL} in the same way as for experimental data. The computed signal must then be fitted, and the decay rate γ_r (or the lifetime τ_r) comes out as a fitting parameter. Two alternatives are present. The simplest one consists in fitting $I_{PL}(t)$ with an exponential decay function:

$$f(t) = f_0 + Ae^{-t\gamma_r} = f_0 + Ae^{-t/\tau_r}. \tag{3.23}$$

This approximation is valid when the variance of the decay rate of the population of emitters is negligible with respect to the mean decay rate. However, in the case of emitters close to the interface, or a distribution that extends over several tens to hundreds of nanometres in depth, the variance in the population may be important, also of the same order of magnitude of the mean value. In this case, the approximation of single exponential is poor, and the more realistic *stretched exponential* function should be used:

$$f(t) = f_0 + Ae^{-(t\gamma_r)^{\beta}} = f_0 + Ae^{-(t/\tau_r)^{\beta}}. \tag{3.24}$$

Strictly speaking, the stretched exponential describes the decay pattern of a population of emitters whose decay rates distribution is Gaussian. This function, however, works better than the single exponential one in the considered conditions. When the stretched exponential is used, the *effective* or mean lifetime is now a function of the fitted τ_r and β:

$$\tau_{eff} = \frac{\tau_r}{\beta}\Gamma\left(\frac{1}{\beta}\right), \tag{3.25}$$

where $\Gamma(x)$ is the *Euler's gamma function.*
An example of code for the computation of the lifetime modification for Wolfram Mathematica is reported in section C.2.

Nanohole Arrays and Modification of LDOS

A Nano Hole Array (NHA) is a (metal) thin film, whose thickness usually ranges from some tens to some hundreds of nanometres, having passing-through holes arranged in an (ordered) 2D array. Optically, NHAs have two interesting features, strictly relate one to the other. The first feature is the ability to couple photons to surface plasmons without needs of a prism, thus acting as a grating (cfr. chap.1). The second feature is the so-called Extraordinary Optical Transmission (EOT) [116]: even if the thickness is by far greater than the attenuation length for photons, and the holes diameter is smaller than the $\lambda/2$ Abbe's limit for transmission, light can pass through the NHA in a way which is forbidden by *geometrical optics.*
The properties of Nano Hole Arrays are related to their ability to efficiently convert light into surface plasmons by providing the necessary extra-momentum for the conservation in the coupling. The extraordinary transmission process can be divided into 3 phases: the coupling of light to the SPP on the inciding surface, the transmission through the hole and the re-emission from the second surface. The EOT thus reside on the coupling relations on both surfaces, and the transmission maximum condition can be derived from the conservation of momentum:

$$\mathbf{k_{sp\parallel}} = \mathbf{k}_{\parallel} \pm m\mathbf{G}, \tag{3.26}$$

where m is an integer, $|\mathbf{G}|$ is a lattice base vector and $\left|k_{\parallel}\right| = 2\pi/\lambda$ is the modulus of momentum of the incident light. For hexagonal lattices, the maximum condition results, for normal light:

$$\lambda_{max} = \frac{a_0}{\sqrt{\frac{4}{3}\left(i^2+ij+j^2\right)}} Re\left[\sqrt{\frac{\varepsilon_m\varepsilon_d}{\varepsilon_m+\varepsilon_d}}\right], \tag{3.27}$$

where ε_m and ε_d stand for the dielectric function of the metal and of the dielectric in contact with it, and i and j are the Miller indexes of the scattering orders. Given the dispersion of the metal, its dielectric function is not constant, and so the relation must be used recursively to get the maximum transmission wavelength. This relation does not take into account the presence of the holes, thus the losses at the edges of the holes are not considered and may modify the position of the maximum. Experimentally, it has been observed [117, 118] that, due to this effect, the resonances result slightly redshifted with respect to the ones foreseen by 3.27. Moreover, the relation is valid for a single interface between two semi-infinite layers. When the second surface of the NHA is in contact with a different dielectric, the maximum position would be different, and the transmittance spectra show two set of peaks, one belonging to one of interface, and one to the other. This is the usual case for a nanohole array on

glass, with air at the other interface. Also the size and shape of the holes has a role in the transmission. In fact, changing holes shape from circular to square changes the transmission pattern [119, 120] of the NHA, as an effect of the change of both the cutoff wavelength and of the LSP modes associated with each hole. However, the SPP modes due to the periodicity of the array dominate in the transmittance spectrum formation [120].
The presence (and the ability of photon coupling) of plasmonic and holes modes is the key in the modification of Local Density of Optical States (LDOS), whose effects on the emitters lifetime will be studied here.

3.3.2. Samples Fabriaction and Characterization

The fabrication of samples involves the processes for the synthesis of both the emitters (Er^{3+} ions) and the nanostructure, as presented in an our work [121]. Fig.3.26 shows a schematical view of the steps in the sample fabrication.

Emitters Embedding

Erbium ions emit at 1.54μm when the ion is coordinated with 6 oxygen atoms from the silica matrix. The emission is quenched when the erbium exceeds about 1% in atomic concentration. The main cause of non-radiative decay is given by the interaction with OH groups, and takes to an intense attenuation of the signal reaching the detector. To fulfill all the conditions for a good emission, thus, erbium ions must not exceed a concentration of 1at%, must be correctly coordinated with oxygens and the concentrations of OH must be negligible. All these three requirements can be achieved by controlling the deposition and the annealing of the samples. For the substrate a high-purity *HSQ-300*, 1 mm thick fused quartz glass from *Heraeus* has been used. The substrates have been cleaned by immersing them in a *Acid Piranha* solution (30% H_2O_2 and 70% H_2SO_4) for 20 minutes and then thoroughly rinsing them with ultrapure water. The deposition of the erbium-doped silica matrix has been performed by magnetron sputtering: one RF source at 13.56MHz for silica and one DC source for erbium. The depositon took place in a reactive atmosphere (95% Ar and 5% O_2) at a pressure of $5 \cdot 10^{-3}$mbar. The RF power on the silica target ($2in.$ diameter) was 250W; the power on the erbium target was $3W$ or $5W$, in order to obtain, respectively, 0.1% and 1.1% in erbium concentration. The concentration has been measured by the Rutherford Back Scattering (RBS) method and the concentration profile by Secondary Ions Mass Spectroscopy (SIMS). Prior to silica and erbium co-deposition, a 75nm thick buffer layer of pure silica was deposited. After the deposition, a spacer of pure silica has been deposited on samples with different thicknesses, in order to vary the distance between the emitters and the nanostructure. All the sputterings have been performed with rotating sample holder, to improve the homogeneity of the depositions. As a final step before optical characterization, in order to restore the matrix defects induced during the Er:SiO_2 film deposition and activate the Er^{3+} luminescence at 1.54μm, the samples were annealed for 2 hours at 900°C in vacuum ($P \sim 10^{-5}$mbar). Er ions diffuse minimally under these conditions, as checked by SIMS.

Films and Nanohole Array Synthesis

The synthesis of an optically thick film ($T \gtrsim 100$nm) of different metals have been performed by magnetron sputtering, followed by a 250°C annealing in vacuum ($P \sim 10^{-5}$mbar) for $4h$

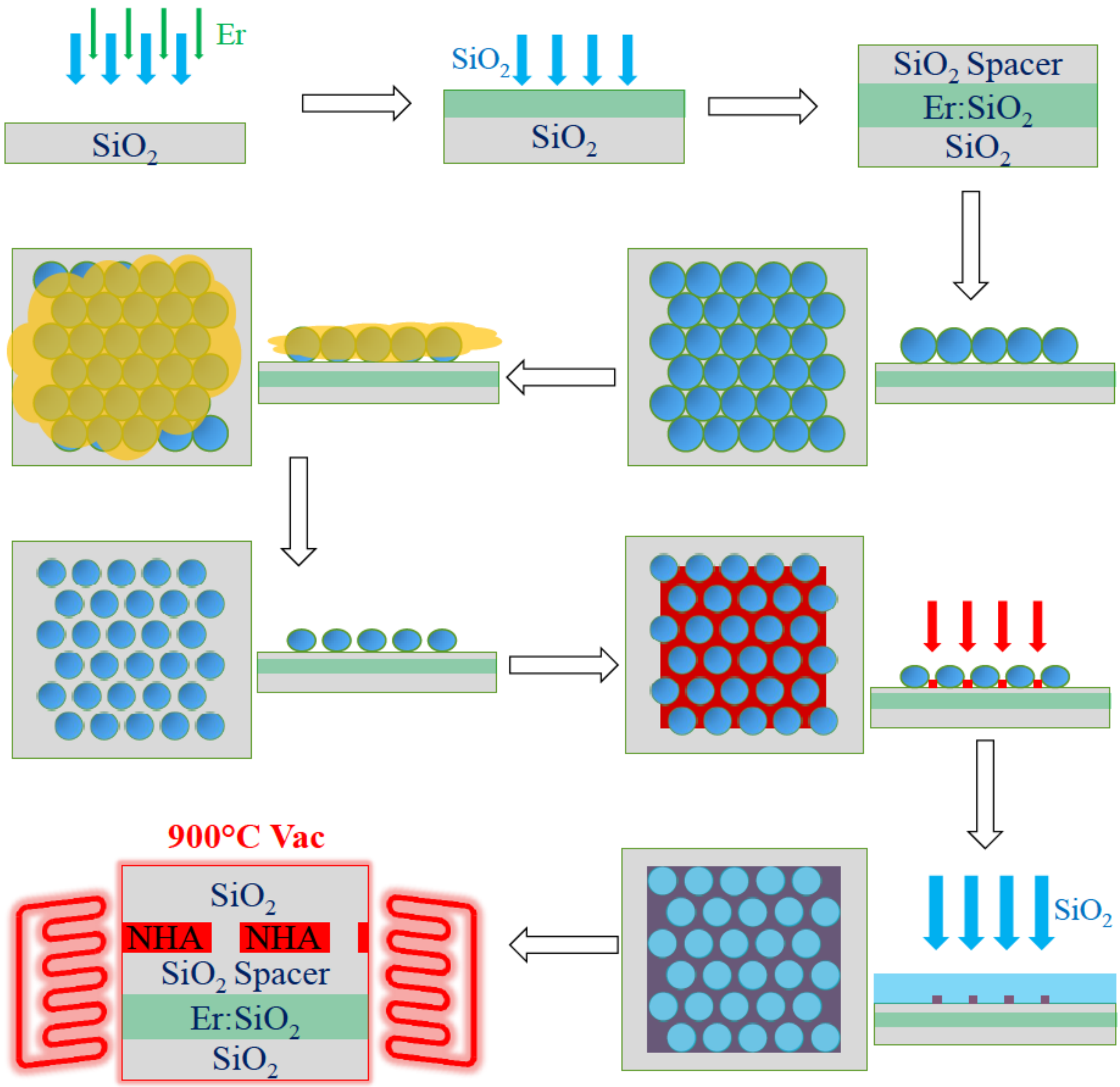

Figure 3.26.: Nanohole Array on Erbium doped silica fabrication by NSL and magnetron sputtering: Er:SiO_2 deposition; SiO_2 spacer deposition; mask deposition; Reactive Ion Etching; metal deposition; SiO_2 deposition; annealing.

in order to enhance the adhesion of the metallic film and the quality of the silica-metal interface. The films obtained in this way have been used to determine the experimental dielectric functions of the metals by ellipsometry, using a VASE of J. A. Woollam Co. spectroscopic ellipsometer.

For the patterning of nanostructures (in this case, NHAs) on the doped substrate, the NSL technique has been used, as described in section 3.1. PS Nanospheres of three different diameters have been used in the NSL, namely 922 nm, 1030 nm and 1280 nm. Once the PS nanosphere array is deposited on the substrate, a Reactive Ion Etching (RIE) has been performed to reduce the size of the spheres without relocating them over the substrate. The RIE has been performed in a (35% O_2, 65% Ar) atmosphere, at power of 25W. The duration of the etching have been tuned such that the radius of the nanospheres (and thus the radius of the obtained nanoholes) is reduced by a factor of about 2/3 from the original. After the etching, a layer of 120nm of gold has been deposited by DC sputtering on the NSL-patterned surface. The nanospheres together with the metal in excess over them have been removed by sonication in toluene for 2 to 5 minutes, in order to clean out nanohole arrays. As a final step, a 400nm thick layer of silica has been sputtered on the NHAs to prevent nanostructures from geometric modifications due to thermal annealing and to enhance the homogeneity around the nanostructure. As for the case of bare doped silica, a 900°C annealing in vacuum was performed both for films and NHAs to activate the Er^{3+} luminescence.

Photoluminescence Measurements

PL measurements, both integrated and time resolved, were performed at room temperature by exciting the samples with a 6Hz mechanically chopped cw Ar laser. Both in-resonance ($\lambda_{exc} = 488$nm) and out-of resonance ($\lambda_{exc} = 476.5$nm) excitation conditions were employed. The PL signal was analysed by a single grating monochromator and detected by a near-infrared photomultiplier tube cooled by liquid nitrogen. The time-resolved PL analysis was carried out by fixing the detected wavelength at 1.54μm and collecting the PL intensity evolution as a function of the time with a digital oscilloscope (Tektronix TDS 7104).

3.3.3. FEM Simulations

Following the ideas of the Chance analytic Electro-Dynamic (ED) model, simulations have been carried out considering one isolated dipole at time. The signal from an arbitrary distribution and the changes in decay rates are then recovered in a similar way by integrating the results from differently placed dipoles.

As a first step, the effect of a semi-infinite film have been modeled, in order to validate the method using the electrodynamical derivation as a benchmark. In this case, the use of periodic boundary conditions is not suitable: this way, a mirrored dipole would exist in each cell, and the simulation would describe a system where dipoles have the same periodicity of the nanostructure (and arbitrarly fixed phase relations), which is not the present case. The alternative is to simulate several unitary cells together, using PML at the boundaries to suppress backscattering. The minimum size of the model to have correct results is the one for which near-field from the dipole emission vanishes before reaching the boundaries. As a simple test of correctness, the comparison with the electrodynamical Chance model has been used. A simulation domain surrounded by a sphere of radius 4.705μm ($\sim 5\lambda_0$) was found to be sufficient for the correct modeling of the emitter emission and interaction with the film, as it will be shown in the following. To simulate the interaction with the film, the domain have been subdivided into two hemispheres, one representing the silica matrix, the other representing the film. The interface has been placed at the $z = 0$ plane. Dipoles have been placed so that their projection on the interface plane falls in the central position of this last ($x = 0$, $y = 0$). The $\hat{z}$ coordinate of the dipoles (i.e. the distance from the interface) have been varied from 1nm to 1000nm. For each z position, the emission pattern from an electrical dipole oriented once in the direction parallel to the interface and once in the orthogonal direction has been computed. To evaluate the modifications of decay rate, the integral of the Poynting vector on a closed surface encircling the dipole (and not encircling any part with an absorbitive material) was used:

$$\frac{\gamma_r}{\Gamma_0^r} = \frac{\int_\Sigma \mathbf{S} \cdot d\sigma}{\int_\Sigma \mathbf{S_0} \cdot \mathrm{d}\sigma}, \tag{3.28}$$

where $\mathbf{S_0}$ is the Poynting vector computed in the case of homogeneous and infinite silica matrix. The resulting values for γ_t and γ_p are plotted in fig.3.27 as a function of the depth z. The comparison with the analytic electrodynamic (ED) model is very good, thus validating this way of simulating the film-emitter interaction.

The simulation of the nanohole array has been carried out similarly to the film. In this case, the whole space is constitued by silica, except for the NHA structure extending in the XY plane, and centered at $z = 0$, as shown by fig.3.28b. Differently from the case of the film, the homogeneity in the XY plane is replaced by the periodic Honeycomb lattice resulting from the NSL process. As pointed out before, the periodic boundary conditions don't give correct results due to the replication of emitter too. So, 19 XY unit cells have been simulated, in a way that the computation domain is the same considered in the film case. Because the periodicity of the lattice, the beahviour of emitter can be sampled in one unitary cell only.

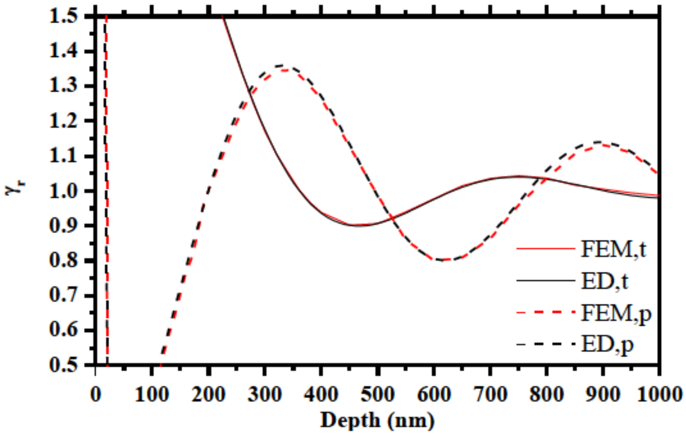

Figure 3.27.: Comparison between FEM simulation (FEM) and analytic electrodynamic model (ED) for film-emitter interaction modified decay rates as a function of depth $\gamma_r(z)$.

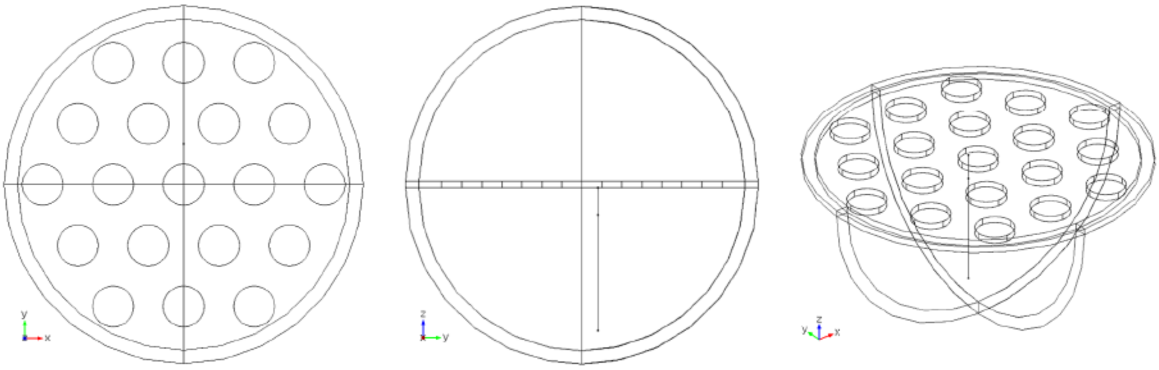

(a) XY (Top) view **(b)** YZ (Cross) view **(c)** XYZ (3D) view

Figure 3.28.: Wireframe views of the NHA-emitter interaction model.

Moreover, given the symmetries in $\hat{x}$ and $\hat{y}$ direction, the full cell can be reduced to only a quarter, as shown by fig.3.29a. Once the minimal cell has been defined, 27 points have been chosen herein, according to fig.3.29b, to sample the positions over the whole cell. To get the time-dependent emission pattern, equation 3.22 must be rewritten to take into account the differences given by the XY position of the emitter. In the $\hat{z}$ direction, the integral is still present. In the XY plane, the integration is substituted by a sum over all the 27 previously defined points of the minimal cell, denoted by the couple of indices i and j:

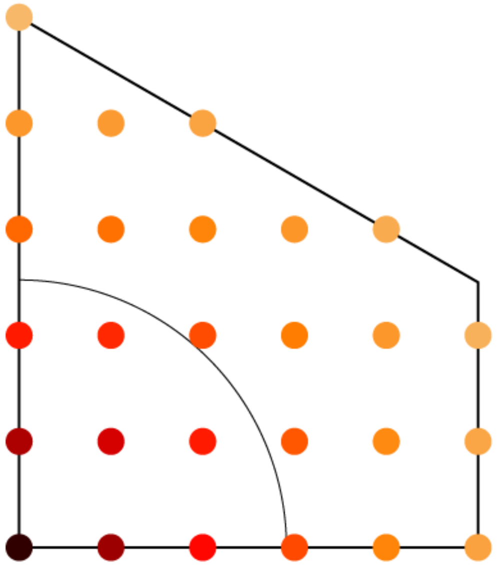

(a) Construction of the Wigner-Seitz cell. Dashed lines are simmetry planes; black line encircles the WS cell; red line encircles the sampled cell exploiting lattice simmetries and $\hat{x}$ and $\hat{y}$ symmetries

(b) Sampling points in the minimal cell: 27 points. Points on the edges and vertices have a coefficient $c_{ij} < 1$ in averages

Figure 3.29.: Wigner-Seitz cell: construction using symmetries and sampling points

$$I_{PL}(t) = I_0 A \sum_{ij} c_{ij} \int_0^{+\infty} f(x_i, y_j, z) \exp\left[-t\gamma_r(x_i, y_j, z)\right] \mathrm{d}z, \tag{3.29}$$

where the coefficients c_{ij} give the normalization for the points that are shared by nearby cells, and $A = 1/\sum_{ij} c_{ij}$ is a global normalization factor. The same steps as in the case of the film have been followed from this point. Fig.3.30 shows an example of the decay rates of emitters with different XY positions in the minimum cell, as a function of the depth: the decay rates even at the same depth have a non-negligible variation, thus the use of stretched exponential fit from eq.3.24 is preferable also for thin (in the $\hat{z}$ direction) distributions. In the same way as before, the effective lifetime can be computed from fit parameters.

Simulations have been carried out for three NHA geometries (a_0 = 922nm, 1030nm and 1280nm), and each one is taylored on experimentally fabricated samples. Tab.3.2 shows the geometric parameters of the NHAs, the experimental and simulated transmittance peak T_{max} and the relative transmittance at 1.54μm $T_R = T_{1.54\mu\mathrm{m}}/T_{max}$. For the comparison with the experimental data, the radiative decay rate must be added to the non radiative decay rate to

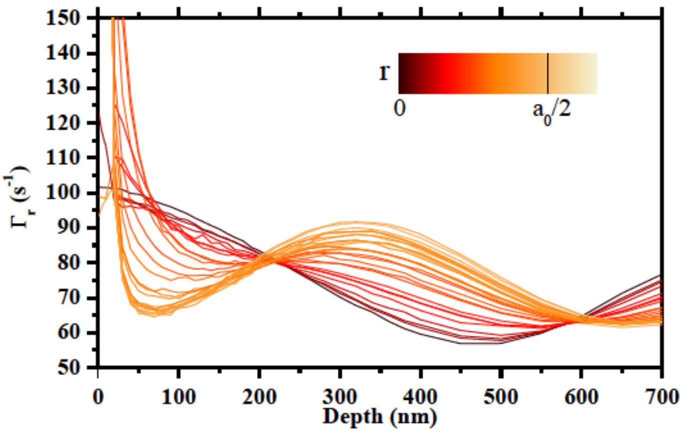

Figure 3.30.: Simulated $\gamma_r(z)$ for emitter placed at different positions in the XY plane for a $a_0 = 1030$nm NHA. The color map indicates the distance from the centre of a hole in the WS cell. The same color map is used for the points in fig.3.29b.

Table 3.2.: Geometric parameters and measured and simulated far-field properties.

Lattice parameter a_0 (nm)	Holes radius R (nm)	λ_{max}^{exp} (nm)	λ_{max}^{sim} (nm)	T_R
720	240	1170	1240	0.22
922	260	1385	1400	0.63
1030	300	1550	1520	0.97
1280	375	2020	>1800	0.12
1340	400	2142	>1800	0.55

obtain the total decay rate:

$$\gamma_{tot} = \gamma_r + \gamma_{nr}. \tag{3.30}$$

Because all the effects of the nanostructures on the LDOS is takent into account in the modification of the radiative decay rate, and possible defects induced by the deposition of metal are corrected by the annealing, the (not optically measurable) γ_{nr} is supposed to be the same as the bulk silica one. To estimate the nonradiative decay rates, a sample for every deposition series is measured without any nanostructure nor film over it. From this sample, the total decay rate $\gamma_{tot}^{(j)}$ for the j series is measured, and the $\gamma_{nr}^{(j)}$ is obtained as

$$\gamma_{nr}^{(j)} = \gamma_{tot}^{(j)} - \gamma_r^0, \tag{3.31}$$

where γ_r^0 is the decay rate measured in bulk silica at low concentrations and with few defects, where the nonradiative decay rate is negligible. To have a comparison with the experimental results, the total decay rates have been converted in lifetimes by using the relation

$$\tau = \frac{1}{\gamma_{tot}}, \tag{3.32}$$

Two different gold NHA have been fabricated and simulated ($a_0 = 1030$nm and a $a_0 = 1280$nm), and three different emitters box-like distributions have been considered ($z \in [10\text{nm}, 30\text{nm}]$,

Table 3.3.: Experimental and Simulated emitters lifetimes (ms) for 2 NHAs and 3 distributions.

	NHA 1030 exp	NHA 1030 sim	NHA 1280 exp	NHA 1280 sim
$z \in [10\text{nm}, 30\text{nm}]$	4.5	5.5	5.9	6.1
$z \in [30\text{nm}, 50\text{nm}]$	5.7	5.8	6.6	6.4
$z \in [100\text{nm}, 120\text{nm}]$	7.2	7.0	7.2	7.1

$z \in [30\text{nm}, 50\text{nm}]$ and $z \in [100\text{nm}, 120\text{nm}]$. An experimental result has been derived also from a $a_0 = 922\text{nm}$, with an box-like emitter distribution from $z = 11\text{nm}$ to $z = 44\text{nm}$. In this case, the experimental lifetime resulted 4.85ms and simulated lifetime resulted 4.98ms. Tab.3.3 shows the comparison of the achieved experiments with simulations lifetimes. From the overall agreement between simulations and experiments, it is clear that simulations can foresee the lifetime modifications of emitters lifetime due to nanostructures. Fig.3.31 shows the integrated average decay rates for the interaction with a film, a $a_0 = 1030\text{nm}$ and a $a_0 = 1280\text{nm}$ NHAs, in the case of a box-like Erbium distribution in the interval $[z, z + 20\text{nm}]$ and $[z, z + 100\text{nm}]$. The differences between the behaviour of the film and the behaviour of a NHA is *peculiar*, in the sense that the NHA-due modifications can't be modeled assuming the nanohole array as an effective medium. In fact, by averaging the metal and holes dielectric refractive indexes using the most used approaches (Bruggeman's model and Maxwell-Garnett's formula), and inserting the resulting effective medium as the overlayer material for the film computations give uncorrect results.

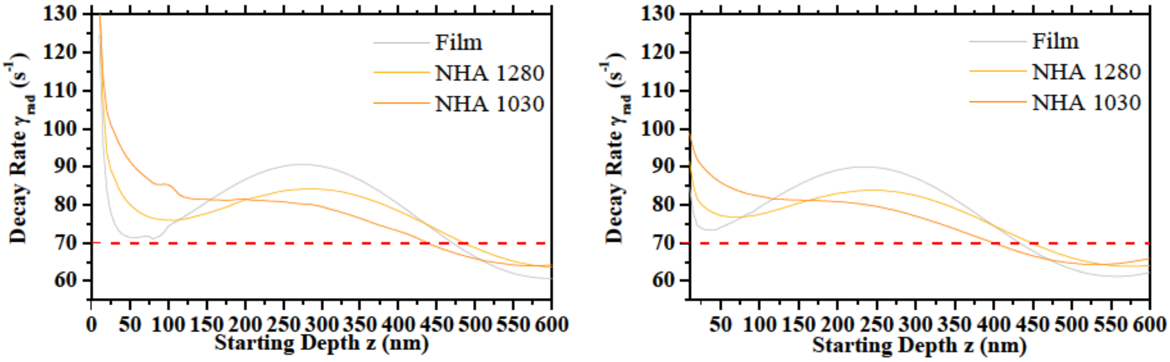

(a) Average decay rates for an box-like Erbium distribution in the interval from z to $z + 20\text{nm}$, interacting with film and NHAs.

(b) Average decay rates for an box-like Erbium distribution in the interval from z to $z + 100\text{nm}$, interacting with film and NHAs.

Figure 3.31.: Average decay rates for two box-like Erbium distributions interacting with film and NHAs.

The role of a resonant coupling to the radiative modes of NHA, present in the $a_0 = 1030\text{nm}$ configuration and absent in the $a_0 = 1280\text{nm}$ one, as shown in transmittance measurements at the Er emission wavelength, is visible in the modifications of the decay rates (fig.3.31). The non-resonant structure acts in a way that is intermediate between the resonant NHA and the film. The presence of photon-coupled surface plasmons on the NHA enhances the emission from Er with respect to the bare film for short distances ($z \lesssim 100\text{nm}$), and the enhancement is better for the resonant configuration.

Fig.3.32 shows far-field radiation pattern in the case of emitter-film interaction, for a 100nm

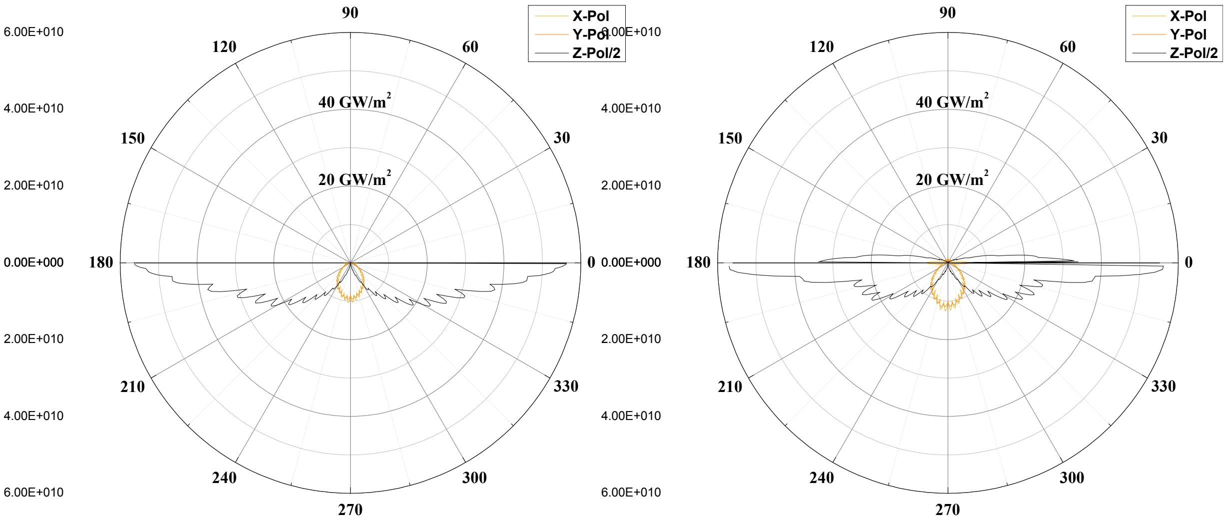

(a) Optically Thick Film ($T = 100$nm) **(b)** Optically Thin Film ($T = 20$nm)

Figure 3.32.: Power Outflow as a function of the angle as probed at the outer edges of the simulated domain when the dipole interacts with a gold film. The emitter is placed 50nm below the surface. The thick film is 100nm thick. The thin film is 20nm thick.

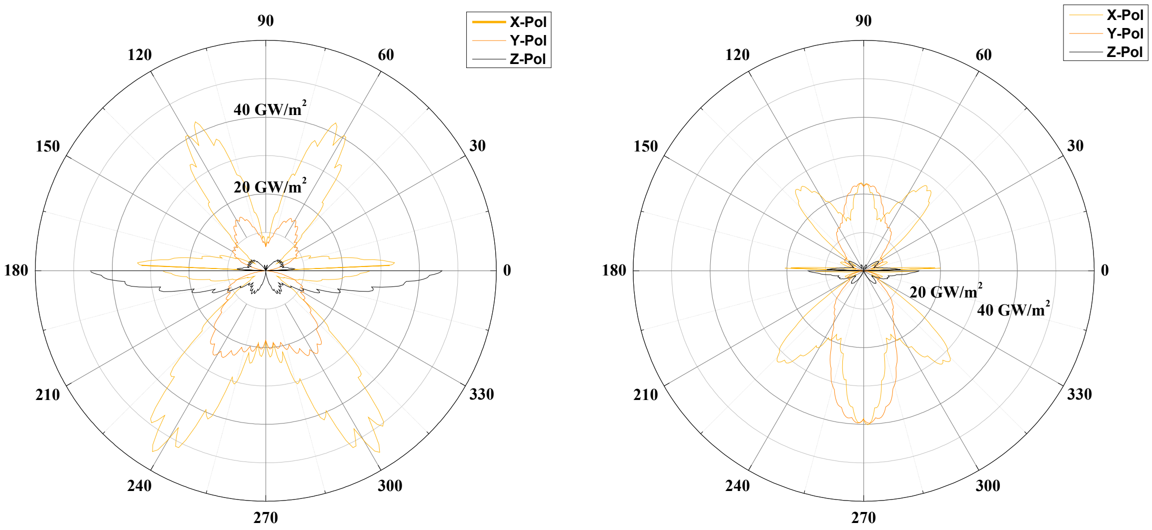

(a) NHA $a_0 = 1030$nm **(b)** NHA $a_0 = 1280$nm

Figure 3.33.: Power Outflow as a function of the angle as probed at the outer edges of the simulated domain when the dipole interacts with a gold NHA. The dipole is placed in the center of the holes, 50nm below the surface, and the polarization indicates the direction along which the dipole oscillates.

thick film and a 20nm thick film. The emission in the upper semi-space is in the first case zero,

Table 3.4.: Quantum Efficiencies comparison between thick and thin films and NanoHole Arrays.

	Thick Film 100nm			Thin Film 20nm		
	% Forward	% Backward	**% Total**	% Forward	% Backward	**% Total**
X-Pol	0	52	52	7	52	70
Y-Pol	0	52	52	7	52	70
Z-Pol	0	34	34	3	34	89
Total	0	36.8	**36.8**	3.7	37.7	**41.4**

	NHA $a_0 = 1030$nm			NHA $a_0 = 1280$nm		
	% Forward	% Backward	**% Total**	% Forward	% Backward	**% Total**
X-Pol	42	56	98	43	55	98
Y-Pol	42	56	98	43	55	98
Z-Pol	25	75	100	23	76	99
Total	36.3	62.3	**98.7**	36.0	62.3	**98.3**

as the metal completely absorbs any possible transmitted photon. In the second case, only a small fraction of radiation is transmitted. In the lower semi-space, the emission is dominated by the z-polarized (transverse) dipoles, and is concentrated at low angles from the film surface, as most of the propagated energy is carried by plasmons living at the interface. The emission from x- and y-polarized (parallel) dipoles is very weak, as the near-field coupling permits the excitation of plasmons on the surface, but the plasmons are not coupled to far-field radiation due to the lack in wave-vector, are not propagating and decay into phonons inside the metal. The great advantage of the NHA configuration, in comparison to the film is shown by fig.3.33, which plots the emission pattern from a dipole placed 50nm under the centre of a hole. In this case it is possible to collect the emitted light from both faces of the NHA. The efficiency of the nanostructures for the emitter-far-field coupling can be found by calculating the *quantum efficiency* of the system, neglecting the non-radiative decay rate in the homogeneous silica. The quantum efficiency is defined as the ratio between the far-field power and the total power emitted by the dipole:

$$q_{eff} = \frac{P_{ff}}{P_{tot}} = \frac{\gamma_r}{\gamma_r + \gamma_{loss}}, \tag{3.33}$$

where in this case γ_{loss} considers the losses inside the metal. Table 3.4 shows the computed quantum efficiencies for a thick and a thin films, an $a_0 = 1030$nm NHA and a $a_0 = 1280$nm NHA. In the case of NHAs, the quantum efficiency is computed for an emitter placed under the centre of the hole, at a distance of 50nm from the NHA. The considered metal is gold in all cases.

The computed *quantum efficiencies* confirm the great advantages of NHAs as Erbium emission enhancers with respect to the classical film setup. The collectable signal in far-field is increased by a factor of 2 to 3 with respect to the film. This is due to two causes: on one hand, the NHA configuration permits the emission to be transmitted in a more efficient way than films, and thus enables the detection from both faces; on the other hand, the propagating plasmons which are excited at the interface can be re-emitted as photons using the grating coupling given by NHA, a decay route which is forbidden with films. Thus, the plasmons are non-radiative in the case of films as they are confined and vanish due to the metal damping. In the case of NHA on the other hand, plasmons can be re-emitted and contribution to the

Table 3.5.: Quantum Efficiencies for dipoles placed in different positions of the WS cell of the $a_0 = 1030$nm NHA. $z = 50$nm.

NHA $a_0 = 1030$nm			
	$x = 0.0; y = 0.0$	$x = 0.0; y = 0.4$	$x = 0.5; y = 0.5$
X-Polarization	98.0	96.9	79.7
Y-Polarization	98.0	95.6	78.8
Z-Polarization	100.0	98.3	96.0
Total	98.4	96.9	93.6

NHA $a_0 = 1030$nm				
	$x = 1.0; y = 0.0$	$x = 0.6; y = 0.0$	$x = 0.0; y = 1.0$	**% Total**
X-Pol	75.6	93.1	78.9	93.4
Y-Pol	79.4	83.2	78.1	92.5
Z-Pol	96.1	94.7	95.4	96.1
Total	93.1	93.1	92.7	**94.9**

radiative part of quantum efficiency. The efficiency does not vary appreciably between in-resonance and out-of-resonance NHAs. On one hand, this suggests that even in resonance the strong coupling does not means large losses due to the plasmon decay in the metal. On the other hand, this opens the possibility to combine in-resonance and out-of-resonance NHAs to get smart excitation-emission configurations without loosing efficiency. Table 3.5 shows that the quantum efficiency is not much influenced by the position in the Wigner-Seitz cell of the NHA. Thus, in the design of a device, it is possible to neglect this dependance, and maximize the performances in the decay rate modifications, choosing to place the emitters in the sites where the lifetimes drop.

3.3.4. Conclusions

Experiments and simulations have shown the possibility of controlling emitters lifetimes by the interaction with nanostructures. Further, the role of LDOS modifications due to the presence of a periodic nanostructure has been observed. The resonant coupling of the emitters with a NHA yields an enhanced emission especially for short distances. For emitters-interface distances below $150-200$nm the resonant NHA is the best of the analyzed systems to enhance the decay rate.

Contrary to the film case, the quantum efficiency computed for NHAs shows that the enhanced emission from Erbium is not modulated by a large absorption in the metal, thus the higher photon flux is in principle almost all available in the far-field. This, together with the ability to transmit an important part of the emitted radiation, makes the NHA a very interesting nanostructure for enhancing the emission from Erbium.

Concluding, the presence of additional modes given by the presence of a nanostructure enhances the emission from Er at 1.54μm better than a continous film. The effect is due to the new modes, and is maximized when the emission is resonantly coupled to the NHA transmission peak. Moreover, the NHA architecture increases the amount of photons reaching the far-field, thus maximizing the quantum efficiency with respect to the film case. All these features make the NHA-emitter architecture a very promising configuration for the development of innovative optical devices such as optical amplifiers, solid state lasers and light sources.

3.4. Quasishells: Fast and Cost-Effective Bi-Metallic Nanostructures

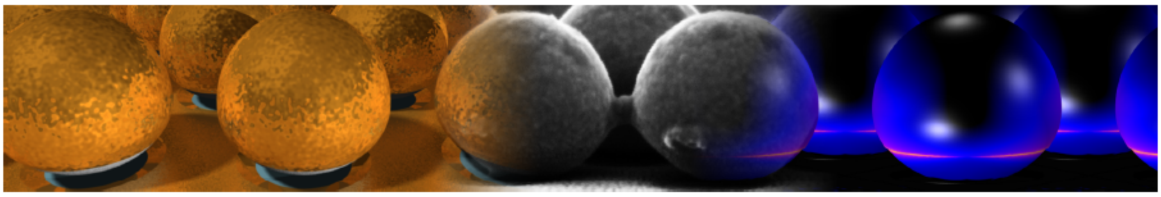

Design, synthesis and modeling of Quasishells.

Among other nanostructures, core-shells constitutes one of the most studied geometries in plasmonics. The availability of fast and cheap chemical methods for the synthesis [122–125] and the presence of the extended Mie formalism for core-shells ([33,34], cfr. sect.1.4.2, together with the wide range of applications, make these structures very interesting both theoretically and experimentally.
A variant of core-shell structures is the Quasi Shell (QS), the structure geometrically obtained from a core-shell by shifting the center of the core with respect to the center of the shell. Depending on the amount of the shift, the obtained structure can be an asymmetric core-shell, a QS, where the core is almost fully covered by the shell, or a semi-shell, when only half of the core has the shell. Quasishells and semishells assume critical importance among distribution-controlled patterns because it is possible to synthesize them by means of thin films technology. In particular, the use of colloidal cores covered by sputtered or evaporated shells is a powerful, top-down - bottom-up hybrid method which combines the low costs of colloidal nano-patterning and the fine control of thin films techniques. Three main approaches have been proposed for this kind of shell production: the first method starts with the dispersion of colloidal dielectric nanospheres on a substrate, and the successive deposition of metal on them; the second strategy uses the NSL patterning method for a high density, close-packed nanospheres array over which the metal is deposited; the last technique is a variation of the second, involving a RIE process on the nanospheres to reduce their radius and, after that, the metal is deposited over the etched spheres. The first approach [126, 127] gives the best control on the shell structure and composition, as the access to the nanospheres is guaranteed by the low density of monomers on the substrate. The drawback of the low density is the low signal from these structures, which makes it difficult to optimally exploit their features

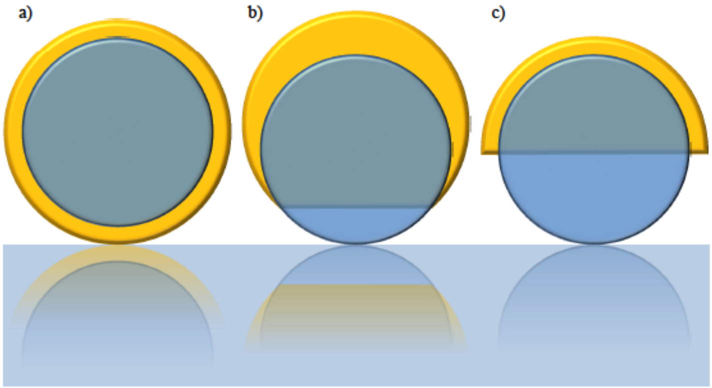

Figure 3.34.: Core-Shell geometries: a) Core-Shell; b) Quasishell; c) Semishell

for applications. The second strategy [128,129] overcomes the low density, but only the upper part of nanospheres can be coated (thus, QS are not achievable this way), and the shells tend to merge together forming the so-called FON structure, which is an hybrid between isolated shells and film. The third approach [130–133], which is followed here, gives the advantages from both the other two. On one hand, the high density of monomers is guaranteed by the NSL technique, and on the other hand the reduction of radius by RIE makes it possible to coat also part of the lower hemisphere and to obtain nevertheless isolated, LSPR-supporting nanostructures.

3.4.1. The Physics of the Problem

As noted in chapter 1, the features of the plasmons strongly depend on the nature of the supporting metal. Alloys enable to obtain metals with hybrid features, such as the AuAg alloy, which retains the inoxydability of gold in a much cheaper material. It can be interesting to merge the properties of plasmonic metals with those of, as an example, ferromagnetic metals, to obtain a magneto-plasmonic medium. However, the processes to build up nano-structured bi-metallic system are not trivial, expecially in the case of LSPR-supporting nanostructures. The methods presented in the previous sections to fabricate NPA and, to a minor extent, NHAs rely on the collimation of the sources, thus a bi-metallic configuration can be achieved only in the multi-layer fashon. Starting from a bi-metallic film (which can be deposited easily by sputtering) it is possible to obtain nanostructures by successive masking and etching, but the process consists of several steps and is quite time- expensive.

Here, a fast and cost-effective method of producing bi-metallic LSPR-supporting nanostructures is presented. The study of the structural, topological and optical properties of these nanostructures have been carried out, and finite elements modeling gave insights on the physics of QS plasmonic resonances.

3.4.2. Fabrication Methods

The fabrication of the QSs is once again based on NSL (cfr. section 3.1. The first steps for this fabrication are the same of the NHA one: the deposition of a polystyrene nanospheres mask on the desired substrate and spheres reduction by RIE. Contrary to the case of NHAs, the deposition of metal in this case is not orthogonal to the substrate, but it is performed at a definite azimuth angle, which, in turn, determines the major or minor extent of the aperture/closure of the lower part of the shell. By using 2 tilted sources it is possible to co-deposit the two desidered materials to form the shell. If the sample holder is rotating, the result will be an alloy of the two metals; if the sample holder is fixed, each side of the polystyrene nanospheres will get one of the two metals, and the obtained nanostructure will be a bi-lobed QS. Fig.3.35 schematically shows the fabrication process. As a last (optional) step, it is possible to separate the shells from the residual NHA which is deposited on the substrate, to get genuine optical properties without the interference of the NHA. For this step, the usual technique, used for example for the semi-shells [127], which relies on the deposition and curing of PDMS, is substituted by a much faster process using NOA 61 as polymer, which is cured by the exposition to UV radiation for 15 minutes. This way, a procedure which lasts 2 or more days (due to the slow PDMS reticolation) is reduced to half an hour. An additional advantage of the NOA usage is the fact that the PDMS is almost inert to both organic solvents and to RIE, the only attacking methods being strong acids (which obviously would damage the

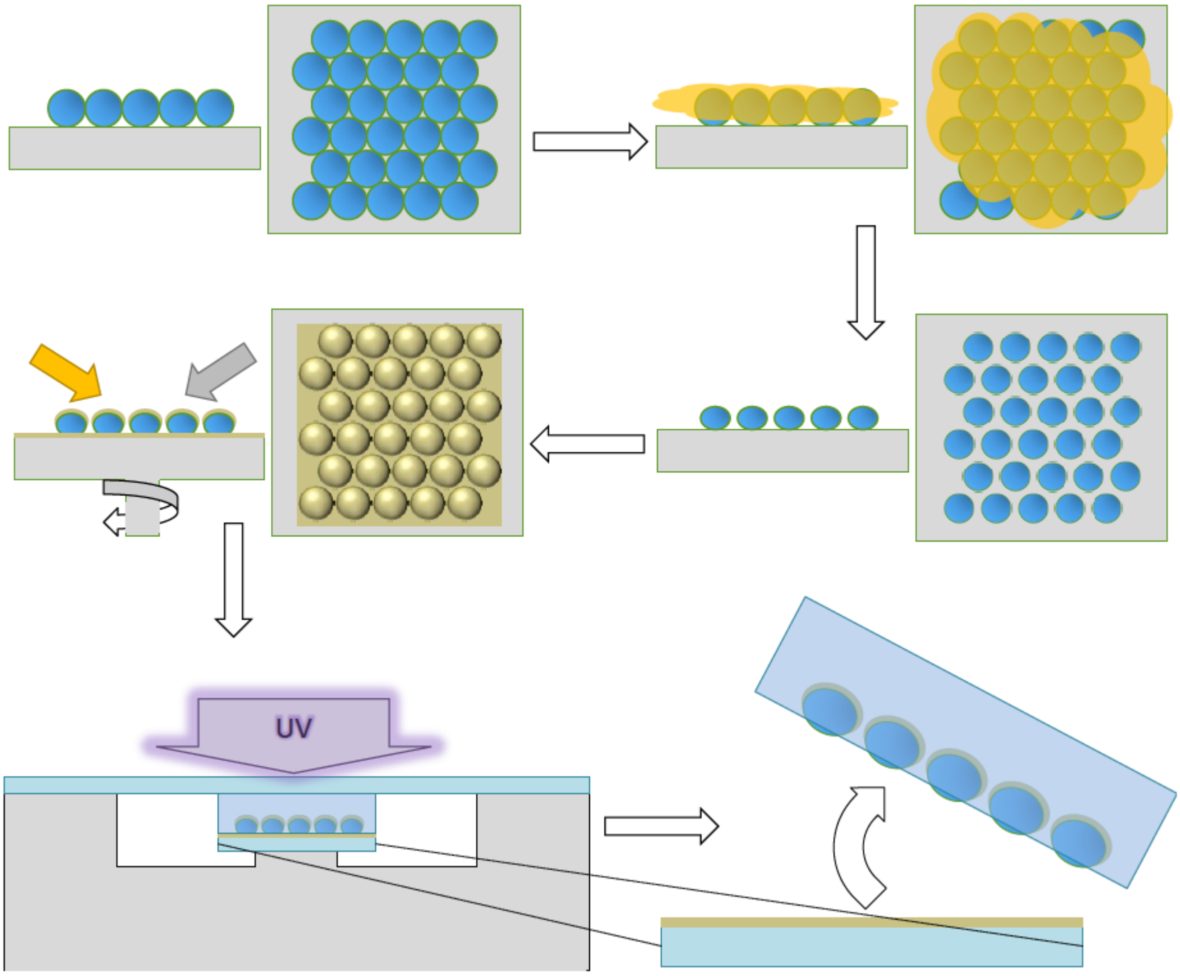

Figure 3.35.: Quasishell fabrication by NSL and bi-metallic magnetron sputtering/evaporation: 1. mask deposition; 2-3. Reactive Ion Etching; 4. metal deposition; (5). Substrate and residual metal removal by NOA.

nanostructures). On the contrary, NOA can be easily attacked by Ar/O_2 RIE, giving access to the embedded part of the nanostructure.

3.4.3. Structural and Topological Characterization

AuAg Quasishells

To define the geometry of the shells it is necessary to know both the topology of the core, i.e. of the reduced polystyrene sphere, and of the outer surface. The two topologies can be probed by SEM imaging, both in *plan* and in *section view*, to get a 3D model of the core-shell system. 3.36 shows the orthogonal images of the nanospheres after the RIE process, and of the complete shell after metalization. Fig.3.37 shows the images in cross (the sample is tilted by 82.5° with respect to the detector) of the same samples, before and after metalization. Using the informations from these images, a model of the shell has been constructed. The role of the various steps in the final form of the QSs has been studied. In particular, the RIE controls the results for some aspects:

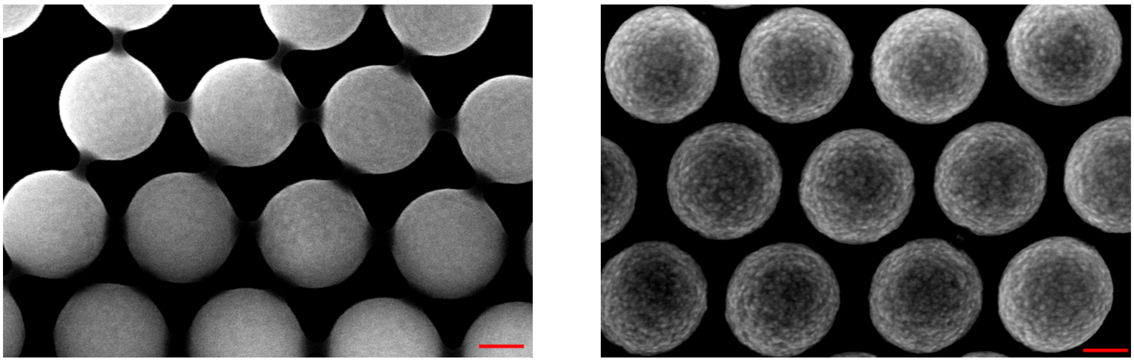

(a) Polystyrene NS after RIE

(b) Quasishells after metalization

Figure 3.36.: SEM images of the quasishells before and after metalization (plan). Bar: 100nm.

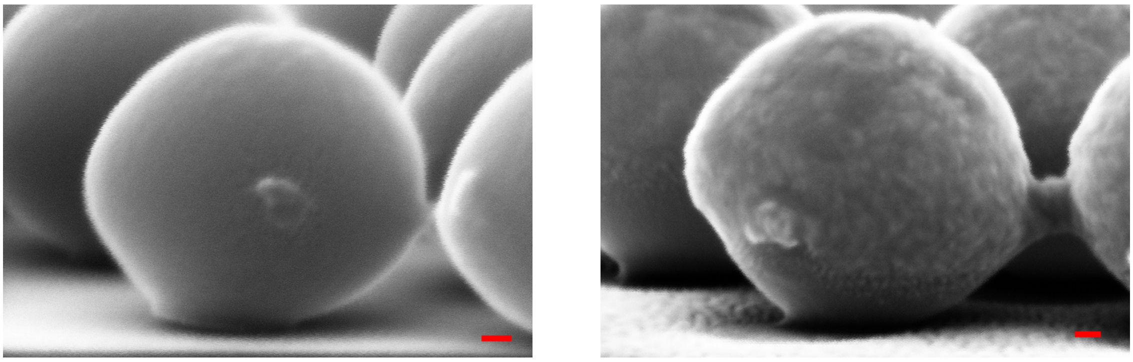

(a) Polystyrene NS after RIE

(b) Quasishells after metalization

Figure 3.37.: SEM images of the quasishells before and after metalization (cross). Bar: 20nm.

- the RIE duration controls the amount of reduction of the spheres, thus the size of the quasishells;

- the size of the quasishells, in turn, controls the level of interaction among nearby quasishells;

- for small RIE reduction, the shade of nearby nanospheres limit the angle of deposition and the closure of the lower part of the shell;

- the relative pressure of the Ar/O_2 mixture controls the etching rate of the treatment: more aggressive conditions (i.e. an excess of Ar) take to a much more rough surface of the nanospheres and, in turn, of the quasishells.

The metal deposition control other features of the finalized QS:

- the relative power of the used sources control the metals ratio in alloys;

- the quantity of metal and thus the shell thickness is controlled by both sources power and deposition duration;

- the angle of deposition determines how much the shell is closed in the perforated hemisphere;
- alloys can be obtained by rotation, multilayers or anisotropic metal compositions can be obtained by moving the samples between successive depositions.

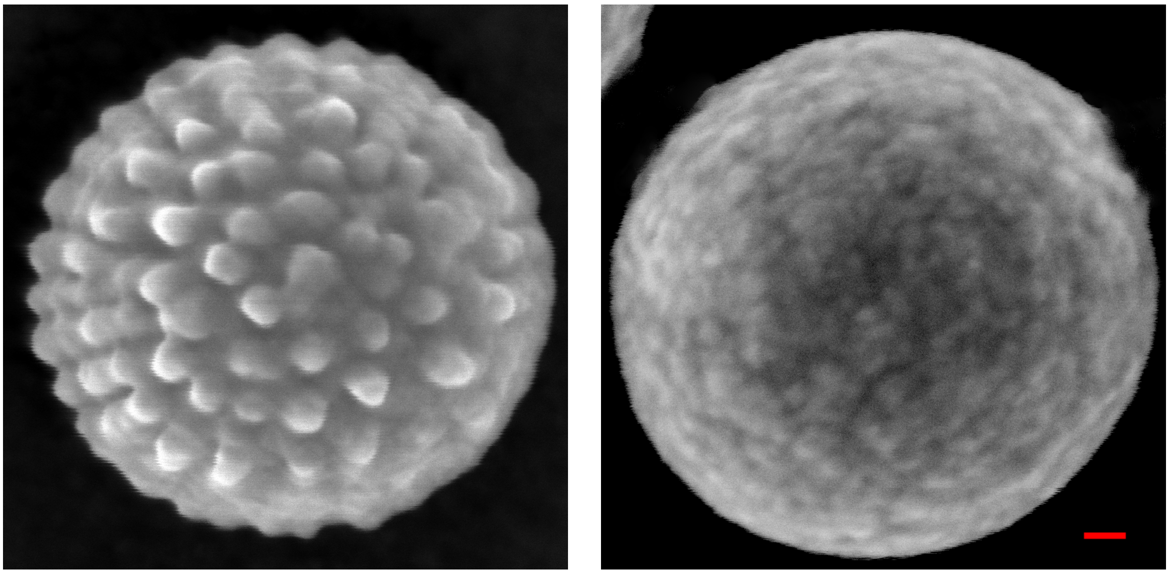

(a) Enhanced roughness QS **(b)** Low roughness QS

Figure 3.38.: Comparison between aggressive (Ar 75%/O_2 25%) and less aggressive (Ar 50%/O_2 50%) RIE configurations. Bar: 20nm.

To get a measure of the amount of deposited metal, the thickness of the film deposited in a region without PS nanospheres has been measured using AFM. Typical depositions yield 25nm to 30nm. The layer deposited on the nanospheres is however thinner due to the geometric configuration. The effects of the size of the QS on the optical properties will be treated in the next subsection. The effect of the more aggressive conditions can be seen in fig.3.38 which shows shells obtained in two different RIE configurations. The two kind of roughness are suitable for different aims: an enhanced roughness surface is ideal for SERS applications, or for sensors where the active area is increased by the roughness; a low roughness quasishell is easier to study and tune, and is ideal for the interaction with other systems exploiting controlled field concentration and scattering, such as emitters, strong laser illumination, etc. The effects of a more or less closed shell, and those of the metal thickness will be considered in the simulation section below. The effect of the sources and sampleholder configurations have been studied both by imaging and microanalysis with SEM. Fig. 3.39 show two different configurations for AuAg quasishells: with rotating sampleholder and with fixed sampleholder, but two successive depositions. Both with tilted samples (45°), a metal per deposition, and the two metals coming from opposite directions. Tab.3.6 shows the results of a semi-quantitative microanalysis performed in different sites of the two samples (as indicated in fig. 3.39). The differences are clear: the rotating sampleholder QS are formed by an alloy of the two metals; the other kind of samples have a different composition in the analyzed sites due to directional depositions.

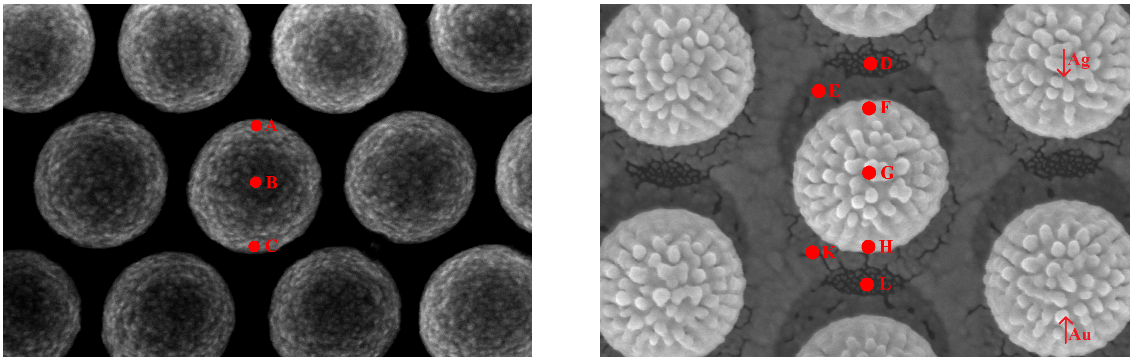

(a) Alloy AuAg QS (tilted sources and rotating sampleholder)

(b) Anisotropic AuAg QS (successive depositions). Silver source was oriented 45° from the normal to the plane downwards of the figure; gold towards the top.

Figure 3.39.: Comparison between AuAg alloy QS and anisotropic bi-metallic QS. Letters indicate sites for EDX analysis (tab.3.6).

Table 3.6.: EDX semi-quantitative analysis from sites defined in fig.3.39. *in the shadows, the remaining composition is the silicon from substrate.

Sample	Site	Description	Au %	Ag %
Alloy	A	Side	48	52
Alloy	B	Centre	47	53
Alloy	C	Side	48	52
Anisotropic	D	Shadow	3*	6*
Anisotropic	E	Au Shadow	13	87
Anisotropic	F	Ag Side	12	88
Anisotropic	G	Centre	50	50
Anisotropic	H	Au Side	99	1
Anisotropic	K	Ag Shadow	71	29
Anisotropic	L	Shadow	6*	1*

As noted in the introduction of this section, one of the avantage of using NOA 61 as the polymer for the peeling step is the possibility to attack this material using RIE. Fig.3.40 shows the quasishells embedded in the NOA 61 after peeling. The surface is the one formerly in contact with the residual NHA, and the peeling process assures the removal of the residual metal. Fig. 3.40a shows the shells as peeled, the shadows of the metallic coating can be seen through the NOA, but the only emerging structures are the domes formed by the part of the polystyrene nanospheres which was in contact with the substrate. After a 30 minutes RIE, the superficial layer of NOA is removed, as fig.3.40b shows. The etching mixture that reduces NOA, however, is the same which reduces PS. As an effect, the removal of the NOA also destroys part of the core, resulting in a collapse of the edge region of the shells. As a further effect, the thermal heating due to the RIE may take to an oxydation of the silver. If the access to the bottom of the shells is important for the applications, a possible solution to these problem may consist in the use of SiO_2 nanospheres in place of the PS ones, together with a RIE process at lower power and/or gas pressures. The removal of NOA makes it possible to get access to the hole of the shells and to study this region which, as it will be shown in the simulation section, is the most interesting one for this kind of nanostructures.

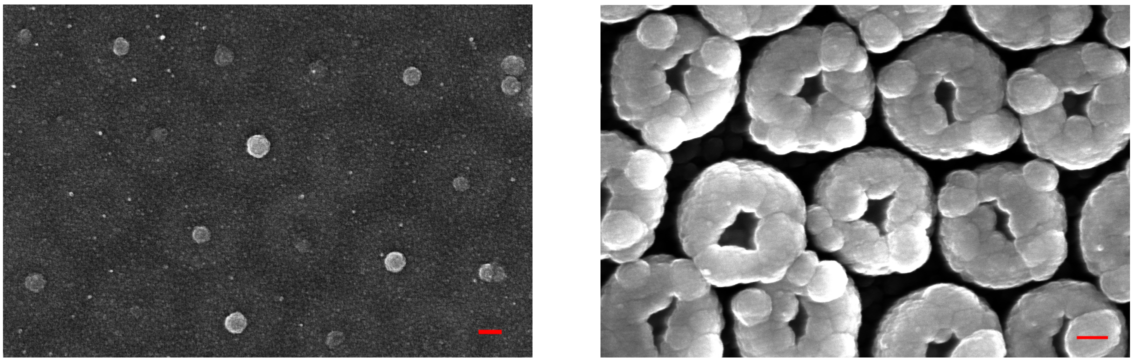

(a) QS as peeled **(b)** QS after RIE removal of NOA

Figure 3.40.: Quasishells embedded in NOA. One of the advantages of this polymer against PDMS is the possibility to attack it by RIE. Bars: 100nm.

AuCo Quasishells

Gold and silver easily form alloys since they are miscible at every relative composition in the bulk. Another interesting application of the process of this section is the possibility to obtain *nanoalloys* (i.e. metastable mixed states) of metals which do not form alloys in the bulk. This is the case of gold-cobalt quasishells. Gold and cobalt do not form an alloy, due to a positive entalpy of mixing in the bulk, and the nanoalloy which can be obtained by co-sputtering, could undergo segregation even for low temperature annealing ($T \sim 200-300$°C). However, a nanoalloy of the two metals is of great interest, as it enables to merge the plasmonic properties of gold with the ferromagnetic ones of cobalt, thus posing as a solid base for magneto-plasmonic nanosystems.

The topological characterization of AuCo QS gives the same results as the AuAg shells. In the case of metals that does not alloy together, however, it is necessary to perform further analyses to demonstrate the possible presence of regions where segregation occours. To this aim, QS samples with different Au:Co ratios (2:1, 1:1, 1:2 %Vol) have been analyzed using synchrotron radiation for EXAFS measurements both at the L2 and L3 edges gold and at the K edge of the cobalt. The measurements have been performed at the GILDA beamline (BM8) at ESRF, Grenoble (France). The interaction between the two metals to form a magneto-optical material has been proved using also X-ray Magnetic Circular Dichroism (XMCD) measurements at ESRF (ID12 beamline) and at Elettra (CiPo beamline), Basovizza (Trieste, Italy).

Both experiments gave positive results: EXAFS spectra showed that, though a small segregation exists, the mixing of gold and cobalt atoms to form an alloy is successful. XMCD measurements confirmed this, as a clear magnetic signal has been recognized in the QS samples studied at the gold edge. In contrast, a reference sample consisting of two superposed layers of cobalt and gold gave no signal as a consequence of the inexistent mixing.

3.4.4. Optical Characterization

The optical properties of the analyzed samples have been investigated using the Jasco V-670 Spectrophotometer in Transmittance mode. The effect of the PS nanospheres diameter, RIE time and alloy/anisotropic mode have been checked for AuAg QS; for the anisotropic shells, also a linear-polarized light measurement have been performed at different angles with respect to the deposition directions.

Dependence on Geometric Parameters

One of the most effective way to control the shape of shells geometry and on the absorption spectra is the duration of the RIE and, as a consequence, the amound of reduction of the size of PS nanospheres.

The first recognizeable effect is the blueshift of the main peak when the RIE duration is increased. This is the well known scale effect in plasmonics: larger nanostructures have resonances at longer wavelengths. For the $a_0 = 497$nm, RIE 15' sample, a second effect may become important: as the distance between the shells decreases, some interaction may be activated. This effect is however more important for QS arrays with shorter lattice parameter. Indeed, figs.3.44 and 3.45 show the optical properties of two sets of QS, having $a_0 = 315$nm; the radius reduction of the two samples is comparable with that of figs. 3.41 and 3.43, respectively. The shift of the resonance is in greater for $a_0 = 315$nm (29% versus 25% in the case of $a_0 = 497$nm). This is due to the fact that a global scaling causes a reduction of both the radius of QS and the shell-shell distance. Samples with the same relative radius reduction, thus, have higher interaction when the lattice parameter is decreased. It is worth noting that the RIE 20' is a limit condition, as longer etching times produce a dramatic increase in defects, due to the too large reduction of PS spheres, which change in shape and are no more well fixed to the substrate, and the result of this is the presence of fallen or even dislocated nanospheres. Thus, using this method it is not possible to reduce arbitrarly the radius of the PS nanospheres without loosing quality.

The second important way to control the resonance position is varying the size of initial PS nanospheres. This has a direct effect on the lattice parameter of the array and is the starting point for the RIE reduction. As RIE does not scale linearly, it is necessary to calibrate its duration and conditions for different PS nanospheres diameters. Fig. 3.46 shows the comparison between four QS arrays having different lattice parameters ($a_0 = 315$nm and $a_0 = 497$nm) and RIE reduction ($R_{out} = 0.6R_0$ and $R_{out} = 0.8R_0$). The effect of the lattice parameter is evident: once more, larger nanostructures resonate at longer wavelenghts with respect to smaller nanostructures. From the analysis of the position of the peaks it is possible to conclude that the effect of the RIE is more important than the effect of the lattice parameter: passing from $R_{out} = 0.6R_0$ to $R_{out} = 0.8R_0$ the redshift is about 27%; passing from $a_0 = 315$nm to $a_0 = 497$nm the redshift is about 14%.

Dependence on Polarization

Anisotropic quasishells are obtained by two successive depositions from opposite directions. The presence of the preferential axis breaks the isotropy otherwise given by rotating sample-holder. To check the role of this anisotropy, a $a_0 = 497$nm, RIE 15', AuAg QS sample has been measured using linearly polarized light at different orientations with respect to the deposition direction. Results are shown in fig.3.47. The difference between 0° (i.e., aligned with

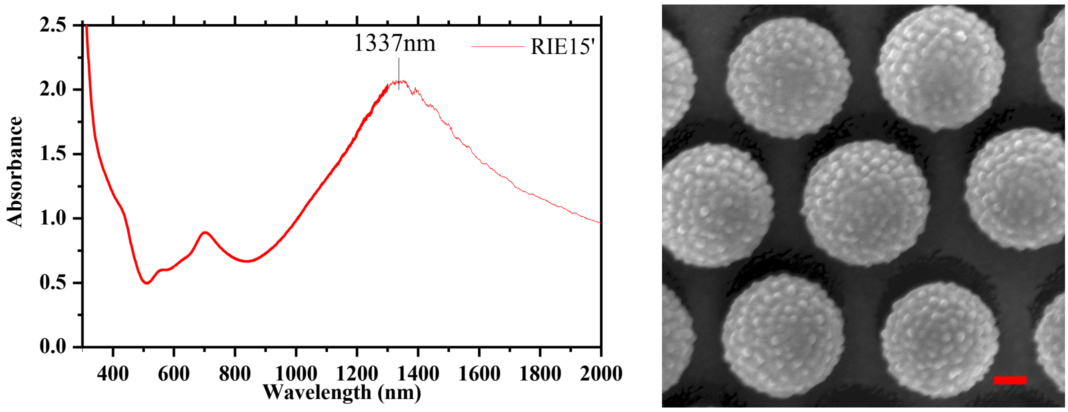

(a) Absorbance spectrum **(b)** SEM image; bar: 100nm

Figure 3.41.: $a_0 = 497\text{nm}$, RIE 15' quasishells absorbance spectrum and SEM image. $R_{out} = 0.78R_0$

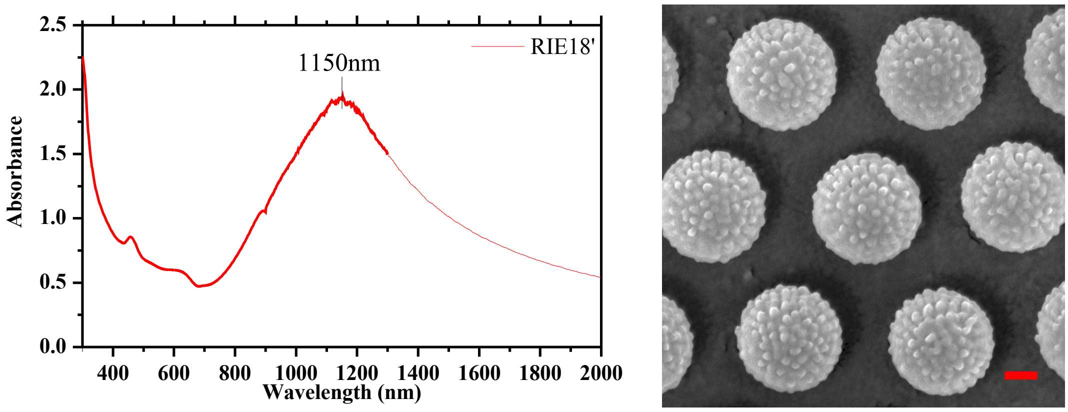

(a) Absorbance spectrum **(b)** SEM image; bar: 100nm

Figure 3.42.: $a_0 = 497\text{nm}$, RIE 18' quasishells absorbance spectrum and SEM image. $R_{out} = 0.68R_0$

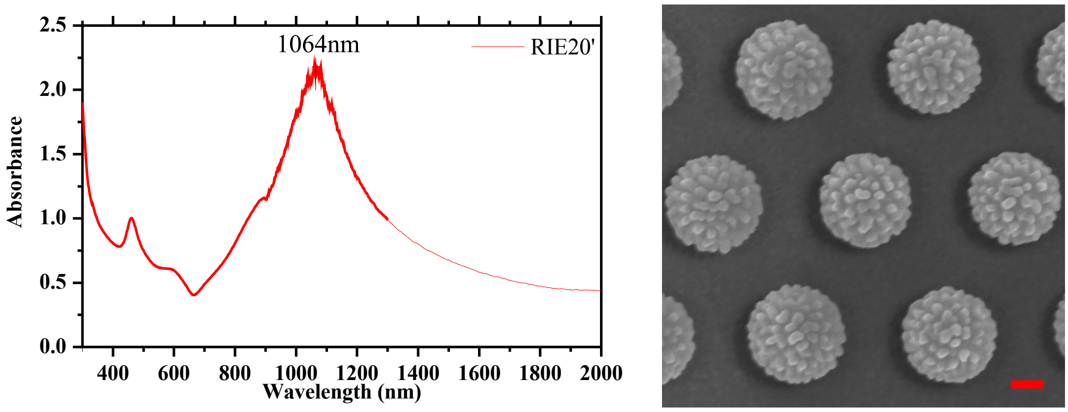

(a) Absorbance spectrum **(b)** SEM image; bar: 100nm

Figure 3.43.: $a_0 = 497\text{nm}$, RIE 20' quasishells absorbance spectrum and SEM image. $R_{out} = 0.60R_0$

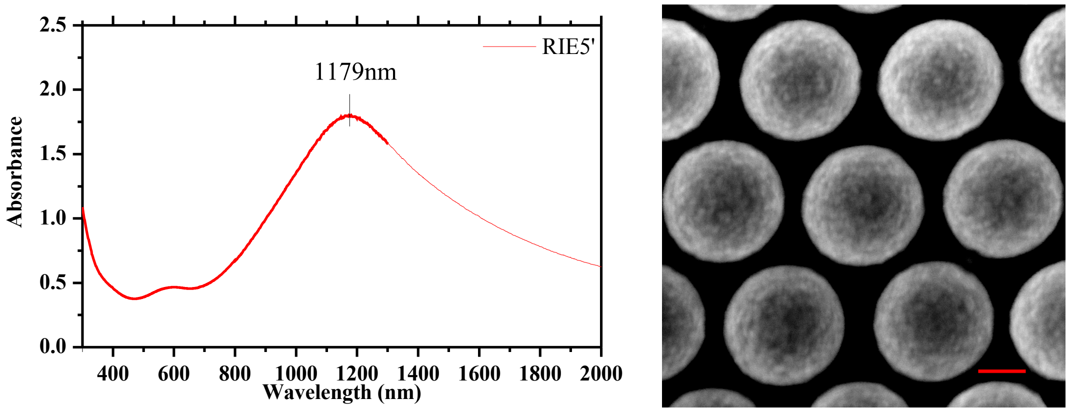

(a) Absorbance spectrum **(b)** SEM image; bar: 100nm

Figure 3.44.: $a_0 = 315\text{nm}$, RIE 5' quasishells absorbance spectrum and SEM image. $R_{out} = 0.82R_0$

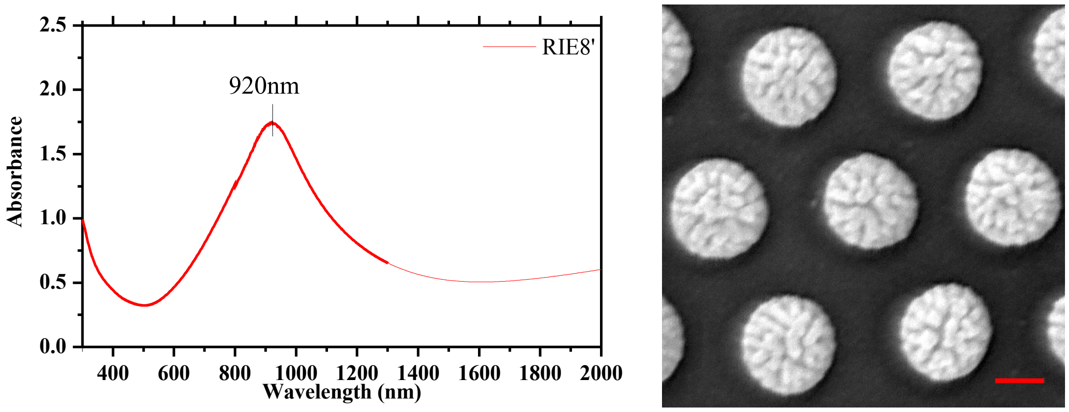

(a) Absorbance spectrum **(b)** SEM image; bar: 100nm

Figure 3.45.: $a_0 = 315\text{nm}$, RIE 8' quasishells absorbance spectrum and SEM image. $R_{out} = 0.62R_0$

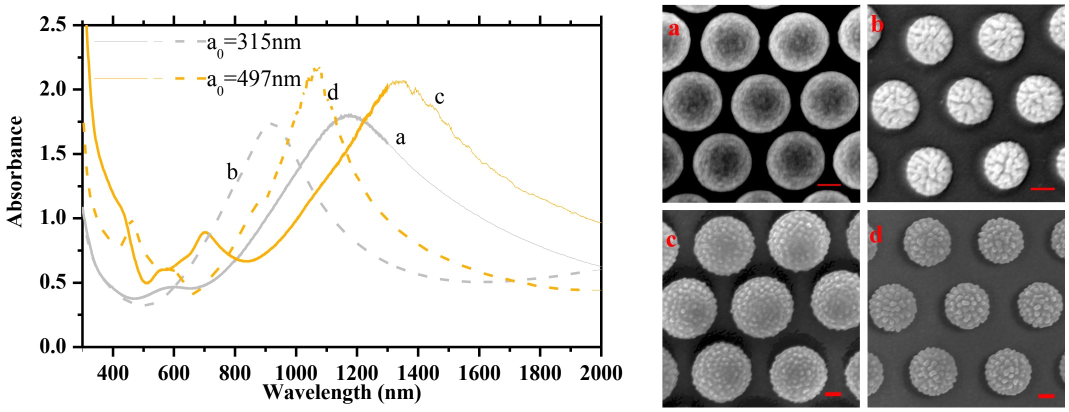

(a) Absorbance spectra **(b)** SEM images; bars: 100nm

Figure 3.46.: Comparison between different QS geometries. Lattice parameter: a,b: $a_0 = 315\text{nm}$; c,d: $a_0 = 497\text{nm}$. Radius reduction: a,c:$R_{out} = 0.8R_0$; b,d: $R_{out} = 0.6R_0$

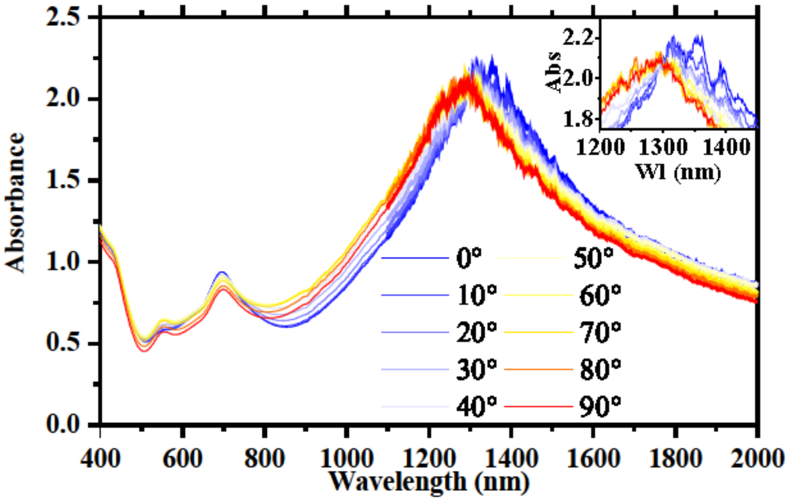

Figure 3.47.: Anisotropic QS absorbance spectra with linearly polarized light. Inset: the main peak region.

the Au-Ag deposition direction) and 90° is less than 40nm, and of the order of magnitude of inter-sample variance. It is possible to conclude that the polarization has limited effects on the resonances. On one hand this is due to the fact that gold and silver in the region of the peaks ($\lambda \sim 1300$nm) are optically very similar, due to the distance from inter-band transitions that are responsible for the differences existing between the two component metals in the visible region. On the other hand, this deposition configuration assures a quite homogenous distribution of metal over the core, making it possible to obtain quasishells with an high degree of isotropy. The small differences can be explained by the slight differences in the closure of the shells in the directions parallel and orthogonal to the depositions, and united to the fact that the dependance of resonance on the closure of the shell is ont large, as it will be shown by simulations. In the parallel direction the quantity of metal deposited on the lower part of the core is higher than that deposited in the orthogonal direction. Thus, plasmons excited by light polarized along the deposition direction (0°) are confined in a structure which is more extended towards the substrate. As it will be shown in the simulation section, the effect of a more close shell is precisely a redshift of the main peak as observed.

Separation of the Contributions from QS and NHA

For a deeper insight into the QS physics and for a correct application of this system, it is useful to separate the contributions to the optical spectra coming from the shells alone and from the residual NHA. In principle, if the shells are decoupled from the NHA, the absorption of the combined system is given by the sum of the two parts (except for slight differences due to the presence of air under the shells alone, using the proposed protocol). On the contrary, if significant differences between the combined system and the simple sum arise, this is a proof of the interaction between the residual NHA and the QSs. To check the possible presence of this interaction, the NOA 61 (a polymeric optical adhesive from Norland Co.) has been used to remove the shells from the substrate, leaving unmodified the NHA on it. The optical spectra have been recorded for the shells alone, the nanohole array alone and the QSs over the NHA. Since the shells can be measured only when embedded in the NOA, a layer of NOA has been placed over the NHA when its spectrum has been measured. Also the QS+NHA

spectrum has been measured with the sample covered by a NOA layer, to get measurements in the same surrounding medium.
The results of these measurements are shown in fig.3.48 for a $a_0 = 315\text{nm}$, RIE 5', AuAg QS array. The first important thing to note, in view of applications, is the spectrum of the NHA: due to the small thickness of the metal film the spectrum is almost flat. This means that the features emerging from optical spectra of the QS+NHA which is the result of the synthesis are controlled only by the shells resonances, the NHA giving only an uniform absorption without important features. This enables the use of the samples as synthesized for applications such as sensors, without the need of residual NHA separation.

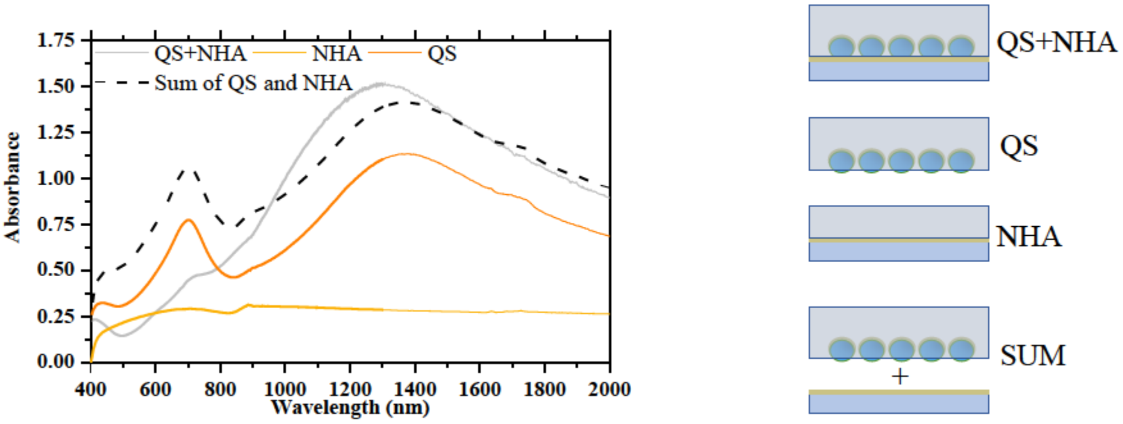

(a) Absorbance spectra **(b)** Scheme of the separation

Figure 3.48.: Separation of the contributions to optical spectra from QS and NHA

The second important result is the fact that the absorbance given by the sum of the NHA spectrum and the QS one is consistent with the absorbance measured for the as synthesized QS+NHA system. On one hand, this assures that the peeling procedure does not damage the shell nor introduces defects in the lattice. On the other hand, it confirms that the interaction with the NHA does not modify the nature of the main resonance in a dramatic way. However, and this is the third important result, some isolated differences exist: in particular, the main resonance is slightly redshifted and its width reduced when the shells are removed from the substrate and this will be discussed using simulations; in the short wavelengths region ($\lambda = 699\text{nm}$) a peak is present in the spectrum of the QS. The feature appears also in the QS+NHA spectrum, but it is damped. This suggests that the presence of NHA activates an interaction between the plasmon associated with this resonance and the metal on the substrate, taking to a damping of the oscillations via the excitation of surface modes on the perforated film. Also this effect will be studied more deeply in the simulations section.

3.4.5. FEM Simulations

Simulations have been performed following a model obtained by analyzing the SEM images as shown in figs. 3.36 and 3.37. The resulting model of a single quasishell, for inner core and outer shell, is depicted in fig.3.49. The shell is placed at the centre of the Honeycomb lattice unit cell as defined in sect.3.2.4. Under the shell, a thin NHA is placed, and its thickness is defined following AFM measurements to 10nm, as reported in tab.3.7. The medium around the shell

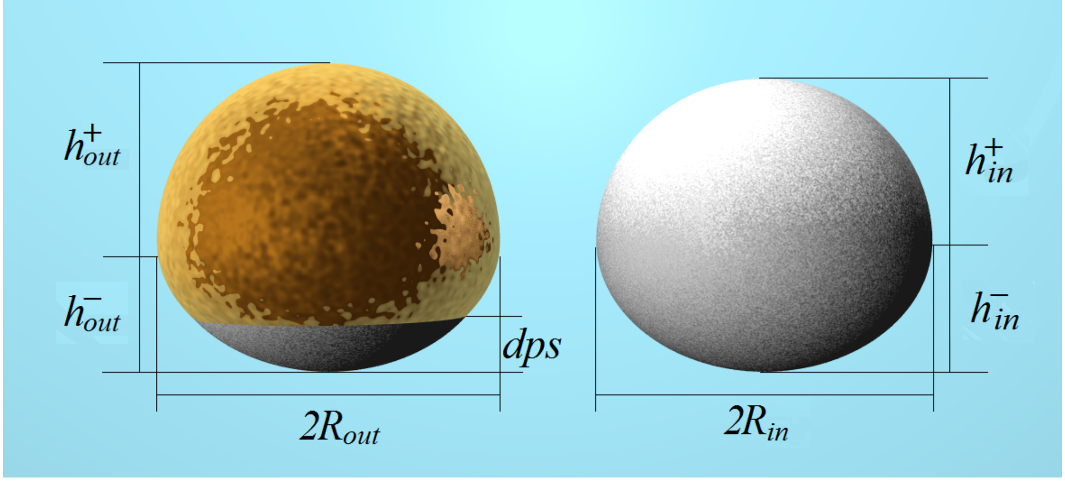

Figure 3.49.: Model for the QS geometry as obtained from the SEM images. The core is modeled as the union of two oblate semi-ellipsoids having the same XY semiaxes R_{in}, and different Z semiaxis, h^+_{in} for the upper part and h^-_{in} for the lower part. The external surface of the shell is defined as the union of two ellipsoids, once again with the same XY semiaxes R_{out} and Z semiaxes h^+_{out} and $h^-_{out} = h^-_{in}$. The shell is truncated at a distance d_{ps} from the substrate plane.

and under the NHA can be modeled to replicate the various situations of the previous section: NOA or air around the shell, metal or air for NHA and silica or air for the substrate. This way, the optical properties of the QS both as deposited on the residual NHA and embedded in NOA. The dielectric function of AuAg alloy has been measured by ellipsometry from an optically thick film deposited in the same conditions of the shells, using a 1:1 composition.
Simulations have been focused on $a_0 = 315$nm, RIE 5' quasishell, to obtain the structure of the samples shown in figs. 3.36 and 3.37. The measured geometric parameters, as defined in fig.3.49 are listed in tab.3.7. For the moment, the roughness of the surfaces of the shells hasn't been simulated; thus, the result refer to smooth QSs.

Table 3.7.: QS simulations geometric parameters. T_{NHA} is the thickness of the residual nanohole array.

Parameter	Value (nm)
R_{in}	120.5
h^+_{in}	118
h^-_{in}	96
R_{out}	131
h^+_{out}	135
d_{ps}	37
T_{NHA}	10

Effects of Metal Thickness and Shell Closure

The effects of the RIE reduction and lattice parameter have been discussed in the previous section. Using simulation, also the effect of the metal thickness and of the closure of the quasishells have been studied. Fig.3.50 shows the effect of the thickness of the metal on the absorbance of the shells. This plot shows an extremely strong dependance of the resonances positions on the metal thickness. The most energetic resonance is in this case supported by the thickest configuration. This is due to the *aspect ratio* of the shell: suppose to "project" the metal layer on a plane; the thickest configuration produces a disk having a larger thickness, and thus an aspect ratio which is closer to 1. Because the plasmonic resonance excited on the metallic layer produces a charges oscillation which is very similar to that of the projected case, the thickness of the metal behaves as the height of a plasmonic disk, and for such a system the most energetic resonances are reached when the aspect ratio is close to 1. When the thickness of metal is decreased, the most energetic peak is splitted in two peaks. The nature of these two peaks will be studied in the following.

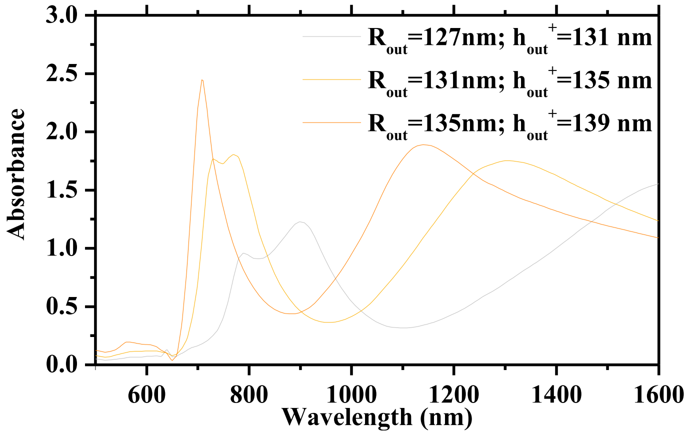

Figure 3.50.: Modifications of the absorbance due to the thickness of metal. In this case, the other parameters are those of tab.3.7.

The effect of the closure of the shell is shown in fig.3.51. In this case, the main resonance is almost not affected by the closure of the shell. On the other hand, the secondary (more energetic) peaks change in strength and shape dramatically. For the most closed shells (low d_{ps} values), these peaks are of the same magnitude, and both comparable to the main peak.

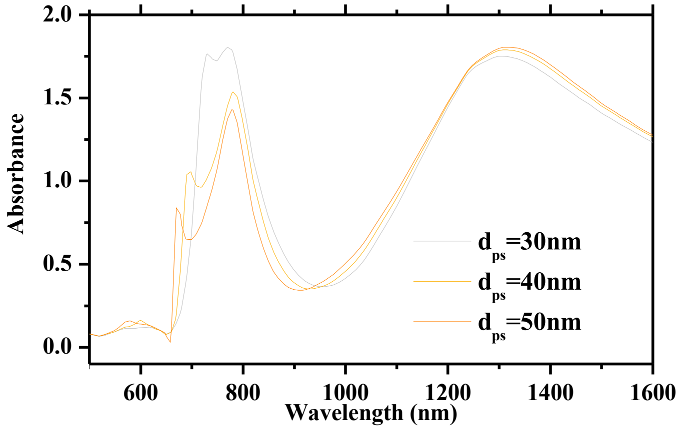

Figure 3.51.: Modifications of the absorbance due to the closure of the shell, parametrized by the distance between the lowest height of the metal and the substrate, d_{ps}. In this case, the other parameters are those of tab.3.7.

For less closed shells, the most energetic peak magnitude drops with respect of the twin peak, and both decrease in strength with respect to the main resonance. Again, the nature of these peaks will be studied in the next section.

Interaction with Residual NHA

If the shells are sufficiently closed (i.e. for low values of d_{ps}), and the thickness of the residual nanohole array is enough, it is possible to activate an interaction between the two structures. As pointed out in the optical characterization section, this phenomenon has been observed as the damping of the $\lambda = 700$nm peak when shells and residual metal are in contact, and in a broadening and blueshifting of the main resonance. The same behaviour has been reproduced in simulations. In this case, due to the absence of defects, the contributions to the main resonance convolution are well separated, and can be studied separately. Fig.3.52 shows the simulated absorbance spectra for a QS placed on the substrate together with the residual NHA of increasing thickness. As the thickness of the residual metal grows, the interaction starts to be more and more important: the $\lambda = 740$nm peak present in the $T_{NHA} = 10$nm is almost completely damped in the $T_{NHA} = 20$nm spectrum. The presence of a new peak, a product of the interaction, accounts for the experimentally-observed broadening of the main resonance peak. The nature of this new peak will be rewieved more deeply in the next section.

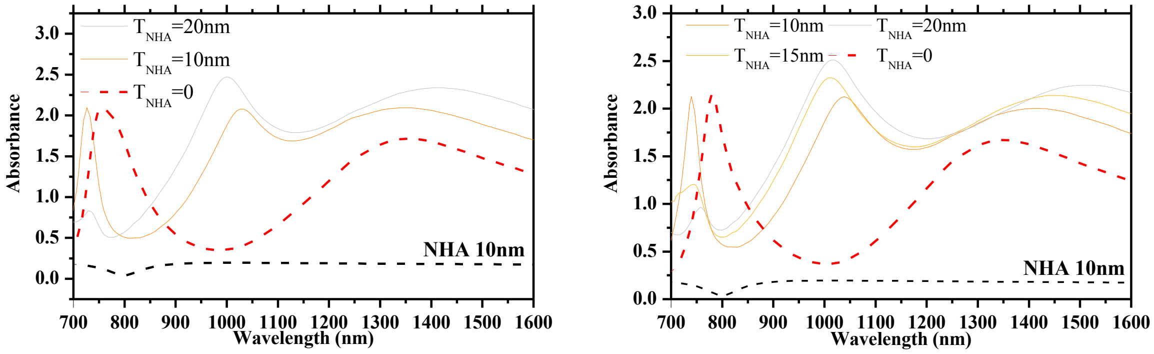

(a) $d_{ps} = 37$nm **(b)** $d_{ps} = 30$nm

Figure 3.52.: Effect of the presence of residual NHA on the resonances. In both cases, $h^{+}_{out} = 135$nm and $R_{out} = 130$nm. The red dashed lines are relative to the QS without any NHA. Black dashed lines indicate the absorption computed for a $T = 10$nm NHA alone.

Local Fields Analysis

Using simulations, a complete analysis of the local fields has been carried out. This helps in explaining the nature of the observed resonances, and of the features evidenced in the previous sections. Moreover, it allows to confirm the interpretation of the interaction of the QS resonances with the residual NHA.

Considering the shell model with the parameters indicated in tab.3.7, the field map has been obtained for the two main resonances, present in the yellow line of fig.3.50. In particular, the spectrum shows three peaks: the twin peaks occourring at 730nm and 770nm, and the main resonance at 1320nm. Fig.3.53 shows the field configurations corresponding to the three peaks, and fig.3.54 shows the phase of the E_x field in the incidence plane. Fig.3.53c shows that the $\lambda = 1320$nm resonance has dipolar symmetry (i.e. $L = 1$ in the Mie formalism). In contrast, the twin peaks at $\lambda = 730$nm and $\lambda = 770$nm show $L = 3$ and $L = 2$ symmetries, respectively. The differences between the two peaks of the multipolar resonances are due to a different phasing of the plasmons: in fig.3.54a the top of the shell experiences a sharp phase flipping with respect to the two upper lobes of the resonance. The dephasing is not present in fig.3.54b, corresponding to $\lambda = 770$nm. The two resonances are associated to two different

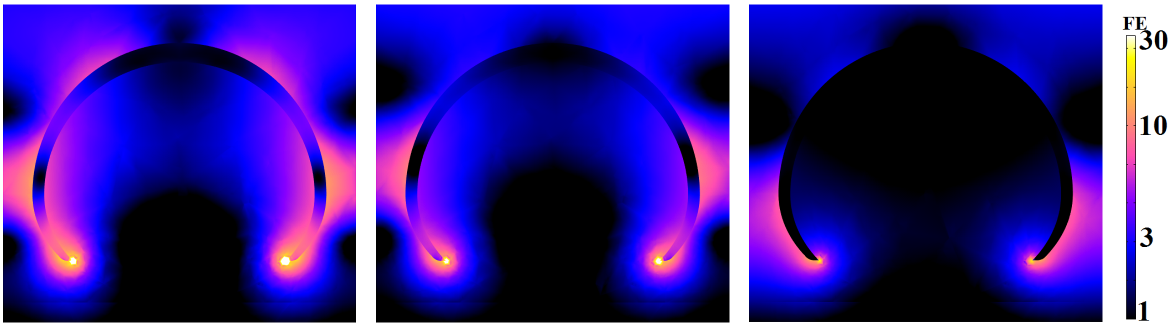

(a) $\lambda = 730$nm **(b)** $\lambda = 770$nm **(c)** $\lambda = 1320$nm

Figure 3.53.: Field maps for the three peaks of the quasishell. Images plot $\log|\mathbf{E}|$, and have the same colour scale. In the images, $\vec{k}$ is directed downwards ($-z$), the electric field is in the $\hat{x}$ axis.

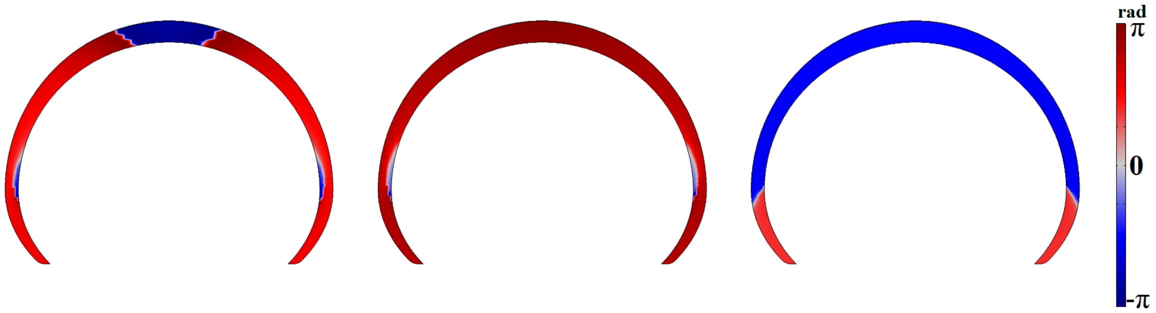

(a) $\lambda = 730$nm **(b)** $\lambda = 770$nm **(c)** $\lambda = 1320$nm

Figure 3.54.: Argument maps for the three peaks of the quasishell. Images plot $\arg E_x$, and have the same colour scale. In the images, $\vec{k}$ is directed downwards ($-z$), the electric field is in the $\hat{x}$ axis.

physical behaviours of the light-plasmon interaction. As expected in axially symmetric structures, the two resonances are associated to the axial mode and to the transverse mode. To explain this difference, fig.3.55 shows the map of the magnetic field associated to the plasmon (H_y) for all the three peaks. From fig.3.55c, it is possible to conclude that the main resonance, at $\lambda = 1320$nm, is a dipole-driven, electroinductive plasmonic mode. On the contrary, the twin peaks resonance has a different origin: in this case, the resonance is due to the current-driven, magnetoinductive plasmonic mode. Figure 3.56 confirms this interpretation: the plot of the induced current density (J_z) shows the dipolar configuration at $\lambda = 1320$nm and the dual-loop current pattern in for the $730 - 770$nm peaks. Finally, plotting the norm of the current density, it is possible to explain the differences between the two twin peaks. Indeed, fig.3.57 illustrates the differences between the two peaks: the most energetic one ($\lambda = 730$nm) is characterized by higher values for both current loops (upper and lower) with respect to the

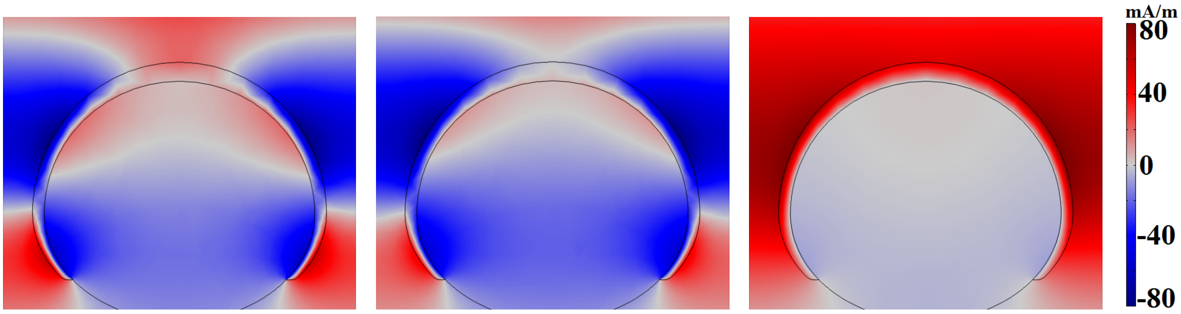

(a) $\lambda = 730$nm **(b)** $\lambda = 770$nm **(c)** $\lambda = 1320$nm

Figure 3.55.: Magnetic field maps for the three peaks of the quasishell. Images plot H_y (orthogonal to the page), and have the same colour scale. In the images, $\vec{k}$ is directed downwards ($-z$), the electric field is in the $\hat{x}$ axis.

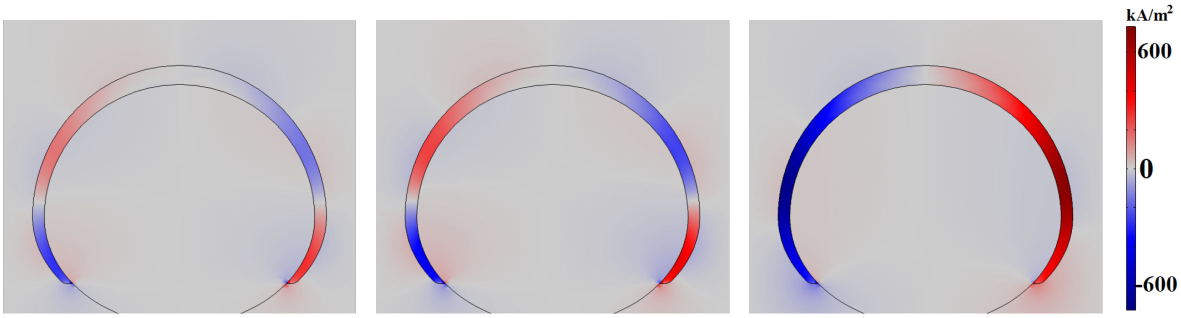

(a) $\lambda = 730$nm **(b)** $\lambda = 770$nm **(c)** $\lambda = 1320$nm

Figure 3.56.: Current density maps for the three peaks of the quasishell. Images plot J_z (vertical on the page), and have the same colour scale. In the images, $\vec{k}$ is directed downwards ($-z$), the electric field is in the $\hat{x}$ axis.

less energetic peak. On the other hand, the $\lambda = 770$nm peak is characterized by a higher current density (and thus losses) in the closure region, and this compensates the lower losses in the rest of the shell, justifying the same value of absorbance of the two peaks.

The effects of the interaction of the quasishells with the residual NHA have been presented in the previous section. The two features of this interaction are the quenching of the high energy resonances and the appearance of a new peak in between the two isolated shell resonances: fig.3.58a shows that, for the $d_{ps} = 37$nm shells, the $\lambda = 760$nm almost totally disappears as the thickness of the NHA approaches 20nm, but is still present for $T_{NHA} = 10$nm, though blueshifted by 30nm. The $\lambda = 1350$nm peak is in this case redshifted by 60nm. A third resonance appears between the two isolated shell peaks, at $\lambda = 1000$nm. The same behaviour is observed in the case of $d_{ps} = 30$nm, and in this case, given the shorter distance between the sell and the substrate, the effects of interaction are even larger: the main resonance shifts to $\lambda = 1500$nm, the $\lambda = 780$nm shifts to $\lambda = 760$nm and almost vanishes. The third peak appears at $lambda = 1020$nm. Using this last geometric configuration ($d_{ps} = 30$nm and $T_{NHA} = 20$nm), field maps have been computed. Regarding the $\lambda = 760$nm peak, field maps confirm the transfer of energy to the NHA: figure 3.59 shows the field enhancement $|\mathbf{E}|/E_0$ on the surface of the NHA. The field enhancement is double in the case of the $T_{NHA} = 20$nm NHA, and reaches a maximum value of 7.5. As a comparison, the field enhancement on the

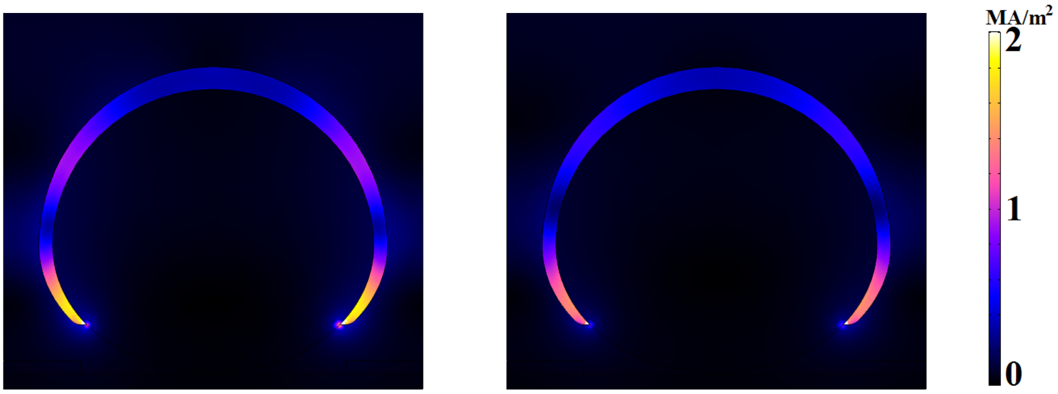

(a) $\lambda = 730\text{nm}$ **(b)** $\lambda = 770\text{nm}$

Figure 3.57.: Current density maps for the two twin peaks of the quasishell. Images plot $|\mathbf{J}|$. In the images, $\vec{k}$ is directed downwards ($-z$), the electric field is in the $\hat{x}$ axis.

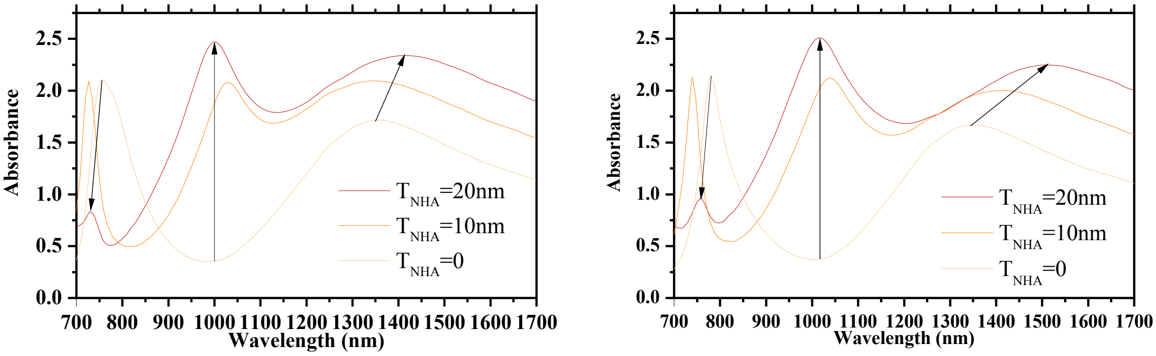

(a) $d_{ps} = 37\text{nm}$ **(b)** $d_{ps} = 30\text{nm}$

Figure 3.58.: Effect of the presence of residual NHA on the resonances. In both cases, $h^{+}_{out} = 135\text{nm}$ and $R_{out} = 130\text{nm}$.

surface of the NHA alone is about 3. This indicates that an important part of the energy stored in the shell resonance is tranfered to the nanohole array by near-field coupling, taking to a damping of the resonance itself. Indeed, in the case of the $T_{NHA} = 10\text{nm}$ NHA, the maximum field enhancement on the surface is 3.9: thus, most of the energy in the NHA can be associated to the direct coupling to light; the transfer of energy from the shell is much weaker, and thus the peak is still present in the absorption spectrum: the field enhancement on the shell is in this case much higher and accounts for this resonant absorption.

The $\lambda = 1350\text{nm}$ peak as noted redshifts to 1500nm, and fig.3.60b shows the current density pattern at this resonance. The pattern is clearly consistent with that observed for the isolated shell (fig.3.56c), thus confirming that the dipole-driven electroinductive resonance is maintained. Fig.3.60a shows, on the other hand, the current density pattern of the newly generated peak, at 1020nm. Again, a quick comparison with fig.3.56b reveals the current-driven origin of the resonance, and the magnetoinductive nature of the mode.

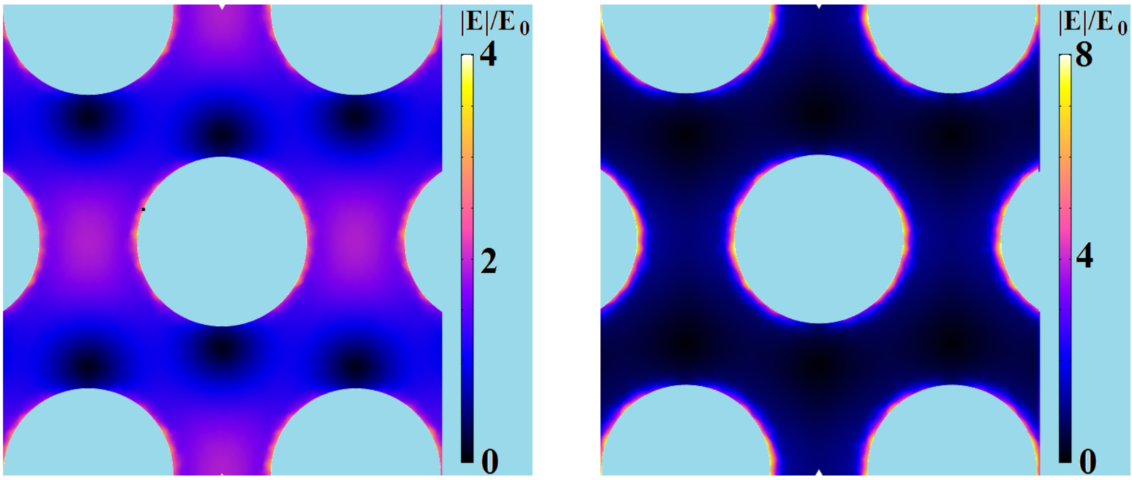

(a) $T_{NHA} = 10$nm **(b)** $T_{NHA} = 20$nm

Figure 3.59.: Surface plasmon electric field component (E_z) on the surface of the NHAs for two thickness values. The surface plasmon is two-fold stronger for the $T_{NHA} = 20$nm NHA.

3.4.6. QuasiShell Arrays as Biosensors

From preliminary results, both from simulation and experiment, AuAg QS showed interesting sensitivity properties when used as biosensors. The sensitivities obtained by simulations, in particular (without modeling the roughness), are interesting. For a $a_0 = 315$nm, $R_{in} = 100$nm, 26nm-thick QS, the local and bulk sensitivities, computed on the dipolar resonance, resulted:

$$S_\infty = 600\,\text{nm/RIU} \tag{3.34}$$

and

$$S_0 = 25\,\text{nm/RIU}, \tag{3.35}$$

thus overcoming the performances of nanoprisms as bulk sensors ($S_\infty^{np} = 362\,\text{nm/RIU}$ from section 3.2.4), and giving still comparable results in the case of thin layers sensors (best performing from section 3.2.4: $S_0 = 44\,\text{nm/RIU}$).

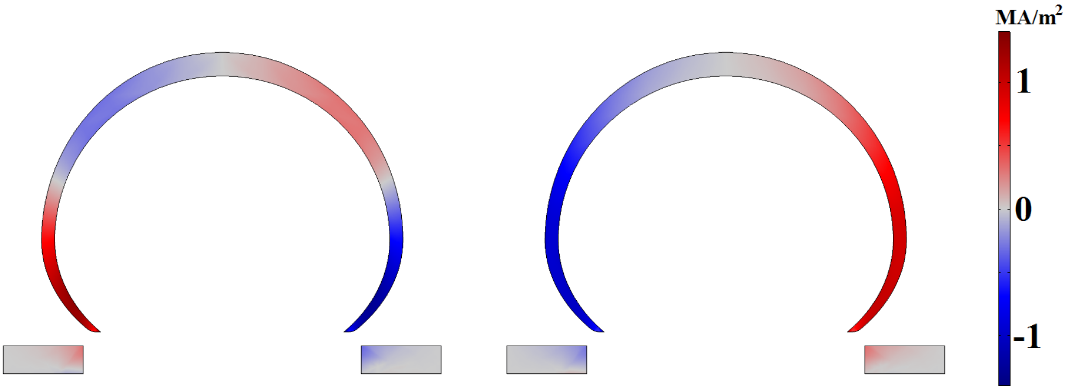

(a) New interaction generated mode, $\lambda =$ 1020nm **(b)** Shifted isolated shell mode, $\lambda =$ 1500nm.

Figure 3.60.: Current density J_z plots of the resonances for QS interacting with the NHA. $d_{ps} = 30$nm and $T_{NHA} = 20$nm.

3.4.7. Conclusions

The synthesis and characterization of bi-metallic Quasishells have been performed. The optical properties of the quasishells have been studied in detail, and the dependance of the optical spectra on various geometrical features of the shells has been identified and explained. Also the separation of the contributions from the shells and the residual nanohole array has been experimentally studied. Using simulations, the nature of the plasmonic oscillations has been determined and the interaction with the residual metal on the substrate has been demonstrated.

The fields of application of the produced samples range from the sensoristics to the light manipulation, passing through magneto-optical effects-based devices. The proposed methods improve the fabrication with respect to the literature under various aspects: the density of nanostructures is optimal; the ability of independently controlling RIE, starting nanospheres, deposition details enables the tuning of the resonances over a wide range and with precision; the use of co-deposition makes it possible to sinthesize amalgames of un-miscible metals with an high degree of mixing; the use of NOA in place of PDMS improves the peeling procedure from some day to half an hour; moreover, the NOA can be easily etched by RIE and this opens the possibility to access the lower part of the shells.

From preliminary studies, quasishell arrays are a promising structure for the fabrication of bio-sensors, particulary for bulk sensors.

Finally, using co-deposition, it has been possible to realize nanostructures made not only of miscible metals, but also of immiscible metals, such as gold and cobalt. Moreover, the EXAFS measurements showed that the used method is able to produce well-mixed samples, and XMCD measurements at the gold edge proved the efficient interaction of the two metals. The result is the fabrication of magneto-plasmonic nanostructures which combine the optical properties of gold and the magnetic response of cobalt.

Concluding, an innovative technique for fabricating bi-metallic nanostructures has been proposed and characterized, and the methods of literature have been improved under many aspects; the nature of the physical phenomena underlying the plasmonic response of this system has been reviewed, discussed and explained.

4. Fractal Nanostructures

In this chapter a non periodic kind of nanosystem will be considered, to get insights on the effect of scale invariance on plasmonic systems. These kind of systems, fractals, have been studied in two fashons. To study a fractal system experimentally, a well known type of fractal, Diffusion Limited Aggregation (DLA), is considered, where, although the process is random, most of fractal attributes are well defined and often a parallel with the deterministic computational results can be made. Secondly, a mathematically simple framework, where all the fractal attributes are known or easily computable, is given by "classic" or deterministic fractals. Some capital properties of fractal plasmonic system are identified by simulation techniques, and put in relations with those observed in the experiment.

4.1. Why Fractals?

Present design of optical devices at nanoscale is dominated by top-down approaches such as EBL [134] or FIB [135] patterning. These approaches are currently limited in resolution, throughput and costs [136–140]. By contrast self-assembling and bottom-up methods can give high-throughput, low cost processes to build complex nanostructures showing interesting, non-trivial optical and plasmonic properties [141–145]. In particular, fractals have been demonstrated to have outstanding properties relying on the scale invariance which is peculiar of such structures. Indeed, fractals are successfully used in spectroscopy as substrates as an example for SERS [9, 146–153]. The high field confinement of fractals, based on their tiny-scale details, permits to study nonlinear properties and the presence of scale invariance makes fractals particularly suitable for higher harmonic generation [154–161], frequency mixing, sum and difference [162–179]. The control over the scale power function plays a fundamental role also in light harvesting, and indeed the surface of solar cells is engineered to maximize the internal scattering by acting on the modulation of structures at different scales [180–184]. In addition, recently a relation between the fractal properties of gold aggregates and those of cancer cells has been found [185], opening a new application field for such structures in medical treatments exploiting an enhanced affinity.

4.2. Plasmonic Properties of Growing Fractal Aggregates

Many techniques provide structures with fractal nature. Fracturing of metals and rocks [186–188] or ablation by light [189], stimulated deposition from electrolites solutions [190], use of molecules or DNA to promote the aggregation of building blocks [191–196] are only a few of methods which can give fractal structures also at nanoscales. In this section a technique which can cheaply give well controlled fractals is studied. A bottom up approach is used, in which gold nanoparticles constitute the building blocks for the aggregation of larger fractals. In particular, the size of the resulting aggregates and their Hausdorff dimension can be controlled finely and easily. Differently from most other methods, in this case the

Hausdorff dimension is conserved at all the scales throughout the whole process, from small aggregates composed by a few of nanoparticles to huge configurations formed by hundreds or thousands of nanoparticles. The conservation of Hausdorff dimension is guaranteed by the presence of two different universal regimes of growth (namely, Diffusion Limited Aggregation, DLA, and Reaction Limited Aggregation, RLA) and is, in perspective, capital for the manipulation and control of particle-particle correlation, which is strongly associated to this parameter. Both regimes of growth have been studied in past years, thus most of the dynamics is known [197–203].

4.2.1. The Physics of the Problem

Fractal aggregates are fractal structures that emerge as a result of a controlled *aggregation process*. The aggregation process is here a random process occourring in a colloidal solution of nanoparticles. In this work, the attention is focused on fractal aggregates made up of gold nanoparticles, so that the fractals will benefit from the gold plasmonic properties.
A typical concentration of colloidal gold nanoparticles in acqueous solution is $c \sim 1 - 10\text{nM}$; at this concentration the gold nanoparticles, as an effect of the diffusion, experience collisions with other particles at a rate of $10^{11} M^{-1} s^{-1}$ [204]. The effect of such an high collision rate would be to generate large aggregates in a few seconds if no protection barrier existed to prevent particles from sticking together. This barrier usually consists of a surface potential on the particles due to the presence of positive charges on the surface. The aggregation process can be started by lowering this barrier, and its level, E_B, (and thus the sticking probability $P \sim e^{-E_B/k_B T}$) controls the dynamic of the aggreagtion. Two universal regimes have been recognized in among aggregation processes: Diffusion Limited Aggregation (DLA) and Reaction Limited Aggregation (RLA). DLAs are formed when $E_B \ll k_B T$, and thus the sticking probability is close to 1 (i.e. particle stick together upon every collision). On the other hand, RLAs are the result of a process in which $E_B \gtrsim k_B T$, and thus the probability of sticking is lower than 1 but still appreciable. The aggregates can be defined by three parameters:

- the cluster structure, defined by the *fractal* or *Hausdorff dimension* $\dim_{\mathrm{H}}$ (cfr. section B.2)
- the aggregation kinetics, described by the average cluster mass at time t, $\bar{M}(t)$
- the shape of cluster mass distribution, which has, in general, the functional form:

$$N(M) = \Psi\left(M/\bar{M}\right)/\bar{M}^2. \tag{4.1}$$

Diffusion Limited Aggregates

DLAs have been studied both experimentally and computationally, as presented in an our work [205], and the main features of this kind of aggregation is known. The fractal dimension resulted, from both experiment [200] and simulations [206]:

$$\dim_{\mathrm{H}}^{(\mathrm{DLA})} = 1.8 \pm 0.1. \tag{4.2}$$

Van Hogen and Ernst proved [207] that the aggregation dynamics is linear in t, the average mass having the form

$$\bar{M} = M_0 \frac{t}{t_0}, \tag{4.3}$$

the timescale t_0 is given by:

$$t_0 = \frac{3\eta}{8k_B T N_0}, \tag{4.4}$$

where η is the viscosity of the solvent and N_0 is the initial particles concentration. The shape of the distribution has been derived [208], and results:

$$N(M) = \frac{N_T}{\bar{M}}\left[1 - \frac{1}{\bar{M}}\right]^{M-1}, \tag{4.5}$$

where $N_T = \sum N(M)$ is the total number of clusters.

Reaction Limited Aggregates

RLAs have been studied both experimentally and computationally , and the main features of this kind of aggregation is known. the fractal dimension resulted, from both experiment [209] and simulations [210]:

$$\dim_{\mathrm{H}}^{(\mathrm{RLA})} = 2.1 \pm 0.1. \tag{4.6}$$

Meakin and Family proved [211] that the dynamics is exponential in t, the average mass having the form

$$\bar{M} = M_0 e^{At}, \tag{4.7}$$

where A depends on the probability of sticking upon a collision. The shape of the distribution has been derived [208], and results:

$$N(M) \sim M^{-\tau} e^{-M/M_c}, \tag{4.8}$$

where M_c is a cutoff mass and τ has been determined $\tau = 1.5 \pm 0.1$.

4.2.2. Synthesis Gold DLA Fractals

The experimental synthesis protocol is divided in three main parts: the synthesis of colloidal gold nanoparticles, the successive aggregation to form fractals and the stopping of the aggregation at any desired stage. The first task is achieved by a Turkevich type technique, whilist the aggregation step is induced by hindering the stheric screening of gold nanoparticles and thus permitting particle-particle collisions and adhesion by adding Pyridine to the solution. The last step is the freezing of the aggregation by the addition of a surfactant which hinders any furter sticking of nanoparticles. A sketch of the whole protocol is shown in fig.4.1.

Gold Nanoparticles Synthesis

The synthesis of the Gold Nanoparticles (AuNP) is achieved by a colloidal formation technique originally due to Turkevich [212], and slightly modified [213]. This technique is based on the reduction of a gold salt in solution, $HAuCl_4$ which takes produces free gold atoms in suspension. Due to diffusion, the atoms start to aggregate to form larger and larger particles, until the surface is passivated by the presence of a surfactant.

In the used method, the Sodium Citrate is used both as the reducing species and as the particle size-limiting agent. The size and dipersion of synthesized nanoparticles is strongly dependent on the concentrations of Gold Salt and Sodium Citrate, and on their ratio. To get $\sim 10-20$nm nanoparticles with a good monodispersity ($\sigma \lesssim 20\%$), the AuNP have been

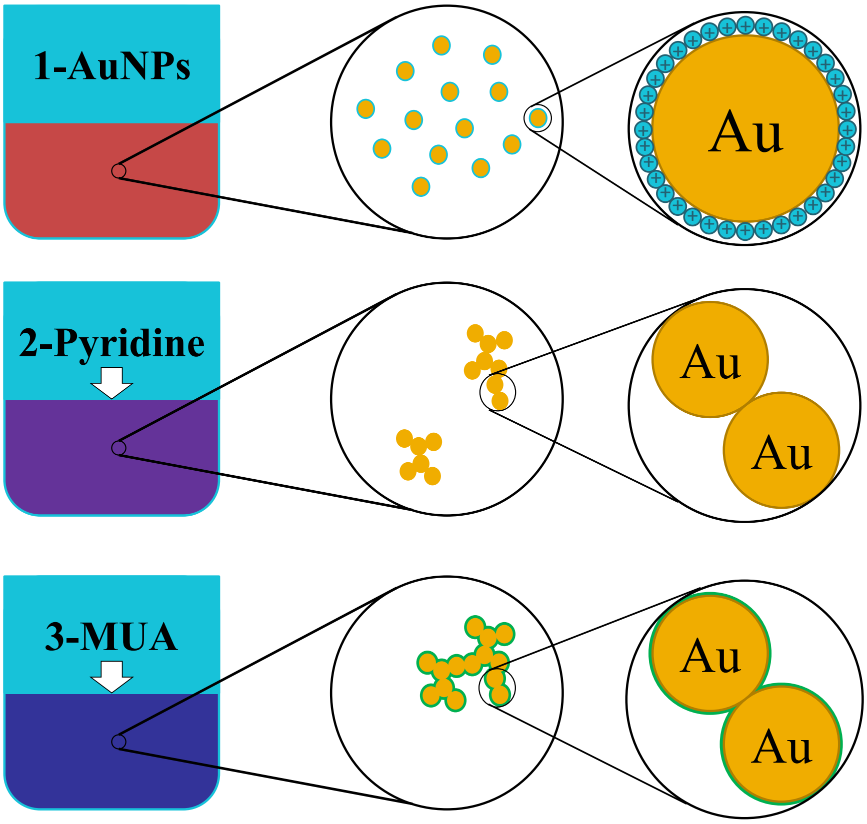

Figure 4.1.: The three steps of the synthesis protocol: production of AuNP; starting of the aggregation; stopping of the aggregation and stabilization.

produced starting with a 1mM solution of $\mathrm{HAuCl_4}$, and by adding Sodium Citrate up to a 1:1 gold/sodium citrate concentration ratio. The process takes place in a constant temperature vessel, set at the temperature of 100°C, and vigorously stirring the solution during all the formation process. The AuNP are formed and stable after a quarter of hour of incubation. After this point, the solution is cooled down to room temperature by simply putting it into air. The obtained nanoparticles have a mean diameter of 15.2nm and the size distribution has a standard deviation of $3.4nm$, as obtained by SEM (fig.4.2a) and TEM(fig.4.2b) imaging. The extinction spectrum (fig.4.3) of the obtained nanoparticles show a strong, definite plasmonic resonance at 523 ± 2nm, as expected for a dipolar Mie resonance for gold in water. The standard starting solution is thus a 1mM solution in gold atoms, corresponding to a 1.83nM solution in particles concentration. The solution is stable (i.e. no aggregation takes place).

Aggregation Process

The aggregation starts when the surface potential on the nanoparticles drops, making it possible for the particles to stick upon collisions. To lower the barrier, a selected quantity of *Pyridine* is added to the nanoparticles solution. As previously pointed out, two distinct regimes exists, DLA and RLA, and the choice between the two is made by varying the quantity of added pyridine. DLA is achieved when pyridine is added at a $C_{Pyr} \sim$ 10mM concentration, whereas RLA is reached for lower pyridine concentrations, $C_{Pyr} \sim 10\mu$M.

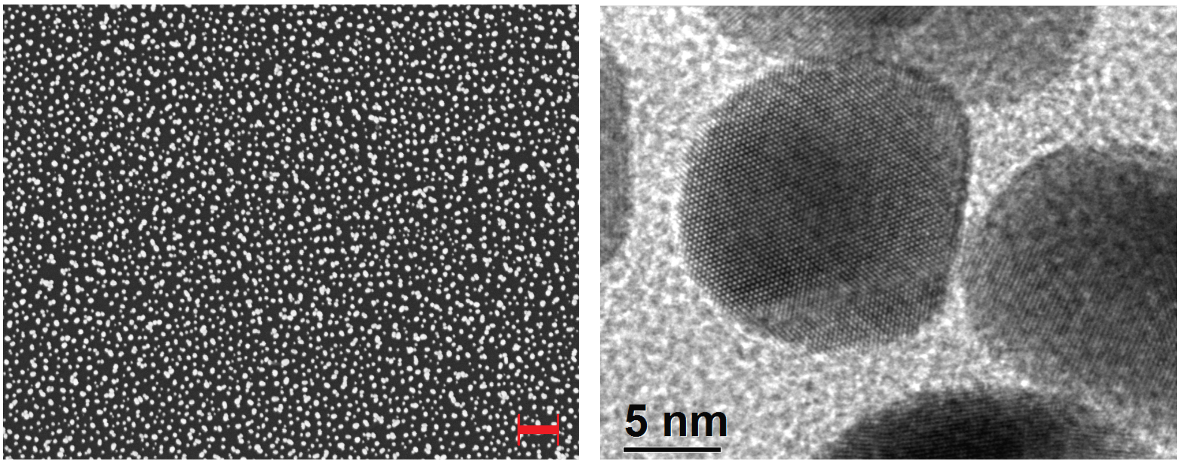

(a) AuNPs as observed by SEM. Bar = 200nm **(b)** AuNPs as observed by TEM. Bar = 5nm

Figure 4.2.: Electron Microscopy images of aggregated clusters.

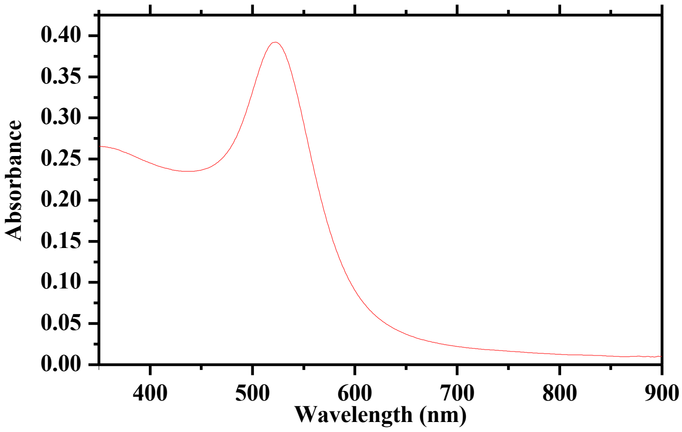

Figure 4.3.: Extinction spectrum of the Gold Nanoparticles in solution. The concentration have been lowered to 50μM in gold atoms for the extinction measurement.

The time scale of aggregation is in both cases function of the starting nanoparticles concentration, thus this parameter can be varied according to needs. For proper nonlinear optics experiments, a higher concentration is important to raise the extinction cross section of the solution, and to permit the deposition on glass. On the other hand, for aggregation dynamics studies, a slower process is desirable, so the concentration should be lowered. As a rule of thumb, for DLAs, the starting concentration in gold atoms is set to $C_0 = 10\mu$M for aggregation studies and to $C_0 = 50\mu$M or $C_0 = 100\mu$M for the production of nonlinear optics samples. A 10mm-thick cuvette is filled with 2mL of AuNPs of selected concentration. The cuvette is placed in the optical path of an Ocean Optics DH-2000-BAL + HR4000CG-UV- NIR source + multiplex specrophotometer system, which acquires real-time extinction spectra of the solution. During the experiments, the spectrophotometer is set to record 1 spectrum per second. At $t = 0$ the chosen quantity of pyridine (corresponding to 8μL of pure pyridine for DLA and to 8μL of 10^{-3}-diluited pyridine for RLA) is added to the cuvette, and a vigorous stirring of about one second assures the spreading of the pyridine and the consequent start of the aggregation.

The optical and plasmonic properties of the forming aggregates are recorded at this stage. At any time it is possible to stop the aggregation process by using a surfactant, the Mercapto Undecanoic Acid (MUA). This surfactant has a thiol (sulphur) group, which binds strongly and with high affinity to the gold atoms on the surface of the Gold Nanoparticles (AuNP). The effect is the stopping of the aggregation process due to the hindering of further particle-particle and particle-cluster sticking. A too low quantity of MUA takes to a slow freezing of the process; on the other hand, high concentrations have been observed to take to instability, as the high affinity of MUA with gold takes to the breaking of some formed clusters. Thus, the best performing MUA quantity has been determined to be 10μL of a 2.5mM solution of MUA. In this case too, a vigorous stirring of about one second assures the freezing of the aggregation all over the volume of the cuvette. Using this protocol, the starting and the stopping of the aggregation takes no longer than a second each, a time comparable to the time span of the recorded spectra. The stopping using MUA has two further advantages: the carboxyl termination of this molecole guarantees the solubility of the formed clusters in water, making it possible to further process the solution. The other advantage is given by the possibility of using the carboxyl group for functionalizations or for deposing the clusters on substrates. A further stabilization has been achieved by placing the solution in a vacuum chamber at a pressure of 1mbar for 30s.

The deposition of aggregates on a silicon wafer is needed for the observation in SEM, whereas the deposition on silica slabs is needed for the nonlinear optical measurements. This step can be achieved using a functionalized substrate, as shown in [214]. (3-Aminopropyl)- triethoxysilane (APTES) molecoles are used to functionalize the substrate. The siloxane group of the molecule binds covalently to both silicon and silica, creating a Self-Assembled Monolayer (SAM) of molecoles. The other end of the molecoles has a ammino group, which bonds with high affinity to the carboxyl group of the stabilized aggregates. A dip of the functionalized substrate in the aggregates solution form a stable layer of aggregates, whose surface concentration can be controlled by varying the concentration of the solution and the time of exposition.

4.2.3. Results and Discussion

Diffusion Limited Aggregation

The effect of addition of pyridine, and thus of the start of aggregation, is a sudden change in the extinction spectrum of aggregated clusters. Fig.4.4 shows the recorded spectra for the first 60 s of a DLA process. At $t = 60\,\mathrm{s}$ from the starting of aggregation, the process has been stopped, and afterwards the spectra has been recorded to check the stabilization of the system. The main change in the spectra is the appearance of a second peak at lower energies with respect to the single particles one. Another feature is the redshift of both peaks during all the aggregation. To better study this phenomenon, the spectra have been fitted by using a double-peaked Lorentz function in order to find the peaks positions at each step. Figure 4.5 shows the fitted positions of the second peak as a function of the aggregation time; in the inset, the same data are plotted using logarithmic time axis. It is possible to recognize, after a short transient, that the redshift of the peak is proportional to the logarithm of the time. As expected, the aggregation speed is proportional to the initial concentration of gold.

By stopping the aggregation process at different times, it has been possible to take SEM images

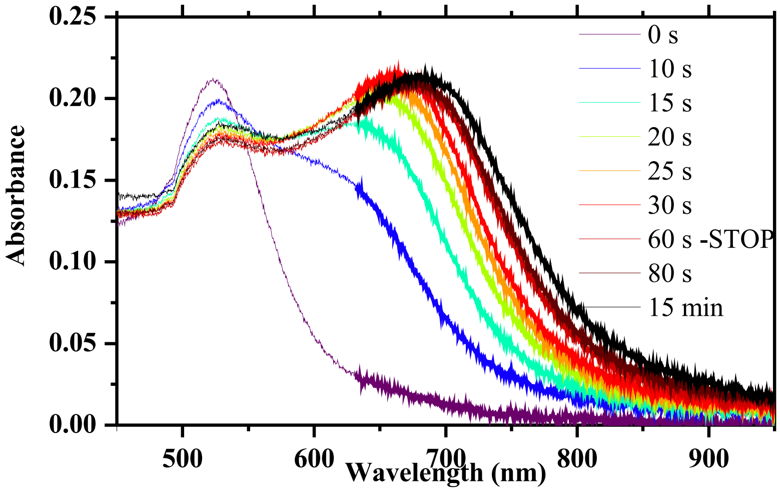

Figure 4.4.: Extinction spectra during the aggregation. The starting concentration is $C_0 = 10\mu$M in gold, and the pyridine is added at a concentration of $C_{pyr} = 12.5\mu$M

of the forming fractals, and it has been possible to deduce the mean number of particles in a cluster by using the relation [215]:

$$N = 1.3 \left(\frac{R_g}{r_0}\right)^{dim_H}, \tag{4.9}$$

where r_0 is the mean radius of particles, $d_H = 1.8$ is the fractal dimension of the aggregates and R_g, the gyration radius, can be easily extracted from images by finding the circumference with the minimum radius encircling the aggregate. Fig. 4.6a shows an example of SEM images at different stages of aggregation. As a reference, fig.4.6b shows how do the three solutions from which the samples have been extracted look. SEM images analysis confirmed that the aggregation process is linear with time. For the $C_0 = 10\mu$M, the timescale resulted $t_0 = 0.36$s, in very good agreement with theoretical value of 0.34s computed using eq.4.4. Using the aggregation process with this initial concentration of nanoparticles, the relation between the mean number of particles in a cluster and the redshift has been derived. Fig.4.7 shows this relation for the two peaks. The redshift of the two peaks follows a similar behaviour: at early stages (i.e. for small clusters), the redshift is proportional to the logarithm of the number of particles, whereas for larger clusters the redshift starts to saturate. The intercept and slope of the relation between the redshift and the logarithm of the number of particles have been computed for both peaks:

$$\Delta\lambda_1\left(\bar{N}\right) = (-19.9 \pm 0.4)\,\text{nm} + (11.2 \pm 0.2)\,\text{nm} \cdot \log \bar{N}, \tag{4.10}$$

$$\Delta\lambda_2\left(\bar{N}\right) = (-26.6 \pm 1.8)\,\text{nm} + (23.1 \pm 0.5)\,\text{nm} \cdot \log \bar{N}. \tag{4.11}$$

The critical cluster size over which the redshift starts to saturate has been determined for both peaks:

$$N_c^{(1)} = 66, \tag{4.12}$$

$$N_c^{(2)} = 35. \tag{4.13}$$

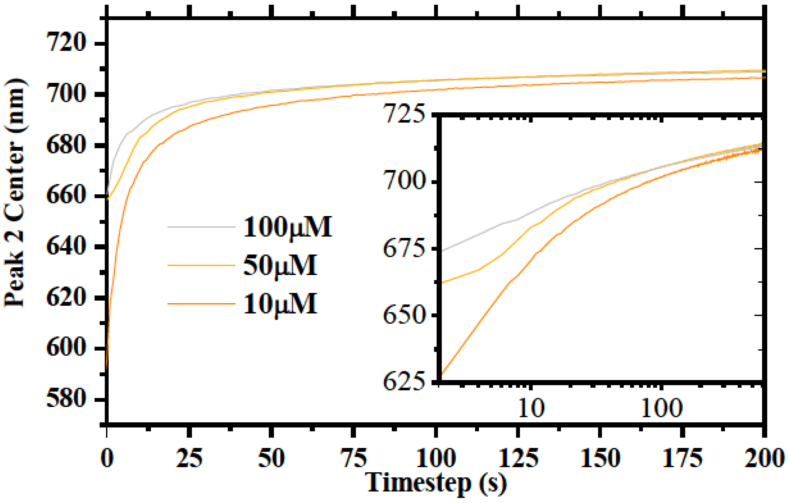

Figure 4.5.: Dynamic evolution of the second absorbace peak position for different of the starting concentration of gold.

Finally, the asymptotic positions of the peaks have been measured in long lasting aggregation processes, and resulted the same for different initial concentrations, thus confirming the universal nature of aggregation in this regime. The resulting redshifts are:

$$\Delta\lambda_1^{(max)} = 39.0 \pm 0.4\text{nm}, \tag{4.14}$$

$$\Delta\lambda_2^{(max)} = 94.6 \pm 0.1\text{nm}, \tag{4.15}$$

corresponding to the final peak positions:

$$\lambda_1^{(max)} = 552.5 \pm 0.4\text{nm}, \tag{4.16}$$

$$\lambda_2^{(max)} = 713.1 \pm 0.1\text{nm}. \tag{4.17}$$

The maximum redshift occours for clusters formed by over about 700 particles for the first peak and about 1500 particles for the second peak.

Summarizing, the evolution of clusters has been observed for the DLA regime under different conditions. Focusing on the plasmonic features of such a system, it is possible to conclude that as a result of the aggregation, beside the single particles extinction peak, a second peak emerge and becomes relatively more and more important as the aggregates grow. Both peaks redshift as an effect of the aggregation, and the analysis for different initial concentrations (i.e. for different aggregation rates) showed that the fundamental parameter which controls this phenomenon is the mean number of particles in an aggregate. Two different regimes have been recognized for the redshift of growing clusters: at early stages (small clusters) the redshift is directly proportional to the logarithm of the average number of particles in a cluster for both peaks, and the slope of this proportionality has been derived for both peaks. As the number of particles exceeds a critical value, the redshift starts to saturate and finally reaches an asymptotic values. This critical size and the asymptotic redshift, different for the two peaks, have been identified in both cases.

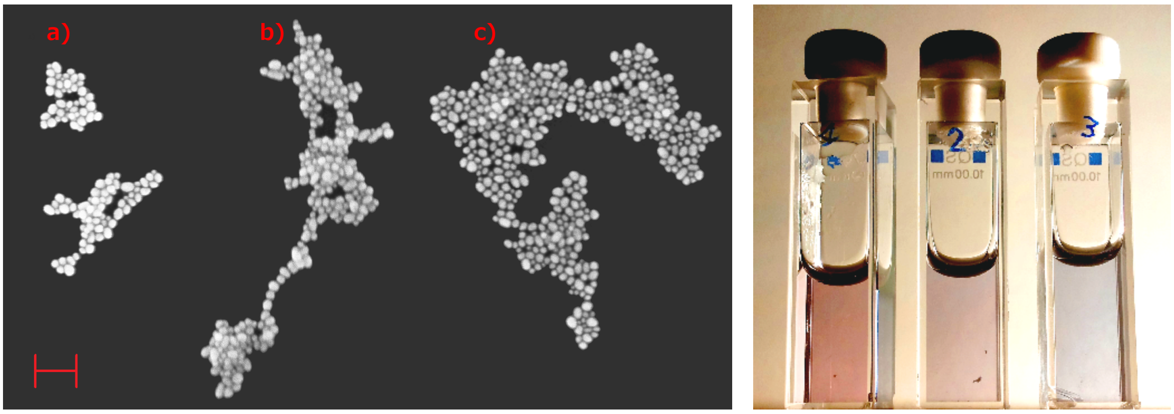

(a) Fractals at SEM. Bar = 200nm **(b)** Photography of the three solutions.

Figure 4.6.: DLA fractals at different aggregation stages. The appearance of the second peak in the red region takes to an absorption which is not present in single particles solution, and thus to a change in colour.

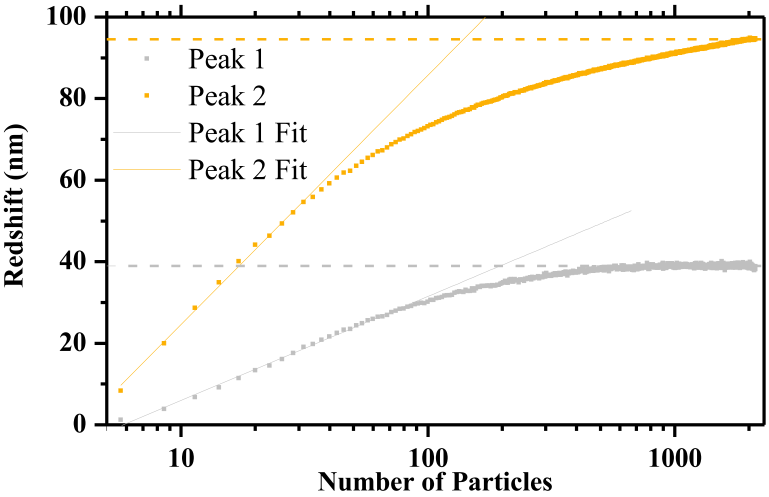

Figure 4.7.: Relation between the redshift and the average number of particle in a cluster. Linear fits have been carried out on the first part of the data considering the logarithm of the number of particles as independent variable. For peak 2, the value of the variance of the centre position is less than 1 nm for $N > 1500$

4.2.4. FEM Model

A finite elements model of clusters has been solved to get further insights on the physics of cluster-light interaction. The growing aggregate has been simulated starting from a simulation code which computes the dynamics of the aggregation process and yields the coordinates of the particles forming the cluster. The particles have been modeled as spheres, whose radius have been determined by SEM and Transmission Electron Microscope (TEM) measurements. The interparticle distance has been obtained by TEM measurements ($R_0 = 7.6$nm). To recover the properties of the realized samples, the medium around the particles is described by the refractive index of water, and the dielectric function has been obtained by ellipsometry measurements on a gold optically thick film.

The model has been solved for different aggregation stages, and the absorbance has been evaluated for all three polarization to take into account the average rotational symmetry in the experimental sample. Fig.4.8a shows the obtained results: as in the experiment, when the number of particle N grows, a second peak appears and both peaks shift towards longer wavelengths. Fig.4.8b show the differences in the absorbance for the three polarization: given the random growth, the geometry in the incidence plane is different in the three cases, and different resonances result excited. In particular, it is possible to see that the y- and z-polarization activate in an enhanced way the second peak resonance, while the x-polarization activates

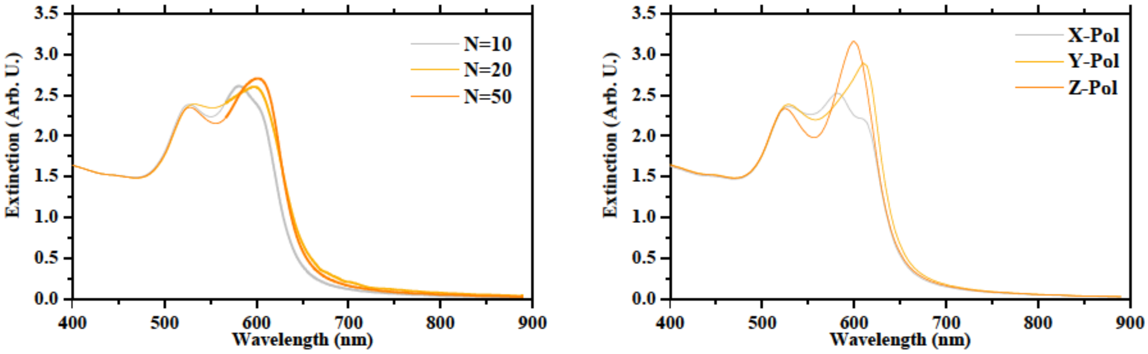

(a) Polarization-averaged extinction of growing clusters.

(b) Extinction from a $N = 20$ particles cluster for the three polarizations.

Figure 4.8.: Simulated extinction of aggregates as a function of number of particles in a cluster and polarization.

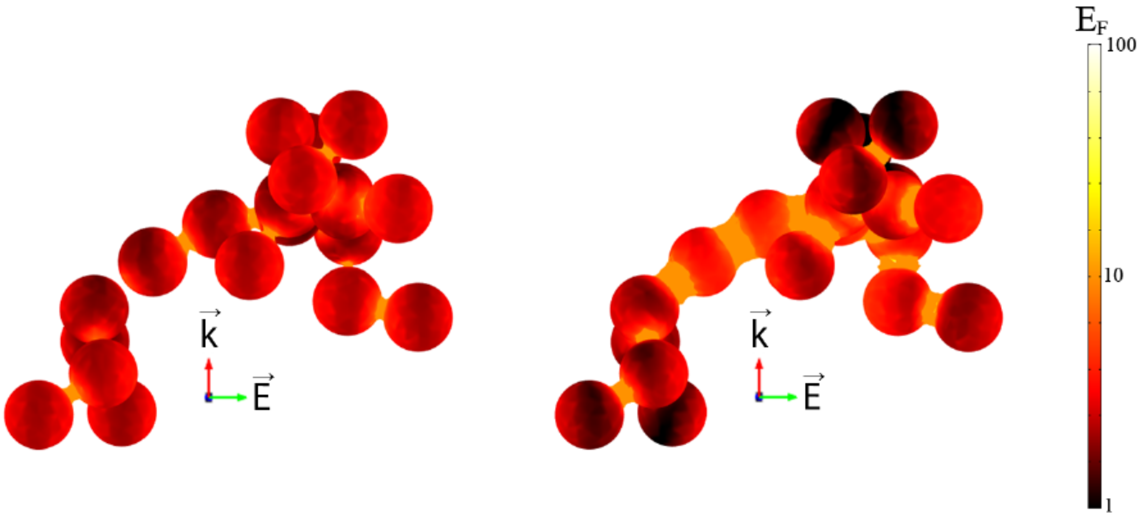

(a) Field Enhancement Map of the resonance at $\lambda = 530$nm.

(b) Field Enhancement Map of the resonance at $\lambda = 600$nm.

Figure 4.9.: Field Enhancement maps of an $N = 20$ aggregate for y-polarization of the elecric field. The orange surface encircles the interparticle domains where the field enhancement is grater than 10.

a less red-shifted and less intense second peak resonance. In all the cases, varying both the polarization and the number of particles in a cluster N, the first peak remains at the same intensity, and experiences a less important redshift with respect to the second peak when increasing N, again, as observed in the experiment. The nature of the two resonance peaks can be clarified by plotting the field maps of the clusters at the two wavelengths, as shown in fig.4.9. The color map stands for the logarithm of the norm of the electric field on the particles surface. The orange surface between the particles indicates the boundary of the region where the field enhancement is greater than 10 .Fig.4.9a shows that the field configuration in the case of the first peak is dominated by the single-particle LSPR, as the field is uniform on the single spheres, and only in the gap regions oriented along the polarization axis a stronger enhancement is visible. On the other hand, fig.4.9b shows the nature of the second peak resonance: in this case the field enhancement on the single sphere is poor, as it is visible on the surface of the particles on top of the figure. The strong field enhancement, which is responsible of the resonance is located in the gaps between the particles, and in particular in the gaps oriented along or near the polarization axis. At this wavelength, if the nanospheres form locally a chain which is conveniently oriented with respect to the polarization, a collective mode is excited, and along the entire chain the field enhancement is strong, in particular in the gaps. The strong orientation dependance of this kind of resonance is visible also in fig. 4.8b: the second peak position, shape and intensity are different for the three polarizations, according to the degree of orientation in the three cases.

The evolution of the clusters in simulations gave qualitatively the same results as the experiment for redshift and saturation of the peaks. Slight differences are due to the shape and size distribution of the experimentally sinthesized particles and to a non uniform interparticle distance in the experiment, not considered in the simulation.

4.2.5. Conclusions

The plasmonic properties of growing fractal aggregates have been observed. Focusing on the plasmonic features of such a system, it is possible to conclude that as a result of the aggregation, beside the single particles extinction peak, a second peak emerge and becomes relatively more and more important as the clusters grow. Both peaks redshift as an effect of the aggregation, and the analysis for different initial concentrations (i.e. for different aggregation speeds) showed that the fundamental parameter which controls this phenomenon is the mean number of particles in a cluster. Two different regimes have been recognized for the redshift of growing clusters: at early stages (small clusters) the redshift is directly proportional to the logarithm of the average number of particles in a cluster for both peaks, and the slope of this proportionality has been derived for both peaks. As the number of particles exceeds a critical value, the redshift starts to saturate and finally reaches an asymptotic values. This critical size and the asymptotic redshift, different for the two peaks, have been identified in both cases.

The physics behind the formation of two distinct peaks has been investigated by solving finite elements models. The two peaks are due to different kinds of resonance: on one hand the most energetic peak (shorter wavelengths) is associated to the bare single particles LSPR, and the position of the peaks in the early aggregation stages, coincident with the single particles peaks, confirms this interpretation. On the other hand, as the clusters grow, the random process causes the formation of aligned chains of nanoparticles. In this case, whenever the light polarization axis is placed along or close to the axis of those chains, the second peak emerge as a *collective fractal* mode.

The position of the resonances, which redshift as the number of particles in clusters grow, can give interesting information about the particle-particle correlation, as will be reviewed in the next section. For a deeper comprehension of the role of correlation in plasmonic fractal systems, "classic fractals" will be considered, exploiting the analytical derivations that these mathematic systems can yield. A parallel with the experimentally observed properties will be carried out, thus generalizing the results for both random aggregates and deterministic fractals and making a link between the two classes. As a results, part of the methods used in well-known deterministic fractal systems will be transferred to the more experimentally interesting aggregates, which can be sinthesized at extremely low costs.

4.3. Plasmonic Properties of Classic Fractals

In this section standard building blocks are arranged to form fractal configurations on a 2D plane. The radiation will incide normally to this plane. The geometric configurations will be defined by classic, deterministic fractals, whose mathematical properties are known and analitically derivable. These kinds of fractals are obtained by recursively applying a map on a starting set, which in this case is a single point at the origin of the coordinates. At each application of the map, a new set of points is defined, and the corresponding plasmonic structure is found by placing the chosen building block at each point in these sets. For each family of fractals, the plasmonic properties at successive steps have been studied, and all the results, also qualitatively in accordance with the previous experimental section, have been condensed in a simple model for the behaviour of plasmonic fractals as a function of their topological and geometrical properties. Since such kind of fractals can only be obtained by EBL techniques, we will restrict to cubic building blocks and not to spheres.

4.3.1. Definitions

For a study of the classic fractals, a bottom-up approach in the evolution of fractals has been adopted mimicking the aggregation dynamics. Thus, a *monomer* has been defined, as the basic building block. This building block is a snipped cube, geometrically defined by its *side*, l, and its *snipping radius* $r_{snip} = s \cdot l$ ($s = 0.1$), as indicated in fig.4.10a. The blocks are then arranged to form successive steps of three fractals, the Cantor Dust (CD), the Cantor Box (CB) and the Sierpinski Carpet (SC), together with the 2D grid. In this operation, the distance between the centers of two nearby sites is the *pitch* p. In the 2D grid, all the sites of the grid are occupied; in the fractal configurations only part of the sites are occupied by a building block. The definition of what sites are occupied is made exploiting the iteration of the fractal maps defined in appendix B.2.3.

4.3.2. Fractals Properties

Four fractal configurations have been considered in this work, three of which are strictly fractals, and the fourth is the 2D grid, which however can be considered as a fractal with $dim_H = 2$. In this last case the successive steps have been obtained by forming a 3×3 set for step 2, a 9×9 set for step 3 and so on. The 2D projection of the first 3 steps of the 2D configuration are plotted in fig.4.11a. In this case the pitch is $p = 30nm$, the side is $l = 20nm$

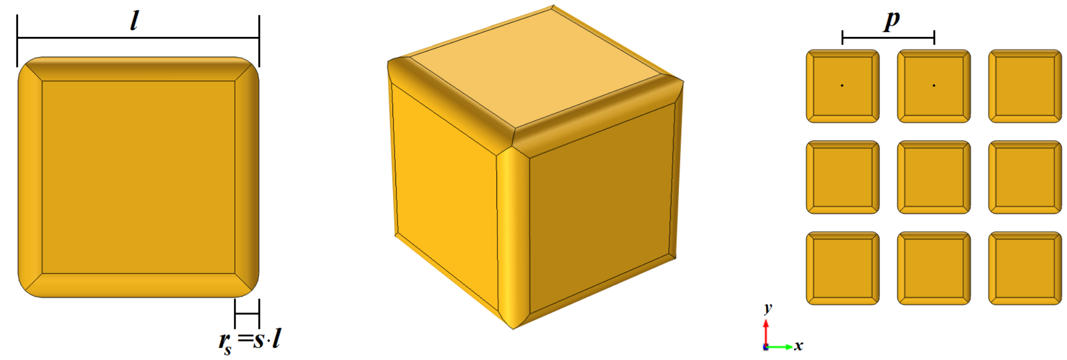

(a) Geometric Parameters **(b)** 3D Rendering **(c)** Grid definition

Figure 4.10.: Shape and definition of parameters of the building blocks and of the lattice grid.

Table 4.1.: Main features of the considered fractals. The last two, not considered here, are examples of fractals having different grid types.

Fractal	dim_H	Internal Ratio	Grid Type	Growth Factor g	Max Steps
Cantor Dust	1.262	1/3	Square	4	4
Cantor Box	1.464	1/3	Square	5	4
Sierpinski Carpet	1.893	1/3	Square	8	3
2D Grid	2.000	1/3	Square	9	3
(Sierpinski Gasket)	1.585	1/2	Triangular	4	-
(Snowflake)	1.631	1/3	Hexagonal	6	-

and the snipping radius is $s = 0.1$.

The other three fractals are *genuine*, in the sense that their fractal dimension is not an integer: $1 < dim_H < 2$. The main features of the three fractals are reported in tab.4.1. Along with the fractal dimension and the internal ratio, also the *growth factor* g is indicated. This parameter is the factor by which the number of monomers is multiplied at each iteration of the map. Thus, the number of monomers can be calculated, for each fractal and at each step n_s by the relation:

$$N\left(n_s\right) = g^{n_s - 1}. \tag{4.18}$$

Figg. 4.11b, 4.11c and 4.11d show the first three steps of, respectively, the Cantor Dust, the Cantor Box and the Sierpinski Carpet. All the figures are plotted assuming $p = 30nm$, $l = 20nm$ and $s = 0.1l$.

Once the fractal geometry is defined, the scattering volume is a $R = 700$nm sphere, centered at the centre of the fractal. Outside this sphere, a PML domain is placed to suppress back reflected waves from the outer boundaries. The electromagnetic properties of the metals (gold, silver, copper) are defined by the dielectric function taken from literature [17], whereas the medium around the fractals is vacuum. The radiation is described by a plane wave, whose wavevector is orthogonal to the fractals plane (XY plane). The polarization is along the $\hat{x}$ direction, and the computations have neglected the $\hat{y}$ polarization, taking into account the $\pi/2$-rotational symmetry of the system. Fig.4.12 shows a sketch of the model.

Three combinations of pitch and building blocks have been analyzed, and tab.4.2 show the used combinations, the obtained SPR wavelength and field decay length normal to the

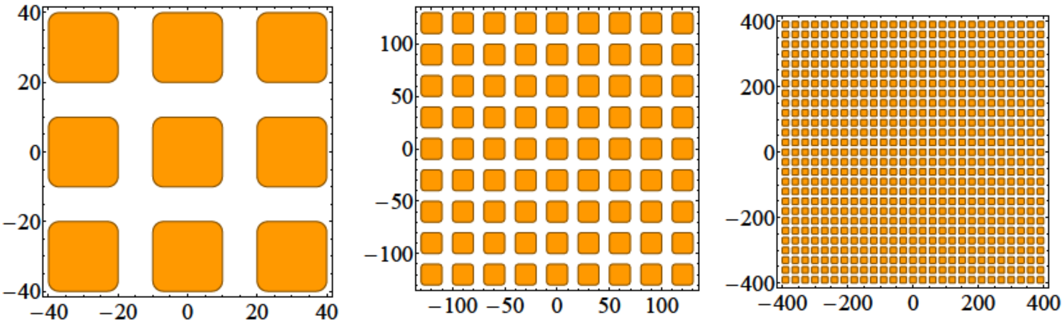

(a) 2D Grid

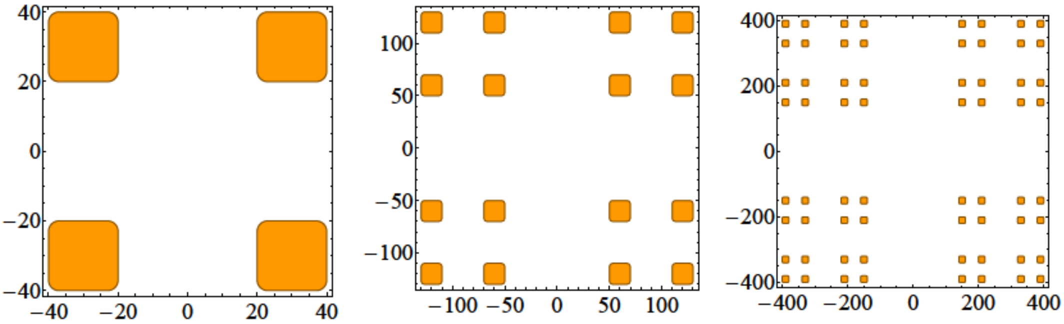

(b) Cantor Dust

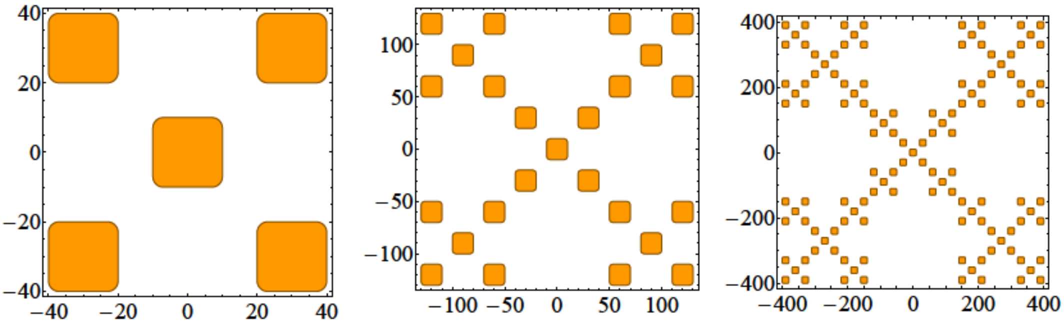

(c) Cantor Box

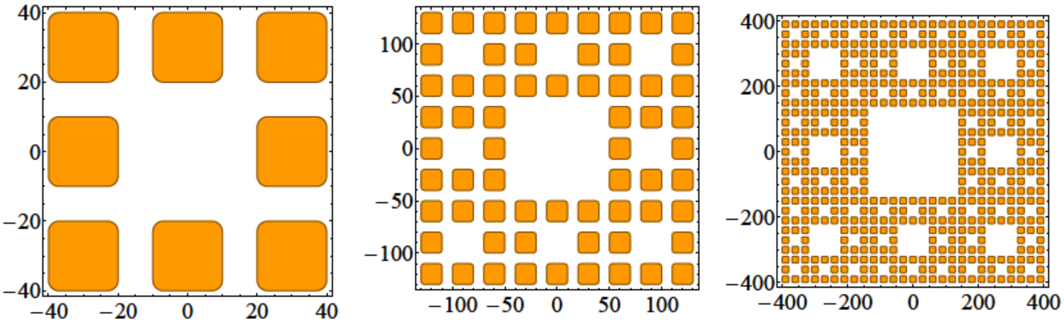

(d) Sierpinski Gasket

Figure 4.11.: First 3 steps of the considered Fractals.

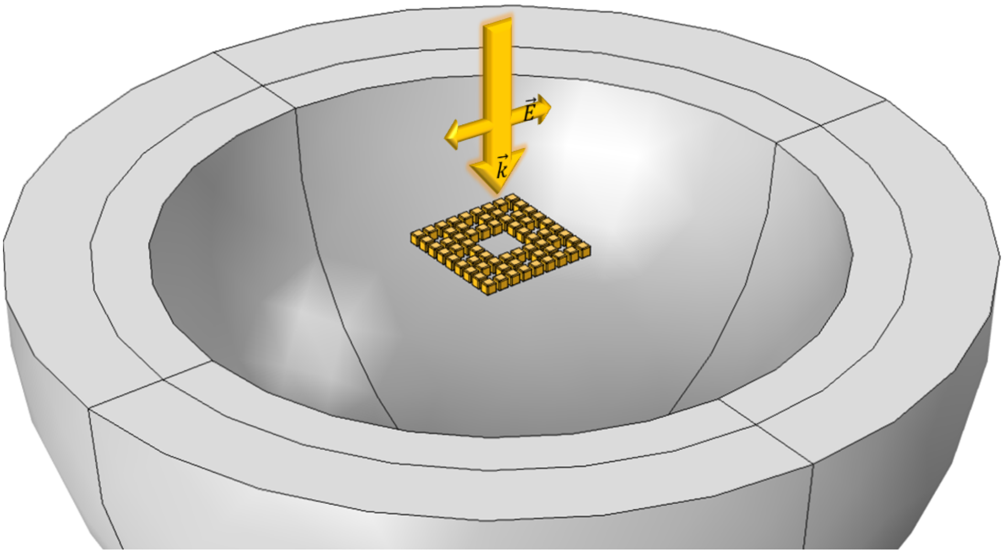

Figure 4.12.: Sketch of the model: at the centre there is the fractal. Around the fractal, a sphere is the scattering volume.

Table 4.2.: Building blocks and pitches used in the analysis.

Pitch p(nm)	Side l(nm)	Metal	SPR wavelength λ_0(nm)	Decay length $t_0$nm
10	9	Ag	398	7.2
		Au	523	6.2
		Cu	522	6.3
12.5	10	Ag	385	6.9
		Au	513	5.8
25	10	Ag	385	6.9
		Au	513	5.8
	20	Ag	386	9.7
		Au	513	8.5

monomer surface of one isolated particle for different metals.

4.3.3. Elaboration and Discussion

The setup of the models has been made to support parametric variation of geometry. Tab.4.3 summarizes the parameters and the properties they control. These parameters have been varied to take into account their effects on the studied plasmonic systems.

To study the plasmonic properties, the optical spectra (far-field) of each configuration have been obtained and elaborated. The spectra are characterized by the usual plasmonic peak, and using a Lorentz fit in the peak region, the LSPR wavelength has been determined. As for the case of the aggregates studied in the previous section, the most important effect of adding building blocks to the fractals is the redshift of the plasmonic peak due to interaction among monomers.

For each fractal family (i.e., for each fractal dimension dim_H) the redshift, $\Delta\lambda$, defined by

$$\lambda_{SPR} = \lambda_0 + \Delta\lambda, \tag{4.19}$$

Table 4.3.: Parameters definition, range and relations.

Parameter	Symbol	Relations	Considered Range
Step Number	n_s	-	$[1;4]$
Growth Factor	g	$N(n_s) = g \cdot N(n_s - 1)$	$[4;9]$
Internal Ratio	r_i	-	3
Fractal dimension	dim_H	$dim_H = \log g / \log r_i$	$[1;2]$
Pitch	p	-	[10nm; 25nm]
Block Side	l	-	[9nm; 20nm]
Snipping Parameter	s	$r_{snip} = s \cdot l$	0.1

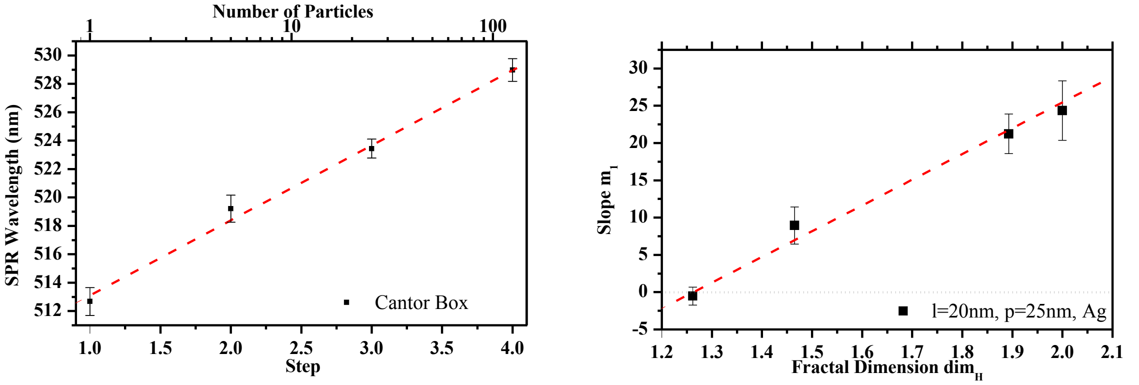

(a) SPR wavelength evolution as a function of the fractal step (bottom axis) and number of particles (top axis, logarithmic).

(b) m_1 coefficient as a function of the fractal dimension.

Figure 4.13.: Linear fitting of λ vs. n_s and of m_1 vs. dim_H.

resulted proportional to the logarithm of the number of particles, as fig.4.13a shows for the Cantor Box:

$$\Delta\lambda \propto \log N. \tag{4.20}$$

The proportionality constant m_1 of this relation have been determined by performing a linear fit on the data, using the equation

$$\Delta\lambda = m_1 \left(n_s - 1\right), \tag{4.21}$$

which is equivalent to

$$\Delta\lambda = m_1 \cdot \log_g N. \tag{4.22}$$

The determined coefficients show, in turn, a proportionality with the Hausdorff dimension, dim_H of the fractals, when the m_1 from different fractal families are compared, as fig.4.13b shows. Again, a linear fit have been performed. The fitting equation is

$$m_1 = \kappa \left(dim_H - dim_0\right), \tag{4.23}$$

where κ is the proportionality constant and dim_0 is the *critical fractal dimension* below which no redshift appears. At the end of this section, tables 4.5, 4.6, 4.7 and 4.8 show the values of these parameters in the case of $l = 9$nm building block and $p = 10$nm, $l = 10$nm b.b. and $p = 12.5$nm, $l = 10$nm b.b. and $p = 25$nm and $l = 20$nm b.b. and $p = 25$nm, respectively.

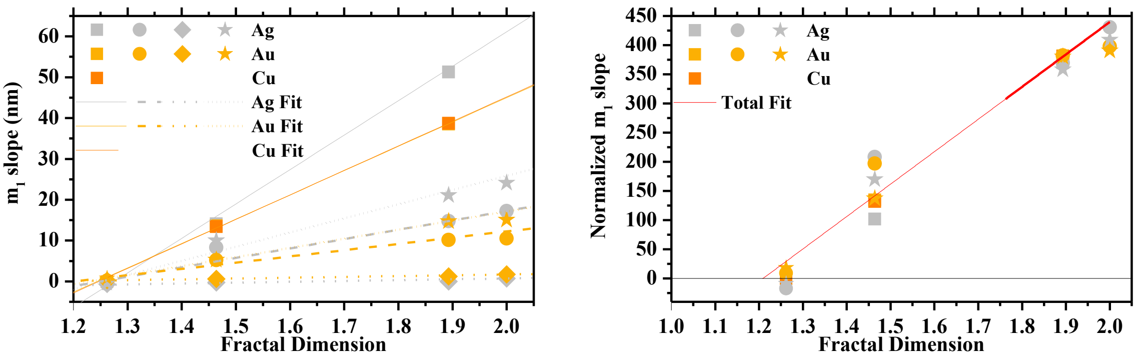

(a) m_1 as a function of the fractal dimension. Colours define the metal, scatters indicate the data points, lines indicate the fits. Data sets: squares and solid lines for $l = 9$nm and $p = 10$nm; circles and dashed lines for $l = 10$nm and $p = 12.5$nm; diamonds and dotted lines for $l = 10$nm and $p = 25$nm; stars and short-dotted lines for $l = 20$nm and $p = 25$nm.

(b) Normalized m_1 as a function of the fractal dimension. Colours define the metal, scatters indicate the data points, lines indicate the fits. Data sets: squares for $l = 9$nm and $p = 10$nm; circles for $l = 10$nm and $p = 12.5$nm; stars for $l = 20$nm and $p = 25$nm. Red line: total fit.

Figure 4.14.: Simulated extinction of aggregates as a function of number of particles in a cluster and polarization.

Fig.4.14a shows the resulting values of the slope m_1 as a function of the fractal dimension, along with the linear fits of the data points for all the data sets.

The $l = 10$nm b.b. and $p = 25$nm configuration yields results with a relative error larger than 100%, due to the very weak interparticle interaction. Therefore, these data won't be considered in the following analysis.

A first *universal* result is the presence of a critical fractal dimension below which the redshift is not present or negligible at each fractal stage. This behaviour is found for the Cantor Dust ($dim_H = 1.262$), and the fits for different metals and side/pitch provide this critical dimension, indicated with α for each data set, as reported in the results tables. From an average of all the obtained values, the universal critical fractal dimension, valid for all the (plasmonic) metals and all the geometric configurations have been determined:

$$\alpha_U = 1.243 \pm 0.001. \tag{4.24}$$

The other value obtained by fits, κ is, on the other hand, dependent on both metals and geometric configuration. To find an universal value for κ too, it is necessary to find a proper normalization. First of all, the obtained κ are normalized by the monomer SPR wavelength, as reported in tab.4.2, to obtain a pure number, the normalized shift:

$$\kappa_r = \frac{\kappa}{\lambda_0}. \tag{4.25}$$

It is useful to take into account the field leakage from the isolated nanostructures, which has, in all cases, an exponential decay pattern outside the monomer surface. The decay length x_0, found as a fitting parameter of the fields using the equation:

$$E\left(x\right) = E\left(x = 0\right)\left(1 - e^{-\frac{x}{x_0}}\right), \tag{4.26}$$

Table 4.4.: Resulting normalization factors f_u and κ_U universal redshift parameters.

Pitch p(nm)	Side l(nm)	Metal	Relative Shift Parameter κ_r	Normalization Factor $f_u(\mathrm{nm}^{-1})$	Universal Shift Parameter κ_U(nm)
10	9	Ag	0.21	0.00035	608
		Au	0.11	0.00019	589
		Cu	0.11	0.00019	590
12.5	10	Ag	0.06	0.00010	575
		Au	0.03	0.00005	578
25	20	Ag	0.09	0.00015	589
		Au	0.04	0.00008	577

where $x = 0$ is the monomer surface. This field decay profile gives a measure of the interaction distance between two plasmonic nanostructures and is thus a relevant parameter in the determination of the correlation between particles and, in turn, of redshift. It is possible to get a global normalization by dividing the normalized shifts by a universal normalization factor f_U, defined as:

$$f_U = \frac{e^{-2\Delta x/x_0}}{\Delta x} \frac{l^3}{\lambda^2 \cdot p}, \tag{4.27}$$

where Δx is the gap between two monomers. The normalization factor takes into account on one hand the (intensity of the) field decay occourring in the gap between two particles, and responsible for an attenuation of the interaction; on the other hand, it takes into account the surface coverage of the monomers, normalized by the wavelength of the considered resonance, and the ratio between the side of the particle and the pitch of the lattice.

As a result of the normalization, it has been possible to find out a *universal redshift parameter* κ_U, defined as:

$$\kappa_U = \frac{\kappa_r}{f_U}. \tag{4.28}$$

The resulting values for f_U and for κ_U are reported in tab.4.4. Averaging the values obtained from the various configurations (which differ by no more than 6% from each other), the determination of the *universal redshift parameter* is

$$\kappa_U = 587\,\mathrm{nm}. \tag{4.29}$$

The meaning of this parameter is that, given the geometrical properties of the monomers and the details on the gap between particles, it is possible to foresee the redshift experienced by a plasmonic resonance as a result of the interaction with other monomers, when these are arranged following a fractal configuration. Fig.4.14b shows the normalized data for the elaborated configurations. As it is clear, using the normalization, all the geometry/metal combinations experience a redshift which is dependent on the fractal dimension in the same way.

This universal result can be interpreted as the effect of the correlation among monomers in the considered configurations. Thus, a general model for the correlation among particles in a fractal plasmonic system can be proposed. This model foresees that the dependance of correlation on fractal dimension is linear if the fractal dimension is greater than a critical value; on the contrary, no plasmonic correlation exists if the fractal dimension is lower than the critical dimension. The value of this critical dimension α_U and of the universal correlation

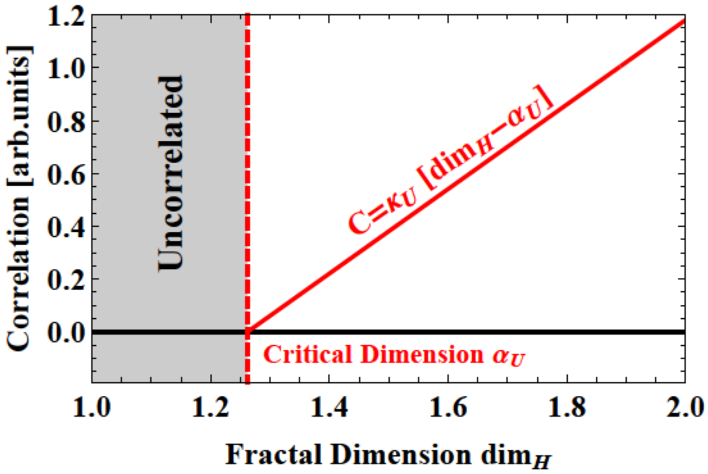

Figure 4.15.: Sketch of the correlation model for plasmonic fractals.

parameter κ_U describe the model. Fig.4.15 shows a sketch of the proposed model.
Now, by inserting the obtained κ_U in eq.4.23 to get m_1, and inserting m_1 in eq.4.22, it is possible to obtain the redshift experienced by a plasmonic resonance as a function of the Hausdorff dimension dim_H, the number of particles in the fractal N and of the growth factor g:

$$\frac{\Delta\lambda}{\lambda_0 f_U} = \kappa_U\,[dim_H - \alpha_U]\left[\log_g(N)\right] = \frac{1}{\log g}\kappa_U\,[dim_H - \alpha_U]\,[\log(N)]\,. \tag{4.30}$$

The result can be viewed in terms of correlation. The redshift of plasmonic peaks is strictly related with the interaction among monomers, in turn controlled by the particle-particle correlation. This latter, in turn, is a consequence of the topological arrangement of the building blocks. The model depicted in fig.4.15 therefore can be interpreted as a scheme which describes how the plasmonic correlation behaves in fractal systems as the number of particles forming an ensamble grows. In particular, the correlation is controlled by two parameters, both well defined in the case of deterministic fractals, the Hausdorff dimension dim_H and the growth factor g.
For random fractals, the concept of g is not defined. However, in the next paragraph, a comparison of this model with the results form DLA, presented in the previous section, will be attempted.

4.3.4. Comparison with DLA

In the case of random fractals, which are not defined by the iteration of a map, the concept of growth factor is not straightforward. However, it is clear the analogy between eq.4.11, here reported:

$$\Delta\lambda\left(\bar{N}\right) = (-26.6 \pm 1.8)\,\mathrm{nm} + (23.1 \pm 0.5)\,\mathrm{nm}\cdot\log\bar{N}, \tag{4.31}$$

and 4.22. Exploiting this analogy, it is possible to obtain a value for m_1 in the case of DLA, as a function of an *effective growth factor* g^*:

$$m_1^{(DLA)} = (23.1 \pm 0.5)\,\mathrm{nm}\log g^*. \tag{4.32}$$

Using this result, it is possible to deduce the value of g^* for which also eq.4.30 holds. To this aim, it is necessary to compute the normalization factor f_U in the case of the synthesized DLA fractals:

$$f_U = \frac{e^{-2\Delta x/x_0}}{\Delta x} \frac{l^3}{\lambda^2 \cdot p} = 1.8 \cdot 10^{-3} \mathrm{nm}^{-1}, \tag{4.33}$$

inserting the geometrical parameter deduced from the previously performed analysis. It is possible to rearrange eq.4.23 to get:

$$\log g^* = \frac{\kappa_U \cdot f_U \cdot \lambda_0 \left[dim_H - \alpha_U \right]}{(23.1 \pm 0.5)\, \mathrm{nm}} \tag{4.34}$$

Resulting in a value for g^*:

$$g^* = 13. \tag{4.35}$$

This value for g^* can be used in the relation between the fractal dimension $dim_H = 1.8$ of the DLA and the internal ratio(s) r present in the topology, and stricly valid for deterministic fractals:

$$dim_H = \frac{\log g}{\log r}, \tag{4.36}$$

this way, it is possible to compute an *effective internal ratio*, r^* for the DLA. The result is:

$$r^* = 2.01. \tag{4.37}$$

The presence of an internal ratio very close to 2 may suggest the importance of the first nearby particle-particle interaction inside the DLA fractals.

As a result, it is possible to conclude that the application of the formalism obtained for deterministic fractal on random aggregates gives interesting analogies, though more investigation is necessary to confirm them.

4.4. Conclusions

The evolution of the optical properties of plasmonic fractal nanostructures has been studied. The behaviour emerged in the self-assembled DLA process has been reproduced and recognized in the evolution of classic fractals. In particular, a general property that emerge from this study is the dependance of the redshift on the logarithm of the number of particles. The analysis of classic fractals allowed to correlate this dependance in a more strict way on the fractal properties such as internal ratios and Hausdorff dimension.

The evolution of the redshift is due to the electromagnetic correlation among the particles, and an accurate analysis of the correlation showed the existence of some universal features in fractal systems. Firstly, a lower critical dimension has been recognized: below this fractal dimension fractal systems do not show correlation at all; this dimension has been proved to be universal in the sense that it is equal for all the three plasmonic metals and for all the tested combinations of monomer side and grid pitch. The determined value for this parameter is $\alpha_U = 1.243 \pm 0.001$. It has been demonstrated that in a fractal the correlation between particles (and thus all the optical properties due to it) depends on the Hausdorff dimension. There is a linear dependance and the slope of the line κ_U is material-independent and monomer-independent once normalized by the proper normalization factor. We determined $\kappa_U = 454$.

The presence of these properties is a very interesting thing both theoretically and technologically. Indeed, on one hand the topologies that show self-similarity, as fractals, become very important to study properties of complex systems, like the correlation between elements of an ensamble. On the other hand, it opens new possibilities in nanostructures design: just as the effects of the dimensions and spacing of particles in a linear chain or in a 2D array are exploited to create devices with well-defined behavior, the exploration of the effects of the fractal properties will enable to design new devices that exploit their effects. Further, the fractal properties of self-assembled systems often depend only on the class of the process (as for the case of DLA/RLA). Thus, if a device is designed to exploit fractal properties, its construction becomes well easier, as the fine details of the structure do not count anymore, being all the important properties defined by the selection of the appropriate self- assembling process.

Table 4.5.: Results of fractals analysis for $l = 9$nm and $p = 10$nm.

Metal	κ(nm/step/dim)	dim_0	dim_H	m_1(nm/step)	n_s	δ_λ(nm)
Ag	84.3	1.275	1.262	-0.1	1	-
					2	2
					3	0
					4	0
			1.464	14.1	1	-
					2	15
					3	30
					4	43
			1.893	51.3	1	-
					2	48
					3	103
Metal	κ(nm/step/dim)		dim_H	m_1(nm/step)	n_s	δ_λ(nm)
Au	59.5	1.244	1.262	-0.1	1	-
					2	2
					3	2
					4	3
			1.464	13.6	1	-
					2	13
					3	28
					4	40
			1.893	38.5	1	-
					2	37
					3	77
Metal	κ(nm/step/dim)		dim_H	m_1(nm/step)	n_s	δ_λ(nm)
Cu	60.0	1.247	1.262	-0.1	1	-
					2	2
					3	1
					4	1
			1.464	14.4	1	-
					2	15
					3	35
					4	42
			1.893	38.7	1	-
					2	23
					3	67

Table 4.6.: Results of fractals analysis for $l = 10$nm and $p = 12.5$nm.

Metal	κ(nm/step/dim)	dim_0	dim_H	m_1(nm/step)	n_s	δ_λ(nm)
Ag	23.0	1.250	1.262	-0.7	1	-
					2	-1
					3	0
					4	-1
			1.464	8.3	1	-
					2	11
					3	23
					4	33
			1.893	14.8	1	-
					2	19
					3	33
			2.000	17.2	1	-
					2	0
					3	2
Metal	κ(nm/step/dim)	dim_0	dim_H	m_1(nm/step)	n_s	δ_λ(nm)
Au	15.3	1.232	1.262	0.2	1	-
					2	3
					3	2
					4	3
			1.464	5.2	1	-
					2	6.3
					3	10.7
					4	13.0
			1.893	10.1	1	-
					2	8.9
					3	19.8
			2.000	10.5	1	-
					2	8.8
					3	20.4

Table 4.7.: Results of fractals analysis for $l = 10$nm and $p = 25$nm.

Metal	κ(nm/step/dim)	dim_0	dim_H	m_1(nm/step)	n_s	δ_λ(nm)
Ag	2.1	1.65	1.262	-0.7	1	-
					2	-1
					3	-2
					4	-1
			1.464	-0.2	1	-
					2	0
					3	-1
					4	-1
			1.893	0	1	-
					2	-3
					3	2
			2.000	0.71639	1	-
					2	0
					3	2
Metal	κ(nm/step/dim)	dim_0	dim_H	m_1(nm/step)	n_s	δ_λ(nm)
Au	2.0	1.15	1.262	0	1	-
					2	0.3
					3	0.9
					4	0.7
			1.464	1	1	-
					2	0.8
					3	1.3
					4	1.8
			1.893	1	1	-
					2	1.2
					3	2.3
			2.000	2	1	-
					2	1.5
					3	3.3

Table 4.8.: Results of fractals analysis for $l = 20$nm and $p = 25$nm.

Metal	κ(nm/step/dim)	dim_0	dim_H	m_1(nm/step)	n_s	δ_λ(nm)
Ag	34.7	1.255	1.262	-0.5	1	-
					2	2
					3	-2
					4	1
			1.464	10.0	1	-
					2	10
					3	21
					4	30
			1.893	21.1	1	-
					2	17
					3	42
			2.000	24.1	1	-
					2	24
					3	48
Metal	κ(nm/step/dim)	dim_0	dim_H	m_1(nm/step)	n_s	δ_λ(nm)
Au	22.3	1.232	1.262	0.7	1	-
					2	2
					3	2
					4	3
			1.464	5.3	1	-
					2	7
					3	11
					4	16
			1.893	14.7	1	-
					2	11
					3	28
			2.000	15.1	1	-
					2	10
					3	28

Conclusions

The work presented here showed that periodicity and self-similarity are two elements of paramount importance in the design of plasmonic nanostructures. The role of the two classes of invariance has been analyzed to point out the advantages and the peculiarities from each one. The fundamental aim of all the analyzed systems is to provide an improvement with respect to the current state of the art in the understanding of the relationship between symmetry or hierarchical organization and functional properties. As a result from the point of view of both a better comprehension of their physical properties and smarter design and tailoring of their possible applications, new interesting results have been achieved. The main results of the present work can be summarized as follows.

Periodic Nanostructures

The role of translational symmetry in these systems is multiple. Two main aspects deeply affect the results from all the three analyzed systems. First of all, the Nanosphere Lithography patterning technique has the periodicity as an essential element in the attainment of reproducible structures. If the structures are not interacting, periodicity nevertheless enables the replica of the building block, resulting in an enhanced signal-to-noise ratio for every application. On the contrary, if the structures can interact, new and improved plasmonic features can emerge, and can be exploited. Another aspect in which periodicity play a preminent role is in the modeling of nanosystems: the periodic boundary conditions are a fundamental element in the correct description of systems in which it is not unfrequent that the unitary cell is tinier than the radiation wavelength, thus otherwise posing serious questions about edge effects. Beside these common osservation, each of the three systems expoit the periodicity different manners. All the three configurations share a cost-effective synthesis protocol, thus making these approaches attractive for a future industrial implementation, as described below.

Nanotriangles Arrays

Finite-element simulations enabled the description of experimental-like nanostructures, provided with the dielectric substrate, and modeled with the correct shape without geometric approxymations. As a result of the simulation analysis, the main features of a localized-plasmons based biosensor have been obtained. First of all, a map of the LSPR wavelength as a function of the lattice parameter of the array and the aspect ratio of the triangles have been computed for both gold and silver. Yet this achievement is important as many applications ask for precise regions where the samples should resonate, and such a map is fundamental for the correct fabrication of the nanostructures according to these needs. The best performances of this class of nanosystem as a biosensor have then been assessed, both for thin layer and bulk sensors. Moreover, the role of the physical mechanisms triggering optimal sensitivities has been discussed in terms of local fields patterns.

Nanohole Arrays Interacting with Emitters

Starting from the frame of emitters coupled with metal films, the interaction between Er_3^+ ions and nanostructures supporting propagating modes has been studied both experimentally and theoretically.
The synthesis has been optimized with the aim of controlling the emitters distribution and of providing a low-cost protocol exploiting all the capabilities of magnetron sputtering. Experiments showed the advantages given by a nanohole array architecture with respect to a simple thin film in terms of enhanced decay, and demonstrated the effectiveness of using a EOT-coupled NHA for the 1.54μm emission line.
Simulations, in agreement with experiments, showed the capabilities of the emitter-NHA coupling, providing the optimal locations for getting the best quantum efficiency from Er. Moreover, the analysis of the far field pattern showed that a major advantage of the NHA is the ability to couple surface plasmons with photons, thus enabling the re-emission of the excitons induced by the emitters. On the contrast, in the film model this is a major source of losses, as the plasmons are confined in the metal and decay according to their dispersion relation. Another major advantage of the NHA architecture is the efficient transmission through the nanostructure, which enable the detection of far field photons from both faces of the samples. The effect of these two features is an outstandigly high quantum efficiency, close to unity, which represents an extraordinary improvement with respect to past results.

Quasishells

A new method for the synthesis of bi-metallic nanostructures has been set up and characterized. Finite elements modeling provided the explaination of the physics behind the plasmonic response of the obtained system.
Topological characterization proved the ability to synthesize large ordered arrays of well reproducible nanostructures. The relation between the obtained results and the main experiment settings has been identified, thus enabling the control of the nanostructure by acting on multiple parameters. Structural characterization confirmed also the possibility of obtaining bimetallic alloys from both michible (AuAg) or immiscible (AuCo) species. In particular the synthesis of AuCo alloy nanostructures has been achieved, and synchrotron radiation measumerements proved the high mixing level of these two unmiscible elements at atomic level, confirmed by the presence of XMCD signal at the gold L2 and L3 edges.
Simulations explained the nature of the plasmonic resonances experimentally observed, and clarified the role of the residual nanohole array under the shells, and of the interaction between the two systems.

Self-Similar Nanostructures

The role of the scale invariance has been investigated in self-similar systems both in experiments and in simulations.
As a general result, the control of fractal dimension enables the control over correlation and, in turn, over the position and shape of the plasmonic peaks. In those systems the role of correlation is enhanced with respect to the periodic configurations and actively influences the overall properties of local field distributions.
A fractal synthesis protocol has been defined, in order to gain control on the aggregation

dynamics of random fractals obtained with DLA. It has been possible to adjust the fractal dimension and the fractals size, and to further process the obtained fractals exploiting the built-in functionalization platform given by MUA. In experimentally synthesized fractal aggregates made up of gold nanoparticles, the appearance of a double-peaked spectrum required the interpretation of the two structures, carried out with finite elements modeling. As a result, two different mechanisms have been recognised as the origin of the two peaks: one is due to the single particle (uncorrelated) plasmons, the other to a collective oscillations from correctly oriented chains of particles.
The fine control of the resonance position has been proved and explained by simulationg classic fractals, in parallel with the random aggrefates, identifing the universal role of correlation and proposing a model for the resonance position in function of the fractal dimension and fractals size.

Outlook

Most of the parts of this thesis can be a starting point for further research and applications. The thorough analysis of the interaction between emitters and nanoholes arrays gave promising results in the control of emission probability and quantum efficiency which extend the previous work carried out on non-nanostructured materials. The setup of a correct finite elements framework is moreover the starting point for the proper design of complex structures, taking into account also the excitation of emitters beyond the emission.
The synthesis method for bi-metallic quasishells has been demonstrated to be a cost-effective, reproducible, robust and versatile way of producing alloy or bimetallic nanostructures also if the miscibility between the two is low. AuAg quasishells are now being studied as biosensors in our group, and the studies on the magneto-plasmonic properties of the obtained shells are in progress. The ability of peeling the nanostructures from the substrate and the access to the bottom of the shells using NOA and RIE open new opportunities in the exploitation of the regions where the field enhancement is maximum.
Fractal aggregates can be obtained in a well controlled way using the proposed protocol. The techniques here used are cost effective, and quick, and can take advantage by a water-friendly, functionalization-affine chemestry of the obtained aggregates. The simultaneous presence of these two resonances opens up a lot of possibilities in anelastic spectroscopy, as the two peaks could be tuned one with the excitation and the other with the emission. On one hand, through the correlation control it is possible to tune the resonances towards this direction; on the other hand, the presence of a functionalization platform makes it easy to bind the desired analyte or sensitizer or emitter in the close proximity of the regions with highest field enhancement.

Bottomline

In the thesis a lot of techniques, both experimental and simulative have been used in coordination with the aim to design, synthesize, characterize, optimize and simulate innovative nanostructures. Plasmonics is nowadays a strongly investigated subset of nanophotonics and the comprehension of the basic physics involved is quite mature, even if new interesting branches are continuously developing, like magneto-plasmonics, chiral plasmonics or quantum plasmonics. Therefore, the research is more and more concentrated on the possible industrial applications. To this aim, part of the *best performing* laboratory samples requirements should

be relaxed to optimize costs yet not losing too performances; on the other hand, a profitable, innovative device should combine different aspects and effects to be efficient, and should be designed accurately, keeping in mind the fundamental role of symmetries in this task.
This is why there's more and more need of cooperation between all the available techniques, methods and procedures for the common effort of producing industrially-exploitable plasmonics. And this is the framework in which the present thesis has been devised and conducted, with the scope of designing nanostructures for the implementation in usable devices.

A. The Finite Elements Method

This appendix summarizes the formalism used to generate the system of equation that the solvers elaborate, starting from the partial differential equations of the modeled problem.

A.1. Finite Elements

The basic idea of finite elements is the possibility to approximate the dependent variables of the problem by a finite number of parameters called DOF. When this approximation is inserted in the set of equations to be solved, a new system of equation is generated for the degrees of freedom. This system is the one that will be solved by solvers. For simplicity, consider the case of a dependent variable defined by the 1-dimensional function $u = u(x)$, and linear elements. Suppose that the mesh is formed by only two mesh intervals, $0 < x < 1$ and $1 < x < 2$. Linear elemtents means that the function u is linear in each mesh interval. In this framework, the only parameters needed to define uniquely the function u are its values at the three nodes $x_1 = 0$, $x_2 = 1$ and $x_3 = 2$. Denoting these values as $U_1 = u(0)$, $U_2 = u(1)$ and $U_3 = u(2)$, U_1, U_2 and U_3 are the degrees of freedom of the problem. The function u can now be rewritten as:

$$u(x) = U_1\varphi_1(x) + U_2\varphi_2(x) + U_3\varphi_3(x), \tag{A.1}$$

where φ_i are a set of linear functions in the correponding intervals. Namely, $\varphi_i(x)$ is the linear function which is equal to 1 at the i^{th} node and is 0 at any other node. As an example,

$$\varphi_1(x) = \begin{cases} 1 - x & \text{if } 0 \leq x \leq 1 \\ 0 & \text{if } 1 \leq x \leq 2 \end{cases} \tag{A.2}$$

is such a function. The functions $\varphi_i(x)$ are called the *basis functions.* The set of functions $u(x)$ forms a vectorial function space called *finite element space.* An improvement in accuracy can be obtained if one uses *quadratic* elements instead of linear ones. This choice essentially corresponds to curved mesh elements, for which the curvature is defined. This also helps in the description of curved surfaces in the geometry. In this case, the $u(x)$ functions are second-order polynomials. The characterization of this kind of nodes can be accomplished by considering additional node points in the middle of each interval. In the case of previous example, $x_4 = 0.5$ and $x_5 = 1.5$. Also the corresponding degrees of freedom $U_i = u(x_i)$ must be introduced. At this point, the second-degree polynomial $u(x)$ is determined by the degrees of freedom:

$$u(x) = U_1\varphi_1(x) + U_2\varphi_2(x) + U_3\varphi_3(x) + U_4\varphi_4(x) + U_5\varphi_5(x), \tag{A.3}$$

where the basis functions $\varphi_i(x)$ are now quadratic on each mesh interval, and equal 1 at the i-th node and equal 0 at all other node points. One of such functions is

$$\varphi_1(x) = \begin{cases} (1 - x)(1 - 2x) & \text{if } 0 \leq x \leq 1 \\ 0 & \text{if } 1 \leq x \leq 2 \end{cases} \tag{A.4}$$

In general, a finite elements space can be defined by giving a set of basis functions. The descriptions of basis functions can be simplified by using the *local coordinates* or *element coordinates.* Consider a mesh element of dimension d, living in an n-dimensional geometry (whose space coordinates are $x_1, \ldots, x_n$). Consider also the *standard d-dimensional simplex*

$$\zeta_1 \geq 0, \zeta_2 \geq 0, \ldots, \zeta_d \geq 0, \zeta_1 + \ldots + \zeta_d \leq 1 \tag{A.5}$$

which resides in the local coordinate space parametrized by the local coordinates $\zeta_1, \ldots, \zeta_d$. In the case of $d = 1$, the simplex is the unit interval; when $d = 2$, it is an isosceles right triangle; if $d = 3$, the simplex is a thetrahedron. The mesh element may now be intended as a linear transformation of the standard simplex. Namely, if the global space coordinates x_i are suitable linear functions of the local coordinates, then the mesh element is the image of the standard simplex.

When described in terms of local coordinates, the basis functions assume one of a few basic shapes. These are called the *shape functions.* Considering the example of 1D, any basis function is one of the following:

$$\varphi = \zeta_1, \quad \varphi = 1 - \zeta_1, \quad \varphi = 0. \tag{A.6}$$

Because the null function is not counted as a shape function, the only two functions for linear 1D elements are the first two. In the case of quatratic elements, the (three) shape functions result:

$$\varphi = (1 - \zeta_1)(1 - 2\zeta_1), \quad \varphi = 4\zeta_1 (1 - \zeta_1), \quad \varphi = \zeta_1 (2\zeta_1 - 1). \tag{A.7}$$

A.2. Lagrange Elements

As said, the use of quadratic (and, generally, of order $k \geq 2$) elements corresponds to curved mesh elements. This correspondance is obtained by writing the global coordinates x_i as polynomials of order k in the local coordinates ζ_j. The order k is calles the *geometry shape order.* The use of curved elements helps in a more detailed description of (curved) boundaries of the geometry. However, inside domains (i.e. for mesh elements not touching boundaries), curved elements are not useful, so they are straight. It is customary to use the same order k here as for the order of the curved element. In this case, the elements are *isoparametric elements.*

The preceding examples are special cases of the *Lagrange element*, which can be defined in the following way. Consider a positive integer, k, which will be the order of the Lagrange element. The functions $u(x)$ are polynomials of degree k on each mesh element. As before, to describe this function, it is sufficients to give its values in the *Lagrange points* of order k. These are the points defined by the condition that their local coordinates are integer multiples of $1/k$. Consider the example of a triangluar mesh in 2D with $k = 2$. The node points are located at the corners and side midpoints of all mesh triangles. As before, for each of these node points p_i, a degree of freedom $U_i = u(p_i)$ and a basis function φ_i exist. The restriction of the basis function φ_i to a mesh elemtent is a polynomial of degree at most k in the local coordinates, with additional conditions that $\varphi_i = 1$ at the node i, and $\varphi_i = 0$ at all other nodes. Basis functions are contiuous and

$$u = \sum_i U_i \varphi_i. \tag{A.8}$$

The Lagrange element of order $k = 1$ is called the linear element. For $k = 2$, the element is referred at as the quadratic element. Though Lagrange elements can exist at any order, the available numerical integration algorithms practically limit the usefulness to orders $k \leq 5$. All the considered mesh in this work are Lagrange elements of suitable order, and always $k \leq 4$.

A.3. Discretization of the Equations

Once the finite elements are defined, the next step is the discretization of the (weak form of the) PDEs. Consider for simplicity a 2D problem, and its weak formulation as a starting point. The first task is the discretization of constraints (derived from the differential equation by using the Green's theorem and using the Neumann boundary conditions expression):

$$
\begin{aligned}
0 =& R^{(2)} \quad \text{on } \Omega && \text{(A.9)}\\
0 =& R^{(1)} \quad \text{on } B && \text{(A.10)}\\
0 =& R^{(0)} \quad \text{on } P, && \text{(A.11)}
\end{aligned}
$$

where Ω indicates the subdomains, B indicates the boundaries and P indicates the edges; starting with the constraints on the boundaries, B. For each element in B, i.e. each mesh edge in B, consider the Lagrange points of some order k, and denote them as $x_{mj}^{(1)}$, where m is the index of the mesh element. The discretization of constraits is at this point in the form:

$$
0 = R^{(1)}\left(x_{mj}^{(1)}\right), \tag{A.12}
$$

the constraints, thus, must hold pointwise at each Lagrange point. In the same way, the constraints on Ω and P can be reduced to equations that hold in the Lagrange points. These equations can be collected in one vectorial equation,

$$
0 = \mathbf{M}, \tag{A.13}
$$

and $\mathbf{M}$ consists of all the right-hands of the constraints A.9.
The dependant variables are approximated with functions in the chosen finite element space. So, the dependent variables are expressed in terms of the degrees of freedom in the form

$$
u_l = \sum_i U_i \varphi_i^{(l)}, \tag{A.14}
$$

where $\varphi_i^{(l)}$ are the basis functions for the variable u_l. Now define the vector $\mathbf{U}$, formed by the degrees of freedom U_i as its components. The $\mathbf{U}$ vector is called the *solution vector*. Additionally, $\mathbf{M}$ depends only on $\mathbf{U}$, thus the constraints can be written as

$$
0 = \mathbf{M}\left(\mathbf{U}\right). \tag{A.15}
$$

For what concerns the equations, consider the weak equation:

$$
0 = \int_\Omega W^{(2)} dA + \int_B \mathbf{W}^{(\mathbf{1})} \cdot d\mathbf{s} + \sum_P W^{(0)} - \int_\Omega v \cdot h^{(2)^T} \mu^{(2)} dA - \int_B v \cdot \mu^{(1)} \mathbf{h}^{(1)^T} \cdot d\mathbf{s} - \sum_P v \cdot h^{(0)^T} \mu^{(0)}, \tag{A.16}
$$

where v is a vector of test functions, h is derived from constraints using the relation $h_{ml}^{(d)} = \partial R_m^{(d)} / \partial u_l$ and the $\mu^{(i)}$ are the Lagrange multipliers. The integrands $W^{(n)}$ are scalar functions involving all the variables $u_1, u_2, ..., u_N$ and all the test functions $v_1, v_2, ..., v_N$. To discretize this equation, the dependent variables are expressed in terms of the degrees of freedom as just described. In a similar way, the *test functions* v are approximated with the same finite elements:

$$v_l = \sum_i V_i \varphi_i^{(l)}. \tag{A.17}$$

Given the linearity of the weak equation in the test functions, it is sufficient to require that the weak equation holds when the test functions are choosen as the basis functions:

$$v_l = \varphi_i^{(l)} \tag{A.18}$$

When the v_l in eq.A.18 are inserted in the weak equation (eq.A.16), a set of equations (one for each i) is defined. Now the Lagrange multipliers can be discretized. Define

$$\Lambda_{mj}^{(d)} = \mu^{(d)} \left(x_{mj}^{(d)} \right) w_{mj}^{(d)}, \tag{A.19}$$

where $x_{mj}^{(d)}$ are the Lagrange points and $w_{mj}^{(d)}$ are suitably chosen weights (see in the following). Now, the term

$$\int_B \varphi_i \cdot \mu^{(1)} \mathbf{h}^{(1)^\mathbf{T}} \cdot d\mathbf{s} \tag{A.20}$$

is approximated as a sum over all mesh elements in B. The contribution from the m mesh element is approximated as:

$$\sum_j \varphi_i \left(x_{mj}^{(1)} \right) \cdot h^{(1)^T} \left(x_{mj}^{(1)} \right) \mu^{(1)} \left(x_{mj}^{(1)} \right) w_{mj}^{(1)} = \sum_j \varphi_i \left(x_{mj}^{(1)} \right) \cdot h^{(1)^T} \left(x_{mj}^{(1)} \right) \Lambda_{mj}^{(1)}, \tag{A.21}$$

where $w_{mj}^{(1)}$ is the integral of $d\mathbf{s}$ over the appropriate part of the mesh element. In a similar way the integral over Ω and the sum over P can be approximated.
In summary, the discretization of the weak equation can be written as

$$0 = \mathbf{L} - N_F \mathbf{\Lambda}, \tag{A.22}$$

where the vector $\mathbf{L}$, called *residual vector*, has the i-th component formed by

$$\int_\Omega W^{(2)} dA + \int_B \mathbf{W}^{(\mathbf{1})} \cdot d\mathbf{s} + \sum_P W^{(0)} \tag{A.23}$$

evaluated for $v_l = \varphi_i^{(l)}$. Λ is a vector containing all the discretized Lagrange multipliers $\Lambda_{mj}^{(d)}$. N_F is a matrix, called *constraint force Jacobian matrix*, whose i-th row is a concatenation of the vectors

$$\varphi_i \left(x_{mj}^{(d)} \right) h^{(d)} \left(x_{mj}^{(d)} \right)^T. \tag{A.24}$$

Finally, the discretization of the stationary problem results

$$\left\{ \begin{array}{l} 0 = \mathbf{L}\left(\mathbf{U}\right) - N_F\left(\mathbf{U}\right)\mathbf{\Lambda} \\ 0 = \mathbf{M}\left(\mathbf{U}\right). \end{array} \right. \tag{A.25}$$

The objective is to solve this system for the solution vector $\mathbf{U}$ and the Lagrange multiplier vector $\mathbf{\Lambda}$.

B. Fractals

This appendix contains some simple results and techniques about fractals used in the thesis. According to a loose description of fractals given by Falconer [216], a set F may be regarded as a fractal if:

i) F has a fine structure, i.e. detail on arbitrarily small scales.

ii) F is too irregular to be described by traditional geometrical language, both locally and globally.

iii) Often F has some form of self-similarity, perhaps approximate or statistical.

iv) Usually, the "fractal dimension" of F (defined in some way) is greater than its topological dimension

v) In most cases, F is defined in a very simple way, perhaps recursively.

B.1. Fractal Classification

Classification of fractal is not unique. In fact there are many possibilities for classifying fractals, based, for example, on their characteristics (*self-similarity*, *self-affinity*, *fractal dimension...*) or on the way a fractal is built (algorithm, iteration of function, evolution of a chaotic system, random walks...). In this thesis on one hand particularly self-similar fractal are regarded, and fractal dimension is considered a parameter of the system. On the other hand, for physical applications the fabrication method is central, so fractals will be subdivided due to the way they are obtained.

Iterated function systems The simplest way of obtaining a fractal is to give an algorithm that, applied recursively, gives the fractal. This is a geometric method, in which a set of rules are exploited to proceed to the following step, starting from a simple figure, such as a line or a circle. A true fractal is obviously obtained in this way only in the limit for infinite steps.
Being strictly defined by the substitution rules and the starting point, these fractals exhibit the strongest self-similarity properties, as they are *exactly identical* at different scales. Often substitution rules also define the *fractal dimension* and the *internal ratio*. Examples of these fractals are Cantor Set, Sierpinski carpet, Sierpinski gasket, Menger sponge, Koch Curve.

Escape-time fractals In this case a convenient function is defined on the whole space in the whole space (often the complex plane, $f : \mathbb{C} \to \mathbb{C}$) and then it is iterated many times on each point. Depending on the starting point, the result of the application of the function may be *close* or not to the starting point after a number of iterations. In the limit for infinite iterations, the set of points for which the result remains close to the starting point forms a fractal.

In this kind of fractals, self-similarity is loose, as at different scales the system may be slightly distorted. This property is called *Quasi-self-similarity.*
The most famous examples of these fractals are Mandelbrot Sets and Julia Sets.

Random fractals Whereas the fractals just considered are deterministic, random fractals are obtained by stochastic processes, for example by adding a random number to iteration of a map on each step. Trajectories of Brownian Motion are an example of such a fractal. As these fractals are the result of a random process, self-affinity in this case is still weaker, and is present only statistically, that is, some kind of statistical measure is conserved under scale transformations.
A very interesting kind of random fractal for this thesis is the so-called Brownian Tree, because it is the result of a physical process known as diffusion-limited aggregation, which can be exploited in a fairy simple way for fractal structures production.

Strange attractors Strange attractors can be obtained by the orbit of initial-value differential equations, when these are non linear. In fact, an Hamiltonian system that is not integrable can take to a strange attractor, when numerical solutions are followed in their orbits.
Strange attractors characterise many chaotic systems in nature, an example is given by meteorology, in which, the so-called Lorenz Attractor comes out, even when considering extremely simplified systems with only few variables. The so-called logistic map, i.e. evolution of a system with disctretised time steps, is also a fractal of this kind.

B.2. Fractal Mathematics

As noted before, fractals may be very irregular, so there aren't much parameters that may characterise any kind of fractal. In these terms, two interesting quantities are *fractal dimension* and *internal ratios.*

B.2.1. Fractal Dimension

One of the characteristics of a fractal is, as previously pointed out, that it often has a fractal dimension grater than the topological one. It's then necessary to define such a dimension, and although there are more than one choice, here Hausdorff dimension will be considered. Its advantages are that it's defined through measures, and that it's in general defined for every set. To define the Hausdorff measure, consider a family of non-empty subsets of $\mathbb{R}^n$, $\{U_i\}$. If $\{U_i\}$ is countable, the diameter of each U_i is $\leq \delta$, and it covers F, then $\{U_i\}$ is said to be a δ-cover of F. Now suppose that F is a subset of $\mathbb{R}^n$, and that s is a non-negative number. It's then defined the function

$$\mathcal{H}^s_\delta (F) = \inf \left\{ \sum_{i=1}^{\infty} |U_i|^s : \{U_i\} \text{ is a } \delta\text{-cover of } F \right\}. \tag{B.1}$$

Taking the limit for $\delta \to 0$, the number of δ-covers decreases, and $\mathcal{H}^s_\delta (F)$ approaches to a limiting value (usually 0 or ∞. This limit is called *s-dimensional Hausdorff measure*:

$$\mathcal{H}^s (F) = \lim_{\delta \to 0} \mathcal{H}^s_\delta (F). \tag{B.2}$$

One can show that in a graph of $\mathcal{H}^s$ against s, there's a critical value of s for which $\mathcal{H}^s$ jumps from ∞ to 0. That value of s is the *Hausdorff dimension*, formally:

Definition B.2.1. The Hausdorff dimension of a set $F \subseteq \mathbb{R}^n$ is

$$\dim_{\mathrm{H}}(F) = \inf\{s \geq 0 : \mathcal{H}^s(F) = 0\} = \sup\{s : \mathcal{H}^s(F) = \infty\}. \tag{B.3}$$

Unfortunately, exact calculation of Hausdorff dimension is in general very complex, both analytically and computationally. An approximate method is then necessary to handle fractals. One of these methods is called *box counting*, and provides a simple way to calculate the dimension of a fractal using a computer. As these calculations are made on *finite* sets of points (given finite processing resources), most problems with box counting dimension are avoided. It's however very important to check whether discretisation process can have effects on dimension. For fractals considered in this thesis box-counting and Hausdorff are equivalent.

Definition B.2.2. The lower and upper box-counting dimension of a subset F of $\mathbb{R}^n$ are given by

$$\underline{\dim}_B F = \underline{\lim}_{\delta \to 0} \frac{\log N_\delta(F)}{-\log \delta} \tag{B.4}$$

$$\overline{\dim}_B F = \overline{\lim}_{\delta \to 0} \frac{\log N_\delta(F)}{-\log \delta}, \tag{B.5}$$

and the box-counting dimension is

$$\dim_B F = \lim_{\delta \to 0} \frac{\log N_\delta(F)}{-\log \delta} \tag{B.6}$$

(if this limit exists), where $N_\delta(F)$ is any of the following:

i) the smallest number of closed balls of radius δ that cover F;

ii) the smallest number of cubes of side δ that cover F;

iii) the number of δ-mesh cubes that intersect F;

iv) the smallest number of sets of diameter at most δ that cover F;

v) the largest number of disjoint balls of radius δ with centres in F;

For practical purposes, the third definition of $N_\delta(F)$ will be used to compute the box-counting dimension, as it's straightforward to sub-divide the space with lattices finer and finer (fig. B.1). In fact, it is sufficient to consider limits in B.6 as δ tends to 0 through a decreasing sequence such as $\delta_k = c^k$, with $0 < c < 1$. So, one can consider successive steps in which grid spacing is half the one in preceding step.

Figure B.1.: A set F and sub-division with two successive δ-meshes.

In physical analysis exact fractal don't exist, as, at least on atomic scales, fine details are lost. It's then important, especially when dealing with nano scales, to find a "cut-off" scale, below which details are not considered. Because box-counting dimension will be used, it's sufficient to evaluate how good is to approximate a theoretical fractal F with the physical, finite set of points E. If d is the Hausdorff distance and $d(E,F) \leq \varepsilon$, then the limit on δ considered in def. B.2.2 results $\delta > \varepsilon$. So, if the lower scale controlled when fabricating a sample is ε, then box counting can be stopped when $\delta \leq \varepsilon$. To obtain the determination of $\dim_B$, it then suffices to make a log-log plot of $\log N_\delta(F)$ against $-\log\delta$, and to make a linear fit: the slope is the Box Counting Dimension.

B.2.2. Internal Ratio

Unlike Hausdorff dimension, internal ratios are not generally defined for every fractal. Moreover it's easy to compute these ratios only for iterated function fractals, whose algorithm embeds the necessary information. However, when using fractals with a well defined internal ratio, it may be interesting to look for its influences on the results.
Consider a transformation $T(\lambda), \lambda \in \mathbb{R}^+$. $T : \mathbb{R}^n \to \mathbb{R}^n$ is a scale transformation on the set F if $T(\lambda)[\vec{x}] \mapsto \lambda\vec{x}$, i.e. every length is multiplied by λ. Self-similarity is then the properties for which $T(\lambda)[F] = F$, except for a roto-translation.

Definition B.2.3. The positive real number r_i is an internal ratio of the set F if $T(r_i)[F] = F$, except for a roto-translation, i.e. it is self-similar under a scale transformation of magnitude r_i.

It's clear that if λ is an internal ratio of F, so are $\lambda^{\pm n}$ too, for $n \in \mathbb{N}$. It's straightforward to find the internal ratio constructing a fractal from an algorithm, e.g. the Cantor set has the fundamental internal ratio $\lambda = \frac{1}{3}$, the Sierpinski gasket has $\lambda = \frac{1}{2}$, the Koch curve has also $\lambda = \frac{1}{3}$, as shown by figure B.2

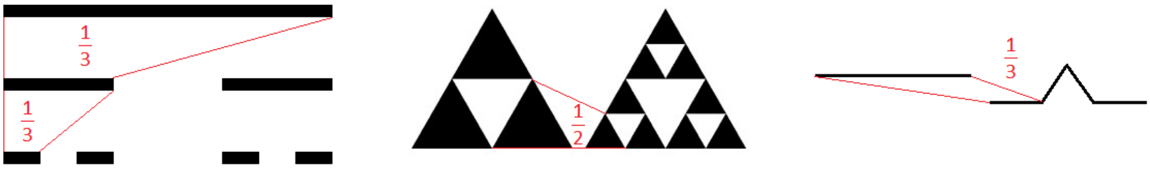

(a) Cantor set **(b)** Sierpinski gasket **(c)** Koch Curve

Figure B.2.: Internal ratios of three fractals.

B.2.3. Selected Deterministic Fractals

In this section the three deterministic fractals used in the thesis will be reviewed.

2D Cantor Dust Set

The 2D Cantor Dust Set is created starting from a square. At each step the square is divided in nine identical squares, whose side is one third of the side of the original one. Then, the squares in the middle of the sides and in the centre are removed, and the same operation is iterated in subsequent steps for the remaining squares. Fig. B.3 shows the first five steps of the construction of the Cantor Dust set in two dimensions. The Cantor Dust Set internal ratio is $\lambda = \frac{1}{3}$, and the Hausdorff dimension is $\dim_{\mathrm{H}} = \log 4/\log 3 \approx 1.262$.

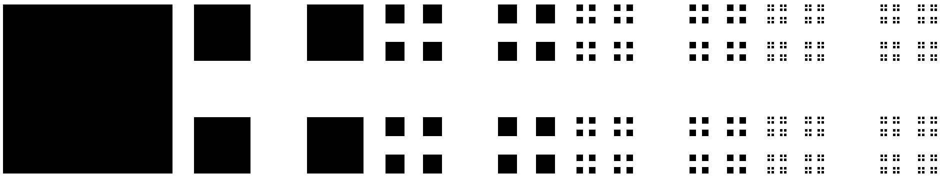

Figure B.3.: First steps of the 2D Cantor Dust Set.

Cantor Box

The Cantor Box is created starting from a square. At each step the square is divided in nine identical squares, whose side is one third of the side of the original one. Then, the squares over, under, at the left and at the right with respect to central one are removed, and the same operation is iterated in subsequent steps for the remaining squares. Fig. B.4 shows the first five steps of the construction of the Cantor Dust set in two dimensions. The Sierpinski Carpet internal ratio is $\lambda = \frac{1}{3}$, and the Hausdorff dimension is $\dim_{\mathrm{H}} = \log 5/\log 3 \approx 1.484$.

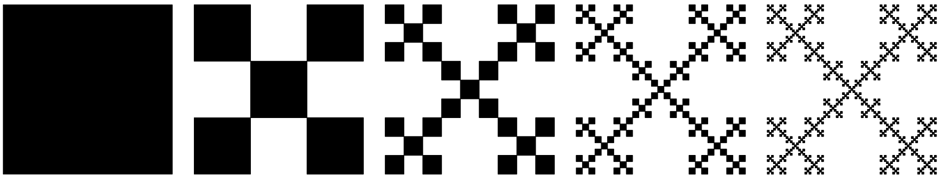

Figure B.4.: First steps of the Cantor Box.

Sierpinski Carpet

The Sierpinski Carpet is created starting from a square. At each step the square is divided in nine identical squares, whose side is one third of the side of the original one. Then, the central square is removed, and the same operation is iterated in subsequent steps for the remaining squares. Fig. B.5 shows the first five steps of the construction of the Cantor Dust set in two dimensions. The Sierpinski Carpet internal ratio is $\lambda = \frac{1}{3}$, and the Hausdorff dimension is $\dim_{\mathrm{H}} = \log 8/\log 3 \approx 1.893$.

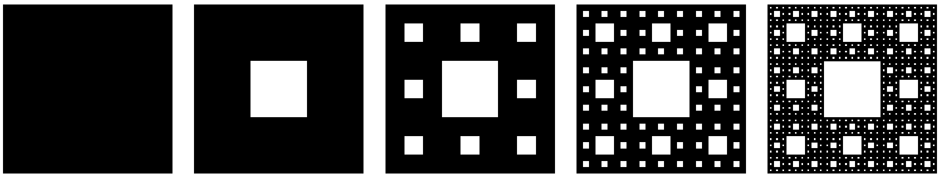

Figure B.5.: First steps of the Sierpinski Carpet.

B.3. Random Fractals

B.3.1. Brownian Motion

Mesoscopic particles suspended on a liquid moves on highly irregular trails, due to the bombardment of the fluid molecules. A simple model for such a phenomenon is that of Brownian motion, which considers this process as stochastic. Moreover, a critical hypothesis is that any "step" should be done randomly, i.e. it should be totally uncorrelated form preceding ones. If $f(t) : \mathbb{R} \to \mathbb{R}^n$ is the position in the space of a particle at time t, both the *trail* $\{f(t) : t_1 \leq t \leq t_2\} \subset \mathbb{R}^n$ and its *graph* $\{(t, f(t)) : t_1 \leq t \leq t_2\} \subset \mathbb{R} \times \mathbb{R}^n$ are fractals.
A model in one dimension may be constructed by considering a random walk, i.e. a process in which at each step the position of a particle on the real line may be incremented or decremented by a unity, and the two cases are equally probable. When the times between steps and the increments become infinitesimal, the limit for a Brownian Motion is reached. A formal definition of a Brownian Motion is:

Definition B.3.1. The Brownian Motion is a random process X such that:

i) with probability 1, $X(0) = 0$, and $X(t)$ is a continuous function of t;

ii) for every $t \geq 0$ and every $h > 0$ the increment $X(t+h) - X(t)$ is normally distributed with mean 0 and variance h, thus

$$\mathbf{P}(X(t+h) - X(t) \leq x) = \frac{1}{\sqrt{2\pi h}} \int_{-\infty}^{x} \exp\left(\frac{-u^2}{2h}\right) \mathrm{d}u; \tag{B.7}$$

iii) if $0 \leq t_1 \leq t_2 \leq \cdots \leq t_{2m}$, the increments $X(t_2) - X(t_1)$, $X(t_4) - X(t_2)$, $X(t_{2m}) - X(t_{2m-1})$ are independent.

In general it's possible to define an n-dimensional Brownian Motion:

Definition B.3.2. A process $X : [0, +\infty) \to \mathbb{R}^n$ given by $X(t) = (X_1(t), \cdots, X_n(t))$ is a n-dimensional Brownian Motion if the random process $X_i(t)$ is a 1D Brownian Motion and $X_1(t_1), \cdots, X_n(t_n)$ are independent for all sets of times $t_1, \cdots, t_n$.

An n-dimensional Brownian Motion is isotropic, as follows immediately by the definition. It's very useful to know the dimension of a Brownian Motion trail:

Proposition B.3.3. *With probability 1, a Brownian trail in $\mathbb{R}^n$ ($n \geq 2$) has Hausdorff dimension and box dimension equal to* 2

Proof. Omitted. □

For simulation purposes, the possibility to obtain random fractals via Brownian Motion is very interesting, and there is also a generalisation to Brownian Motion, called Fractional Brownian Motion, which permits to modulate the dimensions.

Definition B.3.4. The Fractional Brownian Motion is a random process X such that:

i) with probability 1, $X(0) = 0$, and $X(t)$ is a continuous function of t;

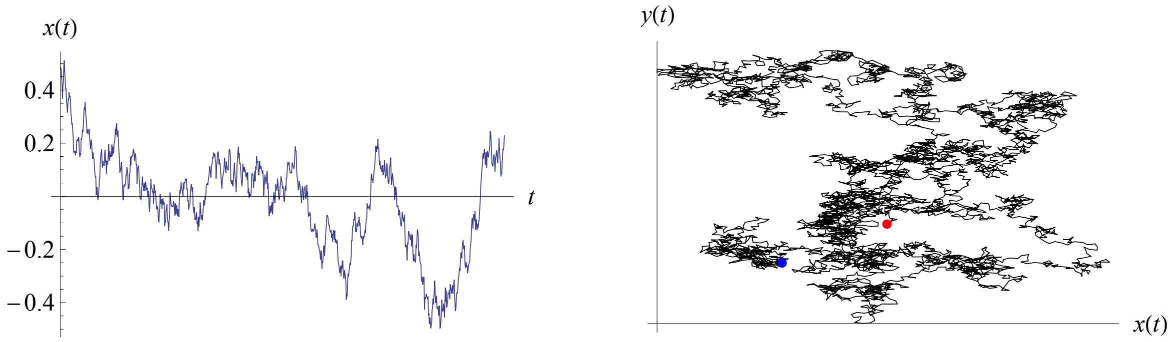

(a) 1-D B.M. Graph **(b)** 2-D B.M. Trail

Figure B.6.: Brownian Motions.

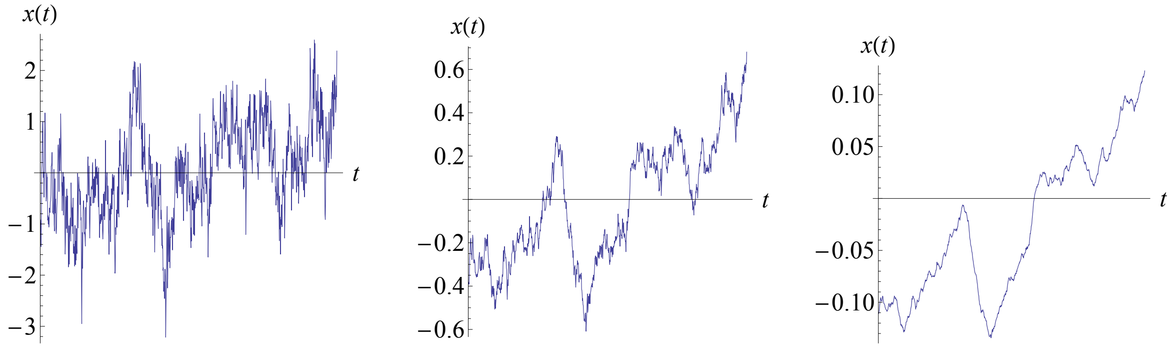

(a) $\alpha = 0.1$ **(b)** $\alpha = 0.5$ (classic BM) **(c)** $\alpha = 0.9$

Figure B.7.: Fractional Brownian Motions.

ii) for every $t \geq 0$ and every $h > 0$ the increment $X(t+h) - X(t)$ is normally distributed with mean 0 and variance $h^{2\alpha}$, thus

$$\mathbf{P}\left(X(t+h) - X(t) \leq x\right) = \frac{1}{h^{\alpha}\sqrt{2\pi}} \int_{-\infty}^{x} \exp\left(\frac{-u^2}{2h^{2\alpha}}\right) \mathrm{d}u. \tag{B.8}$$

Proposition B.3.5. *A Fractional Brownian trail in* $\mathbb{R}^n$ $(n \geq 2)$ *and* $t \in E \subseteq \mathbb{R}$ *has Hausdorff dimension and box dimension equal to:*

$$\dim_{\mathrm{H}} X(E) = \min\left(n, \frac{1}{\alpha} \dim E\right) \tag{B.9}$$

Proof. Omitted. □

In the typical case of a F.B.M. on a plane, $n = 2$, and $\dim E = 1$, it is possible to obtain, for $\alpha > \frac{1}{2}$, sets of dimension < 2.

B.3.2. Diffusion Limited Aggregation

In nature there exist many examples of *fractal growth*, but for most of them a mathematical model is by far too difficult. Some of them, however have a pretty simple explanation, given by *Diffusion Limited Aggregation*. Consider a solution of copper sulfate $(CuSO_4)$

placed on a dish. Then a cathode is suspended in the centre of the dish and a strip of metal is curved around it, to form an anode. Applying a potential of a few volts it's possible to have electrolysis, and the result is the growth of a *dentritic* structure of copper, whose geometry is fractal. This happens because when a copper sulfate molecule dissociates ($CuSO_4 \rightarrow Cu^+ + SO_4^-$), the copper ion follows a random trail until ti recombines or it enters in contact with the copper structure already formed. Because the point of contact is random, the formed fractal is a random fractal. Figure B.9a shows the result of a DLA process. A simple model takes in account a square lattice, in which ions can only make steps left, right, up or down, each direction having probability $\frac{1}{4}$. In the centre there is the cathode, the first seed of the structure, and the corresponding box in fig.B.9b is blackened. A large circle is then tracked around the cathode, and a copper sulfate molecule is supposed to dissociate on the circumference of this circle. As this happens, the positive ion Cu^+ follows a random walk, and there are two possibilities. The ion may exit from the circle, and then it recombines, or follows the random walk until it comes in contact with the cathode. In this case the ion gets an electron from the cathode and settles in that point. As more and more particles settle, the radius of the circle is conveniently increased (corresponding to an enlargement of the region with a small concentration of copper sulfate due to dissociation), and the structure can grow. The result of this model is represented in fig.B.8. The fractal dimension of a DLA fractal may be measured via box-counting. In general, for many physical phenomena involving this kind of growth, the dimension is about 1.4 to 1.7.

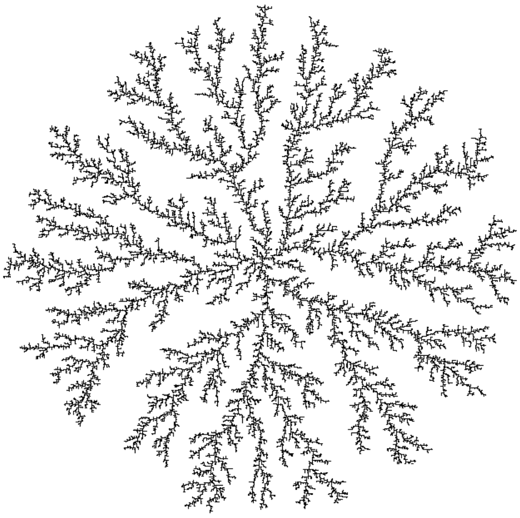

Figure B.8.: The result of a DLA process.

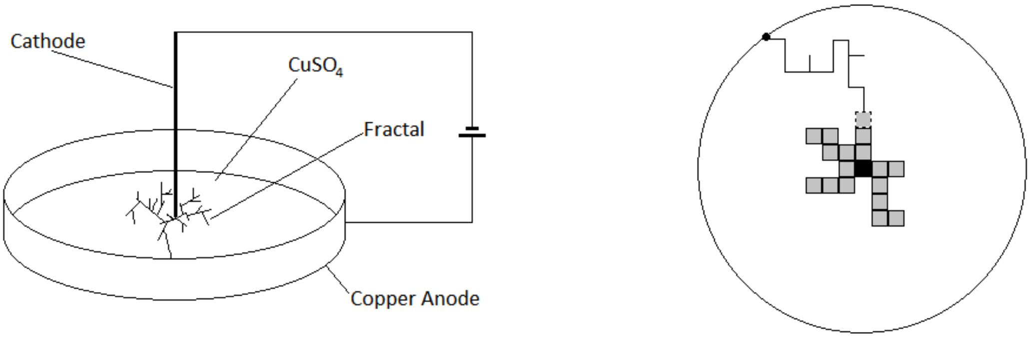

(a) A way of producing a Fractal Growth **(b)** Diffusion Limited Aggregation Model

Figure B.9.: Diffusion Limited Aggregation

C. Wolfram Mathematica Codes

In this appendix the codes used in Wolfram Mathematica are reported. The code works with Wolfram Mathematica 9.0.

C.1. Mie-Type Codes

The built-in definition of bessel functions makes Wolfram Mathematica an ideal tool to study the Mie scattering. In the next codes, the metal properties are modelized by their complex refractive index. Thus, a definition of the function `nn[j,`λ`]` should be made so that $nn[[1,\lambda]] = n[\lambda]$ is the wavelength-wise refractive index function for gold, $nn[[2,\lambda]] = n[\lambda]$ for silver, $nn[[3,\lambda]] = n[\lambda]$ for copper and so on for the wanted materials.
The first task is the definition of the parameters:

```
m[lambda_, j_, nm_] := nn[j, lambda]/nm;
k[lambda_, nm_] := (2 \[Pi] nm)/lambda;
x[lambda_, R_, nm_] := (2 \[Pi] nm R)/lambda; c =
 299792458 10^9;
```

Definition of the Bessel Functions and derivatives:

```
psi[n_, z_] :=  z Sqrt[\[Pi] /(2 z)]  BesselJ[(n + 1/2), z ];

psiPrime[n_, z_] := Evaluate[D[ psi[n, z], z]] ;

eta[n_, z_] := psi[n, z] +
   I z Sqrt[\[Pi] /(2 z)]  BesselY[(n + 1/2), z ] ;

etaPrime[n_, z_] := Evaluate[D[ eta[n, z], z]];

xi[n_, z_] := z Sqrt[\[Pi] /(2 z)] HankelH1[(n + 1/2), z ] ;

xiPrime[n_, z_] := Evaluate[D[ xi[n, z], z]];
chi[n_, z_] := - z Sqrt[\[Pi] /(2 z)]  BesselY[(n + 1/2), z ] ;

chiPrime[n_, z_] := Evaluate[D[ chi[n, z], z]];
```

C.1.1. Sphere in Medium

Definition of the Mie Coefficients:

```
a[lambda_, R_, j_, n_, L_] :=
 (m[lambda, j, n] psi[L,
    m[lambda, j, n] x[lambda, R, n]] psiPrime[L,
    x[lambda, R, n]] - psi[L, x[lambda, R, n]] psiPrime[L,
     m[lambda, j, n] x[lambda, R, n]])/(
  m[lambda, j, n] psi[L,
    m[lambda, j, n] x[lambda, R, n]] etaPrime[L,
```

```
    x[lambda , R, n]] - eta[L, x[lambda , R, n]] psiPrime[L,
     m[lambda , j, n] x[lambda , R, n]])

b[lambda_ , R_ , j_ , n_ , L_] :=
 (psi[L, m[lambda , j, n] x[lambda , R, n]] psiPrime[L,
    x[lambda , R, n]] -
  m[lambda , j, n] psi[L, x[lambda , R, n]] psiPrime[L,
    m[lambda , j, n] x[lambda , R, n]])/(psi[L,
    m[lambda , j, n] x[lambda , R, n]] etaPrime[L,
    x[lambda , R, n]] -
  m[lambda , j, n] eta[L, x[lambda , R, n]] psiPrime[L,
    m[lambda , j, n] x[lambda , R, n]])
```

The Mie Cross sections for a (metal) sphere in a non-dispersive medium can be computed as a function of the light wavelength `lambda`, radius `R`, medium refractive index `n`, metal `j` (according to the definitions of the refractive index, as previously pointed out), and summing `L` multipoles:

```
sigmaext[lambda_ , R_ , n_ , j_ , L_] := (
  2 \[Pi])/(k[lambda ,
    n])^2 Sum[(2 i + 1) Re[
     a[lambda , R, j, n, i] + b[lambda , R, j, n, i]], {i, 1, L}]
sigmasca[lambda_ , R_ , n_ , j_ , L_] := (
  2 \[Pi])/(k[lambda ,
    n])^2 Sum[(2 i + 1) (Abs[a[lambda , R, j, n, i]^2] +
      Abs[b[lambda , R, j, n, i]^2]), {i, 1, L}]
sigmaabs[lambda_ , R_ , n_ , j_ ,
  L_] := sigma[L, lambda , R, j, n] - sigmas[L, lambda , R,
   j, n]
```

C.1.2. Core-Shell

Definition of the additional parameters `m1` (ratio between the metal refractive index and the medium refractive index), `m2` (ratio between the coating refractive index and the medium refractive index) and the respective wavevectors `k1` and `k2`:

```
m1[j_ , lambda_ , nm_] := nn[j, lambda]/nm;
m2[nm_ , ns_] := ns/nm;
k1[nm_ , lambda_ , R_] := (2 \[Pi] nm)/lambda R  ;
k2[nm_ , lambda_ , R_ , d_] := (2 \[Pi] nm)/lambda (R + d);
```

Definition of the Mie Coefficients for the sphere:

```
An[lambda_ , R_ , d_ , j_ , nm_ , ns_ , l_] := (
 m2[nm, ns] psiPrime [ l,
    m1[j, lambda , nm] k1[nm, lambda , R]] psi[l,
    m2[nm, ns] k1[nm, lambda , R]] -
  m1[j, lambda , nm] psi[l,
    m1[j, lambda , nm] k1[nm, lambda , R]] psiPrime[ l,
    m2[nm, ns] k1[nm, lambda , R]])/(
 m2[nm, ns] psiPrime [ l,
    m1[j, lambda , nm] k1[nm, lambda , R]] chi[l,
    m2[nm, ns] k1[nm, lambda , R]] -
  m1[j, lambda , nm] psi[l,
    m1[j, lambda , nm] k1[nm, lambda , R]] chiPrime[ l,
    m2[nm, ns] k1[nm, lambda , R]])
```

```
Bn[lambda_, R_, d_, j_, nm_, ns_, l_] := (
 m2[nm, ns] psiPrime [ l, m2[nm, ns] k1[nm, lambda, R]] psi[
    l, m1[j, lambda, nm] k1[nm, lambda, R]] -
  m1[j, lambda, nm] psi[l,
    m2[nm, ns] k1[nm, lambda, R]] psiPrime[ l,
    m1[j, lambda, nm] k1[nm, lambda, R]])/(
 m2[nm, ns] chiPrime [ l, m2[nm, ns] k1[nm, lambda, R]] psi[
    l, m1[j, lambda, nm] k1[nm, lambda, R]] -
  m1[j, lambda, nm] chi[l,
    m2[nm, ns] k1[nm, lambda, R]] psiPrime[ l,
    m1[j, lambda, nm] k1[nm, lambda, R]]);
```

and for the shell:

```
anc[lambda_, R_, d_, j_, nm_, ns_, l_] :=
 (psi[l,
    k2[nm, lambda, R,
     d]] (psiPrime[ l, m2[nm, ns] k2[nm, lambda, R, d]] -
     An[lambda, R, d, j, nm, ns, l] chiPrime[ l,
       m2[nm, ns] k2[nm, lambda, R, d]]) -
  m2[nm, ns] psiPrime[ l,
    k2[nm, lambda, R,
     d]] (psi[l, m2[nm, ns] k2[nm, lambda, R, d]] -
     An[lambda, R, d, j, nm, ns, l] chi[ l,
       m2[nm, ns] k2[nm, lambda, R, d]]))/(xi[l,
    k2[nm, lambda, R,
     d]] (psiPrime[ l, m2[nm, ns] k2[nm, lambda, R, d]] -
     An[lambda, R, d, j, nm, ns, l] chiPrime[ l,
       m2[nm, ns] k2[nm, lambda, R, d]]) -
  m2[nm, ns] xiPrime[ l,
    k2[nm, lambda, R,
     d]] (psi[l, m2[nm, ns] k2[nm, lambda, R, d]] -
     An[lambda, R, d, j, nm, ns, l] chi[ l,
       m2[nm, ns] k2[nm, lambda, R, d]]))
bnc[lambda_, R_, d_, j_, nm_, ns_, l_] :=
 (m2[nm, ns] psi[l,
    k2[nm, lambda, R,
     d]] (psiPrime[ l, m2[nm, ns] k2[nm, lambda, R, d]] -
     Bn[lambda, R, d, j, nm, ns, l] chiPrime[ l,
       m2[nm, ns] k2[nm, lambda, R, d]]) -  psiPrime[ l,
    k2[nm, lambda, R,
     d]] (psi[l, m2[nm, ns] k2[nm, lambda, R, d]] -
     Bn[lambda, R, d, j, nm, ns, l] chi[ l,
       m2[nm, ns] k2[nm, lambda, R, d]]))/(
 m2[nm, ns] xi[l,
    k2[nm, lambda, R,
     d]] (psiPrime[ l, m2[nm, ns] k2[nm, lambda, R, d]] -
     Bn[lambda, R, d, j, nm, ns, l] chiPrime[ l,
       m2[nm, ns] k2[nm, lambda, R, d]]) - xiPrime[ l,
    k2[nm, lambda, R,
     d]] (psi[l, m2[nm, ns] k2[nm, lambda, R, d]] -
     Bn[lambda, R, d, j, nm, ns, l] chi[ l,
       m2[nm, ns] k2[nm, lambda, R, d]]))
```

The cross sections are computed similarly to the isolated sphere case, as a function of the light wavelength `lambda`, radius `R`, the shell refractive index `ns`, the shell thickness `d`, the medium refractive index `n`, metal `j` (according to the definitions of the refractive index, as previously pointed out), and summing L multipoles:

```
 sigmacext[L_, lambda_, R_, d_, j_, n_, ns_] := (
  2 \[Pi])/(k[lambda,
    n])^2 Sum[(2 i + 1) Re[
     anc[lambda, R, d, j, n, ns, i] +
      bnc[lambda, R, d, j, n, ns, i]], {i, 1, L}]
sigmacsca[L_, lambda_, R_, d_, j_, n_, ns_] := (
  2 \[Pi])/(k[lambda,
    n])^2 Sum[(2 i + 1) (Abs[anc[lambda, R, d, j, n, ns, i]^2] +
      Abs[bnc[lambda, R, d, j, n, ns, i]^2]), {i, 1, L}]
sigmacabs[L_, lambda_, R_, d_, j_, n_,
  ns_] := sigmac[L, lambda, R, d, j, n, ns] - sigmacs[
   L, lambda, R, d, j, n, ns]
```

An interactive graphic can be obtained using the following code:

```
Manipulate[
 Plot[sigma[lambda, R, n, j, L, n]/(\[Pi] R^2), {lambda, 200,
    1500}, PlotRange -> All,
  ImageSize -> 800], {{j, 1,
   "Material: 1-Gold; 2-Silver; 3-Copper"}, {1, 2, 3}}, {{L, 1,
   "Multipoles"}, {1, 2, 3, 4, 5, 6, 7, 8, 9, 10}}, {{R,
   10, "Radius"}, 1, 1000}, {{n, 1.5, "Medium Refractive Index"}, 1,
  5}]
```

C.2. Lifetimes Modifications due to the Interaction with Films

The lifetimes modifications due to the interaction with films, as formulated in section 3.3, can be computed using the followind code.
Definition of parameters (lengths in nanometres):

```
lambda = 1540; n1 = Sqrt[2.09]; epsilon1 = n1^2;
epsilon2 = -115.571 + I*9.59558;
f0 = 1; z0 = 75; z1 = 0; zf = 500; Gamma0 = 70;
a1 = -I*Sqrt[1 - u^2]; a2 = -I*Sqrt[epsilon2/epsilon1 - u^2];
Rt = (a1 - a2)/(a1 + a2);
Rp = (epsilon1*a2 - epsilon2*a1)/(epsilon1*a2 + epsilon2*a1);
```

Definition of the transverse decay rate as a function of the distance from the film z:

```
gammat[z_, Gamma0] := Gamma0*(1 + 3/4 Im[NIntegrate[
  Rp*u^3/a1*Exp[-4 \[Pi] n1 a1 z/lambda], {u, 0, +\[Infinity]},
PrecisionGoal -> 5, MaxRecursion -> 50, AccuracyGoal -> 5]])
```

parallel decay rate:

```
gammap[z_, Gamma0] := Gamma0*(1 - 3/2 Im[NIntegrate[
  ((1 - u^2)*Rp + Rt)*u/a1*Exp[-4 \[Pi] n1 a1 z/lambda], {u, 0, +\[Infinity]},
PrecisionGoal -> 5, MaxRecursion -> 50, AccuracyGoal -> 5]])
```

and total decay rate:

```
gammap[z_, Gamma0] := Gamma0*(1+
1/2 NIntegrate[Im[(-Rp*u^3/a1+((1-u^2)*Rp+Rt)*u/a1)*
Exp[-4\[Pi] n1 a1 z/lambda]],{u,0,+\[Infinity]},
PrecisionGoal->4,MaxRecursion->100,AccuracyGoal->4])
```

Integrating the decay rates over the whole emitters distribution $f(z)$ the photoluminescence spectrum is found:

```
 IC[t_, Gamma0] :=
 NIntegrate[f[z] * Exp[-N[gamma[z, Gamma0]]*t], {z, z0, z1},
   PrecisionGoal -> 5, MaxRecursion -> 50,
   AccuracyGoal -> 5]/
 NIntegrate[f[z], {z, z0, z1}]
```

where `z0` is the distance below which the distribution $f(z)$ is neglectable and `z1` is the distance over which the distribution $f(z)$ is neglectable. The lifetime can now be computed using a fit to the exponential decay function of the signal:

```
intsf = Table[{t, IC[t, 1, 0, 100]}, {t, 0, 5, 0.05}];
tautot = 1/(gamma) /. FindFit[intsf, A*Exp[-(x*gamma)]
+ y0, {{A, 1}, {gamma, 1}, {y0, 0}}, x]
```

C.3. Fractals

C.3.1. Box Counting Routine

The routine `dimbox[fractal,n]`gives the Box Dimension (cf. B.2.2 of a set named `fractal`. The number of steps is n, and the factor scale for δ-meshes is 2.

```
dimbox[myset_,steps_] :=
 Fit[Table[{Log[m], Log[M[m, myset]]}, {m, 2, steps}], {1, x}, x];
dimensione = D[dimbox[insieme], x]
```

C.3.2. 2D Cantor Dust Set

The following code generates the first six steps of the 2D Cantor Dust Set:

```
Quadrato[{v_, l_}] := {v, v + {l, 0}, v + {l, l}, v + {0, l}};
CDust[{v_, l_}] :=
  Delete[Flatten[
    Table[{v + {(n l)/3, (m l)/3}, l/3}, {n, 0, 2}, {m, 0, 2}],
    1], {{2}, {4}, {5}, {6}, {8}}];
CDust2[lista_] := Flatten[Map[CDust, lista], 1];
SierCarpet[v_, l_, n_] := Nest[CDust2, CDust[{v, l}], n];
Particle2D[{a_, b_, c_, d_}] :=
  Rectangle[5/6 a + 1/6 c, 5/6 c + 1/6 a];
DustC[v_, l_, n_] :=
  Graphics[Map[Particle2D, Map[Quadrato, SierCarpet[v, l, n]]],
   Axes -> True, AxesOrigin -> {0, 0}, AxesStyle -> Directive[16],
   AspectRatio -> Automatic];
VertexCentre2D[{a_, b_, c_, d_}] := (a + c)/2;
Centre2D[v_, l_, n_] :=
  Map[VertexCentre2D, Map[Quadrato, SierCarpet[v, l, n]]];
Export[NotebookDirectory[] <> "CD.emf",
  GraphicsGrid[{{DustC[{0, 0}, 90, 0],
     DustC[{0, 0}, 270, 1]}, {DustC[{0, 0}, 810, 2],
     DustC[{0, 0}, 2430, 3]}}], ImageSize -> 1500];
Show[GraphicsGrid[{{DustC[{0, 0}, 90, 0],
    DustC[{0, 0}, 270, 1]}, {DustC[{0, 0}, 810, 2],
    DustC[{0, 0}, 2430, 3]}}], ImageSize -> 1500]
```

C.3.3. Cantor Box 1

The following code generates the first six steps of the Cantor Box (+ orientation):

```
Quadrato[{v_, l_}] := {v, v + {l, 0}, v + {l, l}, v + {0, l}};
CBox[{v_, l_}] :=
  Delete[Flatten[
    Table[{v + {(n l)/3, (m l)/3}, l/3}, {n, 0, 2}, {m, 0, 2}],
    1], {{1}, {3}, {7}, {9}}];
CBox2[lista_] := Flatten[Map[CBox, lista], 1];
SierCarpet[v_, l_, n_] := Nest[CBox2, CBox[{v, l}], n];
Particle2D[{a_, b_, c_, d_}] :=
  Rectangle[5/6 a + 1/6 c, 5/6 c + 1/6 a];
BoxC[v_, l_, n_] :=
  Graphics[Map[Particle2D, Map[Quadrato, SierCarpet[v, l, n]]],
   Axes -> True, AxesOrigin -> {0, 0}, AxesStyle -> Directive[16],
   AspectRatio -> Automatic];
VertexCentre2D[{a_, b_, c_, d_}] := (a + c)/2;
Centre2D[v_, l_, n_] :=
  Map[VertexCentre2D, Map[Quadrato, SierCarpet[v, l, n]]];
Export[NotebookDirectory[] <> "CB1.emf",
  GraphicsGrid[{{BoxC[{0, 0}, 90, 0],
     BoxC[{0, 0}, 270, 1]}, {BoxC[{0, 0}, 810, 2],
     BoxC[{0, 0}, 2430, 3]}}], ImageSize -> 1500];
Show[GraphicsGrid[{{BoxC[{0, 0}, 90, 0],
    BoxC[{0, 0}, 270, 1]}, {BoxC[{0, 0}, 810, 2],
    BoxC[{0, 0}, 2430, 3]}}], ImageSize -> 1500]
```

C.3.4. Cantor Box 2

The following code generates the first six steps of the Cantor Box (× orientation):

```
Quadrato[{v_, l_}] := {v, v + {l, 0}, v + {l, l}, v + {0, l}};
CBox[{v_, l_}] :=
  Delete[Flatten[
    Table[{v + {(n l)/3, (m l)/3}, l/3}, {n, 0, 2}, {m, 0, 2}],
    1], {{2}, {4}, {6}, {8}}];
CBox2[lista_] := Flatten[Map[CBox, lista], 1];
SierCarpet[v_, l_, n_] := Nest[CBox2, CBox[{v, l}], n];
Particle2D[{a_, b_, c_, d_}] :=
  Rectangle[5/6 a + 1/6 c, 5/6 c + 1/6 a];
BoxC[v_, l_, n_] :=
  Graphics[Map[Particle2D, Map[Quadrato, SierCarpet[v, l, n]]],
   Axes -> True, AxesOrigin -> {0, 0}, AxesStyle -> Directive[16],
   AspectRatio -> Automatic];
VertexCentre2D[{a_, b_, c_, d_}] := (a + c)/2;
Centre2D[v_, l_, n_] :=
  Map[VertexCentre2D, Map[Quadrato, SierCarpet[v, l, n]]];
Export[NotebookDirectory[] <> "CB2.emf",
  GraphicsGrid[{{BoxC[{0, 0}, 90, 0],
     BoxC[{0, 0}, 270, 1]}, {BoxC[{0, 0}, 810, 2],
     BoxC[{0, 0}, 2430, 3]}}], ImageSize -> 1500];
Show[GraphicsGrid[{{BoxC[{0, 0}, 90, 0],
    BoxC[{0, 0}, 270, 1]}, {BoxC[{0, 0}, 810, 2],
    BoxC[{0, 0}, 2430, 3]}}], ImageSize -> 1500]
```

C.3.5. Sierpinski Carpet

The following code generates the first six steps of the Sierpinski Carpet:

```
Quadrato[{v_, l_}] := {v, v + {l, 0}, v + {l, l}, v + {0, l}};
SCarpet[{v_, l_}] :=
  Delete[Flatten[
    Table[{v + {(n l)/3, (m l)/3}, l/3}, {n, 0, 2}, {m, 0, 2}], 1], 5];
Scarpet2[lista_] := Flatten[Map[SCarpet, lista], 1];
SierCarpet[v_, l_, n_] := Nest[Scarpet2, SCarpet[{v, l}], n];
Particle2D[{a_, b_, c_, d_}] :=
  Rectangle[5/6 a + 1/6 c, 5/6 c + 1/6 a];
CarpetS[v_, l_, n_] :=
  Graphics[Map[Particle2D, Map[Quadrato, SierCarpet[v, l, n]]],
   Axes -> True, AxesOrigin -> {0, 0}, AxesStyle -> Directive[16],
   AspectRatio -> Automatic];
VertexCentre2D[{a_, b_, c_, d_}] := (a + c)/2;
Centre2D[v_, l_, n_] :=
  Map[VertexCentre2D, Map[Quadrato, SierCarpet[v, l, n]]];
Export[NotebookDirectory[] <> "SC.emf",
  GraphicsGrid[{{CarpetS[{0, 0}, 90, 0],
     CarpetS[{0, 0}, 270, 1]}, {CarpetS[{0, 0}, 810, 2],
     CarpetS[{0, 0}, 2430, 3]}}], ImageSize -> 1500];
Show[GraphicsGrid[{{CarpetS[{0, 0}, 90, 0],
    CarpetS[{0, 0}, 270, 1]}, {CarpetS[{0, 0}, 810, 2],
    CarpetS[{0, 0}, 2430, 3]}}], ImageSize -> 1500]
```

C.3.6. 2D Random Walk

The routine RandomWalk2D[N,l] outputs a *list* containing x-y coordinates of the steps of a 2D Random Walk of N steps and with each step l long.

```
 TwoPi = N[2 Pi];
RandomWalk2D[N_,len_] := Module[{l = {{0, 0}}, x = {0, 0}, i = 0, th},
    Do[
       th = TwoPi Random[];
       x += len*{Cos[th], Sin[th]};
       l = Append[l, x],
       {N}
     ];
    l
  ]
```

C.3.7. Square Lattice Diffusion Limited Aggregation

The `dLA[r,n,m]` routine outputs a *list* containing x-y coordinates of a suqre lattice DLA process (cf. B.3.2). The number of particles is n, the radius of the starting particle is r, and the radius of fugue is $r + m$

```
dLA[r_, n_Integer, m_Integer] :=
 Block[{angle, loc, particleCount = 0,
   stepChoices = {{1, 0}, {0, 1}, {-1, 0}, {0, -1}}, structure = {}},
  occSites = {{0, 0}};
  While[Length[occSites] < n, angle = Random[Real, {0, N[2 Pi]}];
```

```
   loc = Floor[{r Cos[angle], r Sin[angle]}];
   ++particleCount;
   While[Abs[loc[[1]]] < r + m &&
     Abs[loc[[2]]] < r + m && ! MemberQ[occSites, loc] &&
     Length[Intersection[occSites, Map[(# + loc) &, stepChoices]]] ==
      0, loc += stepChoices[[Random[Integer, {1, 4}]]]];
   If[Length[Intersection[occSites, Map[# + loc &, stepChoices]]] =!=
     0, AppendTo[occSites, loc]]];
   occSites]
```

Bibliography

[1] Feynman R, *There's Plenty of Room at the Bottom*. In *The Pleasure of Finding Things Out* (1959). (Cited on page 1).

[2] Taniguchi N, *On the Basic Concept of 'Nano-Technology*. In *Proc. Intl. Conf. Prod. London, Part II* (British Society of Precision Engineering, 1974). (Cited on page 1).

[3] Maier SA, *Plasmonics: fundamentals and applications* (Springer, 2007), illustrated edn. (Cited on pages 2 and 7).

[4] Mandelbrot B, *The Fractal Geometry of Nature* (W.H. Freeman and Company, 1982). (Cited on page 4).

[5] Li K, Stockman MI and Bergman DJ (2003) *Self-Similar Chain of Metal Nanospheres as an Efficient Nanolens*. Phys. Rev. Lett., **vol. 91, no. 22**:p. 227402. (Cited on page 4).

[6] Dai J, Cajko F, Tsukerman I *et al.* (2008) *Electrodynamic effects in plasmonic nanolenses*. Physical Review B, **vol. 77, no. 11**. (Cited on page 4).

[7] Dal Negro L, Feng NN and Gopinath A (2008) *Electromagnetic coupling and plasmon localization in deterministic aperiodic arrays*. Journal Of Optics A-Pure And Applied Optics, **vol. 10, no. 6**. (Cited on page 4).

[8] Gopinath A, Boriskina SV, Yerci S *et al.* (2010) *Enhancement of the 1.54 mu m Er3+ emission from quasiperiodic plasmonic arrays*. Applied Physics Letters, **vol. 96, no. 7**. (Cited on page 4).

[9] Qiu T, Wu XL, Shen JC *et al.* (2008) *Silver fractal networks for surface-enhanced Raman scattering substrates*. Applied Surface Science, **vol. 254, no. 17**:pp. 5399–5402. (Cited on pages 4 and 5).

[10] Bao YJ, Li HM, Chen XC *et al.* (2008) *Tailoring the resonances of surface plasmas on fractal-featured metal film by adjusting aperture configuration*. Applied Physics Letters, **vol. 92, no. 15**. (Cited on page 4).

[11] Agrawal A, Matsui T, Zhu W *et al.* (2009) *Terahertz Spectroscopy of Plasmonic Fractals*. Physical Review Letters, **vol. 102, no. 11**. (Cited on page 4).

[12] Karim MNA, Rahim MKA and Masri T (2009) *Fractal Koch dipole antenna for UHF band application*. Microwave And Optical Technology Letters, **vol. 51, no. 11**:pp. 2612–2614. (Cited on page 4).

[13] Miyamaru F, Saito Y, Takeda MW *et al.* (2009) *Emission of terahertz radiations from fractal antennas*. Applied Physics Letters, **vol. 95, no. 22**. (Cited on page 5).

[14] Goldys EM, Barnett A, Xie F *et al.* (2007) *Plasmon-enhanced fluorescence near metallic nanostructures: biochemical applications*. Applied Physics A-Materials Science & Processing, **vol. 89, no. 2**:pp. 265–271. (Cited on page 5).

[15] Agrawal VV, Kulkarni GU and Rao CNR (2008) *Surfactant-promoted formation of fractal and dendritic nanostructures of gold and silver at the organic-aqueous interface*. Journal Of Colloid And Interface Science, **vol. 318, no. 2**:pp. 501–506. (Cited on page 5).

[16] Bransden B and Joachain C, *Physics of Atoms and Molecules* (Prentice Hall, 2003), 2nd edn. (Cited on page 7).

[17] Johnson PB and Christy RW (1972) *Optical Constants of the Noble Metals*. Phys. Rev. B, **vol. 6, no. 12**:pp. 4370–4379. (Cited on pages 9 and 107).

[18] Hao F and Nordlander P (2007) *Efficient dielectric function for FDTD simulation of the optical properties of silver and gold nanoparticles*. Chemical Physics Letters, **vol. 446, no. 1-3**:pp. 115–118. (Cited on page 10).

[19] Kreibig U and Vollmer M, *Optical Properties of Metal Clusters* (Springer, 1995). (Cited on pages 10 and 11).

[20] Ashcroft NW and Mermin ND, *Solid State Physics* (Brooks Cole, 1976), 1st edn. (Cited on page 11).

[21] Mie G (1908) *Contributions to the optics of diffusing media*. Ann. Physik, **vol. 25**:p. 377. (Cited on pages 14 and 27).

[22] Gans R (1915) *Evaporation-induced self-assembly of gold nanoparticles into a highly organized two-dimensional array*. Ann. Physik, **vol. 47**:p. 270. (Cited on pages 14 and 23).

[23] Jackson JD, *Classical Electrodynamics* (Wiley, 2003), 3rd edn. (Cited on pages 14 and 15).

[24] Bohren CF and Huffman DR, *Absorption and Scattering of Light by Small Particles* (Wiley-Interscience, 1998). (Cited on page 16).

[25] Meier M and Wokaun A (1983) *Enhanced fields on large metal particles: dynamic depolarization*. Optics Letters, **vol. 8, no. 11**:pp. 581–583. (Cited on pages 16 and 17).

[26] Kuwata H, Tamaru H, Esumi K *et al.* (2003) *Resonant light scattering from metal nanoparticles: Practical analysis beyond Rayleigh approximation*. Applied Physics Letters, **vol. 83**:p. 4625. (Cited on page 16).

[27] Kokkinakis T and Alexopoulos K (1972) *Observation of Radiative Decay of Surface Plasmons in Small Silver Particles*. Phys. Rev. Lett., **vol. 28, no. 25**:pp. 1632–1634. (Cited on page 17).

[28] Wokaun A, Gordon JP and Liao PF (1982) *Radiation Damping in Surface-Enhanced Raman Scattering*. Phys. Rev. Lett., **vol. 48, no. 14**:pp. 957–960. (Cited on page 17).

[29] Heilweil E and Hochstrasser R (1985) *Nonlinear spectroscopy and picosecond transient grating study of colloidal gold*. The Journal of Chemical Physics, **vol. 82**:p. 4762. (Cited on page 17).

[30] Link S and El-Sayed M (2000) *Shape and size dependence of radiative, non-radiative and photothermal properties of gold nanocrystals*. International Reviews in Physical Chemistry, **vol. 19, no. 3**:pp. 409–453. (Cited on page 18).

[31] Sönnichsen C, Franzl T, Wilk T *et al.* (2002) *Plasmon resonances in large noble-metal clusters*. New Journal of Physics, **vol. 4**:p. 93. (Cited on page 18).

[32] Stratton JA, *Electromagnetic theory*, vol. 33 (Wiley. com, 2007). (Cited on page 19).

[33] Sinzig J, Radtke U, Quinten M *et al.* (1993) *Binary clusters: homogeneous alloys and nucleus-shell structures*. Zeitschrift für Physik D Atoms, Molecules and Clusters, **vol. 26, no. 1**:pp. 242–245. (Cited on pages 23 and 74).

[34] Sinzig J and Quinten M (1994) *Scattering and absorption by spherical multilayer particles*. Applied Physics A, **vol. 58, no. 2**:pp. 157–162. (Cited on pages 23 and 74).

[35] Gans R (1912) *Über die form ultramikroskopischer goldteilchen*. Annalen der Physik, **vol. 342, no. 5**:pp. 881–900. (Cited on page 23).

[36] de Abajo FG (1999) *Interaction of radiation and fast electrons with clusters of dielectrics: A multiple scattering approach*. Physical review letters, **vol. 82, no. 13**:p. 2776. (Cited on page 24).

[37] de Abajo FG (1999) *Multiple scattering of radiation in clusters of dielectrics*. Physical Review B, **vol. 60, no. 8**:p. 6086. (Cited on page 24).

[38] Garnett J (1904) *Colours in metal glasses and in metallic films*. Philosophical Transactions of the Royal Society of London. Series A, Containing Papers of a Mathematical or Physical Character, **vol. 203**:pp. 385–420. (Cited on page 25).

[39] Xu Yl and Gustafson BÅ (2001) *A generalized multiparticle Mie-solution: further experimental verification*. Journal of Quantitative Spectroscopy and Radiative Transfer, **vol. 70, no. 4**:pp. 395–419. (Cited on page 25).

[40] Messinger BJ, von Raben KU, Chang RK *et al.* (1981) *Local fields at the surface of noble-metal microspheres*. Phys. Rev. B, **vol. 24, no. 2**:pp. 649–657. (Cited on page 26).

[41] Draine B and Flatau P (2009) *User Guide for the Discrete Dipole Approximation Code DDSCAT 7.0*. arXiv.org. (Cited on page 27).

[42] Mishchenko M, Travis L and Lacis A, *Scattering, absorption, and emission of light by small particles* (Cambridge Univ Pr, 2002). (Cited on page 27).

[43] Laven P. *MiePlot Homepage: http://www.philiplaven.com/mieplot.htm*. (Cited on page 27).

[44] Morgan M and Mei K (1979) *Finite-element computation of scattering by inhomogeneous penetrable bodies of revolution*. IEEE Transactions on Antennas and Propagation, **vol. 27, no. 2**:pp. 202–214. (Cited on page 27).

[45] Silvester P and Ferrari R, *Finite elements for electrical engineers* (Cambridge Univ Pr, 1996). (Cited on page 27).

[46] Mittra R and Ramahi O (1990) *Absorbing boundary conditions for the direct solution of partial differential equations arising in electromagnetic scattering problems*. Finite Element and Finite Difference Methods in Electromagnetic Scattering, **vol. 2**. (Cited on page 27).

[47] Yee K (1966) *Numerical solution of inital boundary value problems involving maxwell's equations in isotropic media*. IEEE Transactions on antennas and propagation, **vol. 14, no. 3**:pp. 302–307. (Cited on page 28).

[48] Berenger J (1994) *A perfectly matched layer for the absorption of electromagnetic waves*. Journal of computational physics, **vol. 114, no. 2**:pp. 185–200. (Cited on page 28).

[49] Yang P and Liou K (1998) *An efficient algorithm for truncating spatial domain in modeling light scattering by finite-difference technique*. Journal of Computational Physics, **vol. 140, no. 2**:pp. 346–369. (Cited on page 28).

[50] Sun W, Fu Q and Chen Z (1999) *Finite-difference time-domain solution of light scattering by dielectric particles with a perfectly matched layer absorbing boundary condition*. Appl. Opt, **vol. 38, no. 15**:pp. 3141–3151. (Cited on page 28).

[51] Purcell E and Pennypacker C (1973) *Scattering and absorption of light by nonspherical dielectric grains*. The Astrophysical Journal, **vol. 186, no. 2**:pp. 705–714. (Cited on page 28).

[52] Draine B (1988) *The discrete-dipole approximation and its application to interstellar graphite grains*. Astrophysical Journal, **vol. 333, no. 2**:pp. 848–872. (Cited on page 28).

[53] Draine B and Goodman J (1993) *Beyond Clausius-Mossotti: Wave propagation on a polarizable point lattice and the discrete dipole approximation*. Astrophysical Journal, **vol. 405**:pp. 685–685. (Cited on page 28).

[54] Draine B and Flatau P (2008) *Discrete-dipole approximation for periodic targets: theory and tests*. Journal of the Optical Society of America A, **vol. 25, no. 11**:pp. 2693–2703. (Cited on page 28).

[55] Draine B and Flatau P (1994) *Discrete-dipole approximation for scattering calculations*. Journal of the Optical Society of America A, **vol. 11, no. 4**:pp. 1491–1499. (Cited on page 28).

[56] (2010) *COMSOL Multiphysics Reference Guide*, 4th edn. (Cited on page 28).

[57] Greenbaum A, *Iterative methods for solving linear systems*, vol. 17 (Society for Industrial & Applied Mathematics, 1997). (Cited on page 31).

[58] Saad Y and Schultz MH (1986) *GMRES: A generalized minimal residual algorithm for solving nonsymmetric linear systems*. SIAM Journal on scientific and statistical computing, **vol. 7, no. 3**:pp. 856–869. (Cited on page 31).

[59] Amestoy PR, Duff IS and L'Excellent JY (2000) *Multifrontal parallel distributed symmetric and unsymmetric solvers*. Computer methods in applied mechanics and engineering, **vol. 184, no. 2**:pp. 501–520. (Cited on page 31).

[60] Amestoy PR, Duff IS, L'Excellent JY *et al.* (2001) *A fully asynchronous multifrontal solver using distributed dynamic scheduling*. SIAM Journal on Matrix Analysis and Applications, **vol. 23, no. 1**:pp. 15–41. (Cited on page 31).

[61] Amestoy PR, Duff IS, L'Excellent JY *et al.*, *MUMPS: a general purpose distributed memory sparse solver*. In *Applied Parallel Computing. New Paradigms for HPC in Industry and Academia*, (pp. 121–130) (Springer, 2001). (Cited on page 31).

[62] Schenk O, Bollhöfer M and Römer RA (2008) *On large-scale diagonalization techniques for the Anderson model of localization*. SIAM review, **vol. 50, no. 1**:pp. 91–112. (Cited on page 32).

[63] Schenk O, Wächter A and Hagemann M (2007) *Matching-based preprocessing algorithms to the solution of saddle-point problems in large-scale nonconvex interior-point optimization*. Computational Optimization and Applications, **vol. 36, no. 2-3**:pp. 321–341. (Cited on page 32).

[64] Schenk O and Gärtner K (2004) *Solving unsymmetric sparse systems of linear equations with PARDISO*. Future Generation Computer Systems, **vol. 20, no. 3**:pp. 475–487. (Cited on page 32).

[65] Jin J, Jin J and Jin J, *The finite element method in electromagnetics* (Wiley New York, 2002), 2nd edn. (Cited on page 35).

[66] Haes AJ and Duyne RP (2004) *A unified view of propagating and localized surface plasmon resonance biosensors*. Analytical and Bioanalytical Chemistry, **vol. 379**. (Cited on page 39).

[67] Haynes CL and Van Duyne RP (2001) *Nanosphere Lithography: A Versatile Nanofabrication Tool for Studies of Size-Dependent Nanoparticle Optics*. J. Phys. Chem. B, **vol. 105, no. 24**:pp. 5599–5611. (Cited on pages 39, 41, and 42).

[68] Schatz G (2009) *Self-Assembled Nanospheres: An Exciting Playground*. Acta physica Polonica. A, **vol. 115, no. 2**:pp. 431–434. (Cited on page 41).

[69] Beeram SR and Zamborini FP (2011) *Effect of Protein Binding Coverage, Location, and Distance on the Localized Surface Plasmon Resonance Response of Purified Au Nanoplates Grown Directly on Surfaces*. Journal of Physical Chemistry C, **vol. 115, no. 15**:pp. 7364–7371. WOS:000289403200028. (Cited on page 41).

[70] Malinsky MD, Kelly KL, Schatz GC *et al.* (2001) *Chain length dependence and sensing capabilities of the localized surface plasmon resonance of silver nanoparticles chemically modified with alkanethiol self-assembled monolayers*. Journal of the American Chemical Society, **vol. 123, no. 7**:pp. 1471–1482. WOS:000167031300026. (Cited on page 41).

[71] Mock JJ, Smith DR and Schultz S (2003) *Local refractive index dependence of plasmon resonance spectra from individual nanoparticles*. Nano Letters, **vol. 3, no. 4**:pp. 485–491. WOS:000182201800012. (Cited on page 41).

[72] Chan YH, Chen J, Liu Q *et al.* (2010) *Ultrasensitive Copper(II) Detection Using Plasmon-Enhanced and Photo-Brightened Luminescence of CdSe Quantum Dots*. Analytical Chemistry, **vol. 82, no. 9**:pp. 3671–3678. WOS:000277213400042. (Cited on page 41).

[73] Dondapati SK, Sau TK, Hrelescu C *et al.* (2010) *Label-free Biosensing Based on Single Gold Nanostars as Plasmonic Transducers*. Acs Nano, **vol. 4, no. 11**:pp. 6318–6322. WOS:000284438000004. (Cited on page 41).

[74] Anker JN, Hall WP, Lyandres O *et al.* (2008) *Biosensing with plasmonic nanosensors*. Nature Materials, **vol. 7, no. 6**:pp. 442–453. WOS:000256110200016. (Cited on page 41).

[75] Jain PK, Huang X, El-Sayed IH *et al.* (2008) *Noble Metals on the Nanoscale: Optical and Photothermal Properties and Some Applications in Imaging, Sensing, Biology, and Medicine*. Accounts of Chemical Research, **vol. 41, no. 12**:pp. 1578–1586. WOS:000261767600003. (Cited on page 41).

[76] Haes AJ, Chang L, Klein WL *et al.* (2005) *Detection of a biomarker for Alzheimer's disease from synthetic and clinical samples using a nanoscale optical biosensor*. Journal of the American Chemical Society, **vol. 127, no. 7**:pp. 2264–2271. WOS:000227099400047. (Cited on page 41).

[77] Itoh H, Naka K and Chujo Y (2004) *Synthesis of gold nanoparticles modified with ionic liquid based on the imidazolium cation*. Journal of the American Chemical Society, **vol. 126, no. 10**:pp. 3026–3027. WOS:000220192000011. (Cited on page 41).

[78] Haes AJ and Van Duyne RP (2002) *A nanoscale optical blosensor: Sensitivity and selectivity of an approach based on the localized surface plasmon resonance spectroscopy of triangular silver nanoparticles*. Journal of the American Chemical Society, **vol. 124, no. 35**:pp. 10596–10604. WOS:000177881300057. (Cited on page 41).

[79] Chen H, Kou X, Yang Z *et al.* (2008) *Shape- and size-dependent refractive index sensitivity of gold nanoparticles*. Langmuir, **vol. 24, no. 10**:pp. 5233–5237. WOS:000255856100009. (Cited on page 41).

[80] Chen H, Shao L, Woo KC *et al.* (2009) *Shape-Dependent Refractive Index Sensitivities of Gold Nanocrystals with the Same Plasmon Resonance Wavelength*. Journal of Physical Chemistry C, **vol. 113, no. 41**:pp. 17691–17697. WOS:000270459900018. (Cited on page 41).

[81] Mayer KM and Hafner JH (2011) *Localized Surface Plasmon Resonance Sensors*. Chemical Reviews, **vol. 111, no. 6**:pp. 3828–3857. WOS:000291756700005. (Not cited).

[82] Slaughter L, Chang WS and Link S (2011) *Characterizing Plasmons in Nanoparticles and Their Assemblies with Single Particle Spectroscopy*. Journal of Physical Chemistry Letters, **vol. 2, no. 16**:pp. 2015–2023. WOS:000294076900009. (Cited on page 41).

[83] Slaughter LS, Chang WS, Swanglap P *et al.* (2010) *Single-Particle Spectroscopy of Gold Nanorods beyond the Quasi-Static Limit: Varying the Width at Constant Aspect Ratio*. Journal of Physical Chemistry C, **vol. 114, no. 11**:pp. 4934–4938. WOS:000275708600026. (Cited on page 41).

[84] Bukasov R, Ali TA, Nordlander P *et al.* (2010) *Probing the Plasmonic Near-Field of Gold Nanocrescent Antennas*. Acs Nano, **vol. 4, no. 11**:pp. 6639–6650. WOS:000284438000040. (Cited on page 41).

[85] Busbee BD, Obare SO and Murphy CJ (2003) *An improved synthesis of high-aspect-ratio gold nanorods*. Advanced Materials, **vol. 15, no. 5**:pp. 414–+. WOS:000181713900010. (Cited on page 41).

[86] Lee S, Mayer KM and Hafner JH (2009) *Improved Localized Surface Plasmon Resonance Immunoassay with Gold Bipyramid Substrates*. Analytical Chemistry, **vol. 81, no. 11**:pp. 4450–4455. WOS:000266601800039. (Cited on page 41).

[87] Marinakos SM, Chen S and Chilkoti A (2007) *Plasmonic detection of a model analyte in serum by a gold nanorod sensor*. Analytical Chemistry, **vol. 79, no. 14**:pp. 5278–5283. WOS:000247992600023. (Cited on page 41).

[88] Millstone JE, Park S, Shuford KL *et al.* (2005) *Observation of a quadrupole plasmon mode for a colloidal solution of gold nanoprisms*. Journal of the American Chemical Society, **vol. 127, no. 15**:pp. 5312–5313. WOS:000228408300020. (Cited on page 41).

[89] Nehl CL, Liao HW and Hafner JH (2006) *Optical properties of star-shaped gold nanoparticles*. Nano Letters, **vol. 6, no. 4**:pp. 683–688. WOS:000236916200017. (Cited on page 41).

[90] Wei H, Reyes-Coronado A, Nordlander P *et al.* (2010) *Multipolar Plasmon Resonances in Individual Ag Nanorice*. Acs Nano, **vol. 4, no. 5**:pp. 2649–2654. WOS:000277976900021. (Cited on page 41).

[91] Jain PK, Huang W and El-Sayed MA (2007) *On the universal scaling behavior of the distance decay of plasmon coupling in metal nanoparticle pairs: A plasmon ruler equation*. Nano Letters, **vol. 7, no. 7**:pp. 2080–2088. WOS:000247926400043. (Cited on page 41).

[92] Reinhard BM, Siu M, Agarwal H *et al.* (2005) *Calibration of dynamic molecular rule based on plasmon coupling between gold nanoparticles*. Nano Letters, **vol. 5, no. 11**:pp. 2246–2252. WOS:000233481700026. (Cited on page 41).

[93] Sonnichsen C and Alivisatos AP (2005) *Gold nanorods as novel nonbleaching plasmon-based orientation sensors for polarized single-particle microscopy*. Nano Letters, **vol. 5, no. 2**:pp. 301–304. WOS:000227100500020. (Cited on page 41).

[94] Wang H and Reinhard BM (2009) *Monitoring Simultaneous Distance and Orientation Changes in Discrete Dimers of DNA Linked Gold Nanoparticles*. Journal of Physical Chemistry C, **vol. 113, no. 26**:pp. 11215–11222. WOS:000267324600007. (Cited on page 41).

[95] Michieli N, Kalinic B, Scian C *et al.* (2013) *Optimal Geometric Parameters for Localized Plasmon Bio-Sensors Sensitivity*. submitted. (Cited on page 41).

[96] Michieli N, Kalinic B, Scian C *et al.* (2013) *Simulation of Periodic Nanostructures for Design and Optimization of Plasmonic Biosensors*. submitted. (Cited on page 41).

[97] Brigo L, Michieli N, Artiglia L *et al.* (2014) *Silver nanopyramid arrays coupled to functional hybrid films for LSPR based detection of aromatic hydrocarbons*. submitted. (Cited on page 41).

[98] Hulteen JC, Treichel DA, Smith MT *et al.* (1999) *Nanosphere Lithography: Size-Tunable Silver Nanoparticle and Surface Cluster Arrays*. J. Phys. Chem. B, **vol. 103, no. 19**:pp. 3854–3863. (Cited on page 42).

[99] Jensen TR, Malinsky MD, Haynes CL *et al.* (2000) *Nanosphere Lithography: Tunable Localized Surface Plasmon Resonance Spectra of Silver Nanoparticles*. J. Phys. Chem. B, **vol. 104, no. 45**:pp. 10549–10556. (Cited on page 42).

[100] Perotto G, Pellegrini G, Scian C *et al.* (2013) *Rare Earth Fluorescence Thermometry of Laser Induced Plasmon Heating*. in preparation. (Cited on page 57).

[101] Desurvire E, *Erbium-Doped Fiber Amplifiers, Principles and Applications* (Wiley-Interscience, 2002). (Cited on page 60).

[102] Miniscalco WJ (1991) *Erbium-doped glasses for fiber amplifiers at 1500 nm*. Lightwave Technology, Journal of, **vol. 9, no. 2**:pp. 234–250. (Cited on page 60).

[103] Van den Hoven G, Snoeks E, Polman A *et al.* (1996) *Upconversion in Er-implanted Al 2 O 3 waveguides*. Journal of applied physics, **vol. 79, no. 3**:pp. 1258–1266. (Cited on page 60).

[104] Hunt N, Vredenberg A, Schubert E *et al.*, *Spontaneous emission control in planar structures: Er3+ in Si/SiO2 microcavities*. In *Confined Electrons and Photons*, (pp. 715–728) (Springer, 1995). (Cited on page 60).

[105] Castagna ME, Coffa S, Monaco M *et al.* (2003) *High efficiency light emitting devices in silicon*. Materials Science and Engineering: B, **vol. 105, no. 1**:pp. 83–90. (Cited on page 60).

[106] Snoeks E, Kik P and Polman A (1996) *Concentration quenching in erbium implanted alkali silicate glasses*. Optical Materials, **vol. 5, no. 3**:pp. 159–167. (Cited on page 60).

[107] Purcell E, *Spontaneous emission probabilities at radio frequencies*. In *Confined Electrons and Photons*, (pp. 839–839) (Springer, 1995). (Cited on page 60).

[108] Drexhage K (1970) *Influence of a dielectric interface on fluorescence decay time*. Journal of Luminescence, **vol. 1**:pp. 693–701. (Cited on page 60).

[109] Chance R, Prock A and Silbey R (1978) *Molecular fluorescence and energy transfer near interfaces*. Adv. Chem. Phys, **vol. 37, no. 1**:p. 65. (Cited on pages 60 and 61).

[110] Amos R and Barnes W (1997) *Modification of the spontaneous emission rate of Eu^{3+} ions close to a thin metal mirror*. Physical Review B, **vol. 55, no. 11**:p. 7249. (Cited on page 60).

[111] Barnes W (1998) *Fluorescence near interfaces: the role of photonic mode density*. journal of modern optics, **vol. 45, no. 4**:pp. 661–699. (Cited on page 60).

[112] Zhang JY, Wang XY and Xiao M (2002) *Modification of spontaneous emission from CdSe/CdS quantum dots in the presence of a semiconductor interface*. Optics letters, **vol. 27, no. 14**:pp. 1253–1255. (Cited on page 60).

[113] Zhang Y, Komarala VK, Rodriguez C *et al.* (2008) *Controlling fluorescence intermittency of a single colloidal CdSe/ZnS quantum dot in a half cavity*. Physical Review B, **vol. 78, no. 24**:p. 241301. (Cited on page 60).

[114] Leistikow M, Johansen J, Kettelarij A *et al.* (2009) *Size-dependent oscillator strength and quantum efficiency of CdSe quantum dots controlled via the local density of states*. Physical Review B, **vol. 79, no. 4**:p. 045301. (Cited on page 60).

[115] Genet C and Ebbesen T (2007) *Light in tiny holes*. Nature, **vol. 445, no. 7123**:pp. 39–46. (Cited on page 63).

[116] Barbara A, Quémerais P, Bustarret E *et al.* (2002) *Optical transmission through subwavelength metallic gratings*. Physical Review B, **vol. 66, no. 16**:p. 161403. (Cited on page 63).

[117] Sarrazin M, Vigneron JP and Vigoureux JM (2003) *Role of Wood anomalies in optical properties of thin metallic films with a bidimensional array of subwavelength holes*. Physical Review B, **vol. 67, no. 8**:p. 085415. (Cited on page 63).

[118] Genet C, van Exter MP and Woerdman J (2003) *Fano-type interpretation of red shifts and red tails in hole array transmission spectra*. Optics Communications, **vol. 225, no. 4**:pp. 331–336. (Cited on page 63).

[119] Koerkamp KK, Enoch S, Segerink F *et al.* (2004) *Strong influence of hole shape on extraordinary transmission through periodic arrays of subwavelength holes*. Physical review letters, **vol. 92, no. 18**:p. 183901. (Cited on page 64).

[120] Degiron A and Ebbesen T (2005) *The role of localized surface plasmon modes in the enhanced transmission of periodic subwavelength apertures*. Journal of Optics A: Pure and Applied Optics, **vol. 7, no. 2**:p. S90. (Cited on page 64).

[121] Kalinic B, Cesca T, Michieli N *et al.* (2013) *Controlling the emission rate of Er3+ ions by the interaction with thin films and plasmonic nanostructures*. in review. (Cited on page 64).

[122] Zhou HS, Honma I, Komiyama H *et al.* (1994) *Controlled synthesis and quantum-size effect in gold-coated nanoparticles*. Phys. Rev. B, **vol. 50, no. 16**:pp. 12052–12056. (Cited on page 74).

[123] Averitt RD, Sarkar D and Halas NJ (1997) *Plasmon Resonance Shifts of Au-Coated Au_{2}S Nanoshells: Insight into Multicomponent Nanoparticle Growth*. Phys. Rev. Lett., **vol. 78, no. 22**:pp. 4217–4220. (Cited on page 74).

[124] Sun Y and Xia Y (2002) *Increased Sensitivity of Surface Plasmon Resonance of Gold Nanoshells Compared to That of Gold Solid Colloids in Response to Environmental Changes*. Anal. Chem., **vol. 74, no. 20**:pp. 5297–5305. (Cited on page 74).

[125] Wang H, Brandl DW, Nordlander P *et al.* (2007) *Plasmonic Nanostructures: Artificial Molecules*. Acc. Chem. Res., **vol. 40, no. 1**:pp. 53–62. (Cited on page 74).

[126] Mirin NA and Halas NJ (2009) *Light-Bending Nanoparticles*. Nano Lett., **vol. 9, no. 3**:pp. 1255–1259. (Cited on page 74).

[127] Mirin NA, Ali TA, Nordlander P *et al.* (2010) *Perforated Semishells: Far-Field Directional Control and Optical Frequency Magnetic Response*. ACS Nano, **vol. 4, no. 5**:pp. 2701–2712. (Cited on page 75).

[128] Stuart DA, Yuen JM, Shah N *et al.* (2006) *In Vivo Glucose Measurement by Surface-Enhanced Raman Spectroscopy*. Anal. Chem., **vol. 78, no. 20**:pp. 7211–7215. (Cited on page 75).

[129] Duyne RPV, Hulteen JC and Treichel DA (1993) *Atomic force microscopy and SERS. I. Ag island films and Ag film over polymer nanosphere surfaces supported on glass*. The Journal of Chemical Physics, **vol. 99, no. 3**:pp. 2101–2115. (Cited on page 75).

[130] Ye J, Van Dorpe P, Van Roy W *et al.* (2009) *Fabrication and optical properties of gold semishells*. The Journal of Physical Chemistry C, **vol. 113, no. 8**:pp. 3110–3115. (Cited on page 75).

[131] Wang C, Ruan W, Ji N *et al.* (2010) *Preparation of nanoscale Ag semishell array with tunable interparticle distance and its application in surface-enhanced Raman scattering*. The Journal of Physical Chemistry C, **vol. 114, no. 7**:pp. 2886–2890. (Cited on page 75).

[132] Liu G, Li Y, Duan G *et al.* (2011) *Tunable surface plasmon resonance and strong SERS performances of Au opening-nanoshell ordered arrays*. ACS Applied Materials & Interfaces, **vol. 4, no. 1**:pp. 1–5. (Cited on page 75).

[133] Li X, Hu H, Li D *et al.* (2012) *Ordered array of gold semishells on TiO2 spheres: an ultrasensitive and recyclable SERS substrate*. ACS Applied Materials & Interfaces, **vol. 4, no. 4**:pp. 2180–2185. (Cited on page 75).

[134] Pease RFW (1981) *Electron beam lithography*. Contemporary Physics, **vol. 22, no. 3**:pp. 265–290. (Cited on page 95).

[135] Melngailis J (1987) *Focused ion beam technology and applications*. Journal of Vacuum Science Technology B: Microelectronics and Nanometer Structures, **vol. 5, no. 2**:pp. 469–495. (Cited on page 95).

[136] Reyntjens S and Puers R (2001) *A review of focused ion beam applications in microsystem technology*. J. Micromech. Microeng., **vol. 11, no. 4**:p. 287. (Cited on page 95).

[137] Scholder O, Jefimovs K, Shorubalko I *et al.* (2013) *Helium focused ion beam fabricated plasmonic antennas with sub-5 nm gaps*. Nanotechnology, **vol. 24, no. 39**:p. 395301. (Cited on page 95).

[138] Hartley JG, Crosland N, Dowling RC *et al.*, *Quantifying throughput improvements for electron-beam lithography using a suite of benchmark patterns*. vol. 8680, (pp. 86800P–86800P–13) (2013). (Cited on page 95).

[139] Manfrinato VR, Zhang L, Su D *et al.* (2013) *Resolution Limits of Electron-Beam Lithography toward the Atomic Scale*. Nano Lett., **vol. 13, no. 4**:pp. 1555–1558. (Cited on page 95).

[140] Benkouider A, Berbezier I, Ronda A *et al.* (2013) *Ultimate nanopatterning of Si substrate using filtered liquid metal alloy ion source-focused ion beam*. Thin Solid Films, **vol. 543**:pp. 69–73. (Cited on page 95).

[141] Shimomura M and Sawadaishi T (2001) *Bottom-up strategy of materials fabrication: a new trend in nanotechnology of soft materials*. Current Opinion in Colloid & Interface Science, **vol. 6, no. 1**:pp. 11–16. (Cited on page 95).

[142] Li J, Ye Q, Cassell A *et al.* (2003) *Bottom-up approach for carbon nanotube interconnects*. Applied Physics Letters, **vol. 82, no. 15**:pp. 2491–2493. (Cited on page 95).

[143] Chung SW, Ginger DS, Morales MW *et al.* (2005) *Top-Down Meets Bottom-Up: Dip-Pen Nanolithography and DNA-Directed Assembly of Nanoscale Electrical Circuits*. Small, **vol. 1, no. 1**. (Cited on page 95).

[144] Bennett PB, Pedramrazi Z, Madani A *et al.* (2013) *Bottom-up Graphene Nanoribbon Field-Effect Transistors*. arXiv:1310.0495 [cond-mat]. (Cited on page 95).

[145] Yabu H (2013) *Bottom-Up Approach to Creating Three-Dimensional Nanoring Arrays Composed of Au Nanoparticles*. Langmuir, **vol. 29, no. 4**:pp. 1005–1009. (Cited on page 95).

[146] Weitz D, Lin M and Sandroff C (1985) *Colloidal aggregation revisited: New insights based on fractal structure and surface-enhanced Raman scattering*. Surface Science, **vol. 158, no. 1-3**:pp. 147–164. (Cited on page 95).

[147] Stockman MI, Shalaev VM, Moskovits M *et al.* (1992) *Enhanced Raman scattering by fractal clusters: Scale-invariant theory*. Phys. Rev. B, **vol. 46, no. 5**:pp. 2821–2830. (Cited on page 95).

[148] Kim W, Safonov VP, Shalaev VM *et al.* (1999) *Fractals in Microcavities: Giant Coupled, Multiplicative Enhancement of Optical Responses*. Phys. Rev. Lett., **vol. 82, no. 24**:pp. 4811–4814. (Cited on page 95).

[149] Moskovits M, Tay LL, Yang J *et al.*, *SERS and the Single Molecule*. In VM Shalaev, editor, *Optical Properties of Nanostructured Random Media*, no. 82 in Topics in Applied Physics, (pp. 215–227) (Springer Berlin Heidelberg, 2002). (Cited on page 95).

[150] He L, Kim NJ, Li H *et al.* (2008) *Use of a Fractal-like Gold Nanostructure in Surface-Enhanced Raman Spectroscopy for Detection of Selected Food Contaminants*. J. Agric. Food Chem., **vol. 56, no. 21**:pp. 9843–9847. (Cited on page 95).

[151] Amarandei G, O'Dwyer C, Arshak A *et al.* (2013) *Fractal Patterning of Nanoparticles on Polymer Films and Their SERS Capabilities*. ACS Appl. Mater. Interfaces, **vol. 5, no. 17**:pp. 8655–8662. (Cited on page 95).

[152] Murph SEH and Murphy CJ (2013) *Patchy silica-coated silver nanowires as SERS substrates*. J Nanopart Res, **vol. 15, no. 6**:pp. 1–14. (Cited on page 95).

[153] Grigorenko I (2013) *Nanostructures with the Hilbert curve geometry as surface enhanced Raman scattering substrates*. Applied Physics Letters, **vol. 103, no. 4**:pp. 043123–043123–3. (Cited on page 95).

[154] Zhu Sn, Zhu Yy and Ming Nb (1997) *Quasi-Phase-Matched Third-Harmonic Generation in a Quasi-Periodic Optical Superlattice*. Science, **vol. 278, no. 5339**:pp. 843–846. (Cited on page 95).

[155] Galletto P, Brevet PF, Girault HH *et al.* (1999) *Enhancement of the Second Harmonic Response by Adsorbates on Gold Colloids: The Effect of Aggregation*. J. Phys. Chem. B, **vol. 103, no. 41**:pp. 8706–8710. (Cited on page 95).

[156] Anceau C, Brasselet S, Zyss J *et al.* (2003) *Local second-harmonic generation enhancement on gold nanostructures probed by two-photon microscopy*. Optics Letters, **vol. 28, no. 9**:pp. 713–715. (Cited on page 95).

[157] Stockman MI, Bergman DJ, Anceau C *et al.* (2004) *Enhanced Second-Harmonic Generation by Metal Surfaces with Nanoscale Roughness: Nanoscale Dephasing, Depolarization, and Correlations*. Phys. Rev. Lett., **vol. 92, no. 5**:p. 057402. (Cited on page 95).

[158] Kim IK, Kingsley N, Morton M *et al.* (2005) *Fractal-shaped microstrip coupled-line bandpass filters for suppression of second harmonic*. IEEE Transactions on Microwave Theory and Techniques, **vol. 53, no. 9**:pp. 2943–2948. (Cited on page 95).

[159] Li K, Stockman MI and Bergman DJ (2005) *Enhanced second harmonic generation in a self-similar chain of metal nanospheres*. Phys. Rev. B, **vol. 72, no. 15**:p. 153401. (Cited on page 95).

[160] Ma BQ, Ren ML, Ma DL *et al.* (2013) *Multiple second-harmonic waves in a nonlinear photonic crystal with fractal structure*. Appl. Phys. B, **vol. 111, no. 2**:pp. 183–187. (Cited on page 95).

[161] Wang W, Chen Z, Hou L *et al.* (2013) *Formation and Third-Order Optical Nonlinearities of Fractal Ge Nanocrystals Embedded in Au Matrix*. J. Phys. Chem. C, **vol. 117, no. 17**:pp. 8903–8908. (Cited on page 95).

[162] Rudge AW, Milne K, Olver AD *et al.*, editors, *Handbook of Antenna Design, Vol. 1* (IET, The Institution of Engineering and Technology, Michael Faraday House, Six Hills Way, Stevenage SG1 2AY, UK, 1982). (Cited on page 95).

[163] Kim Y and Jaggard D (1986) *The fractal random array*. Proceedings of the IEEE, **vol. 74, no. 9**:pp. 1278–1280. (Cited on page 95).

[164] Lakhtakia A, Holter N, Varadan V *et al.* (1987) *Self-similarity in diffraction by a self-similar fractal screen*. IEEE Transactions on Antennas and Propagation, **vol. 35, no. 2**:pp. 236–239. (Cited on page 95).

[165] Butenko AV, Chubakov PA, Danilova YE *et al.* (1990) *Nonlinear optics of metal fractal clusters*. Z Phys D - Atoms, Molecules and Clusters, **vol. 17, no. 4**:pp. 283–289. (Cited on page 95).

[166] Shalaev VM, Stockman MI and Botet R (1992) *Resonant excitations and nonlinear optics of fractals*. Physica A: Statistical Mechanics and its Applications, **vol. 185, no. 1-4**:pp. 181–186. (Cited on page 95).

[167] Stockman MI, Pandey LN, Muratov LS *et al.* (1994) *Giant fluctuations of local optical fields in fractal clusters*. Phys. Rev. Lett., **vol. 72, no. 15**:pp. 2486–2489. (Cited on page 95).

[168] Puente-Baliarda C and Pous R (1996) *Fractal design of multiband and low side-lobe arrays*. IEEE Transactions on Antennas and Propagation, **vol. 44, no. 5**:p. 730. (Cited on page 95).

[169] Xu L, Wu Z and Wang W (1996) *Synthesis of fractal patterns from concentric-ring arrays*. Electronics Letters, **vol. 32, no. 21**:p. 1940. (Cited on page 95).

[170] Shalaev VM and Sarychev AK (1998) *Nonlinear optics of random metal-dielectric films*. Phys. Rev. B, **vol. 57, no. 20**:pp. 13265–13288. (Cited on page 95).

[171] Werner D, Haupt R and Werner P (1999) *Fractal antenna engineering: the theory and design of fractal antenna arrays*. IEEE Antennas and Propagation Magazine, **vol. 41, no. 5**:pp. 37–58. (Cited on page 95).

[172] Shalaev VM, *Nonlinear Optics of Random Media: Fractal Composites and Metal-Dielectric Films* (Springer, 2000). (Cited on page 95).

[173] Romeu J and Soler J (2001) *Generalized Sierpinski fractal multiband antenna*. IEEE Transactions on Antennas and Propagation, **vol. 49, no. 8**:pp. 1237–1239. (Cited on page 95).

[174] Gianvittorio J and Rahmat-Samii Y (2002) *Fractal antennas: a novel antenna miniaturization technique, and applications*. IEEE Antennas and Propagation Magazine, **vol. 44, no. 1**:pp. 20–36. (Cited on page 95).

[175] Wqrner D and Ganguly S (2003) *An overview of fractal antenna engineering research*. IEEE Antennas and Propagation Magazine, **vol. 45, no. 1**:pp. 38–57. (Cited on page 95).

[176] Dudley JM, Finot C, Richardson DJ *et al.* (2007) *Self-similarity in ultrafast nonlinear optics*. Nature Physics, **vol. 3, no. 9**:pp. 597–603. (Cited on page 95).

[177] Aziz RS, Alkanhal MAS and Sheta AF (2011) *Multiband Fractal-Like Antennas*. Progress In Electromagnetics Research B, **vol. 29**:pp. 339–354. (Cited on page 95).

[178] Karmakar A, Ghatak R, Banerjee U *et al.* (2013) *An UWB antenna using modified Hilbert curve slot for dual band notch characteristics*. Journal of Electromagnetic Waves and Applications, **vol. 27, no. 13**:pp. 1620–1631. (Cited on page 95).

[179] Kuzyk MG, Pérez-Moreno J and Shafei S (2013) *Sum rules and scaling in nonlinear optics*. Physics Reports, **vol. 529, no. 4**:pp. 297–398. (Cited on page 95).

[180] Yablonovitch E (1982) *Statistical ray optics*. J. Opt. Soc. Am., **vol. 72, no. 7**:pp. 899–907. (Cited on page 95).

[181] Yablonovitch E and Cody G (1982) *Intensity enhancement in textured optical sheets for solar cells*. IEEE Transactions on Electron Devices, **vol. 29, no. 2**:pp. 300–305. (Cited on page 95).

[182] Law M, Greene LE, Johnson JC *et al.* (2005) *Nanowire dye-sensitized solar cells*. Nature Materials, **vol. 4, no. 6**:pp. 455–459. (Cited on page 95).

[183] Vedantam S, Lee H, Tang J *et al.* (2009) *A Plasmonic Dimple Lens for Nanoscale Focusing of Light*. Nano Lett., **vol. 9, no. 10**:pp. 3447–3452. (Cited on page 95).

[184] Yablonovitch E (2009) *Photonics: One-way road for light*. Nature, **vol. 461, no. 7265**:pp. 744–745. (Cited on page 95).

[185] Zhang P, Chen L, Xu T *et al.* (2013) *Programmable Fractal Nanostructured Interfaces for Specific Recognition and Electrochemical Release of Cancer Cells*. Advanced Materials, **vol. 25, no. 26**:pp. 3566–3570. (Cited on page 95).

[186] Barton CC and Larsen E (1985) *Fractal Geometry of Two-Dimensional Fracture Networks at Yucca Mountain, Southwestern Nevada*. (pp. 77–84). (Cited on page 95).

[187] Hirata T (1989) *Fractal dimension of fault systems in Japan: Fractal structure in rock fracture geometry at various scales*. PAGEOPH, **vol. 131, no. 1-2**:pp. 157–170. (Cited on page 95).

[188] Mandelbrot BB, Passoja DE and Paullay AJ (1984) *Fractal character of fracture surfaces of metals*. Nature, **vol. 308, no. 5961**:pp. 721–722. (Cited on page 95).

[189] Musaev OR, Midgley AE, Wrobel JM *et al.* (2009) *Fractal character of titania nanoparticles formed by laser ablation*. Journal of Applied Physics, **vol. 106, no. 5**. (Cited on page 95).

[190] Hurd AJ and Schaefer DW (1985) *Diffusion-Limited Aggregation in Two Dimensions*. Phys. Rev. Lett., **vol. 54, no. 10**:pp. 1043–1046. (Cited on page 95).

[191] Lin S, Li M, Dujardin E *et al.* (2005) *One-Dimensional Plasmon Coupling by Facile Self-Assembly of Gold Nanoparticles into Branched Chain Networks*. Advanced Materials, **vol. 17, no. 21**:pp. 2553–2559. (Cited on page 95).

[192] Jaeger L and Chworos A (2006) *The architectonics of programmable RNA and DNA nanostructures*. Current Opinion in Structural Biology, **vol. 16, no. 4**:pp. 531–543. (Cited on page 95).

[193] Duan JW, Zheng Z, Zhou PP *et al.* (2012) *The architecture of DNA Sierpinski links*. Match-Communications in Mathematical and Computer Chemistry, **vol. 67, no. 3**:p. 817. (Cited on page 95).

[194] Shiers MJ, Leech R, Carmalt CJ *et al.* (2012) *Self-Assembled Ultra-High Aspect Ratio Silver Nanochains*. Advanced Materials, **vol. 24, no. 38**:pp. 5227–5235. (Cited on page 95).

[195] Albuquerque E, Fulco U, Freire V *et al.* (2013) *DNA-based nanobiostructured devices: The role of quasiperiodicity and correlation effects*. Physics Reports. (Cited on page 95).

[196] Darvill D, Centeno A and Xie F (2013) *Plasmonic fluorescence enhancement by metal nanostructures: shaping the future of bionanotechnology*. Phys. Chem. Chem. Phys., **vol. 15, no. 38**:pp. 15709–15726. (Cited on page 95).

[197] Lin MY, Lindsay HM, Weitz DA *et al.* (1989) *Universality in colloid aggregation*. Nature, **vol. 339, no. 6223**:pp. 360–362. (Cited on page 96).

[198] Lin MY, Lindsay HM, Weitz DA *et al.* (1990) *Universal reaction-limited colloid aggregation*. Phys. Rev. A, **vol. 41, no. 4**:p. 2005. (Cited on page 96).

[199] Lin MY, Lindsay HM, Weitz DA *et al.* (1989) *Universality of Fractal Aggregates as Probed by Light Scattering*. Proceedings of the Royal Society of London. A. Mathematical and Physical Sciences, **vol. 423, no. 1864**:pp. 71 –87. (Cited on page 96).

[200] Dimon P, Sinha SK, Weitz DA *et al.* (1986) *Structure of Aggregated Gold Colloids*. Phys. Rev. Lett., **vol. 57, no. 5**:p. 595. (Cited on page 96).

[201] Weitz DA, Huang JS, Lin MY *et al.* (1985) *Limits of the Fractal Dimension for Irreversible Kinetic Aggregation of Gold Colloids*. Phys. Rev. Lett., **vol. 54, no. 13**:p. 1416. (Cited on page 96).

[202] Weitz DA, Huang JS, Lin MY *et al.* (1984) *Dynamics of Diffusion-Limited Kinetic Aggregation*. Phys. Rev. Lett., **vol. 53, no. 17**:p. 1657. (Cited on page 96).

[203] Wilcoxon JP, Martin JE and Schaefer DW (1989) *Aggregation in colloidal gold*. Phys. Rev. A, **vol. 39, no. 5**:p. 2675. (Cited on page 96).

[204] Mulvaney P, Liz-Marzan L, Giersig M *et al.* (2000) *Silica encapsulation of quantum dots and metal clusters*. Journal of Materials Chemistry, **vol. 10, no. 6**:pp. 1259–1270. (Cited on page 96).

[205] Michieli N, Cesca T and Mattei G (2014) *Plasmonic Properties of Fractal Aggregates*. in preparation. (Cited on page 96).

[206] Meakin P (1983) *Formation of Fractal Clusters and Networks by Irreversible Diffusion-Limited Aggregation*. Phys. Rev. Lett., **vol. 51, no. 13**:pp. 1119–1122. (Cited on page 96).

[207] van Dongen PGJ and Ernst MH (1985) *Dynamic Scaling in the Kinetics of Clustering*. Phys. Rev. Lett., **vol. 54, no. 13**:p. 1396. (Cited on page 96).

[208] Cohen RJ and Benedek GB (1982) *Equilibrium and kinetic theory of polymerization and the sol-gel transition*. J. Phys. Chem., **vol. 86, no. 19**:pp. 3696–3714. (Cited on page 97).

[209] Schaefer DW, Martin JE, Wiltzius P *et al.* (1984) *Fractal geometry of colloidal aggregates*. Physical Review Letters, **vol. 52, no. 26**:p. 2371. (Cited on page 97).

[210] Brown WD and Ball RC (1985) *Computer simulation of chemically limited aggregation*. J. Phys. A: Math. Gen., **vol. 18, no. 9**:p. L517. (Cited on page 97).

[211] Meakin P and Family F (1987) *Structure and dynamics of reaction-limited aggregation*. Physical Review A, **vol. 36, no. 11**:p. 5498. (Cited on page 97).

[212] Enustun B and Turkevich J (1963) *Coagulation of colloidal gold*. J. Am. Chem. Soc, **vol. 85, no. 21**:pp. 3317–3328. (Cited on page 97).

[213] Kimling J, Maier M, Okenve B *et al.* (2006) *Turkevich method for gold nanoparticle synthesis revisited*. J. Phys. Chem. B, **vol. 110, no. 32**:pp. 15700–15707. (Cited on page 97).

[214] Buso D, Palmer L, Bello V *et al.* (2009) *Self-assembled gold nanoparticle monolayers in sol–gel matrices: synthesis and gas sensing applications*. Journal of Materials Chemistry, **vol. 19, no. 14**:pp. 2051–2057. (Cited on page 100).

[215] Sorensen CM and Roberts GC (1997) *The prefactor of fractal aggregates*. Journal of colloid and interface science, **vol. 186, no. 2**:pp. 447–452. (Cited on page 101).

[216] Falconer KJ, *Fractal geometry: mathematical foundations and applications* (Wiley, 2003), 2nd edn. (Cited on page 129).

Acknowledgments

The present thesis is the final result of three years of Ph.D fellowship. During this period, I got the opportunity to grow as as a scientist, thanks to many people inside and outside the Physics department.

The first person I'm glad to thank if Professor Giovanni Mattei, a *master* and *mentor*. He gave me a number of opportunities to expand my knowledge in the field of plasmonics and more in general of nanotechnology. Schools, courses, conferences and las but not least, always clever advices have been a huge source of ideas and knowledge. Moreover, I felt his confidence on me and my work, often encouraging and always supporting my efforts for the thesis and for the group.

Two office-mates I wat to particularly thank are Boris and Carlo. The collaboration set with Boris is one of the most profitable I've ever be in. The willingness from Carlo in performing many of the preliminar tasks for the research has been one of the keys of the several achievements of these years. Beyond the work, many exchanges of views with both Boris and Carlo, and much good time passed together will remain in my mind.

The opportunity to work with experienced people made it possible for me to learn the use of techniques and instruments from experts. I want to thank Giovanni Perotto for giving me some of the basics in the chemical-physics lab, and with AF and spectrophotometry. Valentina Bello has been so helpful in the training with electron micorscopy, thanks! Chiara introduced me in the world of synchrotron radiation, and I've greatly apreciated the work with her, which, in addition to the results of the research, offered me new occasions to learn and confront with the physics of the studied phenomena. I enjoyed the sharing of techniques, ideas, results, hints with well-prepared people such as Giovanni Pellegrini and Tiziana.

Many other people helped in making this stay at the department less stressful than it could have been: thanks for this to Andrea, Marcello, Marco, Martina, Massimiliano.

Of course, nobody can achieve any significant result alone: the support and love from Anna have been fundamental for my heart an healt; the constant presence of my parents, Angelo and Gabriella, and more in general of the family gave me the right serenity to put the best that I could in these years and in this work.